ÇUKUROVA UNIVERSITY
INSTITUTE OF NATURAL AND APPLIED SCIENCES

MSc THESIS

Tahir DURHASAN

FLOW CONTROL DOWNSTREAM OF A CIRCULAR CYLINDER BY PERFORATED SEMI CIRCULAR CYLINDER IN SHALLOW WATER

DEPARTMENT OF MECHANICAL ENGINEERING

ADANA, 2013

ÇUKUROVA UNIVERSITY
INSTITUTE OF NATURAL AND APPLIED SCIENCES

FLOW CONTROL DOWNSTREAM OF A CIRCULAR CYLINDER BY PERFORATED SEMI CIRCULAR CYLINDER IN SHALLOW WATER

Tahir DURHASAN

MSc THESIS

DEPARTMENT OF MECHANICAL ENGINEERING

We certify that the thesis titled above was reviewed and approved for the award of degree of the Master of Science by the board of jury on 08/01/2013.

.....	.....	.....
Prof. Dr. Hüseyin AKILLI	Prof. Dr. Beşir ŞAHİN	Assoc. Prof. Dr. M. Sami AKÖZ
SUPERVISOR	MEMBER	MEMBER

This MSc Thesis is written at the Department of Institute of Natural And Applied Sciences of Çukurova University.
Registration Number:

Prof. Dr. Selahattin SERİN
Director
Institute of Natural and Applied Sciences

Not: The usage of the presented specific declerations, tables, figures, and photographs either in this thesis or in any other reference without citiation is subject to "The law of Arts and Intellectual Products" number of 5846 of Turkish Republic

ABSTRACT

MSc THESIS

FLOW CONTROL DOWNSTREAM OF A CIRCULAR CYLINDER BY PERFORATED SEMI CIRCULAR CYLINDER IN SHALLOW WATER

Tahir DURHASAN

ÇUKUROVA UNIVERSITY
INSTITUTE OF NATURAL AND APPLIED SCIENCES
DEPARTMENT OF MECHANICAL ENGINEERING

Supervisor : Prof. Dr. Hüseyin AKILLI
Year: 2013, Page: 167
Jury : Prof. Dr. Hüseyin AKILLI
: Prof. Dr. Beşir ŞAHİN
: Assoc. Prof. Dr. M. Sami AKÖZ

In this study, it was aimed to control the unsteady flow occurred in the near wake of a circular cylinder in shallow water. Outer cylinders of six different porosities (β=0.3, 0.4, 0.5, 0.6, 0.7 and 0.8) and three different arc angles ($\alpha=120^o$, 150^o and 180^o) were used as control equipment. Nine different cylinder diameters (D_i=25mm, 30mm, 40mm, 50mm, 60mm, 70mm, 75mm, 80mm and 90mm) were used in order to examine the effect of the diameter ratio. The depth-averaged free-stream velocity was also kept constant as U=100 mm/s which corresponded to a Reynolds number of Re_{Do}=10,000 based on the outer cylinder diameter. The data obtained from the experiments showed that the arc angle of perforated cylinders affect flow control significantly and that the optimum arc angle was $\alpha=180^o$. It was observed that although the outer cylinders with $\alpha=120^o$ and $\alpha=150^o$ arc angle were effective on smaller diameter ratios, they lost their effectiveness on the flow structure at higher diameter ratios. The time averaged vorticity contours and Turbulence Kinetic Energy statistics show that porosity is highly effective on the flow structure. It was concluded for $\alpha=180^o$ outer cylinder arc angle that the ideal porosities in moving away the unsteady flow in the near wake of cylinder and reducing the peak magnitude of Reynolds stress were β=0.5 and 0.6. It was determined that the most effective diameter ratio with which unsteady vorticity move the point where Turbulence Kinetic Energy contours occur further downstream was D_i/D_o=0.5. D_i/D_o=0.75 was determined the most ideal diameter ratio in reducing Turbulence Kinetic energy value and the peak magnitude of Reynolds stress compare with bare cylinder case.

Key Words: Cylinder, Passive control, PIV, Shallow water, Turbulent Kinetic Energy

ÖZ

YÜKSEK LİSANS TEZİ

SIĞ SUDA DAİRESEL SİLİNDİRİN ARKASINDAKİ AKIŞIN DELİKLİ YARIM SİLİNDİR TARAFINDAN KOTROLÜ

Tahir DURHASAN

ÇUKUROVA ÜNİVERSİTESİ
FEN BİLİMLERİ ENSTİTÜSÜ
MAKİNA MÜHENDİSLİĞİ ANABİLİM DALI

Danışman : Prof. Dr. Hüseyin AKILLI
Yıl: 2013, Sayfa: 167
Jüri : Prof. Dr. Hüseyin AKILLI
: Prof. Dr. Beşir ŞAHİN
: Doç. Dr. M. Sami AKÖZ

Bu çalışmada, sığ su içerisindeki silindir arkasında oluşan daimi olmayan akışın kontrol edilmesi amaçlanmıştır. Kontrol elemanı olarak altı farklı geçirgenlik oranı (β=0.3, 0.4, 0.5, 0.6, 0.7 ve 0.8) ve üç farklı yay ölçüsüne sahip ($\alpha=180^o$, 150^o ve 120^o) dış silindirler kullanılmıştır. Çap oranının etkisini incelemek amacıyla dokuz farklı silindir çapı (D_i=25mm, 30mm, 40mm, 50mm, 60mm, 70mm, 75mm, 80mm ve 90mm) kullanılmıştır. Deneyler, serbest akım hızı U_∞=100 mm/s (Dış silindir çapına bağlı Re_{Dd}=10000) değeri için yapılmıştır. Deneylerden elde edilen verilerden delikli silindirlerin sahip olduğu yay ölçüsünün akış kontrolünde önemli derecede etkili olduğu ve en optimum yay ölçüsünün $\alpha=180^o$ olduğu gözlemlenmiştir. $\alpha=150^o$ ve $\alpha=120^o$ yay uzunluğuna sahip çeyrek dış silindirler düşük çap oranlarında etkili olmasına rağmen, yüksek çap oranlarında akış yapısı üzerindeki etkinliğini kaybettikleri gözlemlenmiştir. Zaman ortalamalı girdap konturları ve Türbülans Kinetik Enerji istatistikleri incelendiği zaman geçirgenlik oranının akış yapısı üzerinde önemli ölçüde etkili olduğu belirlenmiştir. Dış silindir yay uzunluğu $\alpha=180^o$ için silindir arkasında oluşan daimi olmayan girdapların uzaklaştırılmasında ve maksimum Reynolds gerilme değerlerinin düşürülmesinde en ideal geçirgenlik oranının β=0.5 ve 0.6 olduğu sonucuna varılmıştır. Daimi olmayan zaman ortalamalı girdapların, maksimum Türbülans Kinetik Enerji konturlarının oluştuğu noktayı aşağı akım yönünde ileriye taşımada en etkili çap oranının D_i/D_d=0.5 olduğu belirlenmiştir. Yalın silindir durumda ortaya çıkan maksimum Reynolds gerilme değerini ve Türbülans Kinetik Enerji değerini azaltmada en ideal çap oranı D_i/D_d=0.75 olarak belirlenmiştir.

Anahtar Kelimeler: Silindir, Pasif kontrol, PIV, Sığ su, Türbülans Kinetik Enerji

ACKNOWLEDGEMENTS

First of all, I would like to express my sincere gratitude to my advisor, Prof. Dr. Hüseyin AKILLI for his great guidance, support and encouragement to develop myself and my studies. Beginning and starting of this work would not have been possible without his long-sightedness and supervision.

I sincerely thank Prof. Dr. Beşir ŞAHİN for his continuous and effective advices to improve myself.

My heartfelt thanks go to Engin PINAR, Göktürk M. ÖZKAN and Muhammed M. AKSOY. They always have been with me throughout the study. Without their moral and support it might be so difficult to finish this investigation.

I want to thank, Erhan FIRAT and Bengi GÖZMEN for their continuous friendship, geniality and moral support.

I would like to acknowledge the financial support of the Scientific and Technological Research Council of Turkey (TUBITAK) for funding under contract No: 109R001

CONTENTS **PAGE**

ABSTRACT I
ÖZ II
ACKNOWLEDGEMENTS III
CONTENTS IV
LIST OF FIGURES VI
LIST OF ABBREVIATONS XIII
l. INTRODUCTION 1
1.1. Flow around a Cylinder 1
1.2. Karman Vortices and Kelvin-Helmholtz Vortices 3
1.3. Shallow Water 4
1.4. Flow Control 5
1.4.1. Passive Control 6
1.4.1.1. Splitter Plate 7
1.4.1.2. Small Cylinder 8
1.4.1.3. O-Ring 8
1.4.1.4. Base Bleed 9
1.4.2. Active Control 9
1.4.2.1. Feedback Control 9
1.4.2.2. Electro-Magnetic Control 10
1.4.2.3. Rotating Circular Cylinder 12
1.4.2.4. Rotary Oscillation of the Small Cylinders Located Downstream of the Main Cylinder 13
1.4.2.5. Wake Heating 13
1.4.2.6. Suction and Blowing 14
2. PRELIMINARY WORK 15
2.1. Flow Control Techniques 15
2.1.1. Passive Control around Single Cylinder 15
2.1.1.1. Splitter Plate 15
2.1.1.2 Base Bleed 21

2.1.1.3. Wavy Cylinder....23
2.1.1.4. Surface Protrusions....25
2.1.1.5. Control Cylinders....28
2.1.2. Active Control around Single Cylinder....29
2.1.2.1. Perturbation....29
2.1.2.2. Oscillating....31
2.1.2.3. Suction and Blowing....33
2.1.2.4. Acoustic Excitation....35
2.1.2.5. Electromagnetic Control....38
2.2. Shallow Water....39
3. MATERIAL AND METHOD....47
3.1. Experimental Arrangement....47
3.1.1. Water Channel System....47
3.2. Measurement Techniques....48
3.2.1. Particle Image Velocimetry (PIV) Techniques....48
3.2.1.1 Principles of PIV....49
3.2.1.2. PIV parameters used in this study....51
3.2.2. Experimental Model....52
3.2.2.1. Definition of the Porosity for the Meshy Cylinders....52
4. RESULTS AND DISCUSSIONS....55
4.1. PIV Experiments....55
4.1.1. Flow around a Single Cylinder....55
4.1.2. Flow around the Cylinder Surrounded by a Perforated Cylinder....58
4.1.2.1. Half Outer Cylinder Application....59
4.1.2.2. Degree of Arc $\alpha=150^{o}$ Application....94
4.1.2.3. Degree of Arc $\alpha=120^{o}$ Application....126
4.1.2.4. Effect of Outer Geometries on Flow Structure....155
5. CONCLUSIONS....157
REFERENCES....158
CIRRUCULUM VITAE....159

LIST OF FIGURES **PAGE**

Figure 1.1. The vortex shedding mechanism by Gerard (1964) 2

Figure 1.2. The Kelvin-Helmholtz vortices and the Karman vortices from circular cylinder 4

Figure 1.3. Downstream the volcanic island of Rishiri in Japan 6

Figure 1.4. Surface protrusions schematic of diagrams of models 8

Figure 1.5. Lorentz force generated by crossed magnetic fields.....11

Figure 1.6. Sketch of the cylinder equipped for experiments of Weier et. al. 11

Figure 1.7. Rotating circular cylinder flow configuration 12

Figure 1.8. Description of the relative location of the main and control cylinders.....13

Figure 2.1. Plan views of shallow wake instabilities of type "VS", "UB" and "SB", where cylinder diameter D= 430 mm, flow depth h= 30/20/11 mm, $Re_D=UD/\nu$ = 44.000 / 35.000 / 25.000, and Re_H $=UH/\nu$ = 3.100 / 1.600 /640, respectively 42

Figure 3.1. The water channel.....48

Figure 3.2. Interrogation areas 50

Figure 3.3. Calculation of the porosity, β.....52

Figure 3.4. Overview of cylinders.....53

Figure 3.5. Overview of experimental system for side view 54

Figure 3.6. Plan view of the system 54

Figure 4.1. The Reynolds shear stress, vorticity and TKE distribution downstream of the inner cylinder for different diameters, D_i.....56

Figure 4.2. The Reynolds shear stress, vorticity and TKE distribution downstream of the inner cylinder for different diameters, D_i.....57

Figure 4.3. The Reynolds shear stress distribution downstream of the half cylinder ($\alpha=180^o$) for different β cases 60

Figure 4.4. The Reynolds shear stress distribution downstream of the cylinder surrounded with half cylinder ($\alpha=180^o$) for D_i/D_o=0.25 at different β cases.....61

Figure 4.5. The Reynolds shear stress distribution downstream of the cylinder surrounded with half cylinder ($\alpha=180^o$) for $D_i/D_o=0.3$ at different β cases 62
Figure 4.6. The Reynolds shear stress distribution downstream of the cylinder surrounded with half cylinder ($\alpha=180^o$) for $D_i/D_o=0.4$ at different β cases 63
Figure 4.7. The Reynolds shear stress distribution downstream of the cylinder surrounded with half cylinder ($\alpha=180^o$) for $D_i/D_o=0.5$ at different β cases 65
Figure 4.8. The Reynolds shear stress distribution downstream of the cylinder surrounded with half cylinder ($\alpha=180^o$) for $D_i/D_o=0.6$ at different β cases 66
Figure 4.9. The Reynolds shear stress distribution downstream of the cylinder surrounded with half cylinder ($\alpha=180^o$) for $D_i/D_o=0.7$ at different β cases 68
Figure 4.10. The Reynolds shear stress distribution downstream of the cylinder surrounded with half cylinder ($\alpha=180^o$) for $D_i/D_o=0.75$ at different β cases 69
Figure 4.11. The Reynolds shear stress distribution downstream of the cylinder surrounded with half cylinder ($\alpha=180^o$) for $D_i/D_o=0.8$ at different β cases 70
Figure 4.12. The Reynolds shear stress distribution downstream of the cylinder surrounded with half cylinder ($\alpha=180^o$) for $D_i/D_o=0.9$ at different β cases 71
Figure 4.13. The variation of Reynolds $stress_{max}$ with β to demonstrate the effect of D_i/D_o 72
Figure 4.14. The vorticity distribution downstream of the cylinder surrounded with half cylinder ($\alpha=180^o$) for $D_i/D_o=0.25$ at different β cases.....74
Figure 4.15. The vorticity distribution downstream of the cylinder surrounded with half cylinder ($\alpha=180^o$) for $D_i/D_o=0.3$ at different β cases.....75

Figure 4.16. The vorticity distribution downstream of the cylinder surrounded with half cylinder ($\alpha=180^o$) for $D_i/D_o=0.4$ at different β cases 76
Figure 4.17. The vorticity distribution downstream of the cylinder surrounded with half cylinder ($\alpha=180^o$) for $D_i/D_o=0.5$ at different β cases 77
Figure 4.18. The vorticity distribution downstream of the cylinder surrounded with half cylinder ($\alpha=180^o$) for $D_i/D_o=0.6$ at different β cases 78
Figure 4.19. The vorticity distribution downstream of the cylinder surrounded with half cylinder ($\alpha=180^o$) for $D_i/D_o=0.7$ at different β cases 79
Figure 4.20. The vorticity distribution downstream of the cylinder surrounded with half cylinder ($\alpha=180^o$) for $D_i/D_o=0.75$ at different β cases 80
Figure 4.21. The vorticity distribution downstream of the cylinder surrounded with half cylinder ($\alpha=180^o$) for $D_i/D_o=0.8$ at different β cases 81
Figure 4.22. The vorticity distribution downstream of the cylinder surrounded with half cylinder ($\alpha=180^o$) for $D_i/D_o=0.9$ at different β cases 82
Figure 4.23. The TKE distribution downstream of the cylinder surrounded with half cylinder ($\alpha=180^o$) for $D_i/D_o=0.25$ at different β cases 85
Figure 4.24. The TKE distribution downstream of the cylinder surrounded with half cylinder ($\alpha=180^o$) for $D_i/D_o=0.3$ at different β cases 86
Figure 4.25. The TKE distribution downstream of the cylinder surrounded with half cylinder ($\alpha=180^o$) for $D_i/D_o=0.4$ at different β cases 87
Figure 4.26. The TKE distribution downstream of the cylinder surrounded with half cylinder ($\alpha=180^o$) for $D_i/D_o=0.5$ at different β cases 88
Figure 4.27. The TKE distribution downstream of the cylinder surrounded with half cylinder ($\alpha=180^o$) for $D_i/D_o=0.6$ at different β cases 89
Figure 4.28. The TKE distribution downstream of the cylinder surrounded with half cylinder ($\alpha=180^o$) for $D_i/D_o=0.7$ at different β cases 90
Figure 4.29. The TKE distribution downstream of the cylinder surrounded with half cylinder ($\alpha=180^o$) for $D_i/D_o=0.75$ at different β cases 91
Figure 4.30. The TKE distribution downstream of the cylinder surrounded with half cylinder ($\alpha=180^o$) for $D_i/D_o=0.8$ at different β cases 92

Figure 4.31. The TKE distribution downstream of the cylinder surrounded with half cylinder ($\alpha=180^o$) for $D_i/D_o=0.9$ at different β cases 93
Figure 4.32. The variation of TKEmax with β to demonstrate the effect of D_i/D_o....94
Figure 4.33. The Reynolds shear stress distribution downstream of arc ($\alpha=150^o$) for different β cases.....95
Figure 4.34. The The Reynolds shear stress distribution downstream of the cylinder surrounded with arc ($\alpha=150^o$) for $D_i/D_o=0.25$ at different β cases 97
Figure 4.35. The TKE distribution downstream of the cylinder surrounded with arc ($\alpha=150^o$) for $D_i/D_o=0.25$ at different β cases 98
Figure 4.36. The Reynolds shear stress distribution downstream of the cylinder surrounded with arc ($\alpha=150^o$) for $D_i/D_o=0.3$ at different β cases 99
Figure 4.37. The TKE distribution downstream of the cylinder surrounded with arc ($\alpha=150^o$) for $D_i/D_o=0.3$ at different β cases 100
Figure 4.38. The Reynolds shear stress distribution downstream of the cylinder surrounded with arc ($\alpha=150^o$) for $D_i/D_o=0.4$ at different β cases 101
Figure 4.39. The TKE distribution downstream of the cylinder surrounded with arc ($\alpha=150^o$) for $D_i/D_o=0.4$ at different β cases 102
Figure 4.40. The Reynolds shear stress distribution downstream of the cylinder surrounded with arc ($\alpha=150^o$) for $D_i/D_o=0.5$ at different β cases 103
Figure 4.41. The TKE distribution downstream of the cylinder surrounded with arc ($\alpha=150^o$) for $D_i/D_o=0.5$ at different β cases 104
Figure 4.42. The Reynolds shear stress distribution downstream of the cylinder surrounded with arc ($\alpha=150^o$) for $D_i/D_o=0.6$ at different β cases 105
Figure 4.43. The TKE distribution downstream of the cylinder surrounded with arc ($\alpha=150^o$) for $D_i/D_o=0.6$ at different β cases 106
Figure 4.44. The Reynolds shear stress distribution downstream of the cylinder surrounded with arc ($\alpha=150^o$) for $D_i/D_o=0.7$ at different β cases 107
Figure 4.45. The TKE distribution downstream of the cylinder surrounded with arc ($\alpha=150^o$) for $D_i/D_o=0.7$ at different β cases 108

Figure 4.46. The Reynolds shear stress distribution downstream of the cylinder surrounded with arc ($\alpha=150^o$) for $D_i/D_o=0.75$ at different β cases 109
Figure 4.47. The TKE distribution downstream of the cylinder surrounded with arc ($\alpha=150^o$) for $D_i/D_o=0.75$ at different β cases 110
Figure 4.48. The Reynolds shear stress distribution downstream of the cylinder surrounded with arc ($\alpha=150^o$) for $D_i/D_o=0.8$ at different β cases 111
Figure 4.49. The TKE distribution downstream of the cylinder surrounded with arc ($\alpha=150^o$) for $D_i/D_o=0.8$ at different β cases 112
Figure 4.50. The Reynolds shear stress distribution downstream of the cylinder surrounded with arc ($\alpha=150^o$) for $D_i/D_o=0.9$ at different β cases 114
Figure 4.51. The TKE distribution downstream of the cylinder surrounded with arc ($\alpha=150^o$) for $D_i/D_o=0.9$ at different β cases 115
Figure 4.52. The variation of Reynolds $stress_{max}$ and TKE_{max} with β to demonstrate the effect of D_i/D_o for $\alpha=150^o$.....116
Figure 4.53. The vorticity distribution downstream of the cylinder surrounded with arc ($\alpha=150^o$) for $D_i/D_o=0.25$ at different β cases 118
Figure 4.54. The vorticity distribution downstream of the cylinder surrounded with arc ($\alpha=150^o$) for $D_i/D_o=0.3$ at different β cases 119
Figure 4.55. The vorticity distribution downstream of the cylinder surrounded with arc ($\alpha=150^o$) for $D_i/D_o=0.4$ at different β cases 120
Figure 4.56. The vorticity distribution downstream of the cylinder surrounded with arc ($\alpha=150^o$) for $D_i/D_o=0.5$ at different β cases 121
Figure 4.57. The vorticity distribution downstream of the cylinder surrounded with arc ($\alpha=150^o$) for $D_i/D_o=0.6$ at different β cases 122
Figure 4.58. The vorticity distribution downstream of the cylinder surrounded with arc ($\alpha=150^o$) for $D_i/D_o=0.7$ at different β cases 123
Figure 4.59. The vorticity distribution downstream of the cylinder surrounded with arc ($\alpha=150^o$) for $D_i/D_o=0.75$ at different β cases 124
Figure 4.60. The vorticity distribution downstream of the cylinder surrounded with arc ($\alpha=150^o$) for $D_i/D_o=0.8$ (a), $Di/D_o=0.9$ (b) at different β cases 125

Figure 4.61. The Reynolds shear stress distribution downstream of arc ($\alpha=120^o$) for different β cases 127
Figure 4.62. The Reynolds shear stress distribution downstream of the cylinder surrounded with arc ($\alpha=120^o$) for $D_i/D_o=0.25$ at different β cases 128
Figure 4.63. The TKE distribution downstream of the cylinder surrounded with arc ($\alpha=120^o$) for $D_i/D_o=0.25$ at different β cases 129
Figure 4.64. The Reynolds shear stress distribution downstream of the cylinder surrounded with arc ($\alpha=120^o$) for $D_i/D_o=0.3$ at different β cases 130
Figure 4.65. The TKE distribution downstream of the cylinder surrounded with arc ($\alpha=120^o$) for $D_i/D_o=0.3$ at different β cases 131
Figure 4.66. The Reynolds shear stress distribution downstream of the cylinder surrounded with arc ($\alpha=120^o$) for $D_i/D_o=0.4$ at different β cases 132
Figure 4.67. The TKE distribution downstream of the cylinder surrounded with arc ($\alpha=120^o$) for $D_i/D_o=0.4$ at different β cases 133
Figure 4.68. The Reynolds shear stress distribution downstream of the cylinder surrounded with arc ($\alpha=120^o$) for $D_i/D_o=0.5$ at different β cases 134
Figure 4.69. The TKE distribution downstream of the cylinder surrounded with arc ($\alpha=120^o$) for $D_i/D_o=0.5$ at different β cases 135
Figure 4.70. The Reynolds shear stress distribution downstream of the cylinder surrounded with arc ($\alpha=120^o$) for $D_i/D_o=0.6$ at different β cases 136
Figure 4.71. The TKE distribution downstream of the cylinder surrounded with arc ($\alpha=120^o$) for $D_i/D_o=0.6$ at different β cases 137
Figure 4.72. The Reynolds shear stress distribution downstream of the cylinder surrounded with arc ($\alpha=120^o$) for $D_i/D_o=0.7$ at different β cases 138
Figure 4.73. The TKE distribution downstream of the cylinder surrounded with arc ($\alpha=120^o$) for $D_i/D_o=0.7$ at different β cases 139
Figure 4.74. The Reynolds shear stress distribution downstream of the cylinder surrounded with arc ($\alpha=120^o$) for $D_i/D_o=0.75$ at different β cases 141
Figure 4.75. The TKE distribution downstream of the cylinder surrounded with arc ($\alpha=120^o$) for $D_i/D_o=0.75$ at different β cases 142

Figure 4.76. The Reynolds shear stress distribution downstream of the cylinder surrounded with arc ($\alpha=120^o$) for $D_i/D_o=0.8$ at different β cases 143
Figure 4.77. The TKE distribution downstream of the cylinder surrounded with arc ($\alpha=120^o$) for $D_i/D_o=0.8$ at different β cases 144
Figure 4.78. The Reynolds shear stress distribution downstream of the cylinder surrounded with arc ($\alpha=120^o$) for $D_i/D_o=0.9$ at different β cases 145
Figure 4.79. The TKE distribution downstream of the cylinder surrounded with arc ($\alpha=120^o$) for $D_i/D_o=0.9$ at different β cases 146
Figure 4.80. The variation of Reynolds $stress_{max}$ and TKE_{max} with β to demonstrate the effect of D_i/D_o for $\alpha=120^o$.....147
Figure 4.81. The vorticity distribution downstream of the cylinder surrounded with arc ($\alpha=120^o$) for $D_i/D_o=0.25$ at different β cases 148
Figure 4.82. The vorticity distribution downstream of the cylinder surrounded with arc ($\alpha=120^o$) for $D_i/D_o=0.3$ at different β cases 149
Figure 4.83. The vorticity distribution downstream of the cylinder surrounded with arc ($\alpha=120^o$) for $D_i/D_o=0.4$ at different β cases 150
Figure 4.84. The vorticity distribution downstream of the cylinder surrounded with arc ($\alpha=120^o$) for $D_i/D_o=0.5$ at different β cases 151
Figure 4.85. The vorticity distribution downstream of the cylinder surrounded with arc ($\alpha=120^o$) for $D_i/D_o=0.6$ at different β cases 152
Figure 4.86. The vorticity distribution downstream of the cylinder surrounded with arc ($\alpha=120^o$) for $D_i/D_o=0.7$ at different β cases 153
Figure 4.87. The vorticity distribution downstream of the cylinder surrounded with arc ($\alpha=120^o$) for $D_i/D_o=0.75$, 0.8, 0.9 at different β cases 154
Figure 4.88. The variation of Reynolds $stress_{max}$ with β to demonstrate the effect of α for different D_i/D_o 156

LIST OF ABBREVIATONS

D_i : Cylinder diameter

D_o : Perforated cylinder diameter

β : Porosity

α : Angle of arc

d : Hole diameter

h_L : Distance between the plate surface and the laser sheet in plan view planes

h_W : Water level

U_∞ : Free stream velocity

$< u'u' >$: Streamwise Reynolds normal stress

$<\omega>$: Time averaged vorticity

TKE : Turbulent Kinetic Enerji

1. INTRODUCTION

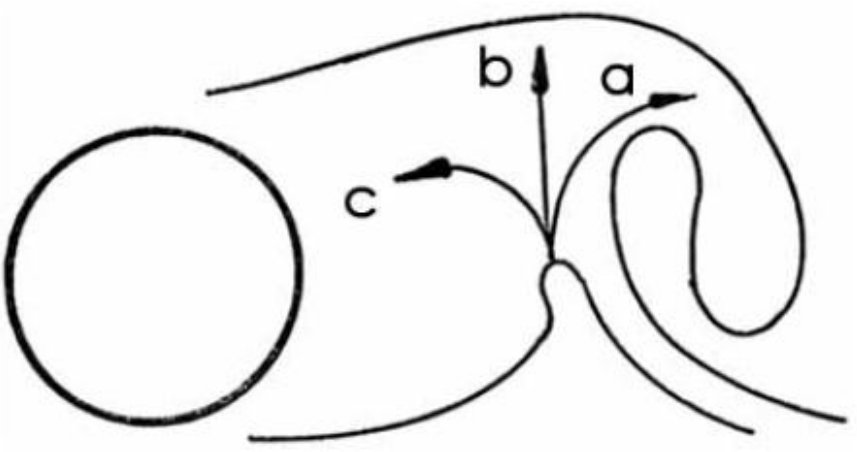
1.1. Flow around a Cylinder

Flow around bluff bodies has been the subject of intense research for decades, due to structure of flow. This structure of flow includes flow characteristics as flow separation, vortex shedding and shear layer instability. Although circular, square and rectangular cross-section cylinder have been used as a bluff body, circular cylinder is still the principal subject of researchers due to its engineering significance and in part due to its tempting simplicity in setting up arrangements in an experimental or computational laboratory.

When a fluid flows over a circular cylinder, flow separation, vortex shedding and shear layer instability etc. take place in different Reynolds numbers and as a result of these there would be unavoidable lift and drag forces exerted to the cylinder. In the absence of external forces, the dynamics of flow around a cylinder depends only on the Reynolds number ($Re = U_\infty D / \nu$ where U_∞ is the free-stream velocity far from the cylinder, d the cylinder diameter and ν the kinematic viscosity). Properties of this flow are well-known for a wide range of flow regimes, from creeping flows ($Re << 1$) to fully turbulent flows ($Re \approx 10^7$). The flow regimes at low Reynolds numbers can be classified as follows:

For $Re < 6$, the flow is steady and two-dimensional, with only one separation point, at the rear stagnation point. In the range $6 < Re < 47$, the flow is still steady and two-dimensional, but a vortex pair appears behind the cylinder, whose recirculation length increases linearly with *Re*. At the critical Reynolds number ($Re \approx 47$), unsteadiness arises spontaneously even though all the imposed conditions are being held steady and vortex shedding appears behind the circular cylinder, resulting in the well-known von Karman vortex street. When a vortex is shed from one side of the cylinder, a negative pressure pulse is generated on the side whereas a positive pressure pulse is generated on the other side; alternate vortex shedding from the upper and lower sides of the cylinder produces negative and positive pulses alternately and thus produces sound pressure waves on both sides; the frequency of

the sound pressure waves is the same as that of vortex shedding as well as the fluctuation frequency of the lift force.



Figue 1.1. The vortex shedding mechanism by Gerard (1964)

When Re <200, vortex shedding occurs in the near wake behind the cylinder accompanying a periodically oscillating lift force. Each half of the period, a vortex breaks off, so the surface pressure distribution around the cylinder changes dramatically as the cylinder experiences a sudden impulse. These vortices generate alternating high and low pressure regions on the lee side of the body in such a way that the cylinder experiences a periodic net force. This oscillation may amplify the vortex shedding, because now the cylinder itself is moving in the flow, forcing the vortex street to occur with large amplitude. The frequency of the vortices is given by dimensionless Strouhal number St (Strouhal number, S_t = f D/ U_∞, where *f* is the frequency, D is the cylinder diameter, U_∞ is the free-stream velocity, and the vortices produced in this manner are termed Strouhal vortices.

Finally for higher values of Re, that is, when Re > 200, the flow becomes three-dimensional and turbulent.

1.2. Karman Vortices and Kelvin-Helmholtz Vortices.

Two types of streamwise vortices have been reported in the laminar and transitional wakes of cylinders. At a sufficiently high value of Reynolds number, so-called "transition waves" appears in the shear layer separating from the surface of the cylinder. These waves are detectable in the region of the wake extending from the separation point on the body to the first appearance of the large-scale Karman vortex. As a result, a vortex is shed from the cylinder when the local pressure changes each time. Therefore, the cylinder is subjected to a fluctuating drag and lift in addition to the mean drag and lift. The drag, lift and vortex shedding frequency are normally expressed in non-dimensional forms as the drag coefficient C_D, the lift coefficient C_L, and the Strouhal number St. These three non-dimensional parameters depend on the nature of both the approaching flow and the cylinder. When the cylinder is located near a plane boundary, the bed proximity and the velocity gradient in the boundary layer, as well as the turbulent characteristics of the boundary layer, also have some influence on these parameters.

When the value of Reynolds number is sufficiently high, then these transition waves take the form of train of Kelvin-Helmholtz vortices shown in Figure 1.1. In the bluff body community, these small-scale vortices are often referred to as Bloor-Gerrard vortices. The onset of "transition waves" is expected to be strong function of the disturbance level of the free stream, in view of the fact that they arise from convective-type instability, as described by Ho and Huerre (1984). Bloor (1964) detected the small-scale vortices for the range of Reynolds number Re>1300, however, Ünal and Rockwell (1988) first noted these vortices at Re_d=1900. Wu et al. (1994) discussed the possible influence of background disturbance levels and observed these waves over the range of Reynolds numbers $1000 \leq Re \leq 3000$.

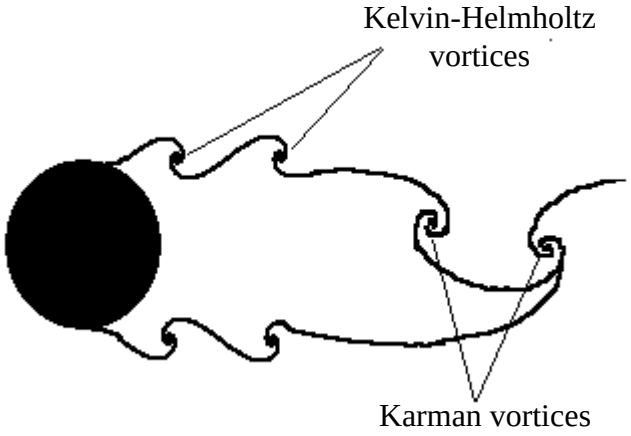


Figure 1.2. The Kelvin-Helmholtz (secondary) vortices and the Karman vortices from circular cylinder.

Kelvin-Helmholtz vortices in the shear layer are an essential feature of the transition from a laminar to turbulent state. As a consequence of this transition process, the first Karman vortex formed from the cylinder at Re_D=5000 is essentially turbulent. A Karman vortex from circular cylinder is shown in figure 1.2.

1.3. Shallow Water

A shallow flow is one in which the horizontal dimensions are much larger than the vertical extent and the vertical component of water particle acceleration is negligible compared with the horizontal acceleration components so that the pressure variation can be assumed hydrostatic. Typical examples include wide rivers, lakes, coastal lagoons (Figure 1.4), estuaries, and so on. The majority of the whole world's population resides near to these areas. Hence, better understanding of the shallow flow hydrodynamics and related processes, such as flooding, sediment transport, spreading and mixing of pollutant and its effects on water quality, is of great importance. Mathematically, shallow flow hydrodynamics may be approximated by the shallow water equations, which include the continuity equation and the x- and y-direction momentum equations, and can be derived by depth integrating the three-dimensional Navier-Stokes equations.

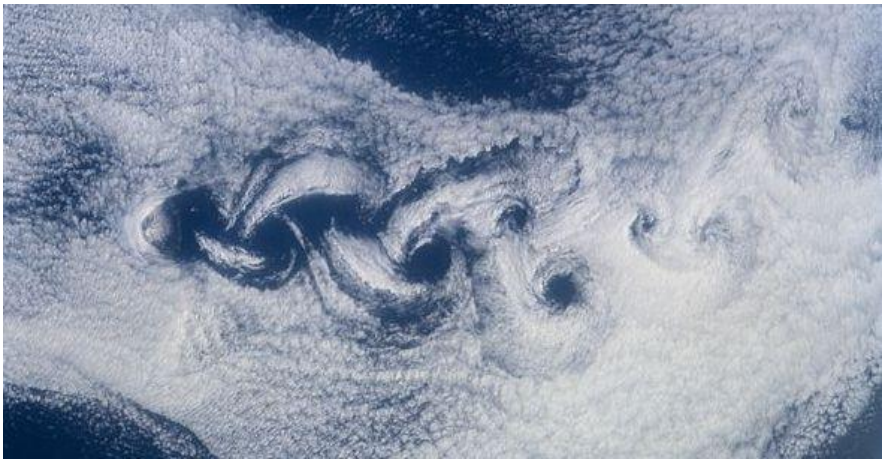


Figure 1.3. Downstream the volcanic island of Rishiri in Japan

Both the bottom friction and kinematical restriction in the vertical direction will dramatically change the wake behavior of cylinder developed in shallow water. The bottom friction generates small-scale, three-dimensional turbulent motions (limited by water depth), which act as an energy sink for the horizontal large-scale transverse motions through the existence of the bottom shear stress. The stabilizing influence of the bottom frictions tends to suppress the self-excited disturbances in the form of horizontal quasi two-dimensional vortex structures.

The study of wakes flows behind cylindrical bodies in shallow turbulent shear flow contributes to the understanding of genesis and preservation principles of the associated large scale eddy structures and helps us to quantify their transport characteristics for momentum and mass.

1.4. Flow Control

If a bluff body exposed to a flow having sufficiently high Re Numbers, the flow separates from a wider section of the body resulting in periodic vortex shedding. This condition results in a significant pressure drop on the rear surface of the body. Vortex shedding from bluff bodies causes serious structural vibrations, acoustic noise and resonance, enhanced mixing (which is also advantageous for better heat transfer) and increases in the mean lift and drag fluctuations. Hence,

effective control of the vortex shedding is very important in many engineering applications.

Roshko first measured the period of Karman vortex shedding behind a bluff body in 1955 and after his invention researchers started to investigate the vortex shedding and near-wake flows. Furthermore, investigators focused on suppression of the vortex shedding since it is a serious problem for many areas of science.

In this manner, many passive and active control methods were carried out to control vortex shedding behind a two-dimensional bluff body, such as a circular cylinder and a two-dimensional blunt-based bluff body. Examples include base bleed, splitter plates, stream-lining the structural geometry, oscillation, suction and blowing, acoustic excitation, and electromagnetic control. For these control techniques, a classification may be done by dividing the control methods into two categories, namely passive and active flow control.

1.4.1. Passive Control

Passive control techniques modify a flow without external energy expenditure. Passive control techniques control the vortex shedding by modifying the shape of the bluff body or by attaching additional devices in the flow stream. Passive control techniques include geometric shaping to manipulate the pressure gradient, the use of fixed mechanical vortex generators for separation control, and placement of longitudinal grooves or riblet on a surface to reduce drag.

Passive control techniques are widely used for flow control applications. they have same advantages of being easier to implement, less expensive in cost, and more stable. The methods have proved successful particularly in offshore explorations and marine hydraulics.

Roshko, 1954 and Zdravkovich, 1981 are among the first investigators, Zdravkovich, 1981 presents control techniques that can be classified into three categories:

(i) The control of shear layer by surface protrusion (tripping wire, fin, helical strakes, helical wires, studs, etc.), which affects flow separation lines (James and

Truong, 1972); this can be further subdivided into omnidirectional and unidirectional. The omnidirectional techniques are those not affected by the direction of flow velocity; for example, helical strakes, helical wires. The unidirectional are those effective only for a given direction of flow velocity; for example, straight fins. The full shrouds are omnidirectional, while incomplete shrouds become unidirectional.

(ii) The control of the entrainment layers by shrouds (perforated gauze, axial rods, etc.) that supply irrotational fluid to the entrainment layers (Knell, 1969)

(iii) The instability control of wakes by near-wake stabilizers (splitter plate, guiding plates, base-bleed, slits cut along the models, etc.) that reduce the interaction of two opposite shear layers (Roshko, 1954, Bearman, 1965, Wood, 1967, Aplet, West and Szewczyck, 1973).

1.4.1.1. Splitter Plate

Controlling vortex shedding by a splitter plate is one of the most successful methods. The use of splitter plates to control bluff bodies' vortex shedding provides an important change in flow structure behind the cylinder. A short splitter plate is placed along the wake center plane. Attached plates perform great changes on the shedding frequency depending on the length. At high Reynolds number, the vortex shedding frequency doesn't decrease monotonically as the length of the splitter plate increases; the shedding frequency decreases for $l<D$ and increases for $D<l<2dD$, and then it decreases as the length of the plate further increases.

The vortex shedding behind a circular cylinder completely disappears when the length of the splitter plate is larger than a critical length, and this critical length is found to be proportional to the Reynolds number.

The net drag is significantly reduced by the splitter plate, and there exists an optimum length of the plate for minimum drag at a given Reynolds number.

This optimum length of the plate is nearly the same as the size of the time-averaged deformed separation bubble due to the plate.

1.4.1.2 Small Cylinder

Vortex shedding past a circular cylinder is controlled over a limited range by the proper placement of a smaller control cylinder close to the main cylinder. There exists a domain close to the main cylinder where the placement of a control cylinder can completely suppress the vortex shedding for flows at a Reynolds number of 80 or less. The actual extent of this domain depends on the Reynolds number of the flow and the ratio of the diameter of the both two cylinders. Even though the flow remains unsteady for Reynolds numbers larger than 80, the presence of the control cylinder has a significant effect on the flow. It has also been reported that in certain cases suppression of vortex shedding is accompanied by a significant reduction in the mean drag coefficient.

1.4.1.3 O-Ring

O-rings are installed as surface protrusions for controlling the flow around a cylinder. The test cylinders are supported at both sides using identical load-cells: one for measuring force and the other a dummy for balancing.

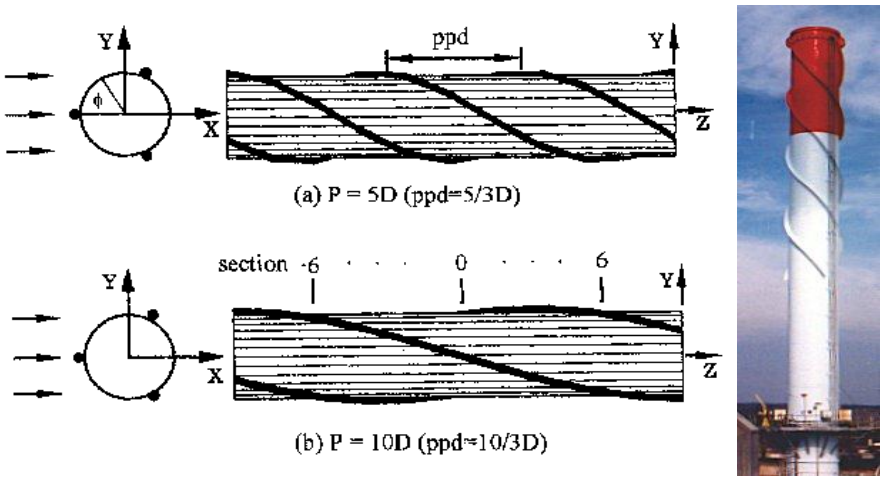


Figure 1.4. Surface protrusions schematic of diagrams of models

1.4.1.4 Base Bleed

Another well-known method for the suppression of vortex shedding from bluff bodies consists in bleeding fluid from the blunt base. The aim is to suppress vortex shedding completely at some supercritical Reynolds number by base bleed.

1.4.2. Active Control

Active control methods, applying some sorts of energy into the flow, have been developed in order to solve vortex shedding problems. The aim of active control is to exploit the instability of the wake, which is the cause of the vortex formation, to indirectly modify the mean wake velocity profile and drag.

There are two primary advantages to active flow control that aren't achievable by passive techniques. First active flow control technology leverages and controls a natural stability of the flow to attain a large effect using small localized energy input. Control is most effective when the control input is introduced locally at a high receptivity region. Secondly, active control can be used to control complex, dynamical processes like turbulence production in turbulent boundary layers to reduce skin friction and hence viscous drag where the reduction is proportional to the surface area covered by the actuators. On the other hand, to put energy from outside is the disadvantage of the active control techniques. There are various active control techniques such as; feedback control, electro-magnetic control, rotating circular cylinder, wake heating, suction and blowing.

1.4.2.1 Feedback Control

Feedback control method has been studied by many researchers in the past two decades. This control method has applied to various problems in thermal and fluid engineering. Very recently; the effect of the feedback control on the fluid force on the cylinder was examined experimentally by Fujisawa et al. (2001).

A hot-film probe, a phase shifter, amplifiers and a dynamic shaker are used to apply feedback control method. In order to produce strong signal of vortex shedding, the hot-film probe is placed in one of the shear flows of the wake. The signals from the feedback probe are phase-shifted and amplified to drive the shaker which is connected to the cylinder to generate perturbations in the wake. A monitor hot-film probe is also placed in the wake to assess the control effect on vortex shedding. Signals from both the feedback and the monitor probes are converted into frequency spectra by a computer.

So as to measure the controlled flow field parameter, a sensor is also placed downstream of the actuator in the feedback control loop.

1.4.2.2 Electro-Magnetic Control

The main advantage of electromagnetic control strategy for electrically conducting fluids is that the Lorentz force acts as a volume force inside the fluid, and it may be tuned to act only in specific region of the flow. Many techniques using electric and magnetic fields have been developed in weakly conducting fluids since 1960s so as to achieve turbulent boundary layer control, transition delay and drag reduction.

The cylinder body is covered with electrodes and the permanent magnets side by side in the order positive electrode, N-pole magnet, negative electrode, S-pole magnet, a sequence which is repeated once more ending with a positive electrode in the axial direction of the circular cylinder. So, the Lorentz force occurs (acts) in the circumferential direction of the cylinder. If it is desired Lorentz force's direction can be changed by altering the poles of the each electrode.

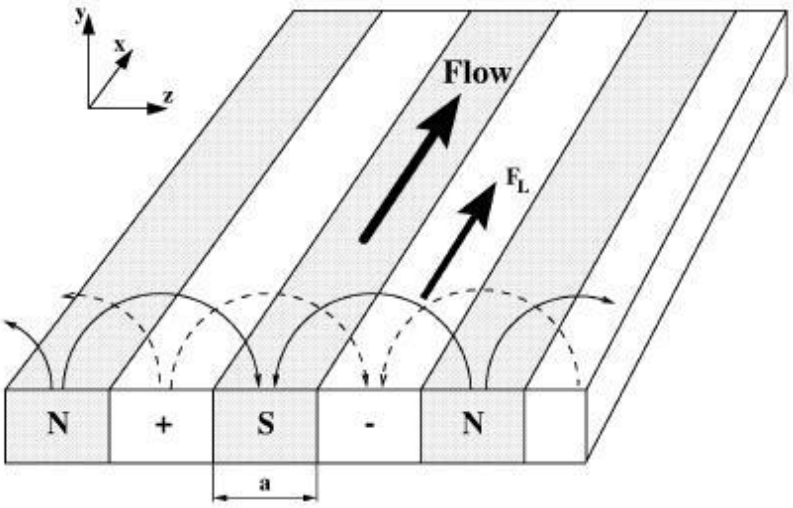


Figure 1.5. Lorentz force generated by crossed magnetic fields

Weier et. al.(1998), visualized the flow field at Re=760, using a 2 cm diameter circular cylinder and numerically simulated at Re=200 under the Lorentz Force directed with the mean flow in the range from 5° to 175° from the stagnation point along the cylinder circumference. Figure 1.6 shows a sketch of the cylinder used for the experiments.

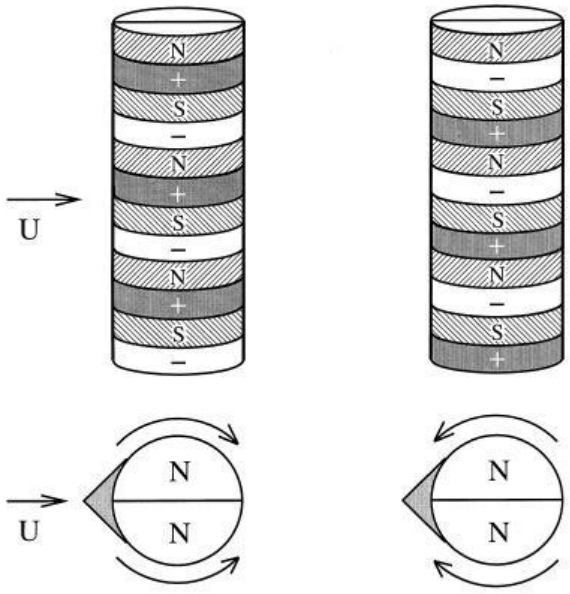


Figure 1.6. Sketch of the cylinder equipped for experiments of Weier et. al.

1.4.2.3 Rotating Circular Cylinder

The flow is controlled by a rotating circular cylinder which is placed in the flow field. At this control method, the forcing frequency and natural shedding frequency are observed: when the forcing frequency is lower than the natural shedding frequency an initial clockwise vortex is formed on the lower half of the cylinder when the cylinder is rotated in the counter-clockwise direction and a counter-clockwise vortex is formed on the upper half when the clockwise rotation starts. This leads to a non-synchronized vortex formation mode which can not lead to the suppression of Karman vortex shedding.

When the forcing frequency is higher than the natural shedding frequency an initial reactive clockwise vortex is formed on the upper half of the cylinder when the cylinder is rotated in the counter clockwise direction and a counter clockwise vortex is formed on the lower half when the clockwise rotation starts which leads to a synchronized vortex mode (this is one of the reasons why the optimal values for the forcing frequency obtained in the previous section cannot be lower than the vortex shedding frequency).

The behavior of the drag coefficient C_D is determined by the fact that flow separation is a major source of pressure drag and the moving-wall effects will postpone this separation. Separation is completely eliminated on the side of the cylinder where the wall and the free-stream move in the same direction and on the other side of the cylinder separation is developed only incompletely.

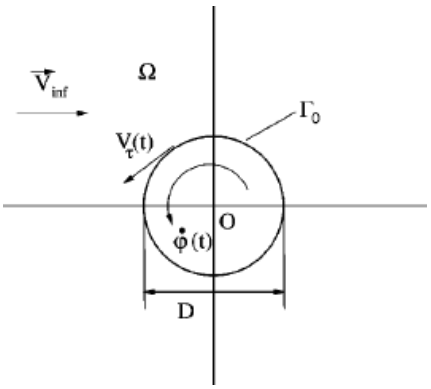


Figure 1.7. Rotating circular cylinder flow configuration

1.4.2.4 Rotary Oscillation of the Small Cylinders Located Downstream of the Main Cylinder

The flow is aimed to control by using small amplitude transverse cylinder oscillations with displacement of a few percent of the cylinder diameter in this technique. Near the main cylinder, two control cylinders are placed and these control cylinders rotate with an obvious rate.

Utilizing rotating control cylinders depends on a variety of parameters. Some of them are the relative sizes of the main and control cylinders, their relative arrangements, and the rotation rate of control cylinder.

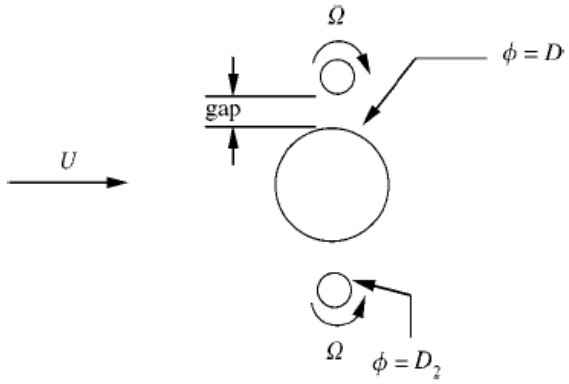


Figure 1.8. Description of the relative location of the main and control cylinders

1.4.2.5. Wake Heating

The control of vortex shedding downstream of a horizontal cylinder or a flat ribbon can be easily realized using heat input to the cylinder. In air flow, increase of the heat input to the cylinder or ribbon leads to a suppression of the vortex shedding while in a liquid flowing around a heated cylinder or ribbon the effect is the opposite. However in liquids the range of heating conditions where the buoyancy effects can be ignored is more limited.

Behaviours of liquids and gases are opposite. And this suggests that this control is due to both changes of dynamic viscosity and density with temperature and does not only dependent on density changes as claimed by Yu and Monkewitz

(1990). This opposite behaviour found in air and in water suggests that the effect of the change of viscosity is predominant. The changes of the density and the viscosity due to the heating of the near wake lead to slight changes in velocity profiles and consequently instability conditions and amplitude of the shedding vortices.

1.3.2.6. Suction and Blowing

One of the methods of active control is suction and blowing. When wake flows controlled by suction and blowing, the flow's global stability state can be interpreted by considering the modification of the near wake profiles, and its implications on the flow's stability properties. There are two main effects of suction applied to cylinder base: the suction increases the magnitude of negative velocities, which acts in favour of instability increase in terms of local temporal growth rate increase. The second effect of suction is that it decreases the length of the recirculation zones and thus decreases the streamwise extent of absolute instability.

On the other hand, the effects of blowing are opposite to suction's effects: linear temporal growth rates in the near wake are expected to decrease, due to decreased back flow, and the extent of absolute instability is expected to increase. Therefore, in both cases, one has to rely on phenomenological observations, to determine which action prevails for a given combination of the problem parameters.

2. PRELIMINARY WORK

2.1. Flow Control Techniques

2.1.1. Passive Control around Single Cylinder

A selective review of various aerodynamic passive control measures which could be adopted to reduce vortex induced vibrations (most general type of flow-induced vibration) is presented by Kumar et al. (2007). They introduced recent patents on this topic and concluding with notes on the current and future developments expected in the passive control of VIV. As mentioned by this study, there are various types of passive control technique in literature which are presented in next sections.

2.1.1.1. Splitter Plate

For a Reynolds number of 1.45×10^4, (Roshko, 1954.) was notably one of the first to report periodic vortex formation suppression using a circular cylinder connected with a splitter plate. He also showed that, by positioning this splitter plate at different fixed distances in the fully developed cylinder-wake, the Strouhal number St diminishes as the distance between the cylinder and the plate increases up to a limit position (G ≈2.7D). He also observed that a splitter plate of chord 5D, attached to the cylinder, results in suppression of shedding. A plate of chord 1D does not inhibit formation of vortices but changes the shedding frequency slightly.

Roshko (1955) observed flow changes at $Re_D=1.45\times10^4$ when splitter plates were inserted behind a cylinder. When the plate was attached on the cylinder base and the length of the splitter plate (l) was larger than 5D, the vortex shedding disappeared, and thus drag was significantly reduced. On the other hand, he also observed flow changes as the plate of l=d moved downstream. When the splitter plate was located downstream less than 4d, the Strouhal number decreased and the base pressure increased as the splitter plate moved downstream. However, when the

splitter plate was located farther downstream, the flow field did not show much difference from the natural vortex shedding.

Bearman (1965) investigated the flow behind a two-dimensional model with a blunt trailing edge and fitted with splitter plates at Reynolds numbers between 140000 and 256000. He measured base pressure and shedding frequency and showed that the existence of a splitter plate increases the base pressure significantly (thereby reducing the pressure drag), even for very short plate length. These studies suggest that the effect of the splitter plate and base bleed is to delay the upper and lower separated shear layers interacting with each other and hence they increase the formation length (position at which the vortices are fully formed or, in a time-average sense, the length of the mean recirculation region). As a result, vortex shedding disappears for a connected splitter plate length Lsp equal to 2D.

Gerrard (1966) studied a mechanism of vortex generation behind a cylinder. He conducted experiments at $Re_D=2\times10^4$ to study the vortex size, frequency, and effect of the splitter plate attached on the cylinder, effects of free-stream turbulence. From that study, he showed that the Strouhal number decreased when the length of the splitter plate was smaller than d, but it increased for $D<L<2D$. He also showed that the swirling formation zone is under a strong elongation in the presence of a SP and that two modes of swirling formation could appear according to the length of the separating element and its distance from the model.

Unal and Rockwell (1987) divided the wake region into two separate regions: the pre-vortex formation region and the post-vortex formation region. They found that the pressure on the splitter plate was suddenly changed when the plate moved from the pre-vortex formation regime to the post-vortex formation regime.

Vortex shedding from bluff bodies with splitter plates was experimentally investigated by Nakamura, 1996. It was shown that vortex shedding from bluff bodies with extended splitter plates is characterized by the impinging shear layer instability, where the Strouhal number in terms of splitter plate length increases stepwise with increasing splitter plate length.

Recently, Kwon and Choi (1995) investigated the effect of the splitter plate on laminar vortex shedding behind a circular cylinder at Reynolds numbers of 80-160.

They showed that for $Re_D \geq 120$ the shedding frequency changed similarly as just described, whereas for $Re_D \leq 100$ the shedding frequency monotonically decreased as the plate length increased. They attributed the increased shedding frequency at L >D in the case of $Re_D \geq 120$ to a generation of the secondary vortex at the tip of the splitter plate. This secondary vortex near the tip of the splitter plate may also be a strong source of the flow-induced noise.

Cimbala and Garg (1991) investigated the effect of the attached splitter plate on the flow characteristics behind a fixed cylinder and a freely rotating cylinder, respectively. For the case of a freely rotating cylinder, the flow field with the plate of L>2D was similar to that of the fixed cylinder with an attached plate. However, when L<2D, the flow field was similar to that without the splitter plate. They also showed for the case of a fixed cylinder that the Strouhal number increased for D<L<2D and it decreased as the length of the plate further increased.

An experimental investigation was carried out by Mansingh and Oosthuizen, (1990) to study the effect of a splitter plate on the two-dimensional wake of a bluff body with fixed separation points. This experimental study has shown that the characteristics of the wake downstream of a bluff body with fixed separation points can be considerably altered by placing a splitter plate on the wake centerline downstream of the bluff body. The effect of splitter plates on the wake flow characteristics of a rectangular cylinder with a splitter plate shows a relatively small change in Reynolds number.

Miau, et al. (1993) carried out measurements of instantaneous pressure fluctuations on a trapezoidal cross-sectional cylinder. Their results indicate that the low frequency variations embedded in the vortex-shedding process can be successfully suppressed by insertion of a splitter plate whose length is twice the maximum width of the trapezoidal cylinder.

The angular motion of a freely rotatable cylinder with splitter plate has been studied numerically by Xu et al. , (1993). It is found that, for subcritical Reynolds numbers, the splitter plate aligns itself in the flow direction. On increasing the Reynolds number, a symmetry breaking bifurcation appears and the splitter plate migrates to a stable off-axis position.

Unal and Rockwell (1988) carried out a similar study with a plate that is detached from the cylinder. They found that by placing the plate appropriately, compared to a cylinder with no control, it is possible to obtain more than double the vortex formation length. For low Re the vortex shedding is completely eliminated while for higher Re the large scale shedding is suppressed but the shear layer instability remains.

Ozono (1999) studied the effect of a plate of length 1D kept at various locations, including those away from the wake centerline, downstream of the cylinder for $6.7\times10^3 < Re_D < 2.5\times10^4$. Beyond a certain critical gap between the plate and the cylinder, for a certain range, the Strouhal number exceeds the natural one. This is because of a flow mode in which the shear layer separated from the cylinder is forced to interact with the splitter plate.

The flow around a circular cylinder with a few interference elements shifted along the wake was investigated (Ozono, 2003). It was concluded that the vortex shedding can be suppressed critically even when the splitter plates are asymmetrically arranged behind the cylinder.

Lin and Wu (1994) conducted a numerical study for the Re_D =100 flow to see the effect of a splitter plate. They found that a splitter plate of length 2D attached to the cylinder is sufficient to completely suppress vortex shedding. It was also found that a splitter plate whose upstream edge is located at more than 2.5D from the cylinder is ineffective of suppressing vortex shedding.

Roshko (1993) controlled the flow around a circular cylinder by attaching a splitter plate behind the cylinder and investigated the suppression of vortex shedding. When the gap between the cylinder and splitter plate was large, the effect of the splitter plate became strong. The parameter that had the greatest effect on the vortex shedding was the gap width rather than the length of splitter plate.

Zhou et al. (2005) conducted a numerical study on suppression of fluid forces on a square cylinder in cross-flow controlled by a flat plate. They found that the existence of the control plate changes the flow features in front of the square cylinder totally. The drag acting on the square cylinder and the total drag acting on the 2 bodies (the square cylinder together with the control plate) are normally reduced by

the control plate. The maximum reduction of the drag acting on the square cylinder and the optimum position of the control plate are given for a particular control plate height. They also revealed that the amplitude of the fluctuating lift on the square cylinder is well suppressed if the control plate is used. The fluctuating lift can be completely suppressed if the control plate with a certain height is placed at an appropriate position.

Akıllı et al. (2005) investigated the effect of splitter plate on the suppression of vortex shedding in shallow water using the Particle Image Velocimetry (PIV) technique. Splitter plates with a length of 50 mm, which is equal to the diameter of the cylinder (D), were used during the experiments. Gap distance between the base of the cylinder and the leading edge of the splitter plate ranged from 0 to 2D. Velocity vector field and corresponding vorticity contours and streamline topology and Reynolds stress concentrations were used to explain the characteristics of the flow. The splitter plates having different thicknesses presented the same influence on the flow characteristics. The splitter plate has a substantial effect on suppression of the vortex shedding for the gap ratio between 0 and 1.75D. In this gap ratios, shear layers extend up to the trailing edge of the splitter plate preventing the entrainment of the free- stream flow into the base region. For G/D=1.75, the normalized Reynolds stress has a peak value of 0.0158 which is approximately 8.5 times smaller than the concentrations occurring for a bare cylinder. After passing the splitter plate, the flow starts to oscillate with smaller frequency compared to the natural frequency of the bare cylinder. When the splitter plate was located at 2D location, no effect of the splitter plate was observed.

Akıllı et al. (2008) investigated experimentally passive control of vortex shedding behind a circular cylinder by splitter plates of various lengths attached on the cylinder base in shallow water flow (Re=6300). At this study the length of the splitter plate was varied from L/D=0.2 to L/D=2.4 in order to see the effect of the splitter plate length on the flow characteristics. Instantaneous and time-averaged flow data clearly indicate that the length of the splitter plate has a substantial effect on the flow characteristics. They found the flow characteristics in the wake region of the

circular cylinder sharply change up to the splitter plate length of L/D=1.0. and above this plate length, small changes occur in the flow characteristics.

Turki (2008) numerically investigated the passive control of flow by introducing a splitter plate behind a square cylinder inside a horizontal channel at Reynolds number range of $110 \leq Re \leq 200$ and for a fixed blockage ratio of $\beta = h/H = 1/4$ and a fixed position of the square cylinder. In examining the instantaneous flow fields, he found that the critical length of the splitter plate L_c, characterizing the disappearance of vortex shedding, can be correlated by a linear relationship: $L_c = 0.0373\ Re – 3.4373$. He also analyzed the effect of the splitter plate length and its location in the wake region on the Strouhal number, and the drag and lift coefficients. He came on the conclusion that, by varying the splitter plate length, the Strouhal number shows two different behaviors for the Reynolds number investigated. And finally he observed that in the variation of the Sr and the C_d with the splitter plate location G and for *Re* = 150 and 200, a sudden increase in those quantities was noticed at the optimal location of G= 3.27.

Shukla et al. (2009) studied the problem of a hinged-splitter plate in the wake of a circular cylinder where the splitter plate can rotate about the hinge at the base of the cylinder due to the unsteady fluid forces acting on it, and hence the communication between the two sides of the wake is not totally disrupted as in the rigid splitter plate case. They investigated that this problem in the limit where the stiffness and internal damping associated with the hinge are negligible, and the mass ratio of the splitter plate is small. It is concluded that the splitter plate oscillations increase with Reynolds numbers at low values of Re, and are found to reach a saturation amplitude level at higher Re, Re > 40000.

Assi et al. (2009) achieved suppression of cross-flow and in-line VIV of a circular cylinder, with resulting drag coefficients less than that for a fixed plain cylinder using two-dimensional control plates. He demonstrated how vortex-induced vibration can be practically eliminated by using free-to-rotate, two-dimensional control plates and further conclusion is that these devices achieve VIV suppression with drag reduction. He found the largest drag reduction to have a drag coefficient

equal to about 60% of that for a plain, fixed cylinder over the Reynolds number range of the experiments, up to 30 000.

Assi et al. (2010) studied on a pair of circular cylinders to investigate the effectiveness of pivoting parallel plates as wake-induced vibration suppressors. Measurements of amplitude of vibration and average drag are presented for a circular cylinder, free to respond in the cross-flow direction, with mass ratio of 2 and a damping level of 0.7% of critical damping. Reduced velocities were up to nearly 30, with associated Reynolds numbers up to $2.3x10^4$ and the results presented are for a centre-to-centre separation of cylinders of 4 diameters. They showed how vortex-induced vibration and wake-induced vibration of the downstream cylinder of a tandem pair can be practically eliminated by using free to rotate parallel plates. They also presented the results for a single splitter plate and helical strakes for comparison, however they were found not to be effective in suppressing wake-induced vibration.

2.1.1.2. Base Bleed

In essence, Chen and Jirka, (1995) demonstrated that it is possible to completely attenuate the mechanism of absolute (global) instability leading to large-scale vortex formation in the shallow wake.

This result is in accord with the investigation of a wake of very large spanwise extent past a porous plate, investigated by Inoue (1985).

These findings build upon the earlier investigation of Castro (1971), who demonstrated attenuation of the near-wake vortex formation via base bleed from porous plates of large spanwise extent.

Base bleed has also been shown to substantially alter the formation process of vortices from a streamlined body with a blunt trailing edge, as demonstrated by Wood (1964, 1967) and Bearman (1967).

Another approach, which is equivalent to the aforementioned concept of base bleed, is self-bleed through a slit cut along the entire span of the cylinder, as described by Igarashi (1978), who demonstrated that the region of vortex formation was displaced significantly downstream, relative to the case of a plain cylinder.

Wong (1985) pursued a more advanced approach involving self-injection at two locations near the base of the cylinder, whereby the injection flow was through an annulus opened at the forward stagnation point. This technique was applied to an elastically mounted cylinder, and it was demonstrated that vibrations could be suppressed completely when the effective injection rate was very small. In all of these investigations involving base bleed, with some exceptions, relatively little information is available on the quantitative flow structure associated with the concept of base bleed.

More recently, in a somewhat broader sense, Amitay et al. (2004) studied wake interference through synthetic surface jets in an effort to alter the aerodynamic performance of two dimensional circular cylinders.

Patnaik and Wei (2002) injected angular momentum into the base region of square cylinders at low Reynolds number to suppress the wake instability, while Lu et al. (1999) reported drag reduction and wake stabilization benefits from base bleeding in spheres. The effects of base bleed (or base injection) in the generic two-dimensional square cylinder configuration have not been studied previously in detail and also only a limited amount of information on the performance of this type of wake interference has been reported for the studied aerofoil type geometries. Additionally the potential value of the above setup or other variants of similar type within the context of an active or passive control flow device warrants further investigations into the details of these complex unsteady separated flows.

Baek and Karniakidis (2009) numerically investigated the hydrodynamic effect of a slit in circular cylinders with the goal of finding a geometric modification that minimizes vortex-induced vibrations (VIV) without any energy consumption. A slit parallel to the incoming flow is introduced and found to be very effective in suppressing VIV by either weakening or detuning vortex shedding. Through a series of simulations, they found the optimal size of the slit to suppress VIV at Reynolds number of 500; this size is smaller at a higher Re = 1000. They confirmed the effectiveness of the slit in suppressing VIV over a wide range of values of the reduced velocity. They also reported that the jet flow through a slit changes the stability in the wake of cylinder by inducing two small pockets of absolute instability

at the back of the cylinder followed by bands of convectively and absolutely unstable regions.

2.1.1.3. Wavy Cylinder

In recent years, increasing attention has been focused on the three-dimensional phenomena in the nominally two-dimensional flow behind a smooth cylinder. As a natural extension of these studies, there has been heightened interest in the flow around cylinders with a wavy geometry. Certain wavy cylinder geometries have been found to bring about considerable drag reduction and suppression of vortex-induced-vibration (VIV) (Bearman and Owen 1998; Owen et al. . 2001), making them suitable for passive flow control. This characteristic has further prompted several studies on flow around wavy cylinders by measuring the drag force, surface pressure and flow velocity profiles.

Bearman and Tombazis (1993) and Tombazis and Bearman (1997) investigated the three-dimensional features of the wake behind a blunt-based model with a wavy trailing edge at a Reynolds number of 40 000. For a two-dimensional body at high Reynolds numbers, it was noted that vortex dislocations appeared in the wake apparently randomly in time and spanwise position. However, they observed that the introduction of a spanwise waviness at the trailing edge fixed the positions of these vortex dislocations along the span of the body. They found that by increasing the wave steepness, defined as the ratio of peak-to-peak wave height divided by the wavelength, the base pressure was increased which resulted in a drag reduction. The maximum drag reduction of 34% at a Reynolds number of 40 000 occurred for a wave steepness of 0.14 (the non-dimensional wavelength, defined as the wavelength divided by the base height, was equal to 3.5). Based on these facts, they concluded that encouraging the formation of dislocations in the wake reduces the drag.

Bearman and Owen (1998) experimentally investigated the influence of spanwise waviness of the separation lines on the flow around common bluff forms. By performing the experiments in wind tunnel, they concluded that the drag of thin plates and rectangular cross-section bodies can be substantially reduced by the

introduction of spanwise waves into the flow separation lines. They also indicated that drag reductions of up to at least 30% are achieved and for wave steepnesses in excess of between 0.06 and 0.09, vortex shedding is completely suppressed.

Keser et al. (2001) used a 3-D discrete vortex method to simulate the separated flow around a circular cylinder with sinusoidal waviness along its span. However, all the above studies were based on various assumed forms for the flow field from the nodal to the saddle point of attachment.

In their experimental study, Ahmed and Bays-Muchmore (1992) measured the surface-pressure distributions of a set of wavy cylinders with different axial wavelengths based on the mean cylinder diameter, D. The Re in their experiment was 20 000 and the mean static pressure data was determined using linear interpolation. Their results showed that the separated flow structures near the geometric nodes were distinctly asymmetric for a large fraction of time, and the sectional drag coefficients at the geometric nodes are greater than at the geometric saddle.

In addition, Ahmed et al. (1993) visualized the wake of a sinusoidal cylinder and measured the total pressure, mean velocity profiles and Reynolds stress. They described the topology of the boundary layer separation lines and the subsequent 3D development of turbulent structure of the wake. Formation of trailing streamwise vortices behind the nodal points of separation resulted in a locally narrower wake, a more rapid wake velocity recovery and suppression of turbulence development within the separated boundary layer.

Lam et al. (2003) used a LDV system to measure the velocity profiles of the wake behind a sinusoidal cylinder in the range of Re=3,000–9,000. They concluded that the long vortex formation length of wavy cylinder should bring about drag reduction and suppression of Vortex induced vibration.

Nguyen (2004) investigated flow characteristics of the near-wake behind two sinusoidal cylinders (model 1 with $\lambda/Dm=1$ and model 2 with $\lambda/Dm=2$) by measuring the drag coefficients, mean velocity and turbulence intensity profiles over Reynolds numbers ranging from 5,000 to 20,000. The sinusoidal cylinder with axial wavelength $\lambda/Dm=2$ was found to reduce the drag coefficient by about 22% at Re=10,000, compared with the corresponding smooth cylinder.

A large eddy simulation of cross-flow around a sinusoidal wavy cylinder at Re = 3000 is performed by Zou and Lin (2008) by introducing the load cell measurement for the validation test. In the study, they presented the mean flow field and the near wake flow structures and compared with those for a circular cylinder at the same Reynolds number. They found that the mean drag coefficient for the wavy cylinder is smaller than that for a corresponding circular cylinder due to the formation of a longer wake vortex generated by the wavy cylinder. The fluctuating lift coefficient of the wavy cylinder is also greatly reduced. This kind of wavy surface leads to the formation of 3-D free shear layers which are more stable than purely 2-D free shear layers. From that study, they also showed that such free shear layers only roll up into mature vortices at further downstream position and significantly modify the near wake structures and the pressure distributions around the wavy cylinder.

2.1.1.4. Surface Protrusions

Zdravkovich (1981) studied various methods of suppressing vortices shed from a cylinder. He mentioned that the main factor governing the efficacy of a vortex suppression method is its ability to modify the vortex formation length. However, he did not study the effect of the vortex suppression methods on the large-scale coherent structure. One effective method for controlling the flow around a body is to install protrusions on the body's surface. These protrusions modify the wake structure by changing separation lines and/or direction of surface f1ow.

Bandyopadhyay (1986) compiled an excellent review of drag reduction technique and surface modification methods in his study on the mean f1ow over longitudinal grooves and outer-layer devices. In addition, many researchers have studied the effects of surface modifications on turbulent boundary layers.

Nebres and Batill (1992) measured time-averaged wake velocity profiles behind two different models (yawed stranded cables and cylinders wrapped with four small helical wires) using a single hot-wire probe, and analyzed the f1ow characteristics around bluff bodies with helical surface protrusions.

Naudascher and Rockwell (1994) used surface modifications to alter the loading and structural vibration of a circular cylinder. They modified the surfaces of cylinders in numerous ways, for example by applying straight and helical wires, staggered wires, and collars and rings.

Lee and Kim (1997) investigated the f1ow characteristics of the wake behind a circular cylinder (D=40 mm) helically wrapped with three small wires (d = 0.075D, d is the wire diameter) with pitches of 5D and 10D. They found that the surface protrusions elongated the vortex formation region, and decreased the vortex shedding frequency and wake width.

Most previous studies have investigated the flow structure over riblet surfaces placed on a flat plate. Walsh 1983 investigated drag reduction of longitudinal ribs of rectangular, triangular, and transversely curved shapes. He reported that the drag reduction was associated with a decrease of momentum thickness and turbulent velocity fluctuations and depended mainly on the riblet configuration such as the height h, spacing s, and shape. He suggested that a riblet with sharp peaks and large valley curvature is one of the optimum riblet shapes for drag reduction.

Owen et al. (2000) carried out an experimental investigation to measure the drag and vortex-induced vibration amplitudes of a circular cylinder, a circular cross-sectional body with a sinuous axis and a circular cylinder with hemispherical bumps attached. They studied a wide range of Reynolds number up to a maximum value of 10^5 and observed suppression of vortex shedding and drag reductions up to 47% for the body with a sinuous axis. They also recorded drag reductions of about 25% and suppression of vortex shedding for the cylinder with bumps.

Lee and Lee, 2001 investigated the flow structure over a semicircular riblet surface. They measured the near-wall turbulent structures over semicircular(U-type) grooves of s=3mm using particle image velocimetry (PIV) velocity field measurement technique and found how the semicircular riblet reduces the drag acting on the surface. As an extension of this study to a bluff body, we tested the U- and V-grooved cylinders having the same groove spacing of s=3 mm in the present study.

Bearman and Brankovic (2003) investigated the vortex-induced vibration of a plain circular cylinder and cylinders fitted with strakes and bumps. They carried out

the experiments in water with mass ratios in a range from about 1.5 to 5.5 and combined mass and damping values between about 2×10^{-3} and 7×10^{-3} by taking the Reynolds number within the range of 10^3 to 10^4. They indicated that although the wakes of fixed cylinders with strakes or bumps show little or no evidence of regular vortex shedding it was found to establish itself across a range of reduced velocity when the mass and damping parameters are sufficiently small. However, the amplitudes of vibration were found to be less than those for a plain cylinder. They also observed that the modes of shedding found for an oscillating plain cylinder are present for a responding cylinder fitted with vortex suppression devices.

Nakamura and Igarashi (2007) attached cylindrical rings along the span of a cylinder at an interval of several diameters to reduce the drag and fluctuating forces caused by fluid flow. They performed the experiments at Reynolds numbers based on the cylinder diameter d ranging between Re_d = 3000 for 38 000 taking the aspect ratio of the cylinder, L/d, as approximately 20. Their experimental results revealed that the drag force on the ring-attached cylinder was lower than for the 2D cylinder, even though the projected area was higher. They found the optimum ring configuration for drag reduction to be D/d = 1.3, W/d = 1.0, and P/d = 6 at Re_d ~ 30 000, where D is the ring diameter, W is the spanwise width of the ring, and P is the spanwise pitch of the ring. This configuration reduced the drag force by 15%.

Turhal and Cuhadaroglu (2010) performed experiments to investigate some aerodynamic parameters of the flow around perforated-surface square, horizontal, and diagonal cylinders. The surface pressures of the perforated surface square cylinders were measured for the cases of injections through the top, rear, top-rear, and all surfaces separately at Re values of 10,000, 16,000, and 24,000. The C_D and St were determined based on pressure coefficient measurements and vortex shedding frequency measurements, respectively. Their experimental results showed that the injection through the various surfaces of a square cylinder has some effects on the aerodynamic characteristics of the square cylinder, depending on the position of the perforated surface. They concluded that C_D of a horizontal square cylinder can be reduced by injection through all the surfaces, and for a diagonal square cylinder; it also can be reduced by injection through the rear surfaces. They also revealed that

the vortex shedding frequency of the flow around a horizontal square cylinder can also be decreased by high-momentum injection through the rear surface.

2.1.1.5. Control Cylinders

Kuo et al. (2007) numerically studied the passive wake control behind a circular cylinder in uniform flow for Re_D ranging from 80 to 300. They used two small control cylinders, with diameter d/D = 1/8, placed at x/D = 0.5 and y/D = ±6 and the Reynolds number is varied from 80 to 300. Their mechanism, which can significantly reduce the fluctuating lift and the form drag on the main cylinder, is explored without completely suppressing the vortex street for Re_D = 80–300. They reported that, by this control, the vortex street behind the main cylinder is still maintained but the fluctuating lift and the form drag on the main cylinder decreases monotonously with increasing Reynolds number.

Passive flow control using two-dimensional hydrofoils to reduce vortex-induced vibrations (VIV) and drag on a cylinder of circular cross-section was studied by Galvao et al. (2008). They test the hypothesis that by using foils to bend the streamlines around the cylinder, and hence forcing the flow to approach potential flow-like patterns VIV and drag will be reduced. They showed that properly positioned foils can significantly alter the flow around a circular cylinder to eliminate VIV and reduce drag.

Kuo and Chen (2009) revealed the wake flow structures behind a circular cylinder manipulated by two small control cylinders and elucidate the primary mechanism that leads to a reduction of the lift and the pressure drag on the main cylinder. They found that when the control cylinders lie within $0.8 \leq X_C/D \leq 3.0$, the fluctuating lift on the main cylinder shows a 70–80% reduction without completely suppressing the vortex street.

2.1.2. Active Control around Single Cylinder

2.1.2.1. Perturbation

Griffin (1992) has given many experimental results to demonstrate the relationship between the cross-flow vibration amplitude and the mass-damping product.

Brika (1993) performed an experimental study of the vortex-induced oscillations of a long flexible circular cylinder. The stationary amplitude they obtained exhibited a hysteresis loop somewhat different from earlier studies.

Techet (1998) measured the forces at both ends of the forced harmonic motion and free vibrations of uniform and tapered cylinders at the Reynolds number (defined via the cylinder diameter) value, Re =3800. Their results showed that free-vibration tests of a uniform cylinder with low equivalent structural damping yield the amplitude response curve as a function of the nominal reduced velocity in agreement with previous results (Khalak and Williamson, 1996)

Dutsch et al. (1998) investigated numerically the laminar flow induced by the harmonic in-line oscillation of a circular cylinder.

With the use of a spectral element spatial discretization, Blackburn (1996) explored the vortex-induced vibration problem by solving the two-dimensional Navier–Stokes equations in an accelerating frame of reference attached to the cylinder at the Reynolds number value Re =250.

Newman (1996) performed a direct numerical simulation (DNS) study of the flow past a freely vibrating cable using body-fitted coordinates at the Reynolds number Re= 100 and 200.

Baz and Kim (1993) made attempts to control the vibration of a cylinder in a cross-flow. In their studies, surface-bonded piezo-ceramic patches were activated by a closed-loop control system to exert a force on the cylinder under resonance, that is, the vortex shedding frequency coincided with the natural frequency of the cylinder. The control increased the flow structure system damping and subsequently reduced the vortex-induced vibration.

Cheng et al. (2003) developed a ‘smart cylinder’ with piezoceramic actuators embedded underneath the structural surface of a rigid square cylinder. The excitation of these actuators created a surface perturbation, which drastically altered the fluid–structure interaction given an appropriate excitation signal.

Griffin and Votaw (1972) concluded that, when the cylinder vibrates transversely to the oncoming flow, the vortex frequency adjusts itself to the forcing frequency. An increase in the relative amplitude, A/D, where A is the vibration amplitude and D is the cylinder diameter, induces an increase in the drag and a reduction in the longitudinal distance of the vortices until they disappear completely at some threshold amplitude.

Smith and Stansby (1988) considered the locking-on of vortex shedding due to cross-stream vibration of the circular cylinder in uniform and shear flows. They showed that, in both flows, the vortex shedding frequency locked onto the cylinder frequency and onto sub-multiples of the cylinder frequency.

Based on the study of a phenomenological model of FIV, Yuan and Cheng (2007) experimentally investigated the high-frequency perturbation effects on the performance of suppressing flow-induced vibration (FIV). They found the possibility to suppress both structural vibration and wake vortex by introducing a perturbation input at a high-frequency range well-exceeding resonant frequency of structure.

Konstantinidis and Balabani (2007) experimentally studied on the symmetric mode in the wake of a circular cylinder induced by periodic perturbations imposed on the in-flow velocity. They examined the wake field by PIV and LDV for Reynolds numbers about 1200 and for a range of perturbation frequencies between three and four times the natural shedding frequency of the unperturbed wake. In this range, they found that a strong competition between symmetric and antisymmetric vortex shedding occurs for the perturbation amplitudes employed. Their results show that symmetric formation of twin vortices occurs close to the cylinder synchronized with the oscillatory component of the flow. The symmetric mode rapidly breaks down and gives rise to an antisymmetric arrangement of vortex structures further downstream. The downstream wake may or may not be phase-locked to the imposed oscillation. The number of cycles for which the symmetric vortices persist in the near

wake is a probabilistic function of the perturbation frequency and amplitude. From that study, they also showed that symmetric shedding is associated with positive energy transfer from the fluid to the cylinder due to the fluctuating drag.

2.1.2.2. Oscillating

Studies on flow past an oscillating cylinder can be divided into the following two categories depending on the motion of the cylinder. In the first category, the cylinder oscillates translationally at an angle of 0º or 90º with respect to the free stream. They are in-line and transverse oscillation, respectively. Many experimentalists [Bishop and Hassan (1964), Koopmann (1967), Taneda (1972) Griffin and Ramberg (1974), Bearman and Currie (1979), Bearman (1984), Ongoren and Rockwell (1988a, b), Williamson and Roshko (1988)] had shown that the vortex shedding phenomenon can be dramatically altered for the cylinder undergoing in-line and transverse oscillation in a fluid stream. For in-line oscillations, vortex lock-on occurs when the oscillation frequencies are approximately twice the Strouhal frequency (the frequency of the vortex shedding from a stationary cylinder). For transverse oscillations, lock-on usually occurs near the Strouhal frequency (Griffin and Hall 1991; Meneghini and Bearman 1995). In the second category, the cylinder performs a rotational oscillation about its axis in mean flow. It is well known that lock-on or resonance occurs when the body and wake oscillations have the same frequency that is near one of the characteristic frequencies of the structures. Vortex lock-on can also be realised with rotational oscillations of a circular cylinder.

Viscous flow around a rotationally oscillating cylinder was investigated experimentally by Okajima et al. (1975) for Reynolds numbers (Re_D) of 40-160 and 3050-6100. Their results showed that, when the oscillation frequency of the cylinder is at or near the frequency of vortex shedding from a stationary cylinder, the vortex shedding synchronizes with the cylinder motion.

Okajima et al. (1975), Taneda (1978) and Filler et al. (1991) studied the effect of rotary oscillations of a circular cylinder at relatively low Reynolds numbers. They demonstrated the possible modification of vortex shedding and found that the

extent of cylinder peripheral speeds which affected the vortex shedding was smaller than 3% of the free-stream velocity.

More recently, the frequency response of the shear layers separating from a circular cylinder undergoing small amplitude rotational oscillation has been investigated experimentally by Filler et al. (1991) in water at a Reynolds number range of 250-1200. By referencing the lock-on analyzer to the cylinder oscillations, the amplitude and phase of the response to different frequency oscillations were measured directly. They found that rotational oscillations corresponding to cylinder peripheral speeds of between 0.5 and 3% of the free-stream velocity can be used to influence the primary (Karman) mode of vortex generation. For Re greater than 500, such oscillations can also excite the shear-layer vortices associated with the instability of separating shear layers.

Ingham (1983) and Badr et al. (1989) numerically investigated the rotating cylinder flow in the laminar steady regime (Re_D <47) for relatively small rotational speeds. They found that, although vortex shedding does not occur in the wake, the rotation delays and even inhibits the boundary-layer separation. The flow in the laminar vortex shedding regime (47≤ Re_D <200) has also been investigated in the literature.

Tokumaru and Dimotakis (1993) experimentally investigated flow past a circular cylinder with both net steady rotation and forced oscillations at $Re_D \approx 10^3$ by suggesting the so-called virtual vortex method. They found that a higher cylinder aspect ratio yields a higher maximum lift coefficient in the case of steady rotation and the addition of forced rotary oscillations to the steady rotation increases or decreases the lift coefficient.

Gioria et al. (2009) investigated the flow around a circular cylinder submitted to forced transverse oscillations. Their goal is to investigate how the transition to turbulence is initiated in the wake for cases with different Reynolds numbers (Re) and displacement amplitudes (A). The procedure consists of performing a Floquet type analysis of time-periodic base flows, computed using the spectral/*hp* element method. With the results of the Floquet calculations, considerations regarding the stability of the system are drawn, and they obtained form of the instability at its

onset. The critical Reynolds number is observed to change with the amplitude of oscillation. They also observed instabilities for the oscillating cylinder are distinctively stronger in the braid shear layers. Other unstable modes similar to mode B are found. Quasi periodic modes are observed in the 2S wake, and sub harmonic mode occurrences are reported in P + S wakes.

The flow characteristics of the near-wake behind a rotationally oscillating circular cylinder are investigated experimentally with varying the frequency ratio FR by Lee et al. (2007). The velocity fields in the near-wake for each system were measured using a dynamic PIV technique. They found the rotational oscillatory motion of a circular cylinder to be an effective and promising method for controlling the near-wake flow structure. In addition, their results show that temporally resolved quantitative and qualitative flow information is useful in understanding the cyclic variation of vortex structure and in analyzing the effect of open-loop active flow control on the near-wake flow structure.

Zhang et al. (2010) numerically studied on the nonlinear optimal control approach based on the adjoint flow field for the cylinder wake control. They obtained the optimal control *N(t)* varying with the transient flow field and found that under the action of *N(t)*, the oscillations of drag and lift are suppressed, the total drag coefficient decreases dramatically where the pressure drag decrease is a dominant effect, and the lift keeps at zero level.

2.1.2.3. Suction and Blowing

Another possibility is flow manipulation through the application of suction or blowing. Early experiments on a porous cylinder made of sintered bronze were carried out by Pankhurst and Thwaites (1950). They made experiments with continuous suction, but also combined suction with a flap in the form of a short splitter plate placed at various angles. At an angle of 180°; i.e., along the downstream symmetry line, and for sufficient suction, the separation is entirely prevented and a remarkably close approximation to the potential flow solution is achieved, as attested by the pressure distribution and by mean flow velocity profiles of the wake. They

concluded from their experiments that the values of $Cq\sqrt{\mathrm{Re}}_D$ larger than ≈30 were needed to avoid separation (a critical value of the bleed coefficient $Cq = U_0 / U_\infty = 0.214$, where U_0 is the bleed velocity) (Antonia and Rajagopalan, 1990). They also reported values of the drag coefficient, but did not do any time-resolved measurements to determine the vortex shedding frequency.

Boundary layer measurements on the same porous cylinder were performed by Hurley and Thwaites (1951) and in general good agreement was found with laminar boundary layer theory.

Continuous blowing through the whole surface has also been studied experimentally by Mathelin et al. (2001a, b).

Glezer and Amitay (2002) show that synthetic jets on selected positions over the cylinder can give a delay of separation for different Reynolds number (i.e., both for a turbulent and a laminar boundary layer). They argued that this delay was caused by increased mixing within the boundary layer. In addition, the interaction between the jet and the cross flow has a profound effect both on the separated shear layer and on the wake; the magnitude of the Reynolds stresses is reduced indicating that the delay in separation is not merely the result of a transition to turbulence in the boundary layer.

Feng et al. (2010) studied to control the flow around a circular cylinder by a synthetic jet positioned at the rear stagnation point using a novel synthetic jet. The suction duty cycle factor k, defined as the ratio between the time duration of the suction cycle and the blowing cycle, is used as the parameter to characterize the novel synthetic jet signal They indicated that, when increasing the suction duty cycle factor, the momentum coefficient is also enhanced, and a stronger and larger scale synthetic jet vortex pair is generated and it can reach further downstream. This characteristic has a significant influence on the wake vortex shedding of the circular cylinder

Similar study is experimentally investigated with a two-dimensional particle image velocimeter (PIV) system in quiescent flow by Wang et al. (2010). The novel signal wave pattern realized by changing the suction duty cycle factor k for a two

dimensional synthetic jet and the development and evolution of the vortex pair trajectories, jet velocity, jet width, flow flux and momentum flux were obtained for different k values. They found that the distributions of the mean and turbulent flow fields for synthetic jets generated at different k values have similar features to those exhibited for the conventional synthetic jet. Moreover, the vortex pairs generated in the present way have larger convection velocity, stronger entrainment and higher momentum at larger K, which would be of benefit for flow control applications.

2.1.2.4. Acoustic Excitation

The active control of vortex shedding using the internal acoustic excitation was first introduced by Hsiao and Shyu (1991). They investigated the influence of acoustic excitation on the aerodynamic performance of a cylinder, where the acoustic excitation was introduced internally to the flow over a circular cylinder through a slit with a loud speaker.

Baz and Ro (1991) used an electromagnetic actuator installed inside a cylinder to exert a force on the cylinder. The actuator was driven by a feedback hotwire signal measured in the wake, thus increasing damping to the cylinder and effectively reducing the vortex-induced vibration at the occurrence of resonance, when the vortex shedding frequency, f_s, coincided with the natural frequency, f'_n of the system. One common feature in these investigations is to alter the structural dynamics, subsequently influencing the flow field. Another approach is to use acoustic excitation to control the flow- field.

Ffowcs et al (1989) were able to demonstrate, with active, control of vortex shedding behind a cylinder with a diameter of 0.6 cm at a speed of 1 m/s and Reynolds number of 400.

Roussopoulos (1993) concluded that the feedback control was possible only at a Reynolds number 20% higher than at the critical Reynolds number. He claimed that Ffowcs Williams' active control of vortex shedding of around transitional Reynolds number at about 400 was really an active probe when affected, and prevented a second sensor from detecting a vortex shedding. He attempted to show

this interference of probes was actually claimed to be control of vortex shedding as claimed by them. He visualized the flow in a water channel and tried to show that there was no control of vortex shedding.

Tao et al. (1996) provided visualization photos between Reynolds numbers 48.5 and 51. This range is 18-24% above the onset of Reynolds number at the shedding frequency of about 1.05-1.1 Hz. At x/d=10 and 30 locations a complete elimination of vortex shedding is achieved, and flow-streak lines are reduced to almost a straight line in the cylinder wake.

Thereafter and Keles (1996) demonstrated experimental details of the transition to turbulence in the wake of a circular cylinder at Re_D=170. In those findings by Keles (1996) the data in the wake of cylinder first time, provides a clear picture of the feedback transition control. The distribution of the amplitude of velocity fluctuation's control was achieved for transitional at about Re_D =170.

The effect of externally imposed sound on the flow over a single cylinder has been reported by Blevins (1985), who concluded that sound levels greater than 130 dB resulted in a reduction in the small variation of the vortex-shedding frequency.

Hsiao and Shyu (1991) investigated the effect of acoustic excitation introduced internally to a circular cylinder through a slit to improve the aerodynamic performance of the cylinder in a uniform flow. They emitted the acoustic disturbances from a speaker system through the slit to the flow over the cylinder with sound pressure levels as high as 130 dB. The dimension of the slit was 1mm wide and 80mm long, while the cylinder diameter was 60mm with the length 200 mm, so that the aspect ratio of the cylinder was as small as 3.3. The drag was evaluated from wake velocity measurements and was found to be reduced by up to 40% at the optimum condition of the forcing frequency and slit location at a Reynolds number 2×10^4. However, the measurement of pressure distributions did not indicate any drag reduction, which suggests that further research should be conducted to confirm the drag reduction by the acoustic excitation.

Amitay et al. (1997) studied the surface pressure distributions around a circular cylinder under internal excitation by using fluidic actuators and found a drag reduction of 25% at higher Reynolds number, Re=75500.

Caillaud et al. (2000) attempted to actively alter the damping of a flexible tube bundle in a cross-flow using velocity feedback to derive critical velocities, at which fluid elastic instabilities occur. An attempt has been made to employ acoustic signals to control the flow field.

Lewit (1992) used a feedback hot-wire signal to activate sound waves inside a circular tube. The sound waves interacted with flow through two rows of holes, arranged at ±90º away from the forward stagnation line of the tube, respectively, so that the sound waves through the two rows of holes were in antiphase, thus suppressing vortex shedding from the tube up to $Re_D=10^4$.

Williams et al. (1992) introduced symmetric and antisymmetric acoustic excitations into a water flow (Re=470) at a frequency of about 2 f_s through two rows of holes located at ±45º, respectively, away from the forward stagnation line of the cylinder. He observed a modified behavior of f_s and the flow structure.

Fujisawa and Takeda (2003) investigated the mean fluid forces on a circular cylinder under acoustic excitation control by measuring the time-averaged pressure distributions over the cylinder. The result indicates that the mean drag is reduced up to 30% at Reynolds number 9000. They also measured the distributions of mean and periodic velocities around the cylinder using a standard PIV system and showed that the near-wake velocity profile was considerably modified by the acoustic excitation control.

Muddada and Patnaik (2009) numerically investigated the flow over a circular cylinder with the aid of a control algorithm using multiple-feedback sensors and actuators. They found that the rate of steady state injection depends on the proportionality coefficient, i.e. higher the rate of injection, the faster it will reach steady state and viceversa. They also demonstrated that energy expenditure can be further optimized through nimble control by enabling periodic switch on and off capability.

Jukes and Choi (2009) experimentally investigated the possibility of controlling the global flow field in the near wake of a circular cylinder at Re = 6500 using high-speed Particle Image Velocimetry. Surface plasma actuators were mounted at strategic locations around the cylinder (both fore and aft of the separation

point) and used for flow control by producing a body force close to the wall. They found that the plasma can significantly alter the vortex shedding in the wake of the cylinder, with effectiveness depending upon the actuator location and forcing frequency. They also observed that most dramatic effects were observed when the plasma was located very close to the natural laminar separation point.

2.1.2.5. Electromagnetic Control

Nosenchuck and Brown (1993) measured a reduction of skin friction of up to 90% by means of chessboardlike arranged electrodes/magnets to induce a wall-normal Lorentz force in a flat plate boundary layer. The injection of an electrolyte generated a non-uniform electrical conductivity. Spanwise oscillating Lorentz-force (see Berger et al., 2000) was successfully used to reduce the skin friction in a turbulent boundary layer. A considerable scatter of results was found even on very similar arrangements. This could result from inadequate calculations of the Lorentz force in numerics or difficulties with established measurement techniques.

There have been some researches to apply the magnetic fields to control the vortical structure in the wake. They investigated the effect of magnetic fields on the flow structure past a cylinder. Lahjomri et al. (1993) carried out an experimental study and showed that an aligned magnetic field leaded to the suppression of vortex shedding.

Shatrov et al. (1997) and Mutschke et al. (1997) and Mutschke et al. (1998) and Mutschke et al. (2001) investigated the flow instability in the wake in the presence of magnetic fields from their numerical studies. They carried out the stability analysis using the numerical simulation techniques for the time-dependent two- and three-dimensional flow. Depending on the magnitude of applied magnetic fields in the two-dimensional flow region, the vortex shedding can be suppressed or eliminated and as a result the flow becomes stabilized.

Kim and Lee (2000) introduced the electromagnetic force to control the flow around a circular cylinder. They investigated the effect of the electromagnetic force

on the cross-flow of a circular cylinder by placing electrodes and permanent magnets side by side alternately in the axial direction of the cylinder.

Chen and Aubry (2003) developed an efficient active control algorithm for manipulating wake flows past a solid cylinder in an electrically low-conducting fluid (e.g. seawater). Their intent is to avoid both vortex shedding and flow separation from the body with reduction in the mean drag significantly. They introduced a Lorentz force in the azimuthal direction generated by an array of permanent magnets and electrodes located on the solid structure and found that vortex shedding behind the cylinder weakens and eventually disappears completely when the Lorentz force is sufficiently large.

A nonlinear adjoint-based optimal control approach of cylinder wake by electromagnetic force is investigated numerically by Zhang et al. (2010). They constituted a cost functional representing the balance of the regulated quantities with different weights and interaction parameter N (Lorentz force), where the regulated quantities related with flow and force are taken as targets of regulation and the Lorentz force, (as interaction parameter N), is taken as a control input. They observed that under the action of optimal N(t), the flow separation is suppressed fully, so that the oscillations of drag and lift are suppressed and the total drag coefficient decreases dramatically. For the different regulations, the control effects have some differences due to the different values of optimal inputs corresponding to the different adjoint flow fields.

2.3. Shallow Water

Wolanski et al. (1984) investigated wake flows behind Rattray Island in shallow coastal waters The island is located in northeast Australia. Their results showed that the length of the wake in the lee of the island, as documented by aerial photographs and satellite imagine, appeared to equal that of wake behind a flat in two-dimensional flow at Reynolds number of 10.

Ingram and Chu (1987) studied shear flows on the effect of bottom (bed) friction around an island. They observed two basic pattern of wake flow around the

island. A vortex street wake was formed when transverse shear was large, as in flow around the small islands. On the other hand, for small transverse shear, as in flows around large islands, the shear layers were stabilized by bottom friction and, in that case, a clear water wake of low turbulence and low sediment concentration was observed. They made a laboratory demonstration of bottom friction influence on the turbulent wake in shallow water using shallow water table. A wake stability parameter was found for wake classification and for correlation of field and laboratory data. Their results showed that vortex street wakes were observed in nine out of 27 events when the wake was less than critical value. This result was consistent with the laboratory and numerical simulation results.

Chu et al. (1991) theoretically studied the stability of shear flows in shallow open channels and defined a dimensionless stability number S also known as shallow wake parameter to account for the stabilizing effect of the bed friction and destabilizing effect of the transverse shear. The S parameter for the bluff body is $S = C_f D / h$. It is based on the ratio of the small-scale kinetic energy loss to the production of large-scale turbulence kinetic energy. Here, h is the water depth and C_f is the friction coefficient.

Schar and Smith (1993) studied the global normal mode of instability for an inviscid flow as it passes an isolated topography. Their studies consisted of two parts. In the first part of their study, steady numerical solutions for flow past circular topography were obtained by imposing symmetrical conditions that essentially suppressed vortex shedding. In the second part, this symmetrical condition was relaxed in order to study the transition into vortex shedding regime. They used finite difference numerical simulations to derive the most unstable global normal mode leading to the break-up of the study wake into an oscillating Karman vortex street. The frequency of eddy shedding in their numerical simulations agreed well with that from observations of eddies behind mountainous islands.

Grubisic et al. (1995) carried out a local absolute stability analysis for a piecewise-linear velocity profile, which missed the two inflection points. The reserve flow velocity was determined by magnitude of bottom friction, which also defined

the velocity profile. A surface number r was defined as the product of the drag coefficient and the ratio of horizontal length scale and the height of fluid layer. (This definition is analogous to the wake stability parameter S given above but differs by a factor of due to the choice of the drag coefficient.) A critical value of r =1 was obtained from their stability analysis.

Chen and Jirka (1995) performed experimental studies on the shallow two-dimensional turbulent wake flows on the large-scale water table. The "shallow wake "was generated by vertical cylindrical bodies extending over the water depth. The ambient flow was characterized by two main features: one was the existence of a free surface and bottom by which the shallow water layer was bounded and the other was a fully developed turbulent layer. Here, the transverse body dimension D greatly exceeds the water depth h (D/h >1). The wake Reynolds number $Re_D = U_\infty D/\nu$ was greater than 10000, while the ambient flow Reynolds number that governs the shear flow in the transverse dimension $Re_h = U_\infty h/\nu$ was always larger than 1500. U_∞ is the depth-averaged ambient velocity and ν is the kinematic viscosity. Re_h is thus well above the transition value of about 500. Different types of bodies were investigated, including cylinders, flat plates and porous plates oriented transversely to the ambient flow. The flow patterns fell into three categories: First type of stability (vortex Street- VS) showed a formation, which resembled a von Karman vortex street, although here the cylinder Reynolds number Re_D was substantially larger than that of in the unbounded case (see Figure 2.1). It was characterized by the alternate separation of large vertical structures directly from the cylinder shoulders, which were then advected downstream and decayed due to the continuous influence of bottom shear. If, compared to the ambient flow conditions in the VS case, the stabilizing effect of bottom friction increases or the destabilizing transverse shear is reduced, the convectively unstable VS wake flow undergoes transition: an absolutely unstable recirculating region (unsteady bubble-UB) develops behind the obstacle, alternately large eddies shed from the downstream edge of the bubble and advect downstream until disintegrate and the flow stabilizes. If the forcing due to transverse shear is even weaker, then generation of large-scale vortices at the end of recirculation zone is completely suppressed ("steady bubble"-SB).

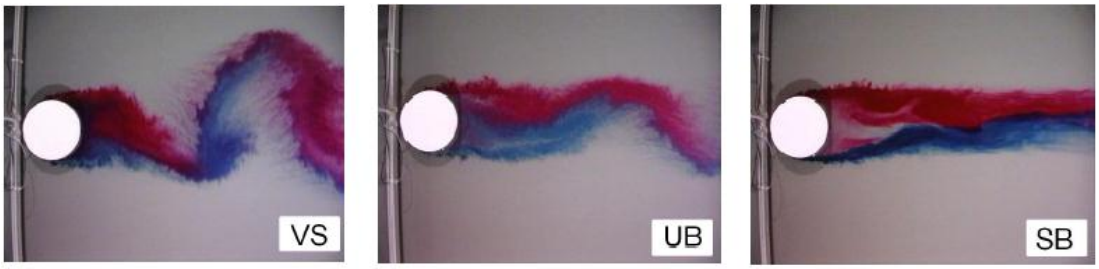


Figure 2.1. Plan views of shallow wake instabilities of type “VS”, “UB” and “SB”, where cylinder diameter D= 430 mm, flow depth h= 30/20/11 mm, Re_D=UD/ν = 44.000 / 35.000 / 25.000, and Re_H =UH/ν = 3.100 / 1.600 / 640, respectively

Chen and Jirka (1997) investigated the effect of bottom friction on absolute/convective and local/global stability characteristic of shallow wake flows by means of a linear stability analysis and interpreted and compared it with the results of their previous experiments (1995). They also proposed critical values of S (denoted as S_c) to signify the onset of particular flow patterns.

Lloyd and Stansby (1997) made extensive experimental and numerical investigations in shallow wakes behind conical model islands with gentle slopes. Four islands were used with side shapes ranging from 8.0 to 33.1 degrees. For small values of the wake stability parameter, for example S< 0.2, the island wakes were characterized well-organized vortex shedding systems. The island side slope had a small effect on the wakes produced. With slope angles varying from 8.0 to 33.1 degrees, the basic mechanism generating the wake was found to be the same.

In shallow flows, bed friction effects became very important and were quantified in terms of a friction length scale, which is usually defined as the ratio of depth of flow (h) to the skin friction coefficient (C_f). Balachandar et al. . (1997) have defined a bed friction parameter ($S=C_fX/h$) as Chu et al. (1991) to describe the influence of bed friction in shallow flows. Here, X is a horizontal length scale. It is clear that, the bed friction effects are expected to be minimized in deep flows.

Balachandar et al. (1999) developed a theoretical model to predict the spread of wake in shallow flows. They investigated the effects of flow depth and plate width on the spread of the wake. Some useful remarks on the wake stability parameter were

presented therein. The range of velocities and the depths (10 mm ≤ h ≤ 80 mm) of flow considered in Balachandar et al. (1999) and Lloyd and Stansby (1997) studies are similar. However, the size of the wake generators used by Lloyd and Stansby (1997) are about 8 to 30 times larger than that used by Balachandar et al. (1999). From careful visual observations and concentration measurements, it was found by Balachandar et al. . (1999) that for S ≤ 0.008 distinct and continuous Karman vortices were noted. For S ≈ 0.009-0.018, weak and intermittent Karman vortices were observed, while the Karman vortex street was completely annihilated when S ≥ 0.021. In fact, for a given velocity and cylinder of plate width, no significant difference between the nature of the Karman vortex street and the development (or spread) of the wake was observed for h ≥ 30 mm. Based on these observations, shallow wakes were reclassified into shallow-wakes and deep-shallow wakes. Given the significant difference in the reported values of the critical wake stability parameter, an alternate measure using the wake velocity data may be more appropriate. In the study reported by Balachandar et al. . (1999), only an intermittent Karman vortex street was observed at a flow depth of 20 mm in the wakes generated by a 20 mm and a 40 mm wide flat plate.

Balachandar et al. (2000) investigated characteristics of shallow turbulence near wakes at low Reynolds numbers. Reynolds number based on the test body width was maintained nearly constant ($Re_D \approx 4.000$). Velocity and the concentration in the near region of shallow turbulent wakes were measured using a LDA and video-imaging techniques. A 40 mm wide flat plate placed normal to the flow was used as a wake generator. It was concluded that the wake stability parameter pointed out earlier was not quite approximate to characterize the relative effects of transverse and bed friction. In their study, a new definition as a transverse parameter was proposed to characterize wake stability. It was reported that the wake velocity defect data collapsed fairly onto a single curve and were independent of the measurement location and depth of the flow. The wake half-width data based on the concentration profiles show a higher spread compared with the velocity data.

Tachie and Balachandar (2001) investigated behaviour of the shallow turbulent wakes generated on smooth and rough surfaces. They used a flat plate as the wake

generator placed normal to the flow. The wakes were generated on two types of surfaces: i) a hydraulically smooth surface (brass channel bottom) and ii) a rough surface created using wire mesh. The mesh was made of a 0.6 mm diameter wire with 7.0 mm centerline spacing. The wire was 1.8 m long and 0.45 m wide and fixed to the channel bottom by means of a double-sided tape. They measured mean and turbulence intensity to understand shallow wakes generated on smooth and rough surfaces. Using the local minimum and maximum velocity at any axial location to define velocity scale, the velocity profiles across the wake generated on smooth and rough surfaces collapsed onto a single curve. Their study indicates that for $x/D \leq 5.0$ (d is the plate width), the width of the wake increases from the wake generator with increasing axial distance, attains a maximum value at about x/D=2.0 and decreases to a minimum value at x/D=5.0. It was found that at similar Re_d the spread rate of the wake on rough surface was significantly lower than observed for a smooth surface due to a stronger bed friction effect.

Balachandar and Tachie (2001) investigated the interaction between the boundary layer on a horizontal floor of a shallow open channel flow and the wake of a thin flat plate mounted vertically on the floor of a channel. They used LDA technique to measure the velocity of the flow. Measurements were obtained upstream and downstream of a smooth flat plate wake generator. They used plates are two having different aspect ratios. Their results showed that the profiles in the near wake region were quite distorted and the recovery of the boundary layer to the upstream condition was slow. They stated that the inner region appeared to develop more quickly than the outer region of the boundary layer. When compared with the approaching flow, the stream wise turbulence intensity values increased in the near wake region followed by a gradual but slow decrease with increasing axial distance.

Akıllı and Rockwell (2002) investigated the near wake of a vertical, circular cylinder in shallow water using a combination of a visualization marker and particle image velocimetry technique. They located laser sheets parallel to the bed of the water channel at different heights to investigate the flow characteristics at the bed and at the various locations above it. At the bed, the time averaged streamline topology downstream of the base of the cylinder took on a form known as an owl

face of the first kind, which was originally defined for a completely different exterior flow. Immediately adjacent to the base of the cylinder, an additional system of saddle points was located at either end of a nodal line. At locations above the bed, one of the two principle saddle points of the owl face of the first kind disappeared and the principle foci were transformed from a stable to an unstable state.

Kahraman et al. (2002) investigated vortex formation of a vertical cylinder in shallow water and the control technique of these vortices. In order to control vortex formation behind a cylinder, a narrow transverse strip of roughness elements having different heights was placed behind the cylinder on the bottom surface channel. They employed a technique of high-image-density particle image velocimetry (PIV) to obtain global, instantaneous representations of the flow patterns, which lead to phase- and time-averaged patterns of streamline topology, velocity, vorticity and Reynolds stress on planes above the bed.

Akıllı et al. (2004) investigated experimentally the flow around two and three side-by-side circular cylinders of equal diameter (Re_D=5000) in shallow water using the particle image Velocimetry (PIV) technique, over a transverse gap ratio in the range of G/D= 1.0-3.0 with an increment of 0.25 For the two side-by-side cylinder case, They found that the flow structure behind the cylinders is asymmetrical at small gap ratios as a result of jet-like flow between the cylinders. The jet-like flow tends to deflect toward the narrow wake region that has a higher vortex shedding frequency. In the case of three cylinders, they observed both an asymmetrical flow structure at small gap ratio (G/D= 1.25) and a symmetrical flow structure at intermediate gap ratios (1.5<G/D<2). He also observed bistable wake regions for the asymmetrical cases.

Akıllı et al. (2005) investigated the effect of splitter plate on the suppression of vortex shedding in shallow water using the Particle Image Velocimetry (PIV) technique. Splitter plates with a length of 50 mm, which is equal to the diameter of the cylinder (D), were used during the experiments. Gap distance between the base of the cylinder and the leading edge of the splitter plate ranged from 0 to 2D. Velocity vector field and corresponding vorticity contours and streamline topology and Reynolds stress concentrations were used to explain the characteristics of the flow.

The splitter plates having different thicknesses presented the same influence on the flow characteristics. The splitter plate has a substantial effect on suppression of the vortex shedding for the gap ratio between 0 and 1.75D. In this gap ratios, shear layers extend up to the trailing edge of the splitter plate preventing the entrainment of the free- stream flow into the base region. For G/D=1.75, the normalized Reynolds stress has a peak value of 0.0158 which is approximately 8.5 times smaller than the concentrations occurring for a bare cylinder. After passing the splitter plate, the flow starts to oscillate with smaller frequency compared to the natural frequency of the bare cylinder. When the splitter plate was located at 2D location, no effect of the splitter plate was observed.

Akilli et al. (2008) investigated experimentally passive control of vortex shedding behind a circular cylinder by splitter plates of various lengths attached on the cylinder base in shallow water flow (Re_D=6300). At this study the length of the splitter plate was varied from L/D=0.2 to L/D=2.4 in order to see the effect of the splitter plate length on the flow characteristics. Instantaneous and time-averaged flow data clearly indicate that the length of the splitter plate has a substantial effect on the flow characteristics. They found the flow characteristics in the wake region of the circular cylinder sharply change up to the splitter plate length of L/D=1 and above this plate length, small changes occur in the flow characteristics.

3. MATERIAL and METHOD

3.1. Experimental Arrangement

Increasing technological developments, especially in electric and electronic engineering, provide new measuring techniques. All measurement techniques have some advantages and disadvantages associated with the specific method. It is increasingly important not only to measure the mean values at a point in space, but also to measure and characterize turbulent and instantaneous values in the investigated flow field. Particle Image Velocimetry, PIV, is a non-intrusive technique used to measure an instantaneous two dimensional velocity vector field under investigated area. The velocity is determined by measuring the displacement of particles in a flow field that is illuminated by a laser sheet.

3.1.1 Water Channel System

Experiments were undertaken in low turbulence closed-loop open-surface water channel test section having the following dimensions: a length of 8000 mm, width of 1000 mm, and depth of 750 mm. This facility was built for PIV experiments for steady and un steady flows. Longitudinal free-stream turbulence intensity is less than 0.5%. A pump driven by an electric motor having a variable speed controller was used to create a desired mean flow in the test section. Water was pumped into a settling chamber through a honeycomb section. The water was then conveyed through a two-dimensional two-to-one contraction to reach the test section which was constructed of 15 mm thick clear Plexiglas sheet. The overall length of the water channel is approximately 14000 mm. An overview of the water channel system is shown Fig. 3.1

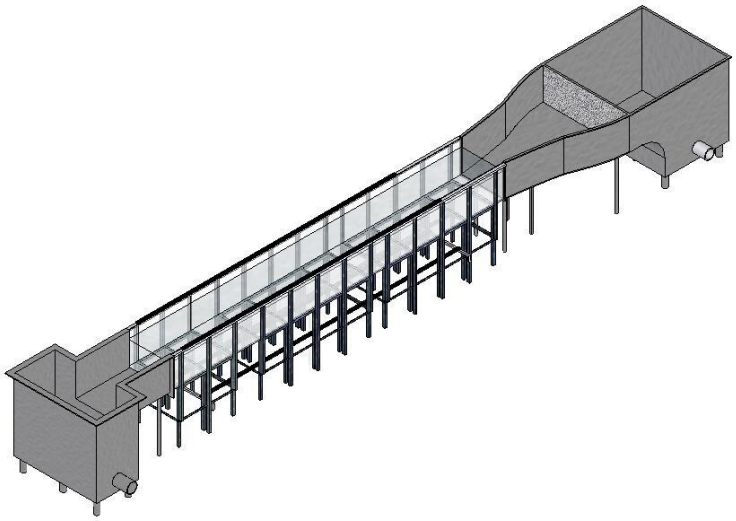


Figure 3.1. The water channel

3.2. Measurement Techniques

3.2.1. Particle Image Velocimetry (PIV) Tecniques

Particle Image Velocimetry (PIV) is a non-intrusive measurement technique used to simultaneously determine the velocities at many points in a flow field. The technique involves seeding the flow field, illuminating the region under investigation and capturing two images of that region in rapid succession. From the displacement of the tracer particles, provided that the time interval between image captures is known, a velocity vector map can be calculated in the flow field.

The theory of PIV was introduced by Adrian (1988) in the late 1980s with the first experimental implementations following shortly afterwards (Kean et al. 1990 and Kean et al. 1991). At the stage, due to hardware limitations, a single photographic frame was multiply exposed and analysed using an auto-correlation technique. However, improved speed of photographic recording soon allowed images

to be captured on separate frames for analysis by cross-correlation (Kean et al. 1992). The introduction of digital camera technology to PIV enabled the direct recording of particle images (Willert et al. 1991), at the expense of reduced resolution, resulting in the development of digital PIV Westerweel, 1997). As well as these hardware advances, many new algorithms have been developed in the last decade, increasing the accuracy and speed of PIV analysis. One key advantage of the PIV technique over other conventional techniques such as LDV or hotwire anemometry is ability to obtain instantaneous flow-field information is important for probing the structure of turbulent flow fields (Westerweel et al. 1996; Meinhart and Adrian 1995).

3.2.1.1. Principles of PIV

Particle Image Velocimetry (PIV) is a measurement technique for obtaining instantaneous whole field velocities. It is based on the well known equation

Speed =Distance / Time

In PIV the property actually measured is the distance traveled by particles in the flow field within a known time interval. These particles are added to the flow and known as seeding. Different types of seeding particle are used depending on the nature of the flow for PIV experiments. The type of seeding particle is chosen to follow the flow, and in order to detect their movement, an area of the flow field is illuminated by a light-sheet. The light-sheet, which is generated by a laser and a system of optical components, is not continuous/permanent, but pulsed to produce a stroboscopic effect, freezing the movement of the seeding particles. The time between the light pulses is the denominator in the equation above. To detect the position of the illuminated seeding particles, a CCD-camera (CCD = Charge Coupled Device) is positioned at right angles to the light-sheet, and particle positions will appear as light specks on a dark background on each camera frame. The pulsing light-sheet and the camera are synchronzed so that particle positions at the instant of

light pulse number 1 are registered on frame 1 of the camera, and particle positions from pulse number 2 are on frame 2. (Older generations of CCD cameras couldn't switch frames fast enough, so both the first and the second pulse of the light sheet was recorded on the same camera frame).

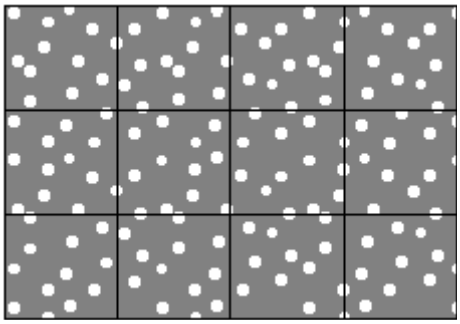


Figure 3.2. Interrogation areas

The camera images are divided into square regions called interrogation areas or interrogation regions, and for each of these interrogation areas the image from the first and the second pulse of the light-sheet are correlated to produce an average particle displacement vector. Doing the same process for all interrogation regions produce a vector map of average particle displacements. Dividing with the known time between the two images captured, the displacement vectors are converted into a map of so-called raw velocity vectors. Then validation algorithms can be applied to the raw vector maps, so that outliers, the term for erroneous vectors, can be detected and removed. In the FlowMap PIV system, for reasons of experimental reproducibility, the raw vector map is archived and a new validated vector map is output, and further analysis can produce streamlines, vorticity and so on.

From the basic principles the following main topics of PIV emerge:

- Seeding
- Illumination
- Cameras
- Synchronization
- Correlation
- Validation and further analysis

3.2.1.2. PIV parameters used in this study

The experiments were performed and the measured data were processed using Dantec Dynamics PIV system and FLOW MANAGER Software installed on a computer. The measurement field was illuminated by a thin and an intense laser light sheet by using a pair of double-pulsed Nd:YAG (yttrium aluminum garnet) laser units each having a maximum energy output of 120 mJ at 532 nm wavelength.

The image capturing was performed by an 8 bit cross-correlation charge-coupled device (CCD) camera having a resolution of 1008×1016 pixels, equipped with a Nikon AF Micro 60 *f* / 2.8*D* lens. In the image processing, 32×32 rectangular interrogation pixels were used and an overlap of 50% was employed. A total of 3844 (62×62) velocity vectors were obtained for an instantaneous velocity field at a rate of 15 frames/ s. The plan view of measuring planes covers the downstream of the cylinder with the area of 200mm x 200mm for all configurations and the image magnification was 0.0709 mm/pixel. The laser sheet was oriented parallel to the bottom surface of the water channel and the experiments were carried out at the mid-plane of the water height. Water heights were taken to be 50mm. The time interval between pulses was 1.75 ms for all experiments and the thickness of the laser sheet illuminating the measurement plane was approximately 2 mm. The time interval and the laser sheet thickness were selected such that the maximum amount of particles in the interrogation window was obtained. The number of particles in an interrogation area was in between 20 and 25. The uncertainty in velocity relative to depth averaged velocity is about 2% in the present experiments. The water was seeded with 12 μm diameter hollow glass sphere particles. The instantaneous images were captured, recorded, and stored in order to obtain averaged-velocity vectors and other statistical properties of the flow field. Spurious velocity vectors (less than 3%) were removed using the local median-filter technique and replaced by using a bilinear least squares fit technique between surrounding vectors. The velocity vector field was also smoothed to avoid dramatic changes in the velocity field using the Gaussian

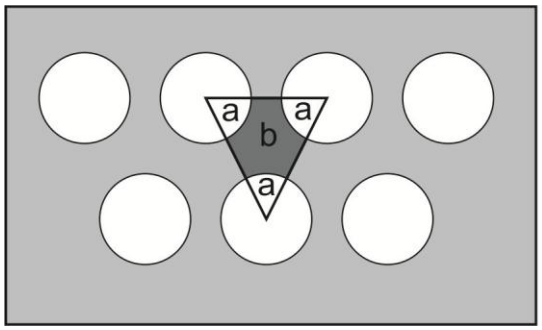
smoothing technique. The vorticity value at each grid point was calculated from the circulation around the eight neighboring points.

All experiments were carried out above a platform, having a length of 2300mm to obtain fully developed shallow flow conditions.

3.2.2. Experimental Model

3.2.2.1. Definition of the Porosity and Semi Cylinder

In this study, the method for controlling the vortex shedding behind cylinder (inner cylinder) was surrounded by an outer semi cylinder which is constructed from perforated steal sheet. Nine different inner cylinders (D_i =25mm, 30mm, 40mm, 50mm, 60mm, 70mm, 75mm, 80mm and 90mm) were used in the experiments. Ratio of the perforated surface area to the whole surface area was identified as porosity β (Figure 3.3).



$$\beta = \frac{3a}{3a+b}$$

Figure 3.3. Calculation of the porosity, β

In order to investigate the effect of porosity on the unsteady flow structure created in the near wake region of the inner cylinders, half and quarter ($\alpha=180^0$, 150^0 and 120^0) outer cylinders of six different porosity (β=0.3, 0.4, 0.5, 0.6, 0.7 and 0.8)

were used. Perforated half and quarter outer cylinders were obtained by perforating d=5mm diameter holes on 1 mm stainless steel plates and then bending the plates. Spring length of the perforated half and quarter outer cylinders were respectively 157.08 mm, 130.09 mm and 104.72 mm. In order to investigate the effect of diameter ratio (inner cylinder diameter / outer cylinder diameter) nine different diameter ratio were used as D_i/D_o=0.25, 0.3, 0.4, 0.5, 0.6, 0.7, 0.8 and 0.9. During the experiments inner cylinder and perforated cylinder were positioned in a way that they are concentric. Outer cylinder was positioned towards downstream direction, in a concentric way and in near wake region of the inner cylinder.

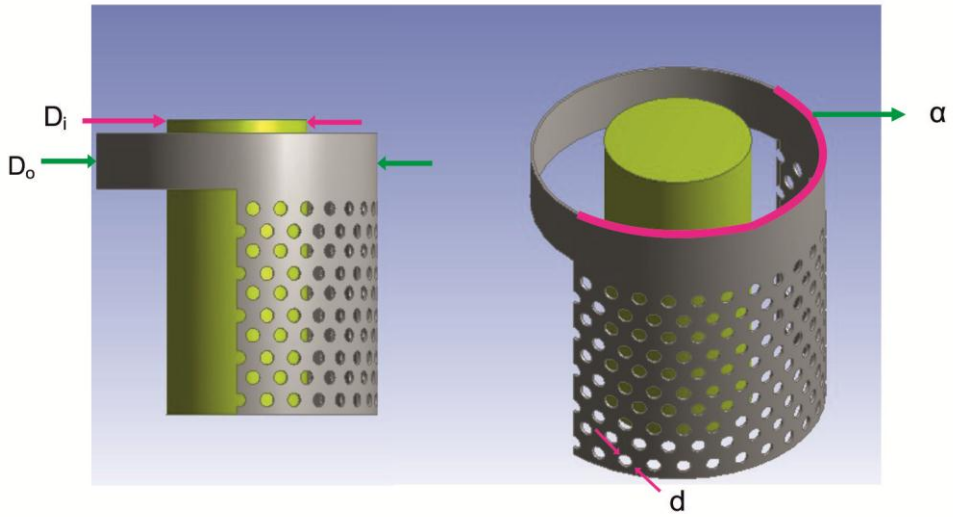


Figure 3.4. Overview of cylinders

A view of the experimental setup is presented in figures 3.4 and 3.5. All measurements were done on the plan view for water heights of h_w= 50mm, laser sheet was located parallel to the bottom of the water channel at heights of h_L=25mm for each case.

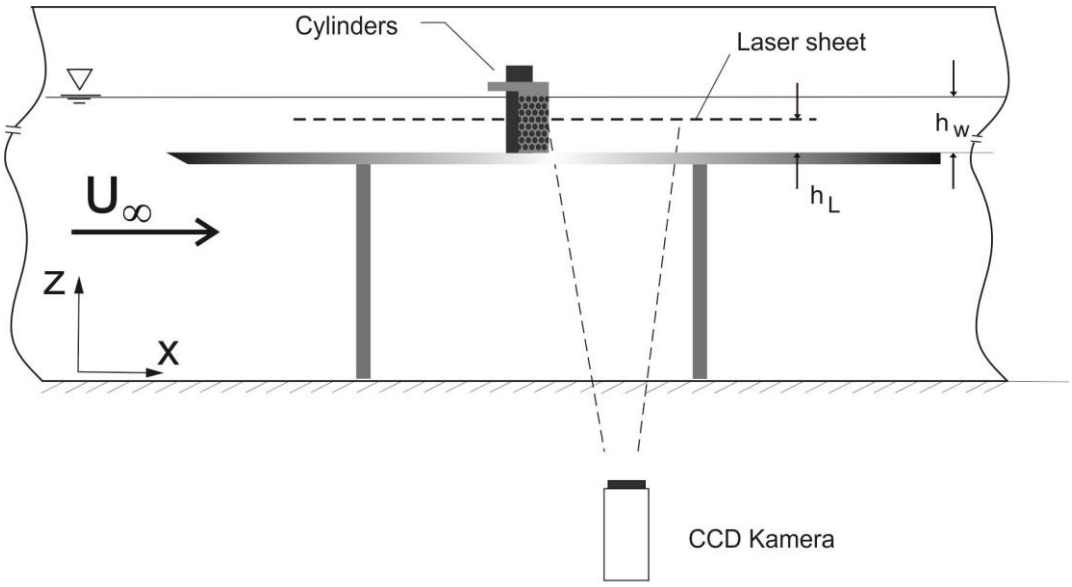


Figure 3.5. Overview of experimental system for side view

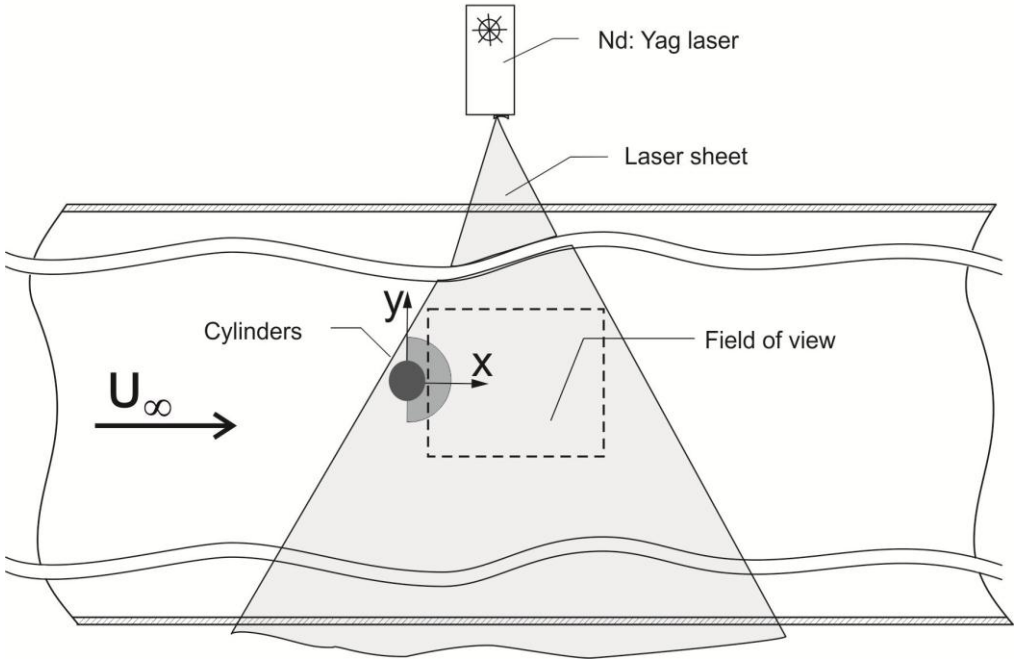


Figure 3.6. Plan view of the system

4. RESULTS AND DISCUSSIONS

4.1. PIV Experiments

4.1.1. Flow around a Single Cylinder

In this study, it was aimed to control the flow in near wake region of cylinders of varying diameters (D_i=25mm, 30mm, 40mm, 50mm, 60mm, 70mm, 75mm, 80mm and 90mm). In order to constitute reference and carry out comparison it is initially necessary to determine the flow characteristics in near wake region of the bare cylinder.

The contours of Turbulent Kinetic Energy (TKE), normalized Reynolds shear stress $< u'v' >$ are presented in figure 4.1 and 4.2 for the natural case. These parameters have been nondimensionalized by dividing them with the square of the depth-averaged free-stream velocity, U^2 for better comparisons. Figure 4.1 and 4.2 show average dimensionless Reynolds sheer stresses in the first column, time averaged vorticity contours $< \omega >$ in the second column and dimensionless turbulence kinetic energy (TKE) contours in the third column obtained from PIV experiments for inner cylinders of varying diameters. Results for cylinders of different diameters are shown in each row. The minimum and incremental values of Reynolds shear stress contours were taken as ±0.004 and 0.004, respectively. The solid and dashed lines present positive (counterclockwise) and negative (clockwise) Reynolds shear stresses, respectively. Reynolds shear stress contours for the bare cylinder case are formed on the near wake region of the cylinder. It is seen from Figures 4.1 and 4.2 that with the increasing cylinder diameter wake region grows and the intensity of Reynolds shear stress increases. The minimum and incremental values of time averaged vorticity $< \omega >$ contours were taken as ±2 and 2, respectively. It is observed that the time averaged vorticity in the near wake region of the bare cylinders have a symmetric structure and get closer to each other in the wake region.

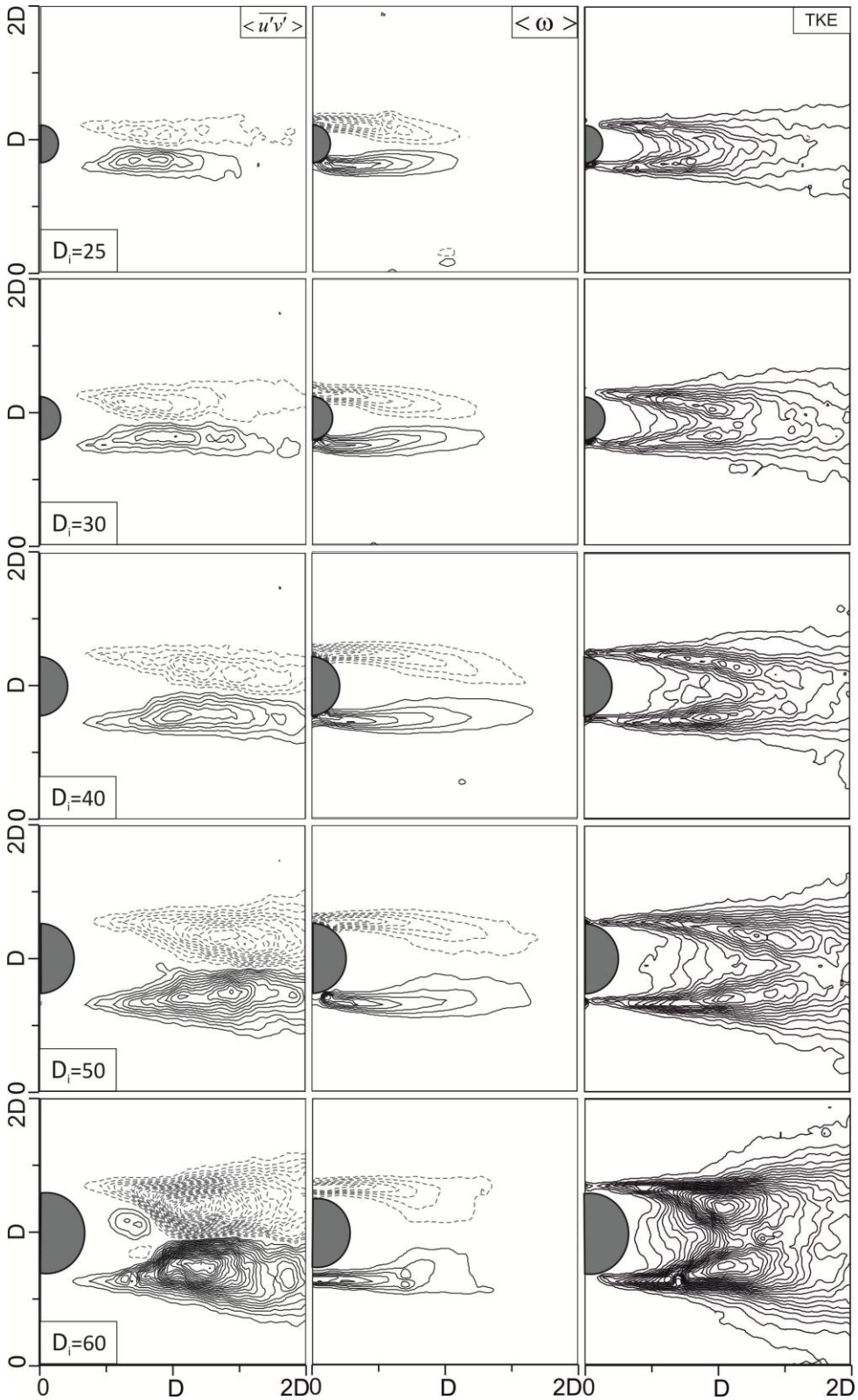


Figure 4.1. The Reynolds shear stress, vorticity and TKE distribution downstream of the *inner cylinder* for different diameters, D_i

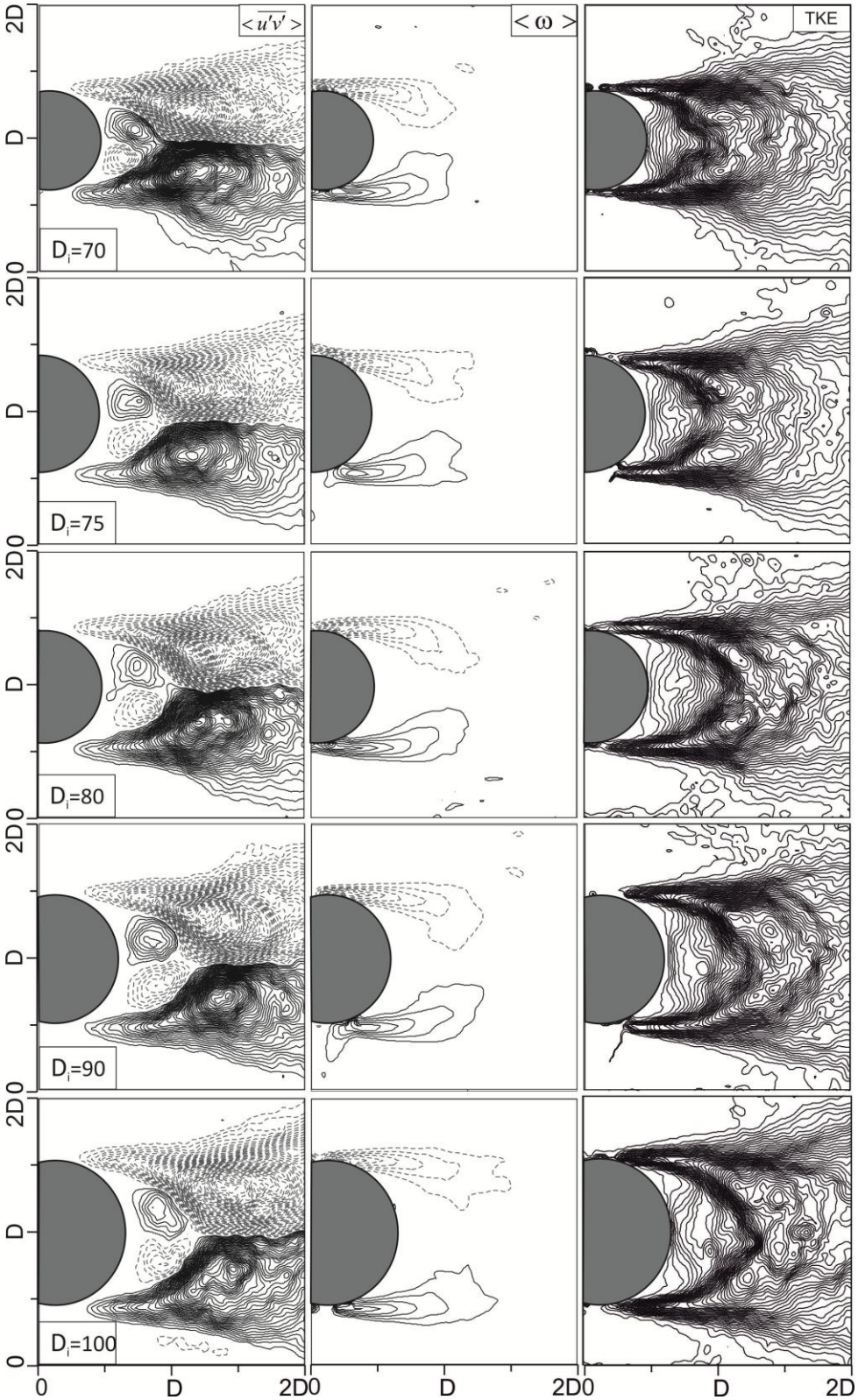


Figure 4.2. The Reynolds shear stress, vorticity and TKE distribution downstream of the *inner cylinder* for different diameters, D_i

. In two-dimensional PIV, the values of $< u'u' >$ and $< v'v' >$ can be calculated in the usual manner (by subtracting the mean values of the velocity components from their instantaneous values and then by averaging the products) from the 350 instantaneous data. Assuming isotropic flow, the third fluctuating velocity component can be estimated by a 2D approximation (Sheng et al. 2000), namely the third component has been supposed to be equal to the half of $(< u'u' > + < v'v' >)$, then TKE can be calculated with the following expression

$$\mathrm{TKE} = \frac{3}{4}\left(< u'u' > + < v'v' >\right) \quad (1)$$

.

In the third columns of Figures 4.1 and 4.2 TKE contours are presented. . The minimum and incremental values of TKE contours were taken as 0.001. It is observed that the flow causes turbulence in wake region of bare cylinders and with the increasing diameter also turbulence intensity increases and forms a more distinct structure in the near wake region of the cylinder.

4.1.2. Flow around the Cylinder surrounded by a Perforated Cylinder

In order to control the near wake region flow, perforated half cylinders with varying arc angle were used as the control elements of the study. The effect of porosity for each different diameter was investigated by changing the perforated cylinders with the same inner cylinder. From the PIV results obtained by the existence of control elements, it was concluded that a single field of view is inadequate for determining the flow characteristics of the whole wake region, therefore experiments were performed for multiple fields of view. Other fields of view were obtained by keeping the cylinders fixed and shifting the camera and laser 200 mm on the direction of flow (field of view 200mmX200mm). The effects of porosity are presented in each row for all figures. The parameter, D represents the outer cylinder diameter, D_o which was taken as Do=100mm.

4.1.2.1. Half Outer Cylinder Application

In order to better analyze the flow formation in the wake region of cylinder couple, experiments were performed for the case where only outer cylinder (half cylinder) were present. Figure 4.3 presents the Reynolds stress contours. The minimum and incremental values of Reynolds shear stress contours were taken as ±0.0015 and 0.0015, respectively. It was observed that at low porosities, particularly at β=0.3 and 0.4, half cylinders affected the flow structure and at both sides of the outer cylinder the shear layers elongate in downstream direction.

Figures from 4.4 to 4.12 show the Reynolds shear stress contours obtained from the PIV experiments at D_i/D_o=0.25, 0.3, 0.4, 0.5, 0.6, 0.7, 0.8 and 0.9 diameter ratios, respectively. The minimum and incremental values of Reynolds shear stress contours were taken as ±0.0015 and 0.0015, respectively. The effect of porosity on Reynolds shear stress at D_i/D_o=0.25 diameter ratio is presented in Figure 4.4. It is observed that at low porosities Reynolds shear stresses are caused by the outer cylinder rather than the inner cylinder. This is particularly clear when β=0.3 and 0.4 are compared with Figure 4.3. Beginning from porosity β=0.5 obvious reductions take place in Reynolds stress values. At β=0.8, the effect of inner cylinder on unsteady flow structure is dominated. The cause of the clusters seen in Reynolds stresses is the presence of the inner cylinder. It is demonstrated that high porosity does not have a significant effect on the flow structure.

Figures 4.5 and 4.6 present the Reynolds stress contours for different porosities at D_i/D_o=0.3 and 0.4, respectively. The case here is also similar to the previous diameter. At these diameter ratios, the maximum value of the least Reynolds stress occurs at β=0.7. However, Reynolds shear stress contours obtained for D_i/D_o=0.3 and 0.4 diameter ratio at β=0.7 porosity shows that the lowest value of the maximum Reynolds stress did not occur due to an effective control. The occurrence of Reynolds stress contours based on the near wake inner cylinder is the indication of this. At β=0.8 value of porosity the effect of the inner cylinder is observed more clearly.

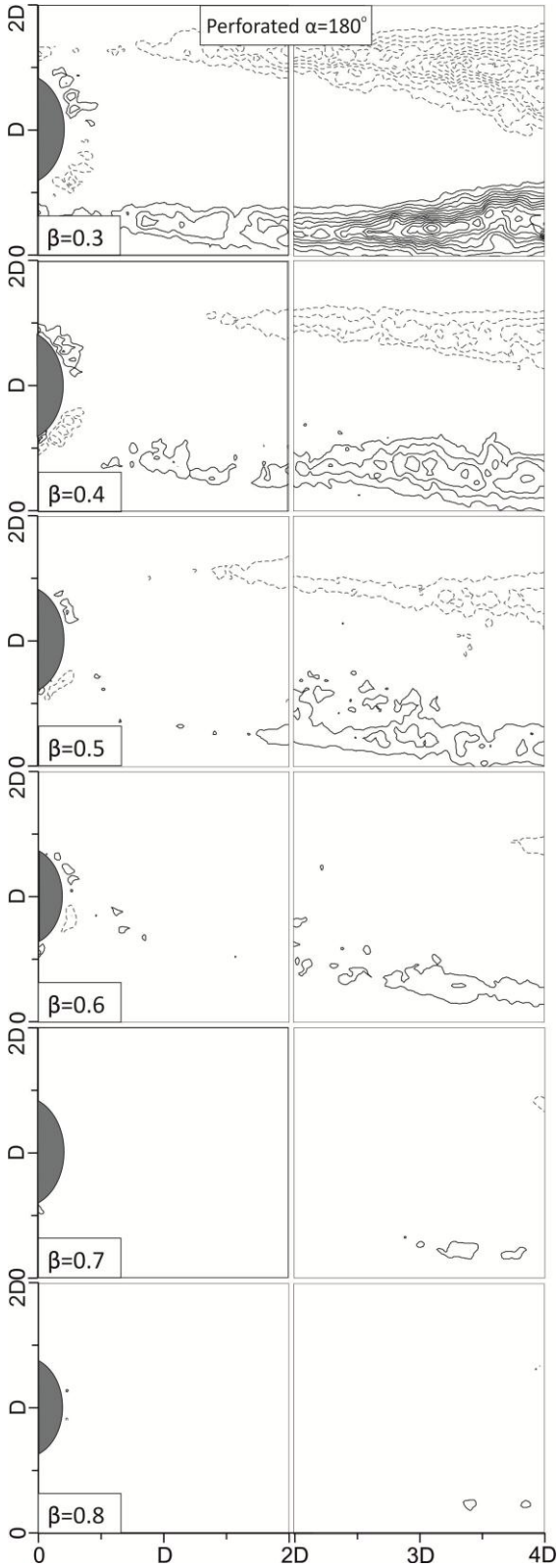


Figure 4.3. The Reynolds shear stress distribution downstream of the half cylinder ($\alpha=180^o$) for different β cases

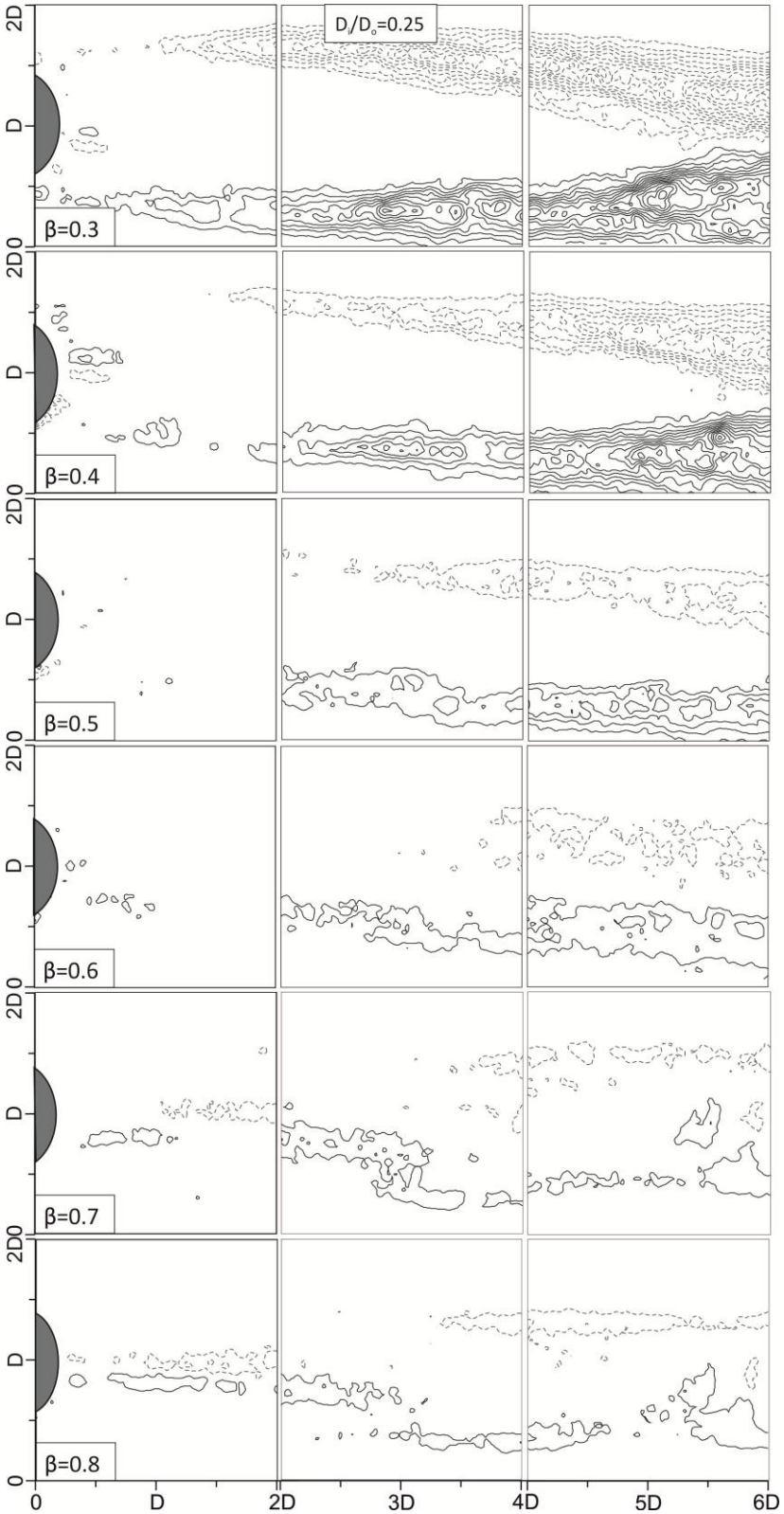


Figure 4.4. The Reynolds shear stress distribution downstream of the cylinder surrounded with half cylinder ($\alpha=180^o$) for $D_i/D_o=0.25$ at different β cases

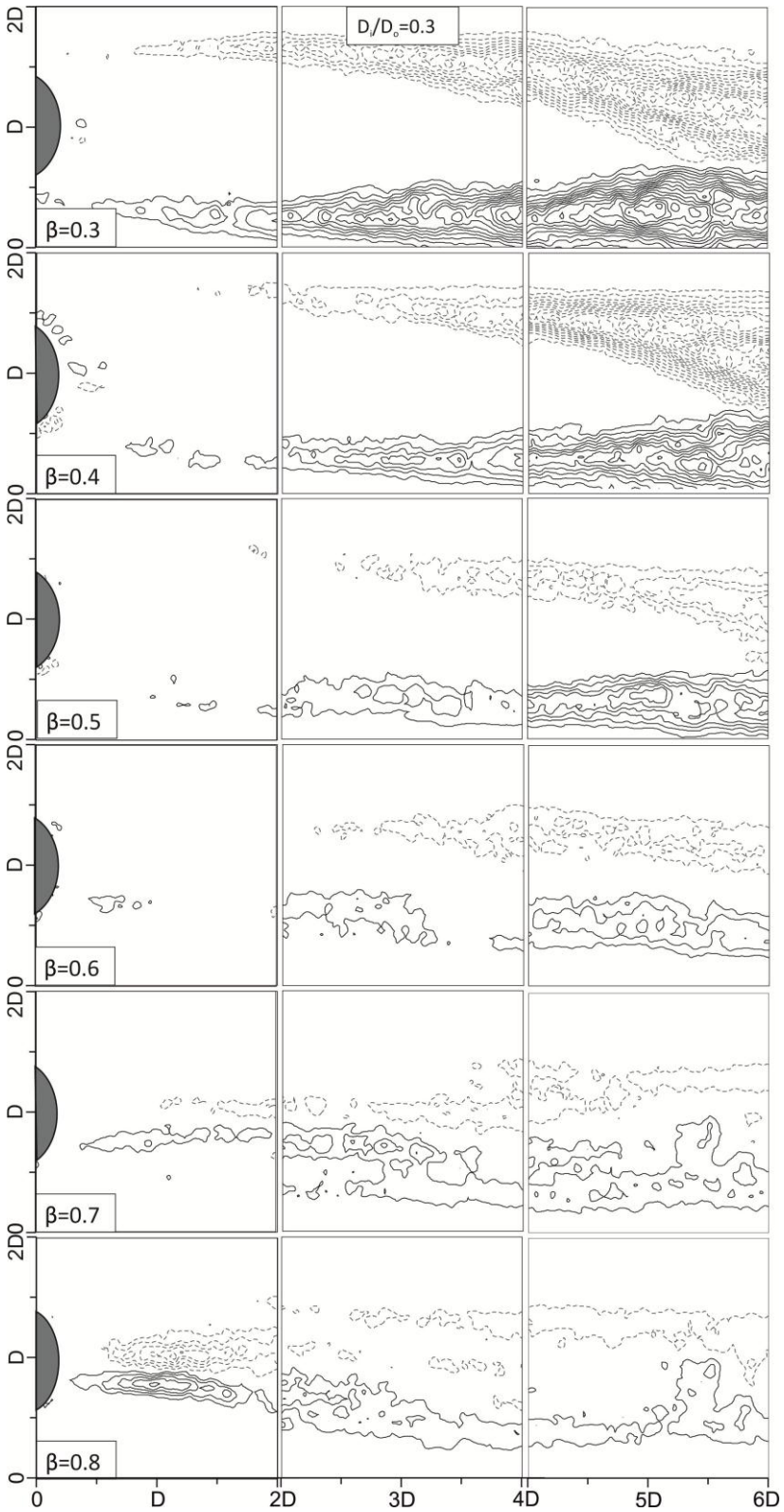


Figure 4.5. The Reynolds shear stress distribution downstream of the cylinder surrounded with half cylinder ($\alpha=180^o$) for $D_i/D_o=0.3$ at different β cases

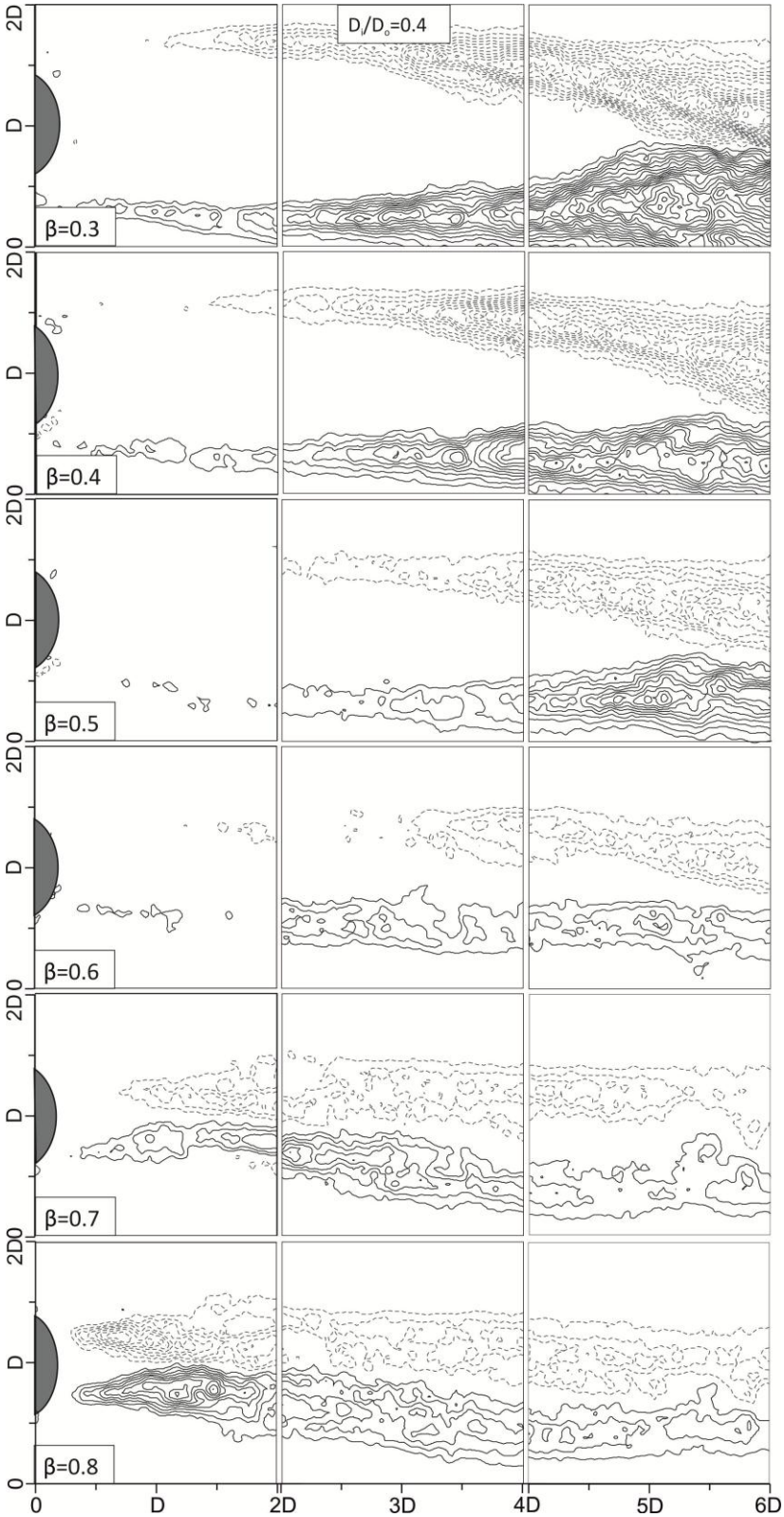


Figure 4.6. The Reynolds shear stress distribution downstream of the cylinder surrounded with half cylinder ($\alpha=180^o$) for $D_i/D_o=0.4$ at different β cases

With increase of the inner cylinder diameter, the wake region grows and also the intensity of Reynolds stress increases. The effect of the perforated half cylinder ($\alpha=180^o$) on flow control is clearly seen by comparing the structure that occurs in Figure 4.7 for $D_i/D_o=0.5$ with the bare cylinder in Figure 4.1 with $D_i=50$ mm diameter. Reynolds shear stress contours that occur in all porosities until $\beta=0.7$ take place only in the free shear layer that is formed between the free stream region at both sides of the outer cylinder and the wake region. In this range of porosity, outer cylinder was completely effective on the inner cylinder. Particularly the porosities $\beta=0.5$ and 0.6 were highly effective on reducing the intensity of the Reynolds stress that formed on the near wake of the cylinders. The shear layers formed in the both sides of the cylinder couple are elongated downstream direction and interacted with the third field of view. The points, where the maximum Reynolds stress was formed in these porosities, were in the third field of view. Reynolds shear stress intensity in the third field of view of $0.3\leq\beta\leq0.6$ range is more than the region near the cylinder. Because of wake region exhibits 'S' shaped unsteady oscillations similar to Karman vortex streets at approximately 5D (D= outer cylinder diameter) distance from the cylinder couple. This oscillatory wake region structure causes quite minor damage to near wake region structure than the Karman vortices. After the porosity $\beta=0.7$, with the outer cylinder starting to lose its effect on the inner cylinder intensity of the Reynolds shear stress contours formed from the cylinder couple starts to increase in the region near the cylinder.

Figure 4.8 presents the Reynolds stresses obtained from varying porosities at $D_i/D_o=0.6$ diameter ratio. It is found that the porosity for optimum flow control is $\beta=0.6$. Considering the previous diameter ratios, it is clearly seen that at all porosities the peak magnitude of Reynolds shear stress obviously increase for this diameter ratio. For instance, while the peak magnitude of Reynolds shear stress was 0.014 for $D_i/D_o=0.5$ diameter ratio at $\beta=0.6$ porosity, it was found to be 0.03 at $D_i/D_o=0.6$ diameter ratio. As the diameter ratio increases, the effect of the outer cylinder on flow structure decreases due to decreasing distance between the inner and outer cylinders.

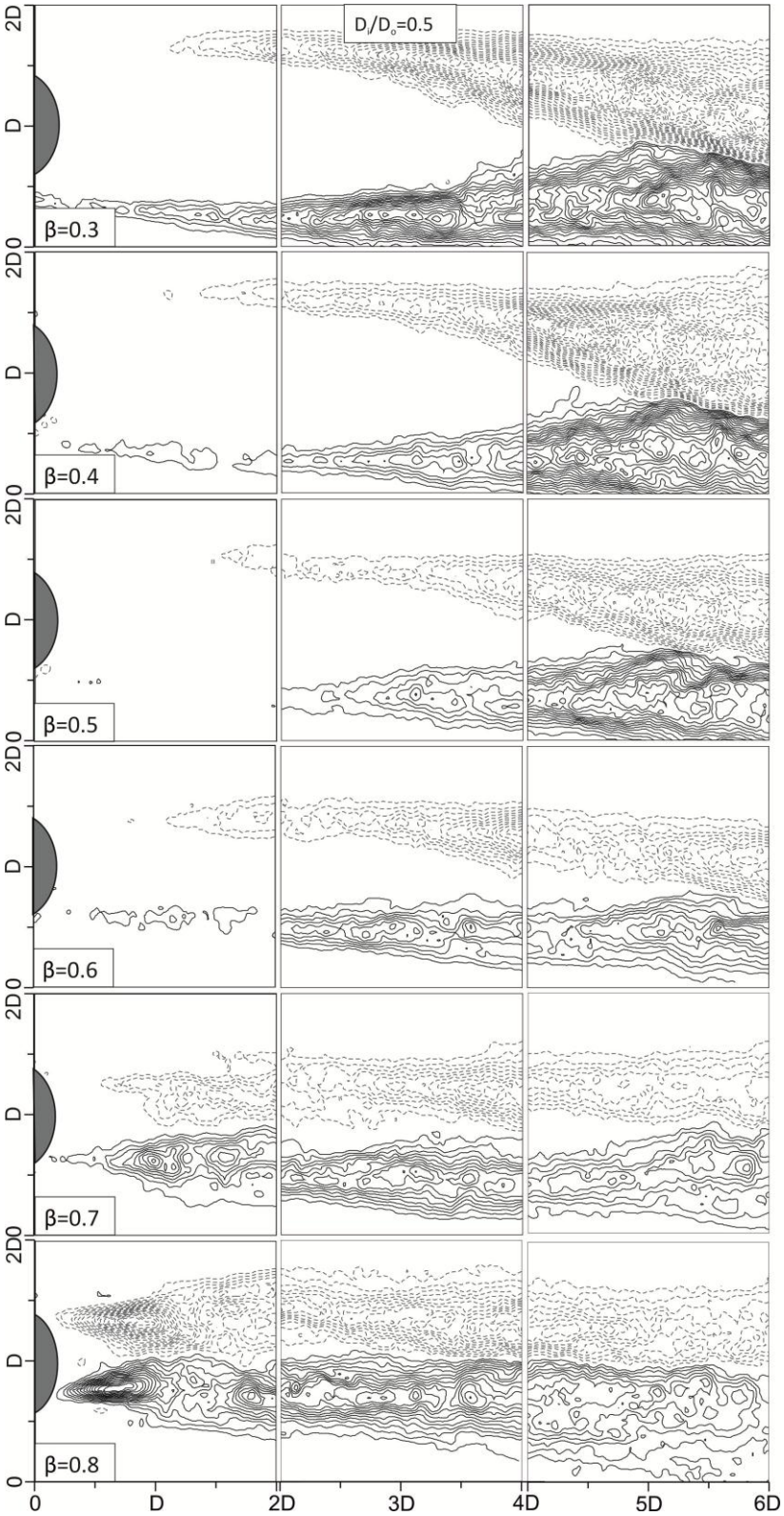


Figure 4.7. The Reynolds shear stress distribution downstream of the cylinder surrounded with half cylinder ($\alpha=180^o$) for $D_i/D_o=0.5$ at different β cases

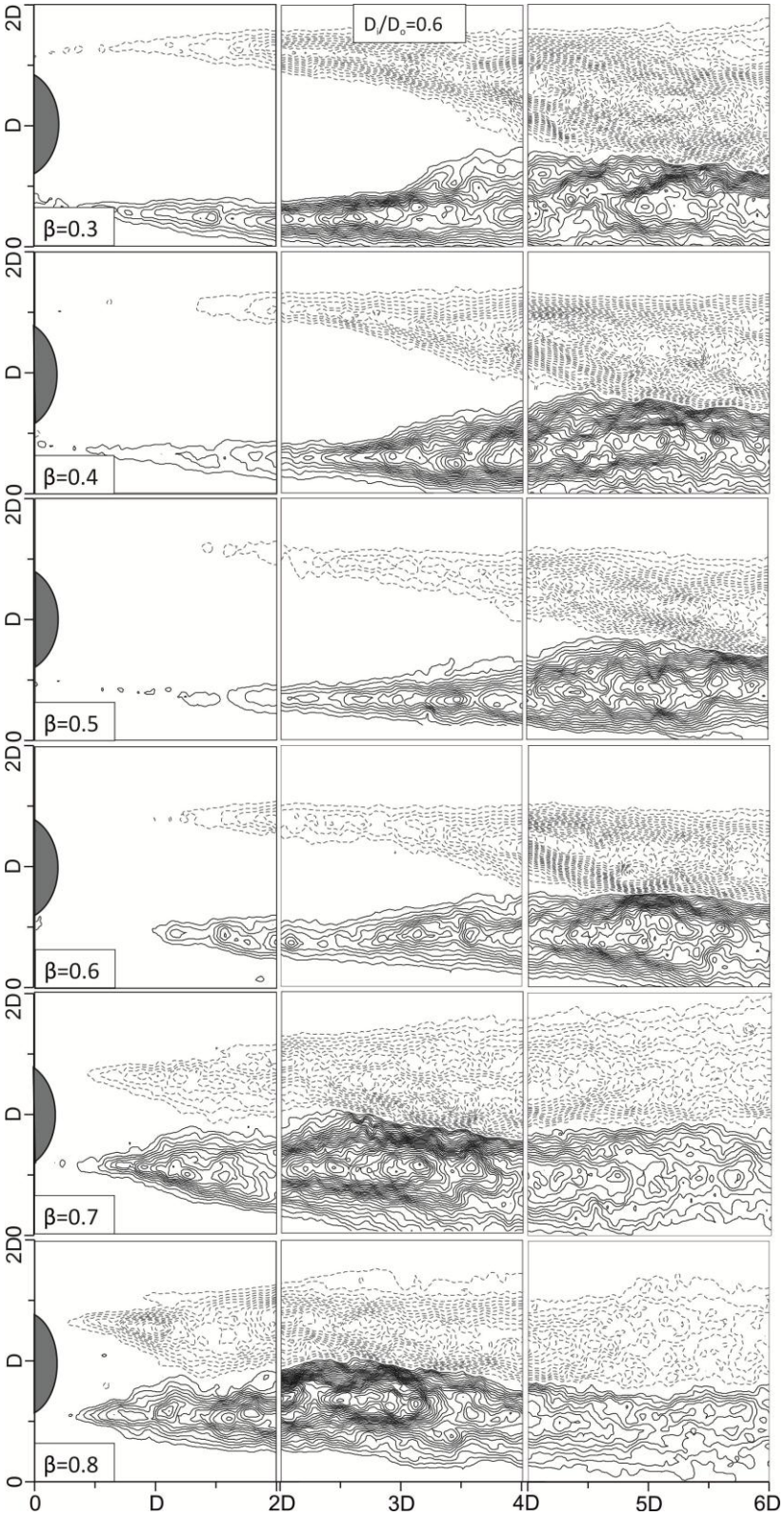


Figure 4.8. The Reynolds shear stress distribution downstream of the cylinder surrounded with half cylinder ($\alpha=180^o$) for $D_i/D_o=0.6$ at different β cases

Effect of varying porosities to D_i/D_o=0.7 diameter ratio is presented in Figure 4.9. The intensity of the shear layer occurred at both sides of the cylinder couple continues to increase and the point where these shear layers interact gets closer to the cylinder couple.

Figure 4.10 shows Reynolds shear stress contours obtained at varying porosities for diameter ratio of Di/D_o=0.75. In all porosities, the points where the peak magnitude of Reynolds shear stress occurs were in the second field of view. Due to this reason, at D_i/D_o=0.75 diameter ratio experiments for the third field of view were not performed. As distinct from the other diameter ratios, the least Reynolds shear stress value was obtained from porosity β=0.5. The peak magnitude of Reynolds shear stress obtained from the bare cylinder (D_i=75 mm) was 0.135. At porosity of β=0.5, the peak magnitude of Reynolds shear stress decreases down to 0.024. At low porosities high intensity of Reynolds shear stress values are obtained in the near wake region of outer half cylinder. For instance, for porosity β=0.3 the maximum Reynolds shear stress value was computed as 0.039.

Figures 4.11 and 4.12 show Reynolds shear stress contours respectively at D_i/D_o=0.8 and 0.9 values of diameter ratio. Although Reynolds shear stress values at these diameter ratios were higher than those obtained from the previous diameter ratios, when the peak magnitude of Reynolds shear stress are compared with bare inner cylinder it is observed that porosity ratio was effective. For instance, in the case that only bare cylinder was present while Reynolds shear stress values were found out to be 0.18 and 0.2 for D_i=80 mm and 90 mm, maximum Reynolds shear stress values decrease to 0.035 and 0.085 with the respective diameter ratios of D_i/D_o= 0.8 and 0.9.

Figure 4.13 shows the effect of porosity on maximum Reynolds shear stresses that occur in the near wake of cylinders of varying diameter ratios. Although the least maximum Reynolds shear stresses were obtained at low diameter ratios, when compared with the case where only bare cylinder was present it is observed that Reynolds shear stress value was increased at low porosities. It is demonstrated that higher diameter ratios are more effective on reducing the Reynolds shear stress values compared to the bare cylinder case.

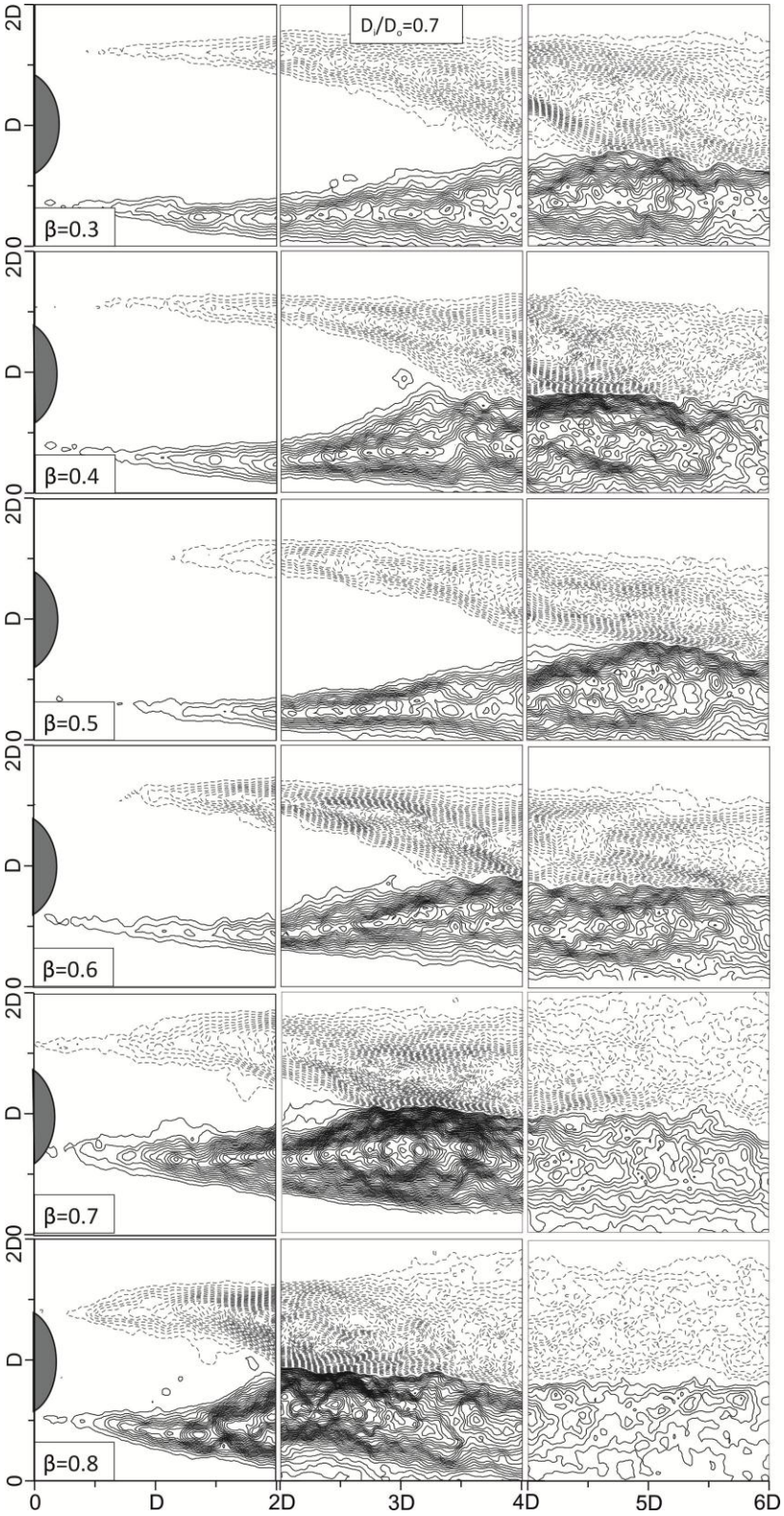


Figure 4.9. The Reynolds shear stress distribution downstream of the cylinder surrounded with half cylinder ($\alpha=180^o$) for $D_i/D_o=0.7$ at different β cases

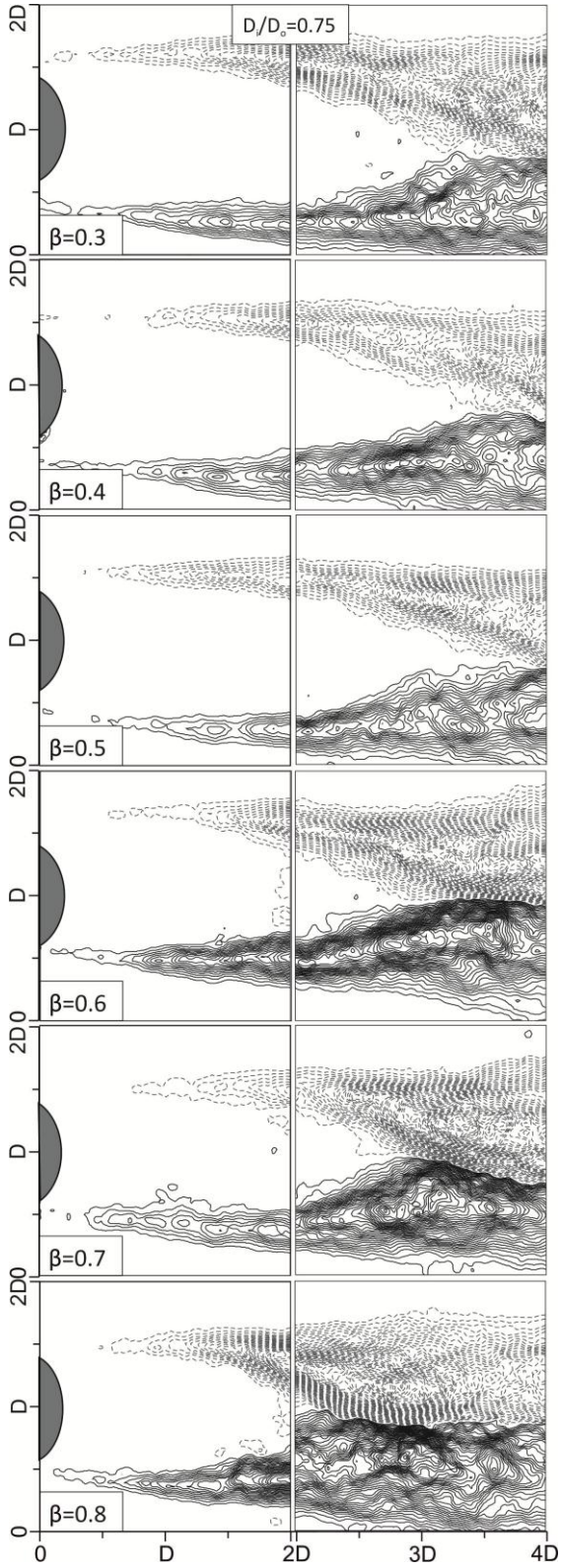


Figure 4.10. The Reynolds shear stress distribution downstream of the cylinder surrounded with half cylinder ($\alpha=180^o$) for $D_i/D_o=0.75$ at different β cases

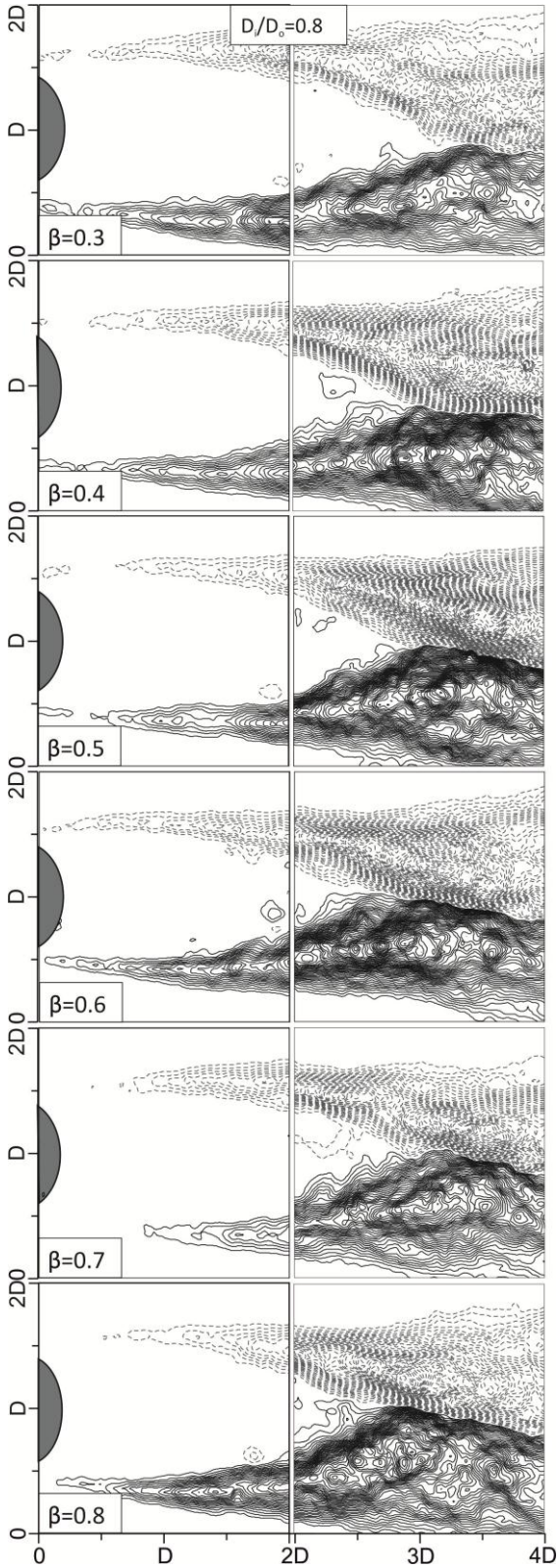


Figure 4.11. The Reynolds shear stress distribution downstream of the cylinder surrounded with half cylinder ($\alpha=180^o$) for $D_i/D_o=0.8$ at different β cases

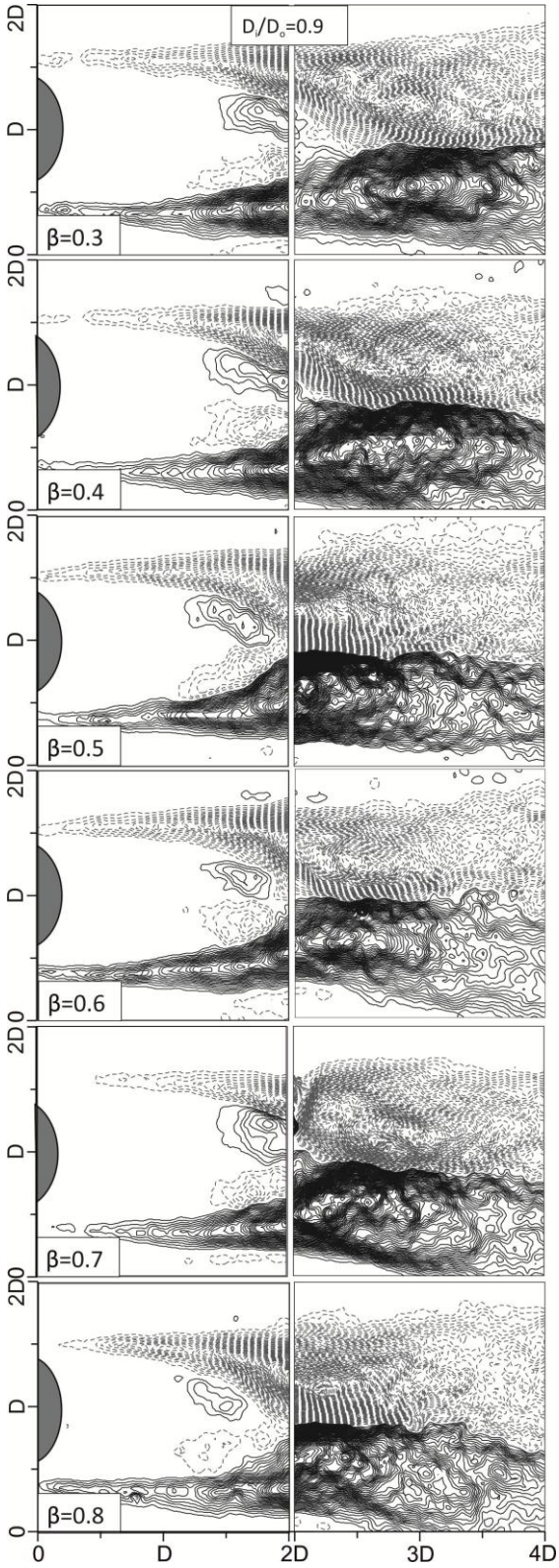


Figure 4.12. The Reynolds shear stress distribution downstream of the cylinder surrounded with half cylinder ($\alpha=180^o$) for $D_i/D_o=0.9$ at different β cases

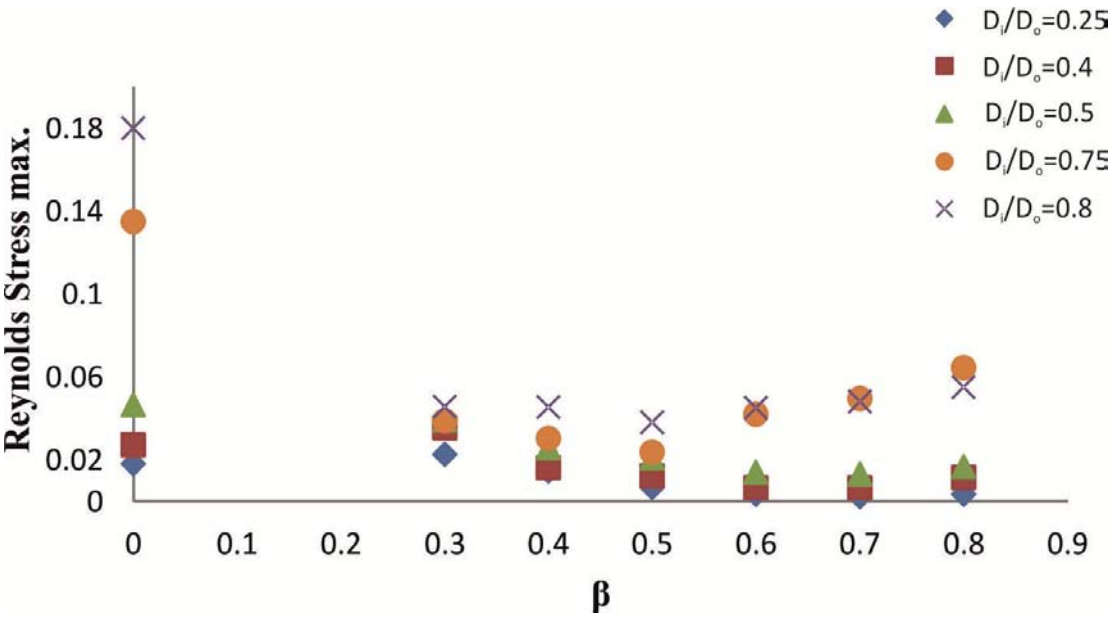


Figure 4.13. The variation of Reynolds stress$_{max}$ with β to demonstrate the effect of D_i/D_o

Figures from 4.14 to 4.22 show the time averaged vorticity contours in the near wake of the cylinder couple where the inner cylinder was surrounded by perforated half cylinders of varying porosities. Each figure shows the effect of porosity within the range of $0.3 \leq \beta \leq 0.8$ on the inner cylinder. While the solid lines indicate positive vorticity contours, dashed lines show negative contours. The minimum and incremental values of time averaged vorticity contours were taken ±1 and 1, respectively.

Figure 4.14 shows the effect of porosity on the vorticity occurred in near wake of cylinder couple at $D_i/D_o=0.25$ diameter ratio. First of all, positive and negative time averaged vorticity distribution has almost symmetrical structure. The vorticity occurred in the near wake of inner cylinder - half outer cylinder configuration shows that the perforated half outer cylinder has a significant effect on the flow structure. In bare cylinder case in Figure 4.1, the shear layers formed on the upper and lower part of the cylinder affect each other in the wake region. Due to the entry of flow into wake region from the perforated half cylinder, interaction of the shear layers decreases. As a result, it can be seen from Figure 4.13 that, within the

range of $0.3 \leq \beta \leq 0.6$, the shear layers elongate in streamwise direction and get close to each other in the third field of view ($5D_o$). It is observed that porosity is a factor that is effective on the flow structure. At low porosities the shear layers occurring at the both sides of the cylinder couple are generated from the outer cylinder. It is found that the most effective porosity for reducing the vorticity couple magnitude is $\beta=0.5$. Comparing $\beta=0.7$ and 0.8 porosities with the other ones shows that the effect of the perforated outer cylinder on the flow structure resulting from the inner cylinder is reduced. A lower magnitude vorticity pair (B) is evident in Figure 4.13 for $\beta=0.7$ and 0.8. This vorticity pair, which occurs due to the presence of the inner cylinder, moves towards the primary vorticity layers (A).

Figures 4.15, 4.16 and 4.17 present vorticity contours for $D_i/D_o=0.3$, $D_i/D_o=0.4$ and $D_i/D_o=0.5$ diameter ratios, respectively. Although in these diameter ratios the flow characteristics are similar to those in $D_i/D_o=0.25$, with increasing diameter ratios it is observed that shear layer gradually shortens and grows in magnitude. For porosities $\beta=0.7$ and 0.8, the negative and positive vorticity in near wake region of the cylinder couple get closer to each other. Therefore it is concluded that diameter ratio is a parameter that is effective on the flow characteristics.

Figures 4.18, 4.19 and 4.20 show the time averaged vorticity contours at $D_i/D_o=0.6$, 0.7 and 0.75, respectively. Increasing diameter ratio is more effective than porosity in affecting flow characteristics. Within the range of $0.3 \leq \beta \leq 0.6$ porosity, structures of the vorticity occurring in the near wake region of the cylinder are approximately the same. However with increasing diameter ratios, the vorticity couple shortens and increases in their magnitude continue. At low diameter ratios it is observed that the vorticity couples (A and B) occurring at $\beta=0.7$ and 0.8 porosities merge with each other. It is seen in Figure 4.20 that, at $D_i/D_o=0.75$ diameter ratio positive and negative vorticity couples get closer to each other in the second field of view for all porosities. Due to this reason third field of view were not investigated.

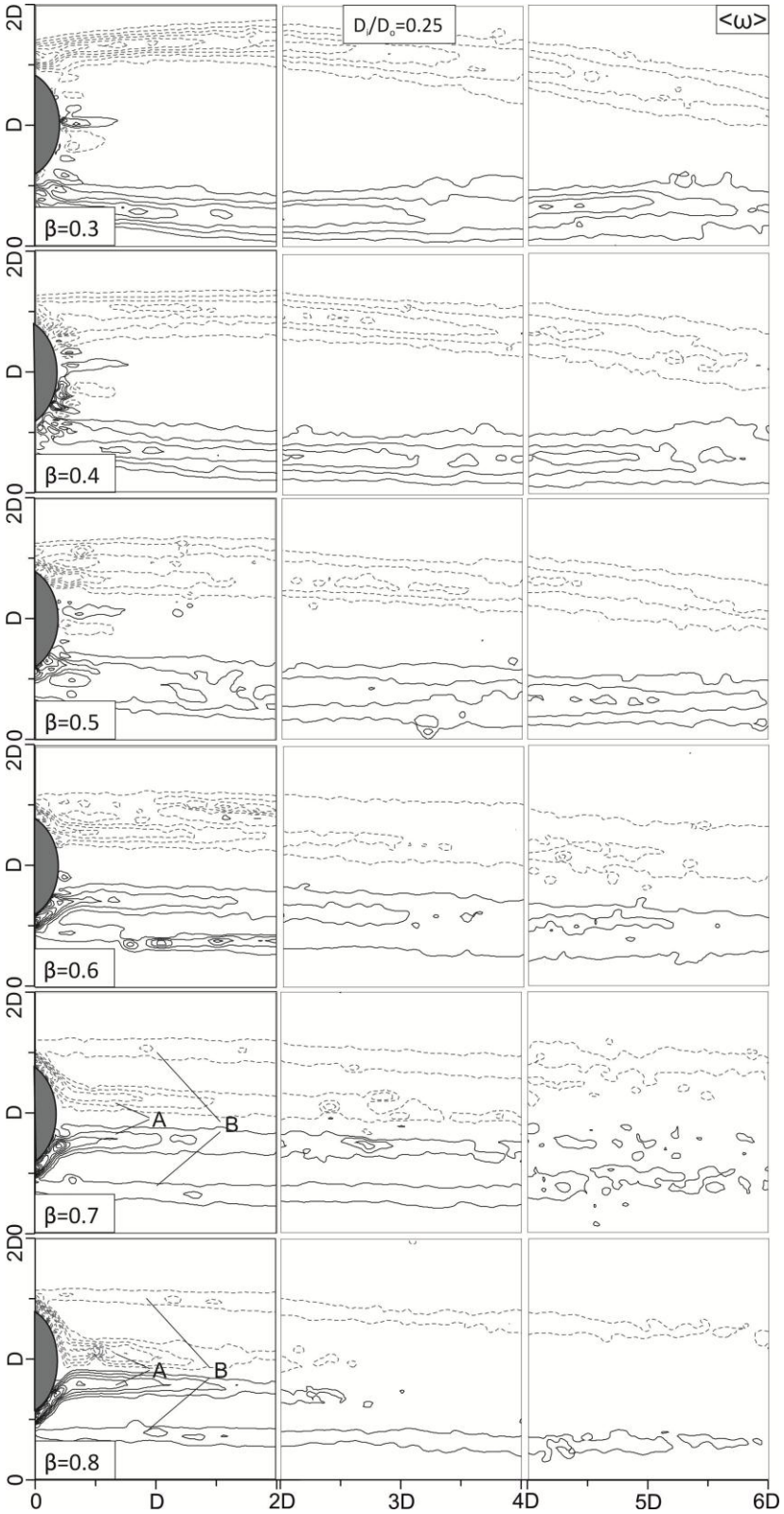


Figure 4.14. The vorticity distribution downstream of the cylinder surrounded with half cylinder ($\alpha=180^o$) for $D_i/D_o=0.25$ at different β cases

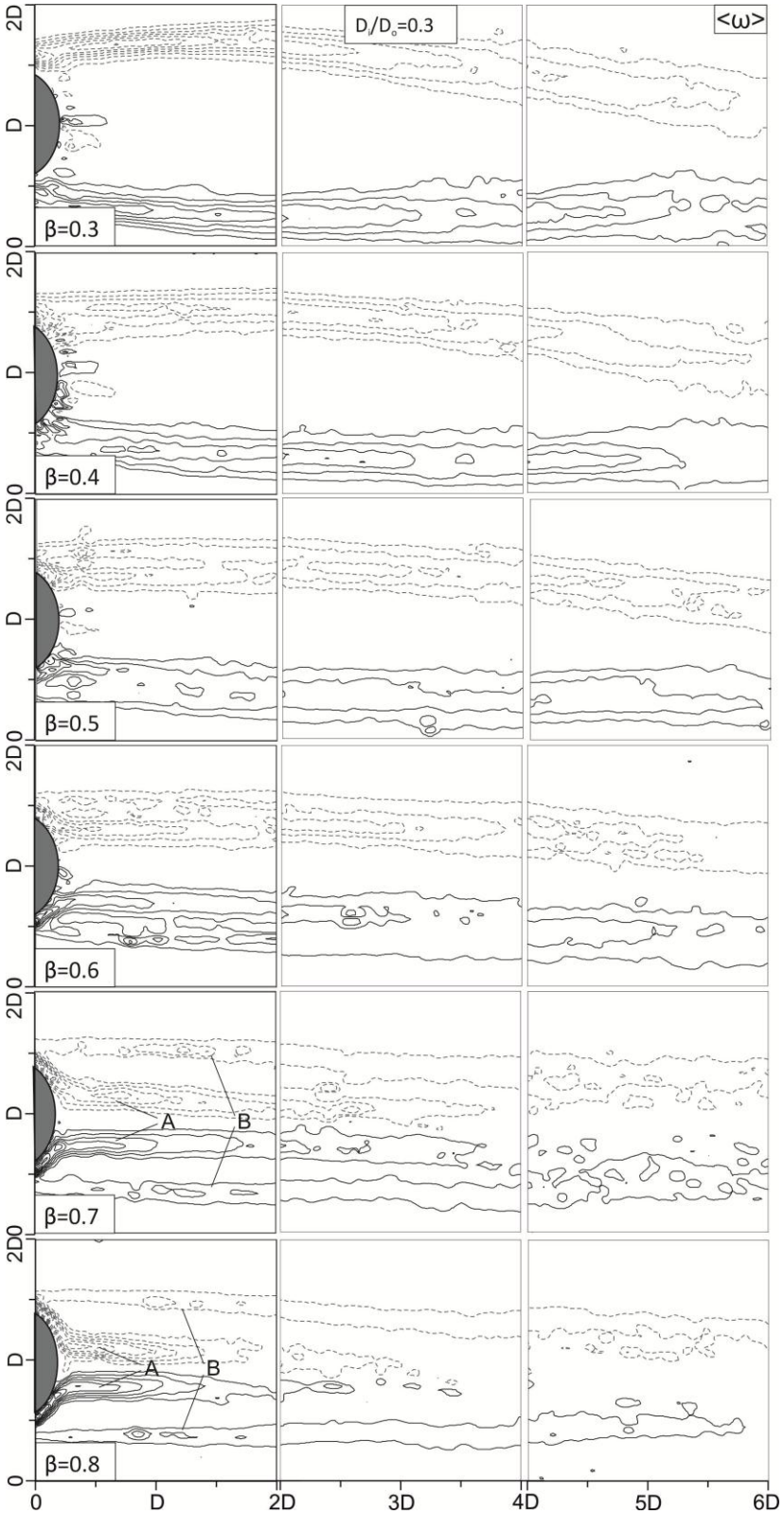


Figure 4.15. The vorticity distribution downstream of the cylinder surrounded with half cylinder ($\alpha=180^o$) for $D_i/D_o=0.3$ at different β cases

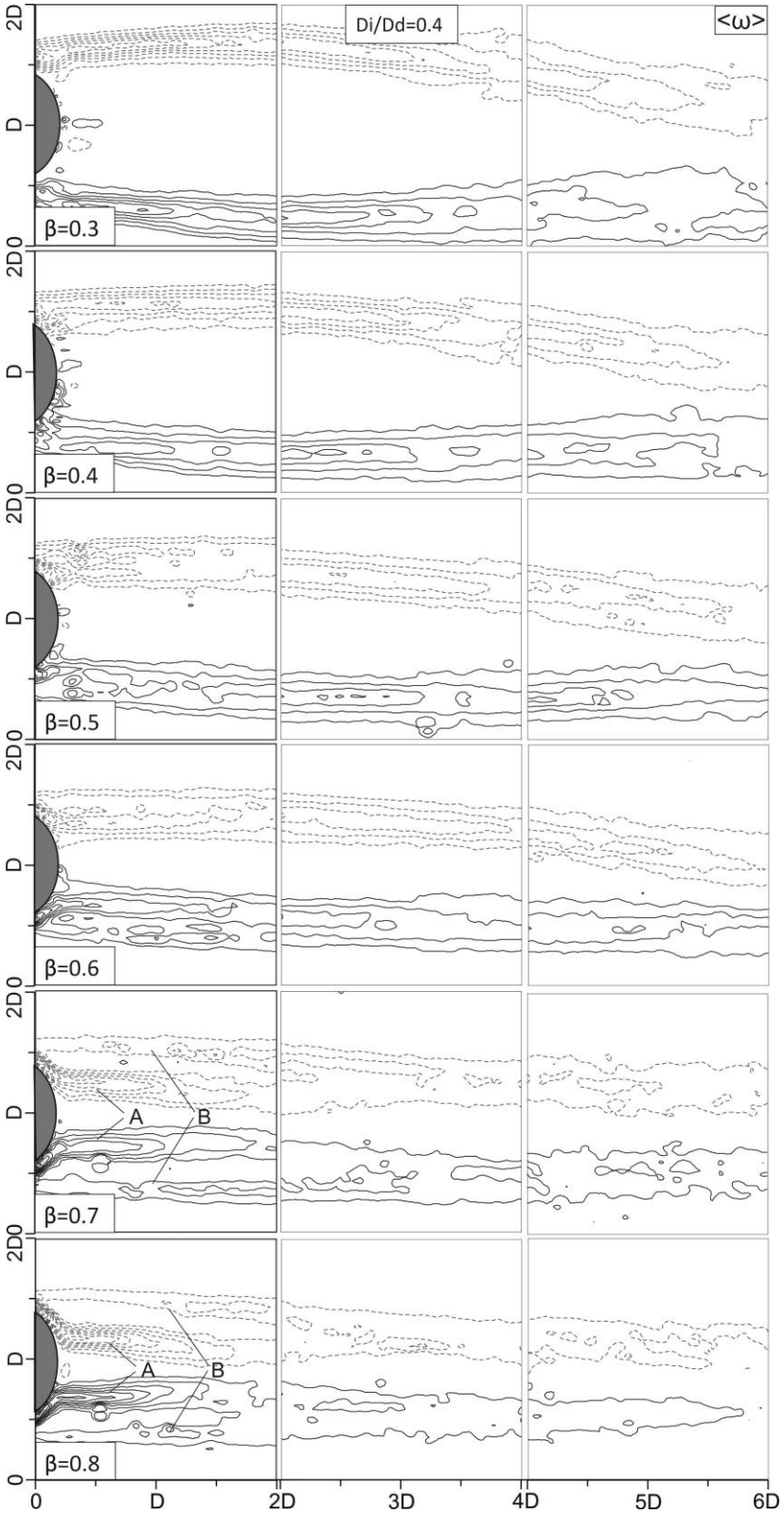


Figure 4.16. The vorticity distribution downstream of the cylinder surrounded with half cylinder ($\alpha=180^o$) for $D_i/D_o=0.4$ at different β cases

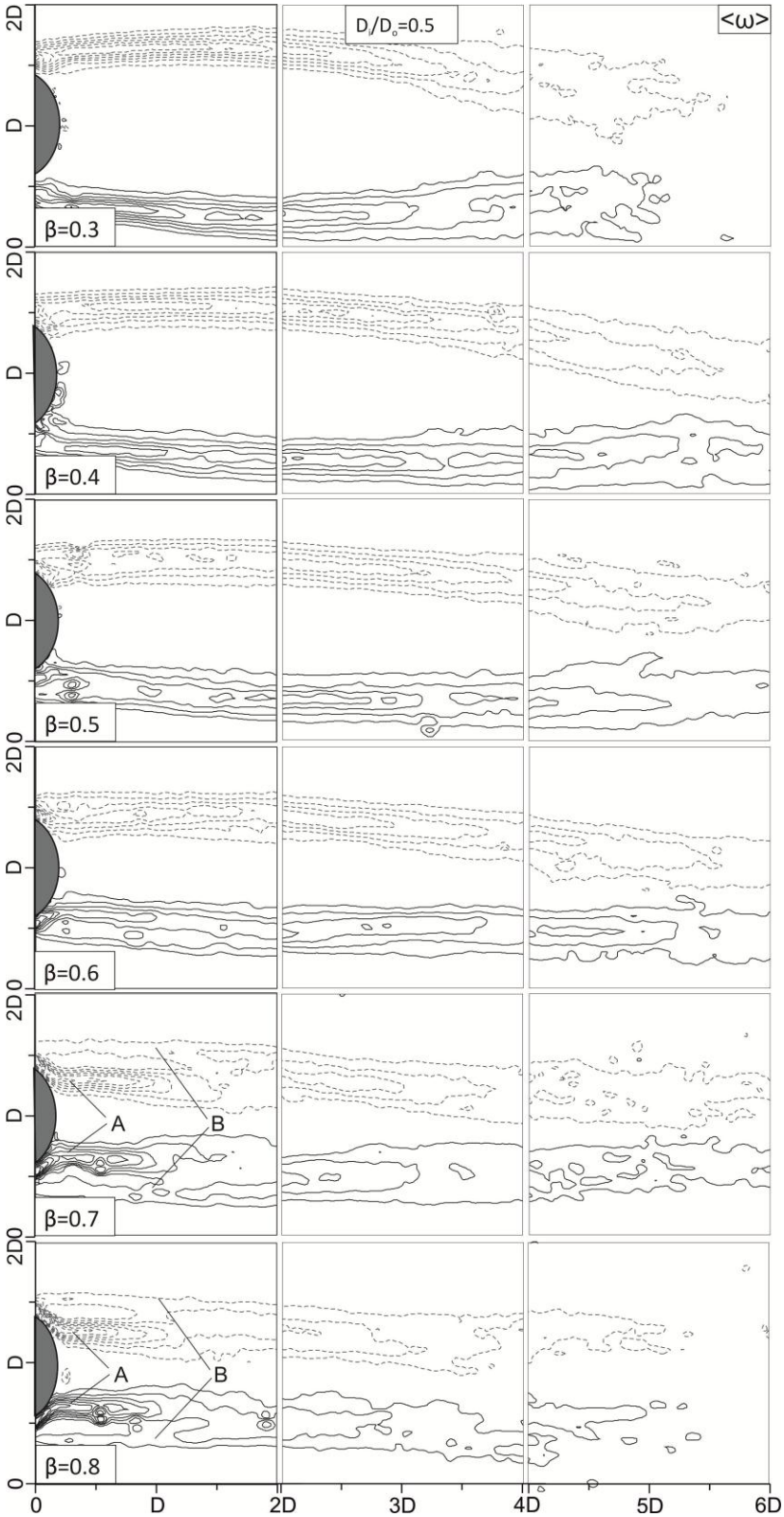


Figure 4.17. The vorticity distribution downstream of the cylinder surrounded with half cylinder ($\alpha=180^o$) for $D_i/D_o=0.5$ at different β cases

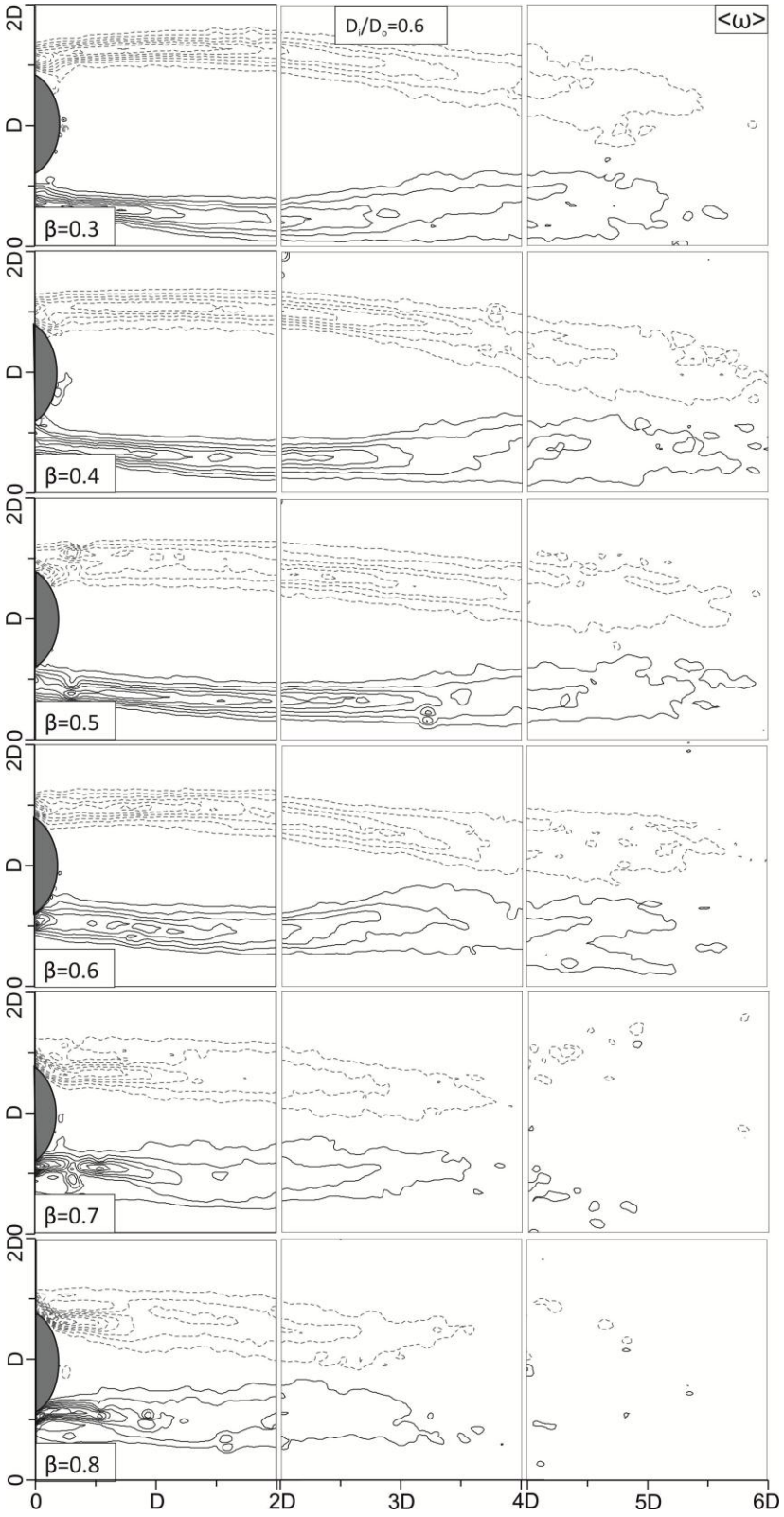


Figure 4.18. The vorticity distribution downstream of the cylinder surrounded with half cylinder ($\alpha=180^o$) for $D_i/D_o=0.6$ at different β cases

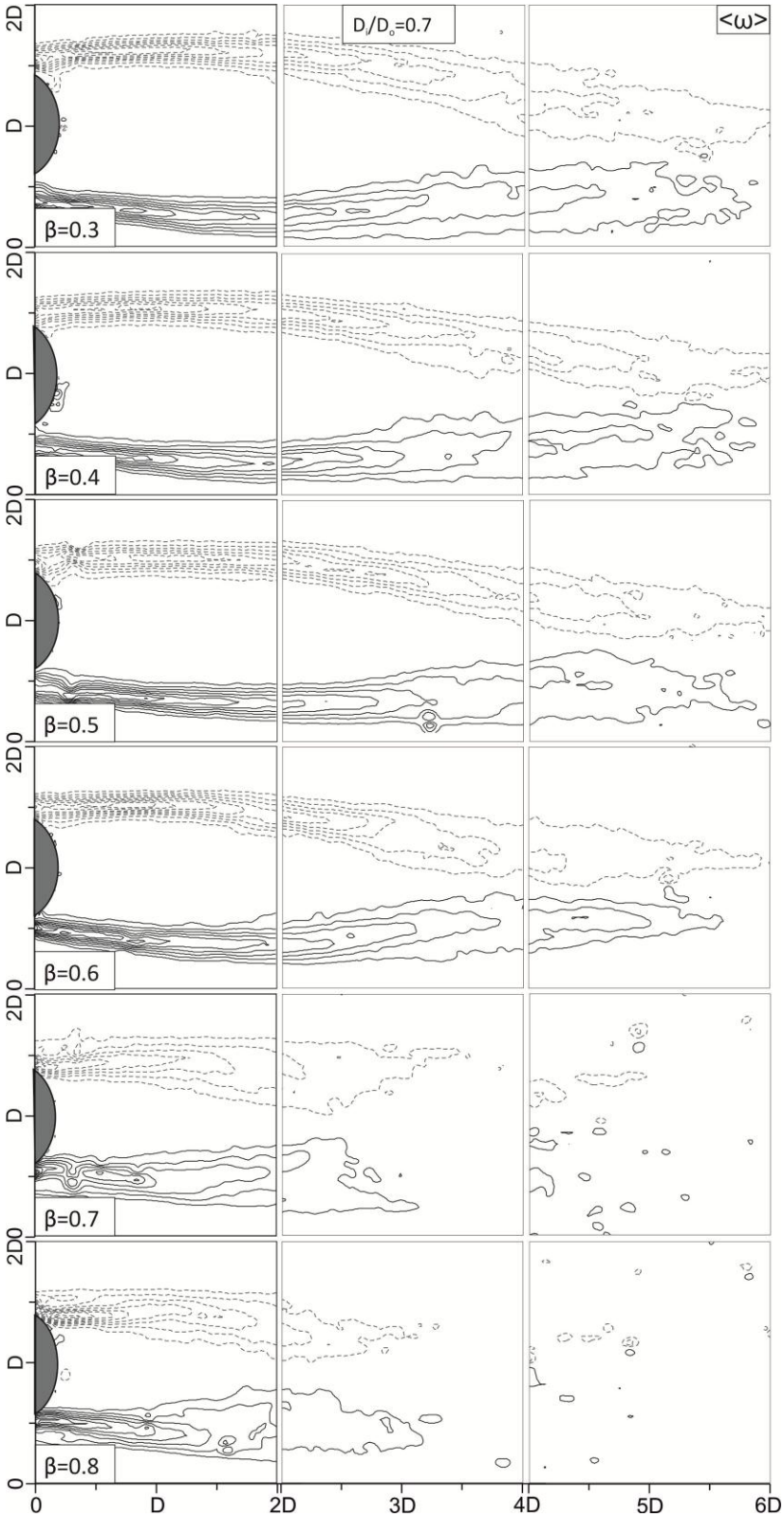


Figure 4.19. The vorticity distribution downstream of the cylinder surrounded with half cylinder ($\alpha=180^o$) for $D_i/D_o=0.7$ at different β cases

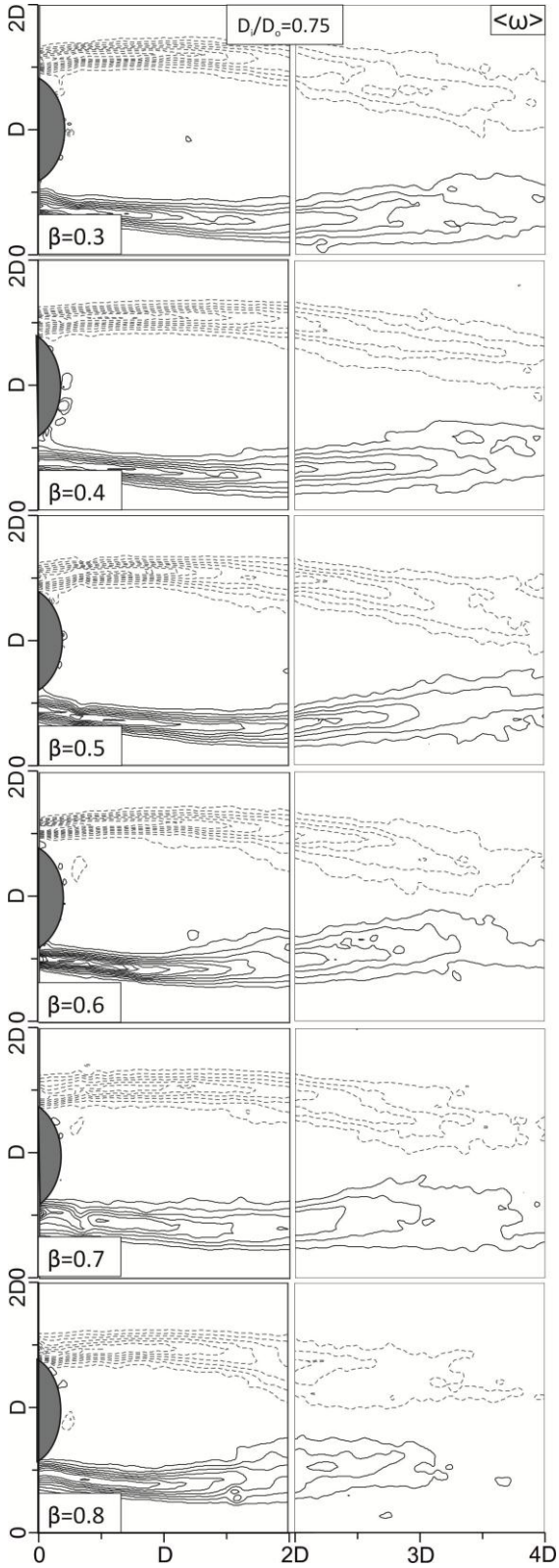


Figure 4.20. The vorticity distribution downstream of the cylinder surrounded with half cylinder ($\alpha=180^o$) for $D_i/D_o=0.75$ at different β cases

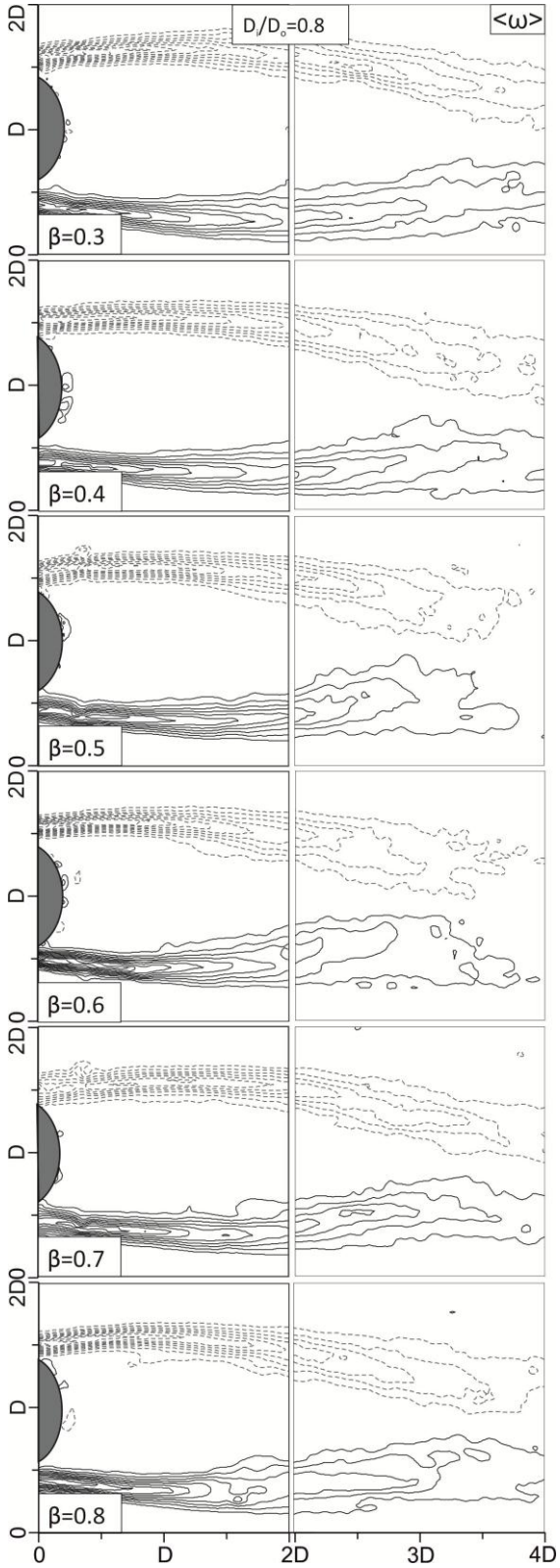


Figure 4.21. The vorticity distribution downstream of the cylinder surrounded with half cylinder ($\alpha=180^o$) for $D_i/D_o=0.8$ at different β cases

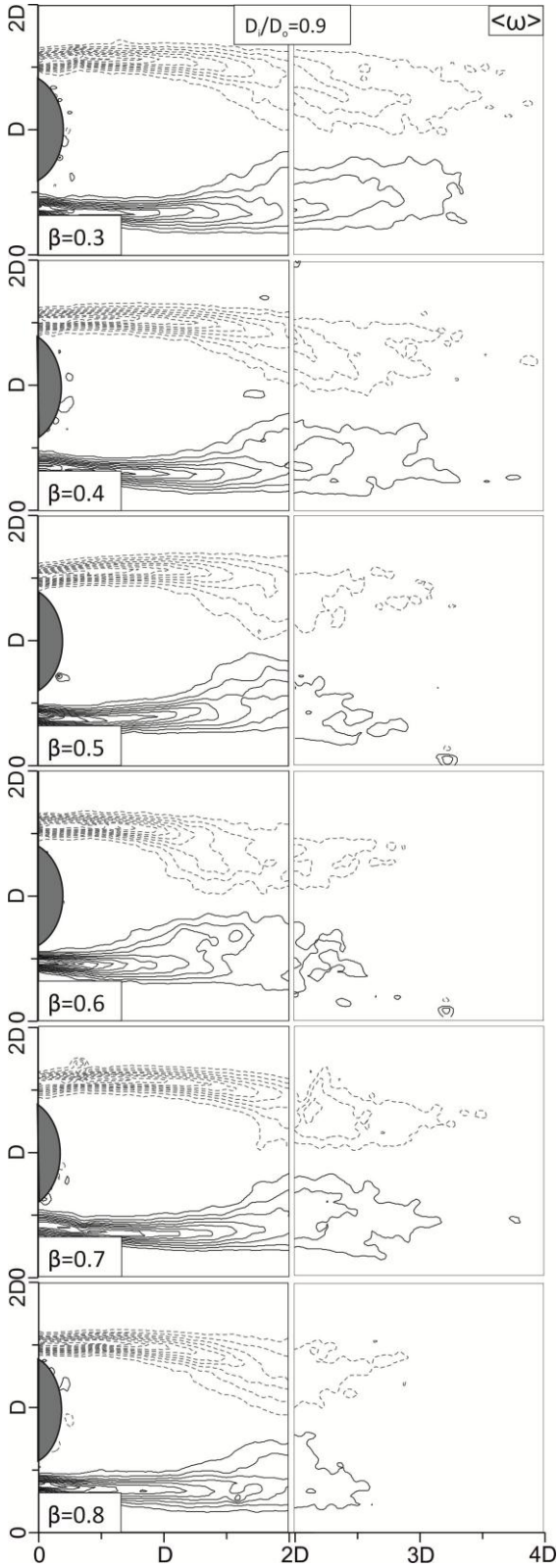


Figure 4.22. The vorticity distribution downstream of the cylinder surrounded with half cylinder ($\alpha=180^o$) for $D_i/D_o=0.9$ at different β cases

Figures 4.21 and 4.22 show the time averaged vorticity contours for D_i/D_o=0.8 and D_i/D_o=0.9 diameter ratios respectively. It is seen from Figure 4.21 that all porosities affect vorticity structure at approximately the same levels. A similar vorticity structure is occurred in Figure 4.22. In addition, it is observed that the shear layer shortens even further and gets close to the first field of view. When compared with the bare cylinder in Figure 4.2, the effect of the perforated half cylinder continues on the control of vorticity. Due to the decrease in the distance between the inner cylinder and outer half cylinder with the increasing diameter ratios, flow entry into the wake region through the perforated half cylinder is reduced. Thus, the effect of the perforated half cylinder decreases with the increasing diameter ratios.

In order to observe the effect of the perforated half cylinder on the turbulence statistics that take place in the near wake, TKE contours for all diameter ranges are shown respectively from Figure 4.23 to 4.31. The minimum and incremental values of TKE contours were taken as 0.007. Figure 4.23 shows the effect of porosity (β) on TKE for D_i/D_o=0.25. At porosity β=0.3 and β=0.4, TKE intensity in the near wake of the cylinder couple decreases. However, TKE intensity builds within the shear layers at the sides of the cylinders. The reasoning of this is the turbulence caused by the outer cylinder which was observed in Reynolds stress contours. While the effect of porosity β on the flow structure decreases with the increasing porosity, the effectiveness of the inner cylinder increases. The same case is occurred for D_i/D_o=0.3 diameter ratio presented in Figure 4.24.

Figures 4.25 and 4.26 respectively show the TKE contours for D_i/D_o=0.4 and D_i/D_o=0.5. At these diameter ratios and especially for D_i/D_o=0.5, β has a significant effect on the flow structure. Within the $0.3 \leq \beta \leq 0.6$ range of porosity, the TKE intensity in shear layers decreases with the increasing porosity and interact with each other along downstream in the third field of view. The reason of this kinetic energy intensification in shear layers is the result of preventing Karman vortices, however, the Kelvin-Helmholtz vorticity becomes more effective in the shear layer between the free stream region and the wake region (Akilli et al., 2011). These shear layers elongated and interacted with each other in the third field of view. It is observed that, as from the β=0.7, density of TKE contours increases and gets closer to the cylinder.

Especially for $\beta \leq 0.6$, the flow emanating through the holes on the outer half cylinder causing a jet flow effect, prevents the vorticity on each side of the cylinder by preventing the interaction of vortices thus reducing the momentum entry into the wake region. Therefore, vorticity occurrence and breakage is shifted to the farther regions of downstream flow. As a result, TKE value in the wake region reduces in comparison to the bare cylinder case. With the increase in the porosity, the number of holes on the perforated cylinder increase and therefore jet effect of the flow decreases. In this case vorticity couples interact in a closer region and increase turbulence accordingly. Therefore TKE tends to increase again for $\beta > 0.6$.

The interaction between shear layers downstream of the wake region of the cylinder configuration for $D_i/D_o=0.6$ diameter ratio is presented in Figure 4.27. TKE intensity of shear layers increases. From Figure 4.28 it can be seen that the flow characteristics at $D_i/D_o=0.7$ diameter ratio are similar to those at $D_i/D_o=0.6$. The increase in TKE values continues and the most effective porosity for establishing control is $\beta=0.5$.

TKE contours for $D_i/D_o=0.75$ and 0.8 shows that the effect of the inner cylinder on the perforated half cylinder is increasing. Maximum TKE points are formed in the second field of view. The flow structures formed in $\beta=0.7$ and $\beta=0.8$ seem to be more effective when compared with lower diameter ratios. The reason for this is that with the increasing diameter ratio, the location of the inner cylinder moves along downstream direction and accordingly the flow structure is formed further downstream locations.

The TKE results obtained at $D_i/D_o=0.9$ as shown in Figure 4.31 clearly indicate that variations in porosity do not have any significant effect on the flow structure. Comparing the flow structure formed at this diameter ratio with $D_i=90$ in Figure 4.2 still shows the effect of the control element.

The effect of porosity on the maximum TKE values that occur between the cylinders at varying diameter ratios is presented in a two dimensional graph in Figure 4.32. Comparing only the diameter ratios shows that the least values are obtained at low diameter ratios. However, when compared with the bare cylinder, the effect of outer cylinder is seen more clearly at high diameter ratios.

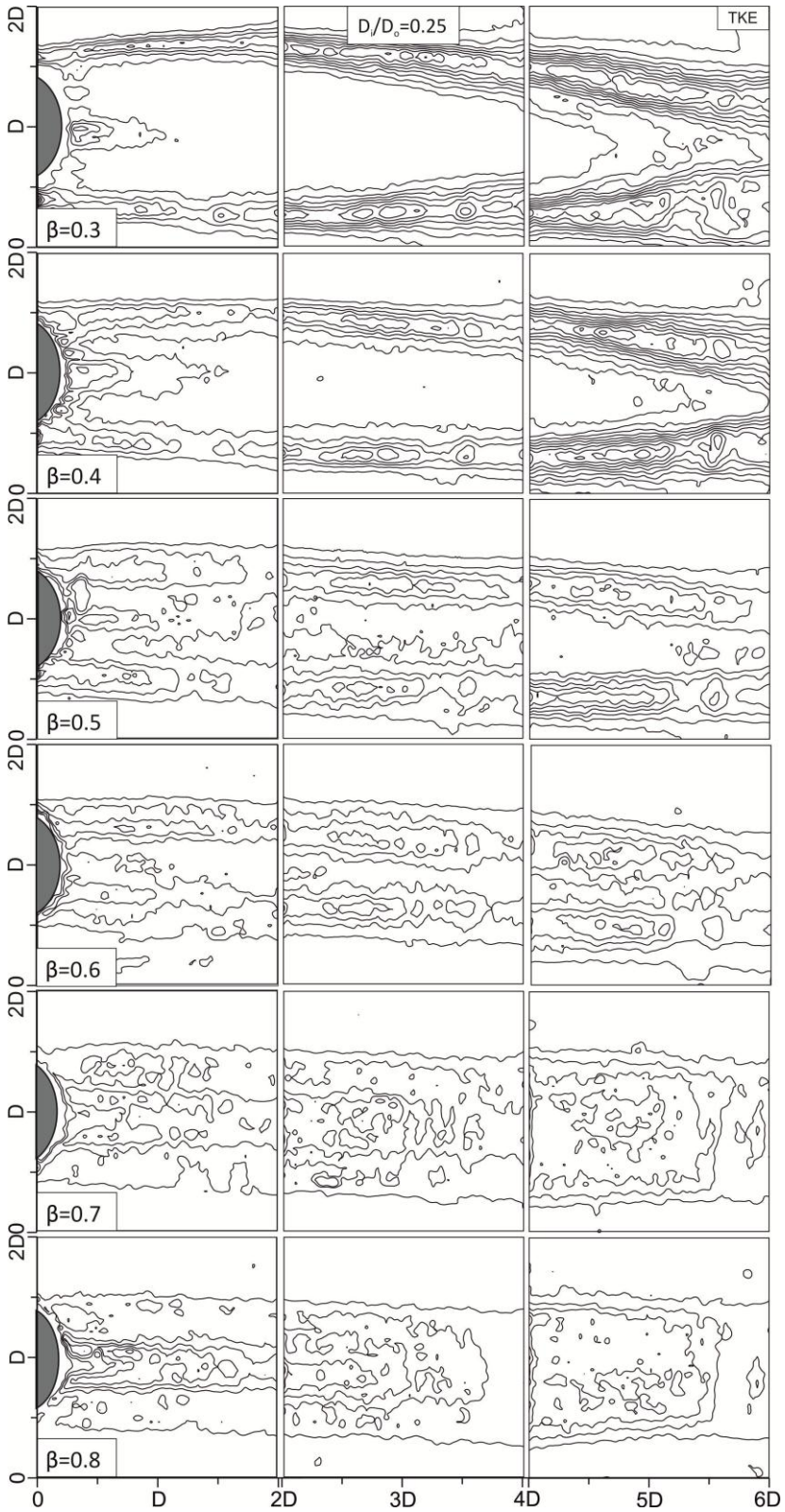


Figure 4.23. The TKE distribution downstream of the cylinder surrounded with half cylinder ($\alpha=180^o$) for D_i/D_o=0.25 at different β cases

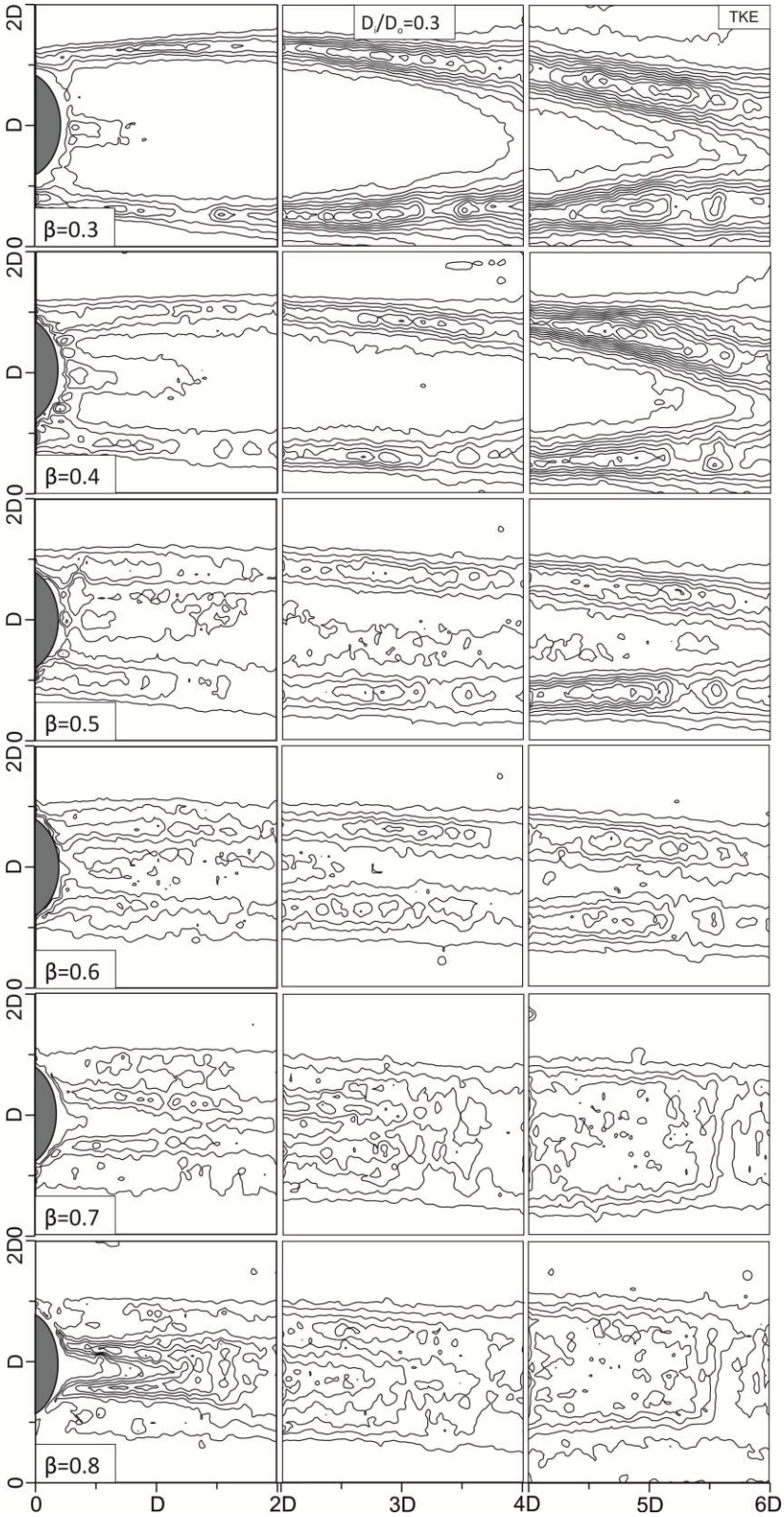


Figure 4.24. The TKE distribution downstream of the cylinder surrounded with half cylinder ($\alpha=180^o$) for $D_i/D_o=0.3$ at different β cases

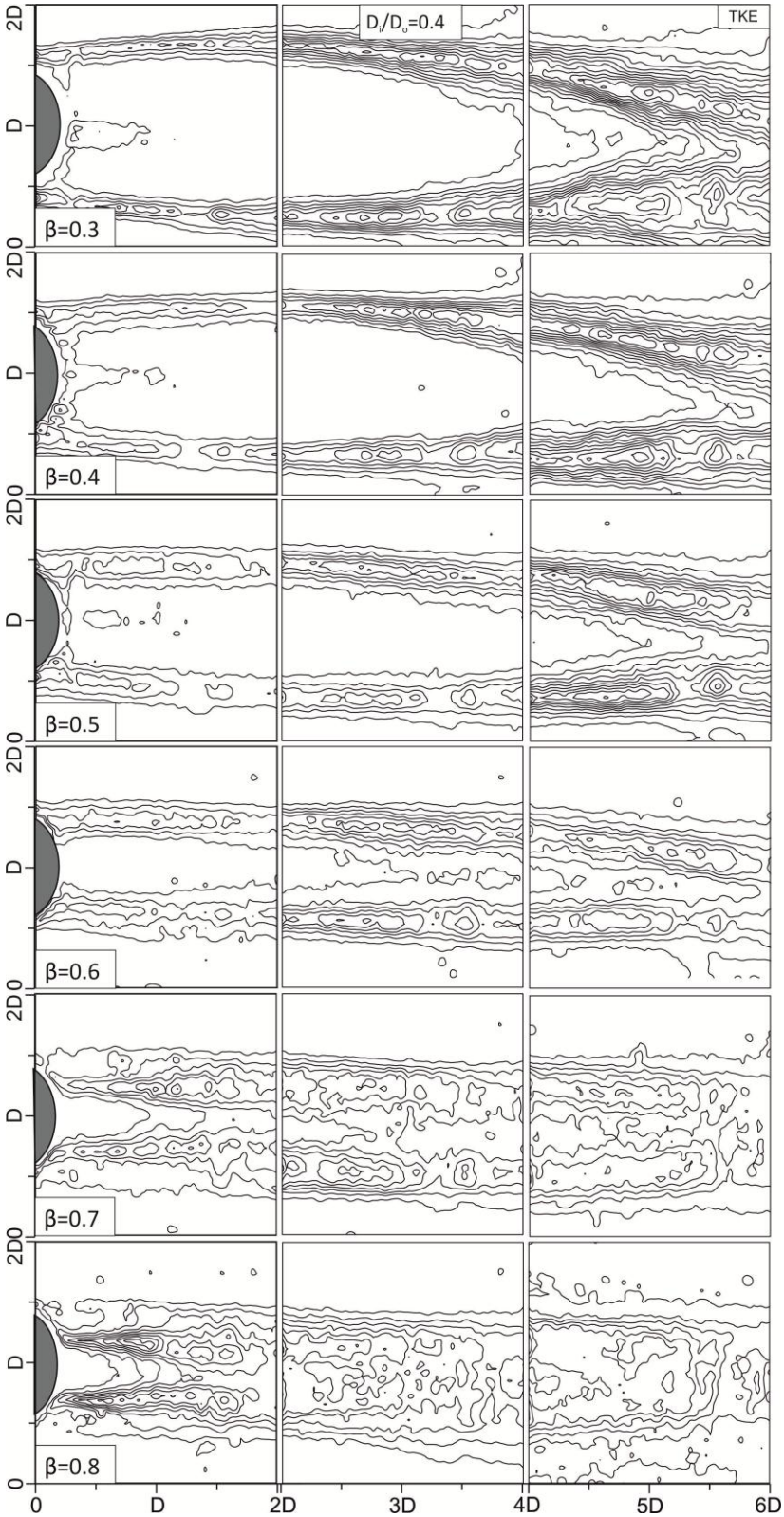


Figure 4.25. The TKE distribution downstream of the cylinder surrounded with half cylinder ($\alpha=180^o$) for $D_i/D_o=0.4$ at different β cases

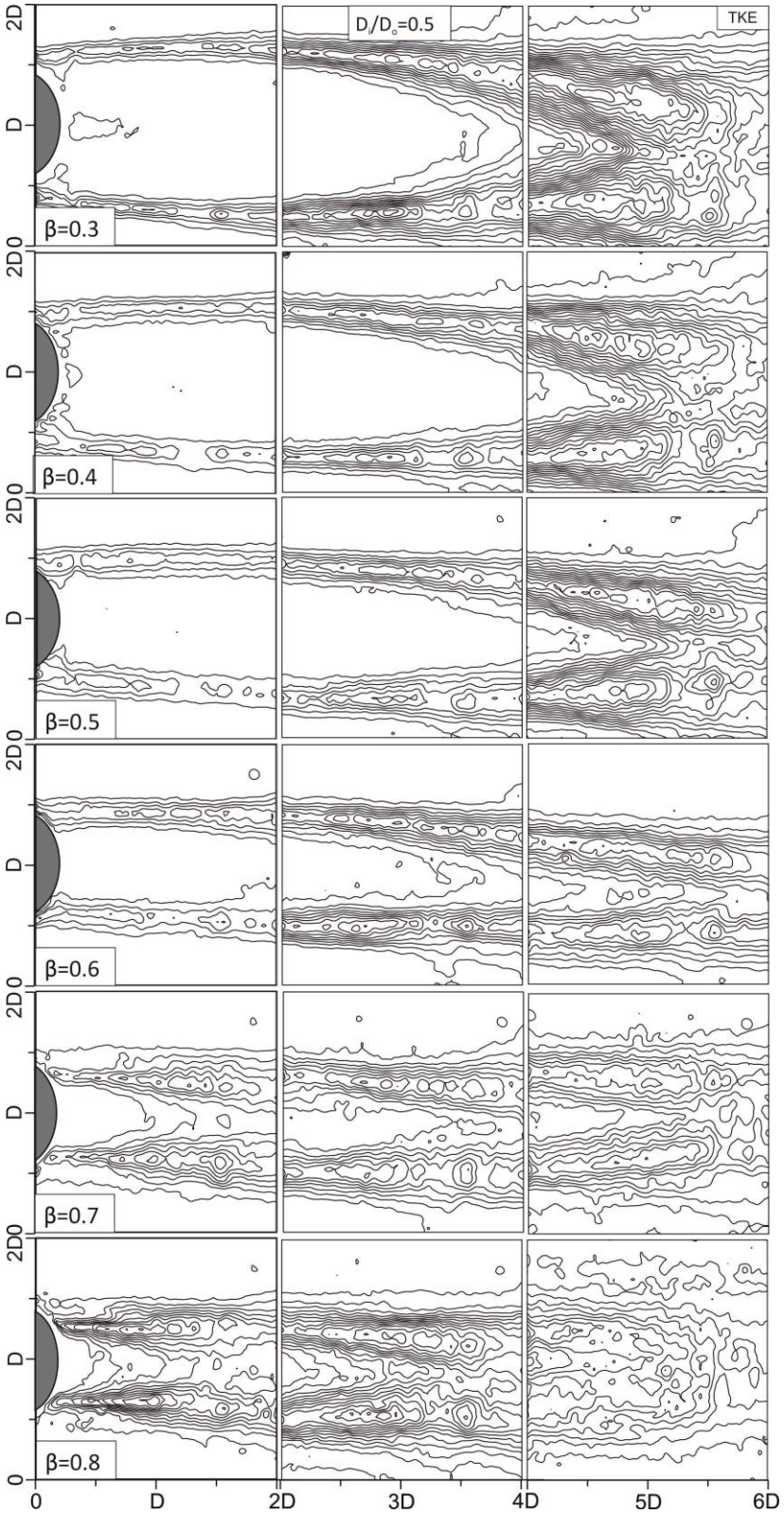


Figure 4.26. The TKE distribution downstream of the cylinder surrounded with half cylinder ($\alpha=180^o$) for $D_i/D_o=0.5$ at different β cases

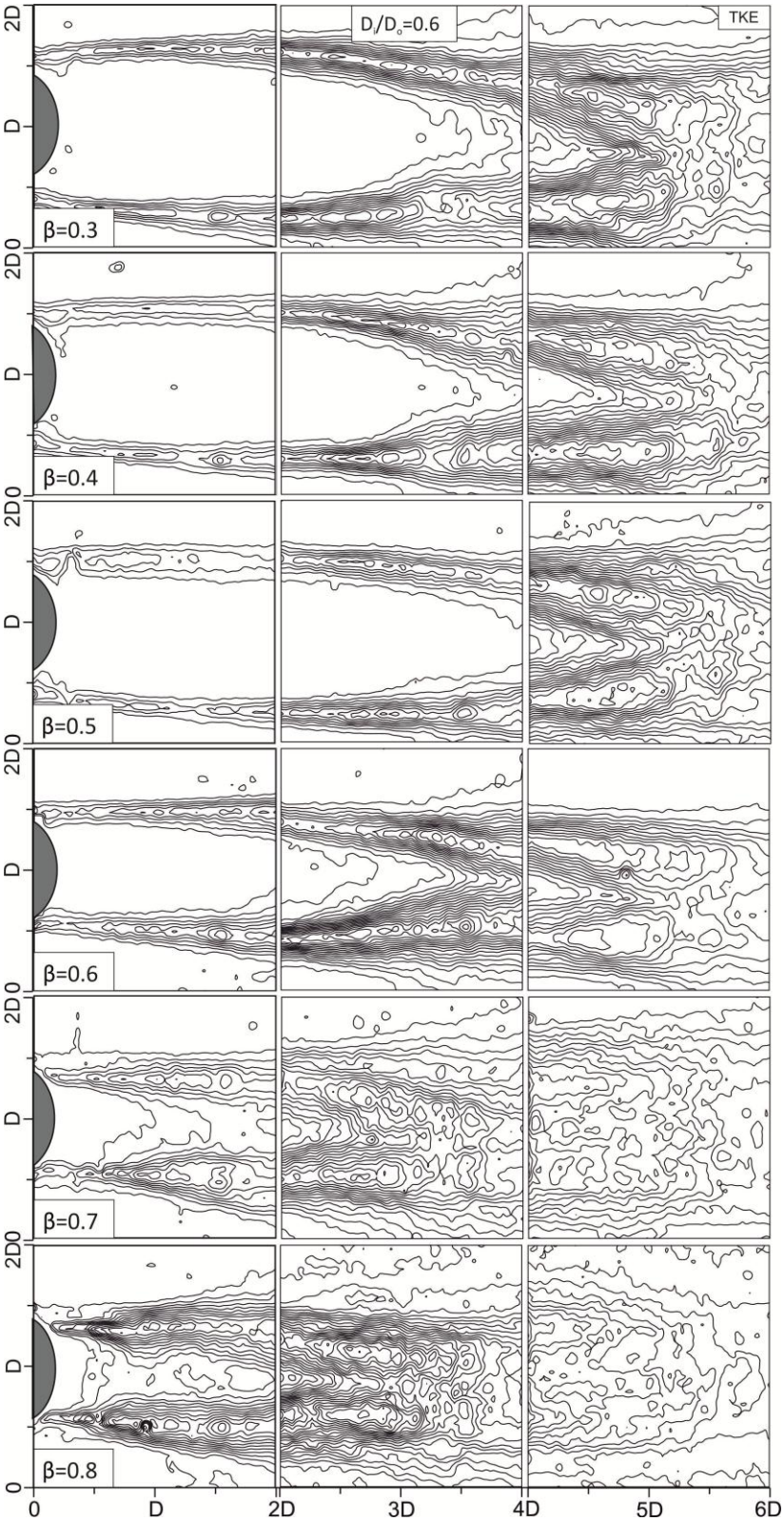


Figure 4.27. The TKE distribution downstream of the cylinder surrounded with half cylinder ($\alpha=180^o$) for $D_i/D_o=0.6$ at different β cases

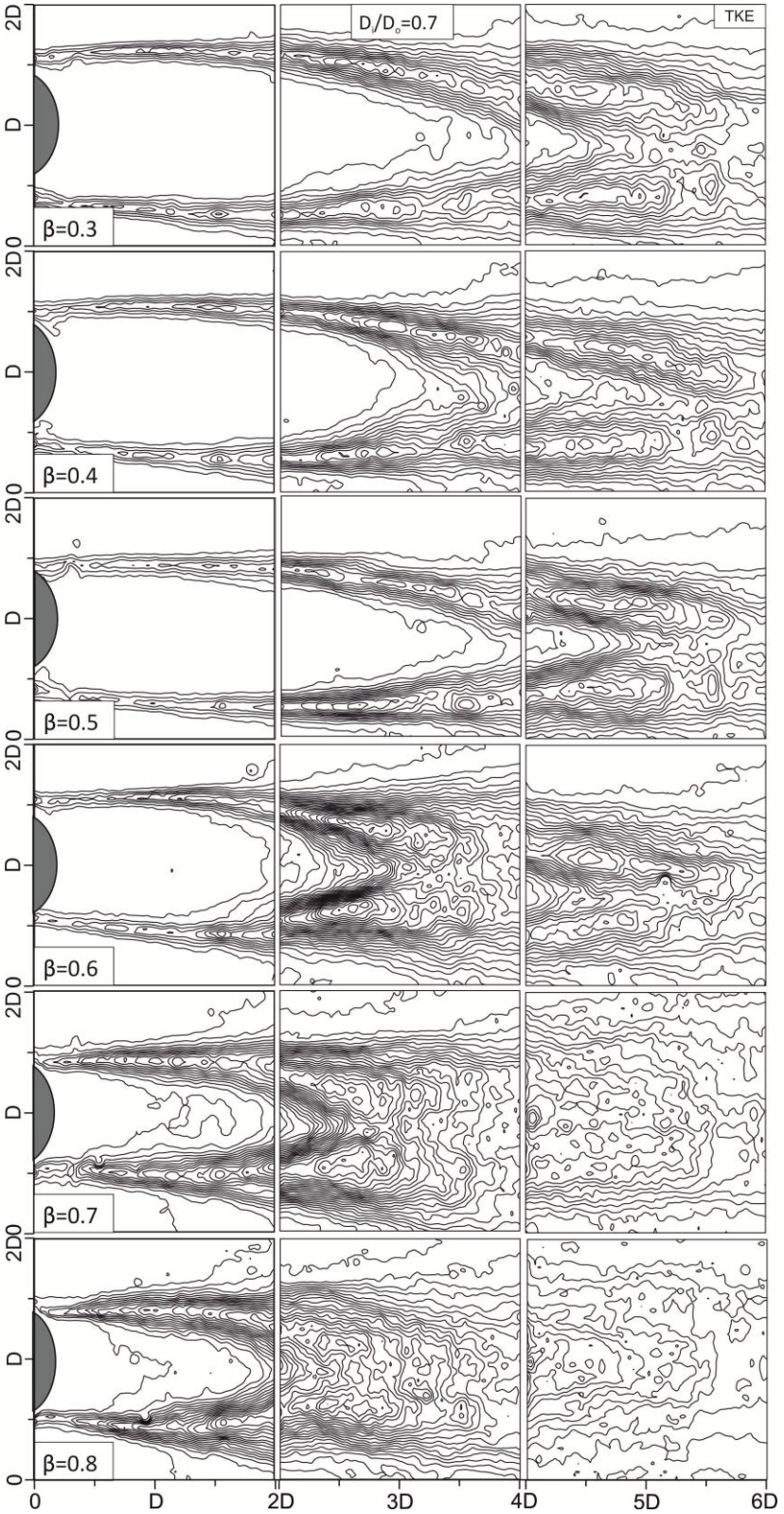


Figure 4.28. The TKE distribution downstream of the cylinder surrounded with half cylinder ($\alpha=180^o$) for $D_i/D_o=0.7$ at different β cases

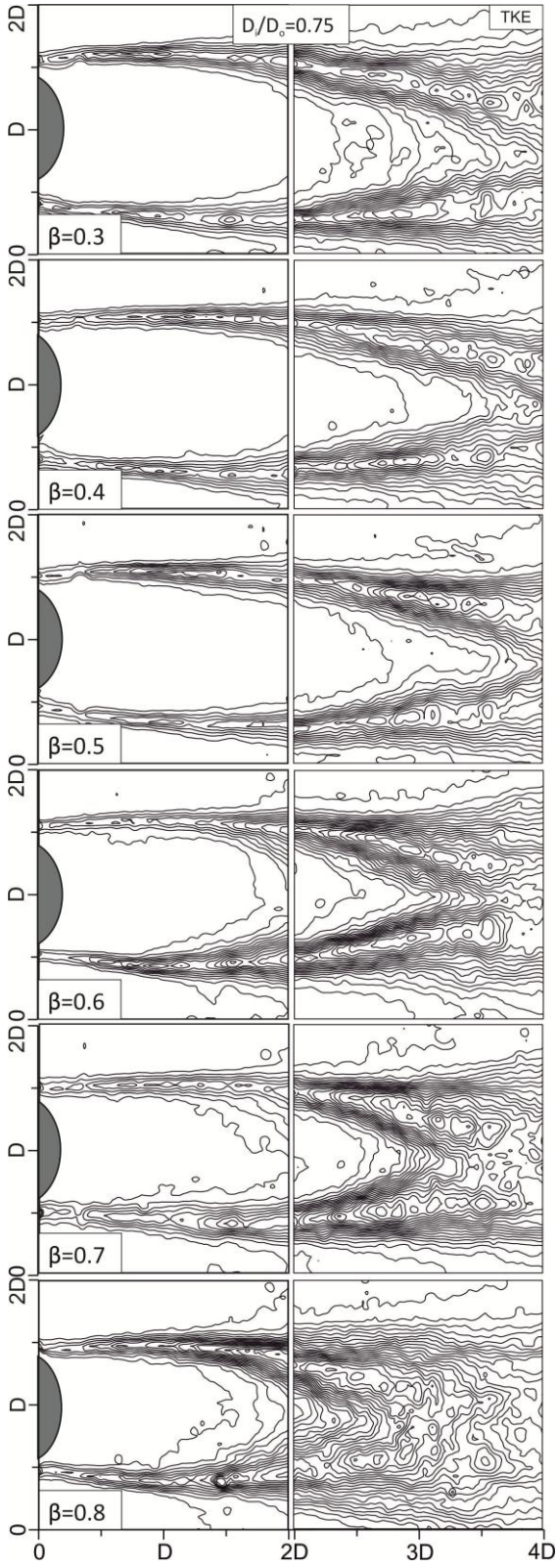


Figure 4.28. The TKE distribution downstream of the cylinder surrounded with half cylinder ($\alpha=180^o$) for D_i/D_o=0.75 at different β cases

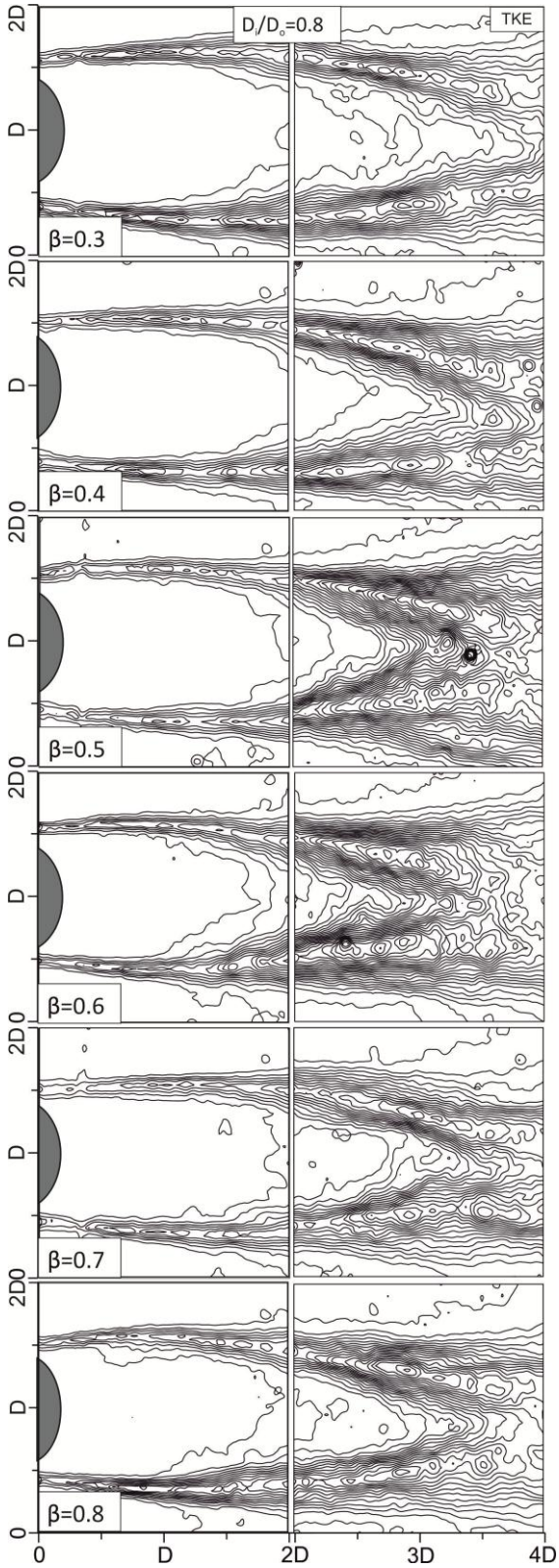


Figure 4.30. The TKE distribution downstream of the cylinder surrounded with half cylinder ($\alpha=180^o$) for D_i/D_o=0.8 at different β cases

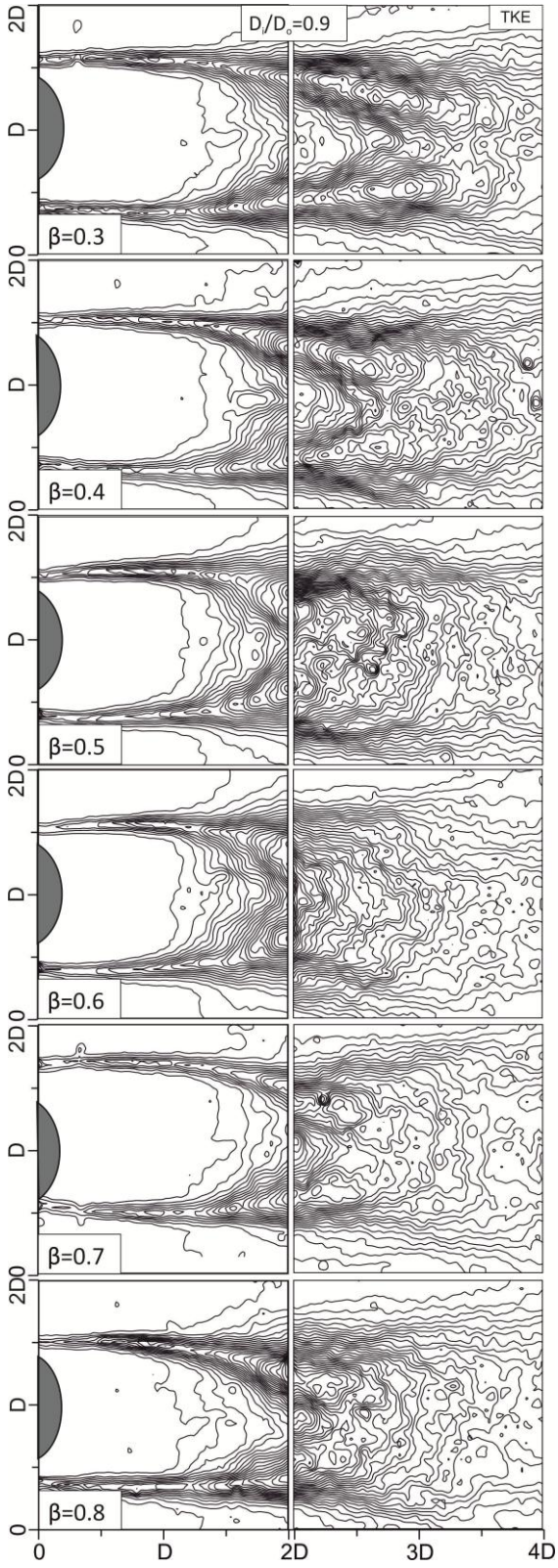


Figure 4.31. The TKE distribution downstream of the cylinder surrounded with half cylinder ($\alpha=180^o$) for D_i/D_o=0.9 at different β cases

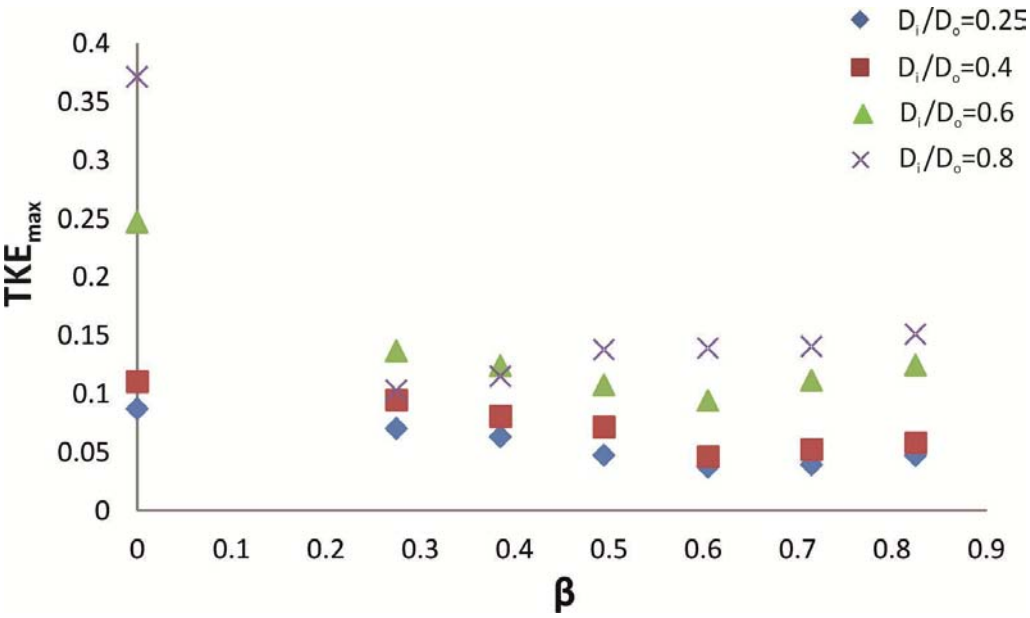


Figure 4.32. The variation of TKE_{max} with β to demonstrate the effect of D_i/D_o

4.1.2.2. Angle of Arc α=150^o Application

In the case that the outer cylinder is an arc of α=150^o and is positioned symmetrically in the wake region of the inner cylinder, experiments were carried out for Reynolds number 10000, porosity β=0.3, 0.4, 0.5, 0.6, 0.7 and 0.8 and diameter ratio D_i/D_o =0.25, 0.3, 0.4, 0.5, 0.6, 0.7, 0.75, 0.8 and 0.9. The Reynolds shear stresses obtained from the existence of a quarter outer cylinder of 150^o arc angle are provided in Figure 4.33. Reynolds shear and TKE results obtained via PIV measurement for different combinations which also include the inner cylinder are presented from Figure 4.34 to Figure 4.50. The results generally indicate that the quarter outer cylinder of α=150^o starts to be inadequate in achieving flow control compared with the case of half outer cylinder (α=180^o).

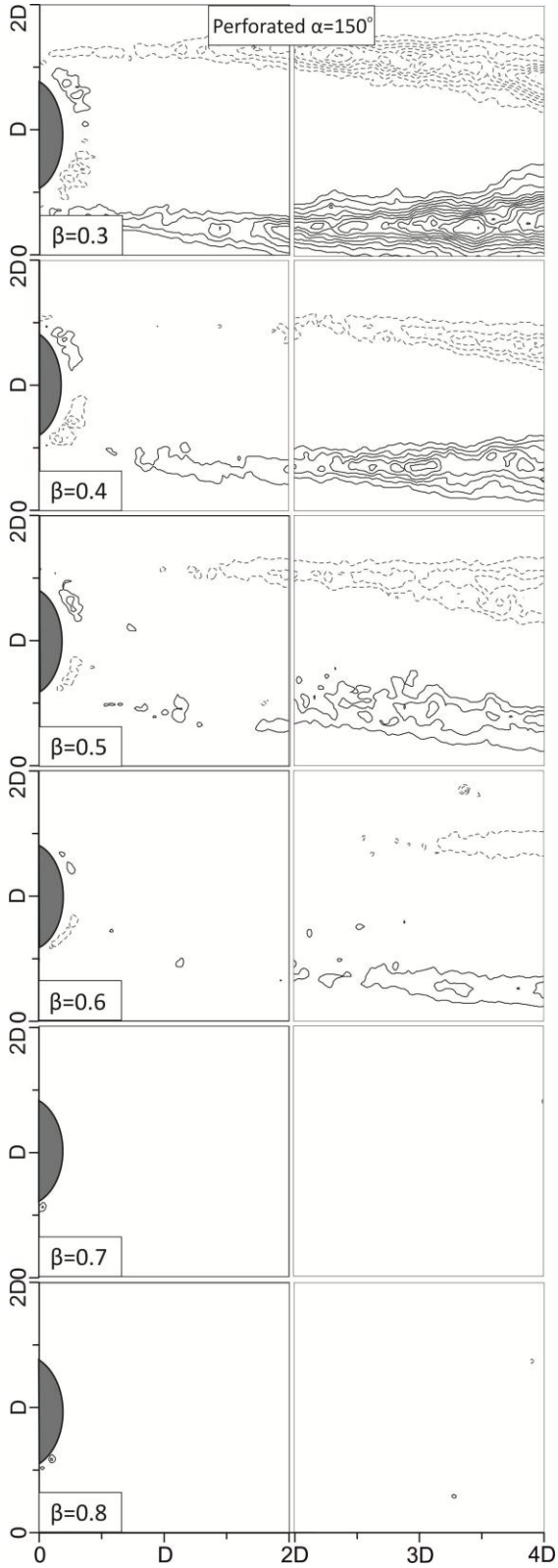


Figure 4.33. The Reynolds shear stress distribution downstream of arc ($\alpha=150^o$) for different β cases

Reynolds shear and TKE results obtained from varying porosities at D_i/D_o=0.25 and 0.3 diameter ratios are presented from Figure 4.34 to 4.37. Within the range of $0.3 \leq \beta \leq 0.5$ porosity, the shear layers are generated from outer cylinder. With the increasing porosity, outer cylinder loses its effect on the flow structure occurring in the near wake of the cylinder couple and the effect of the inner cylinder starts to increase.

In the case of D_i/D_o=0.4 diameter ratio, the effects of porosity on Reynolds stress and TKE intensity are presented respectively in Figures 4.38 and 4.39. It is indicated that the optimum porosity for reducing the peak magnitude of Reynolds stress and TKE is β=0.6. The peak magnitude of Reynolds stress and TKE obtained at this porosity are significantly lower than those obtained with the bare cylinder. Comparing the same diameter ratio with half outer cylinder ($\alpha=180^o$) application exhibits increases in the peak magnitude of Reynolds shear stress and TKE. For instance, in bare cylinder case (D_i=40 mm) the peak magnitude of Reynolds shear stress and TKE were 0.027 and 0.11, respectively. At diameter ratio D_i/D_o=0.4 and porosity β=0.6 the same values were 0.006 and 0.046 for $\alpha=180^o$ and 0.011 and 0.052 for $\alpha=180^o$. This is an indicator of the fact that arc angle is a parameter that is effective on the flow structure.

Reynolds stresses and TKE contours obtained for D_i/D_o=0.5 and 0.6 at varying porosity are respectively shown from Figures 4.40 to 4.43. It is observed that at these diameter ratios, intensity of TKE and Reynolds stress contours increases even further with regard to the previous diameter ratios. When compared with the bare cylinder, it is observed that an effective control is achieved at β=0.5 and 0.6.

From Figure 4.44 to 4.49 Reynolds stress and TKE contours obtained for D_i/D_o=0.7, 0.75 and 0.8 are presented. With the increasing diameter ratio, turbulence in the shear layer that occurs in the both sides of the cylinder couple increases and interact with each other at a closer distance to the cylinder. In the case of inner cylinder diameter D_i=75 mm, the peak magnitude Reynolds shear stress and TKE were respectively 0.135 and 0.34. While the peak magnitude of Reynolds shear stress and TKE were 0.024 and 0.138 respectively at diameter ratio D_i/D_o=0.75, β=0.5 and $\alpha=180^o$, in the case of $\alpha=150^o$ the values were found to be 0.055 and 0.156.

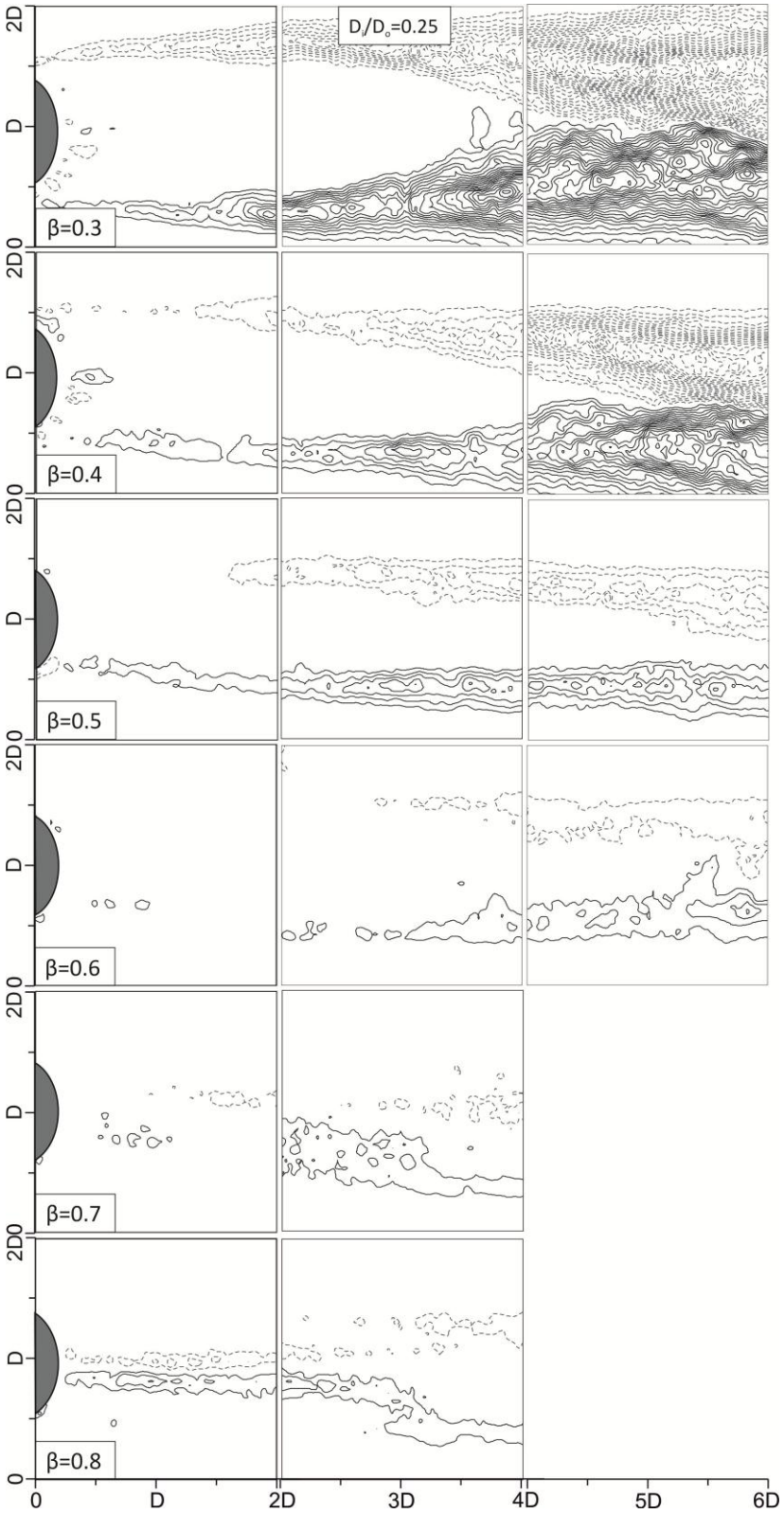


Figure 4.34. The Reynolds shear stress distribution downstream of the cylinder surrounded with arc ($\alpha=150^o$) for $D_i/D_o=0.25$ at different β cases

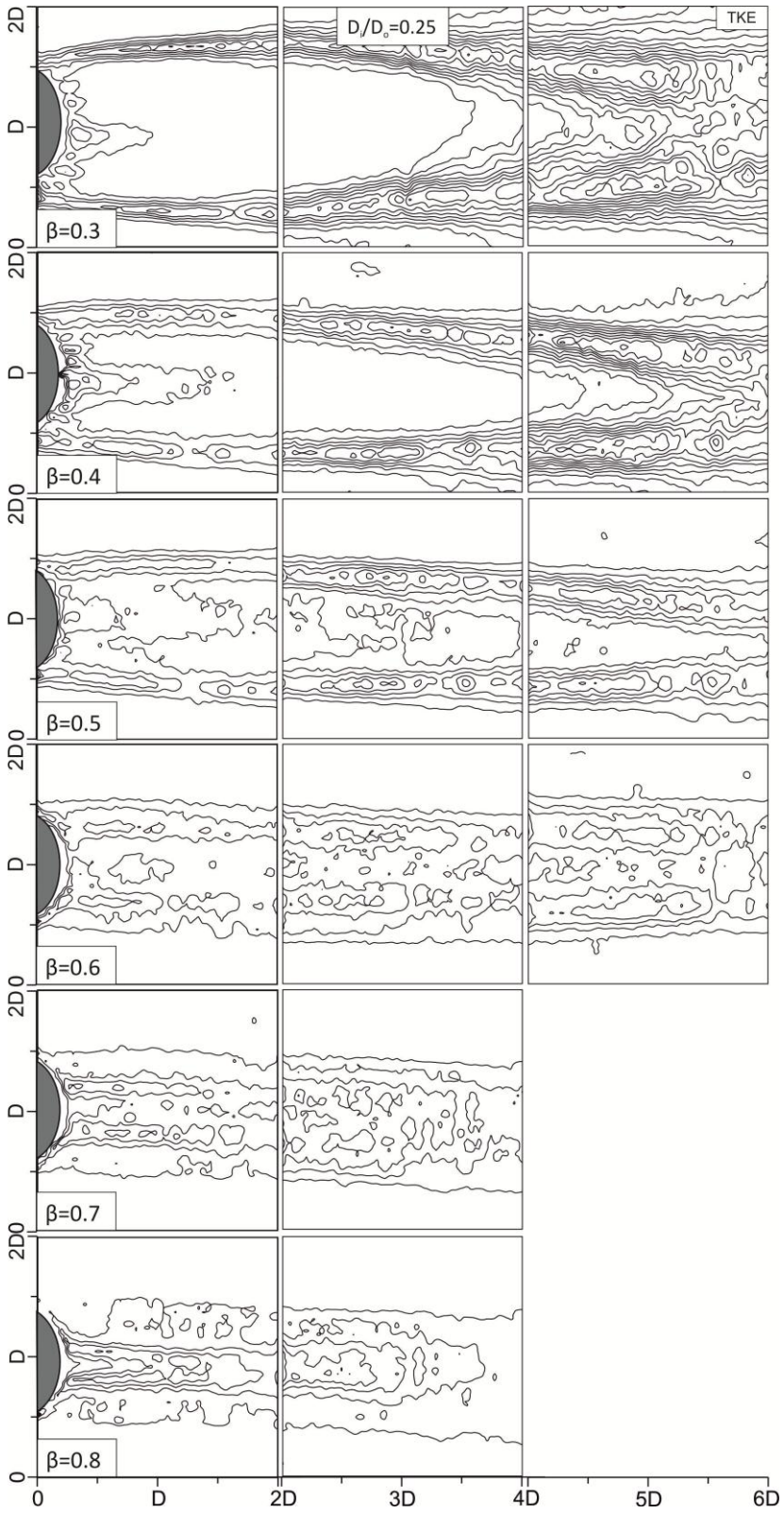


Figure 4.35. The TKE distribution downstream of the cylinder surrounded with arc (α=150^o) for D_i/D_o=0.25 at different β cases

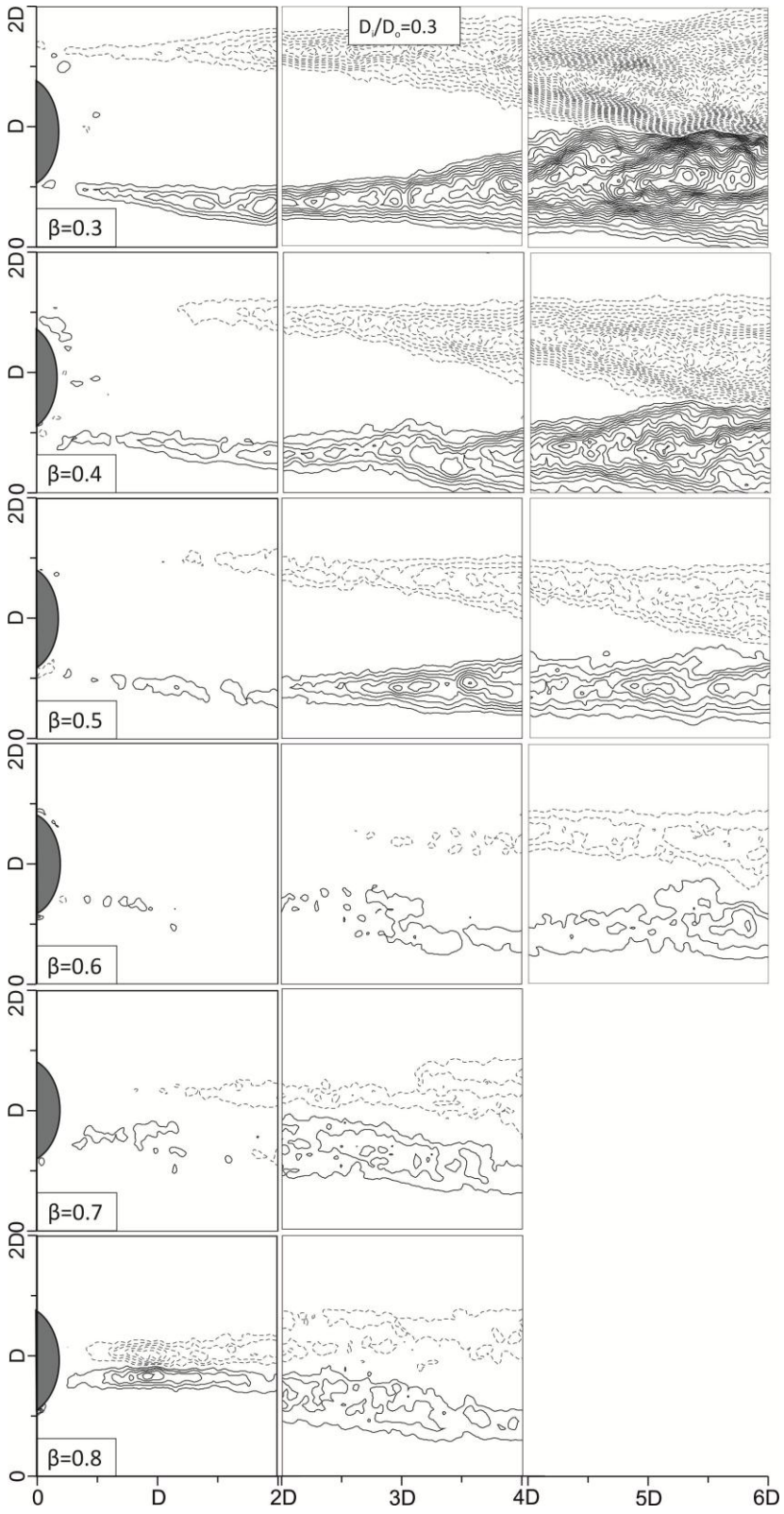


Figure 4.38. The Reynolds shear stress distribution downstream of the cylinder surrounded with arc ($\alpha=150^o$) for $D_i/D_o=0.3$ at different β cases

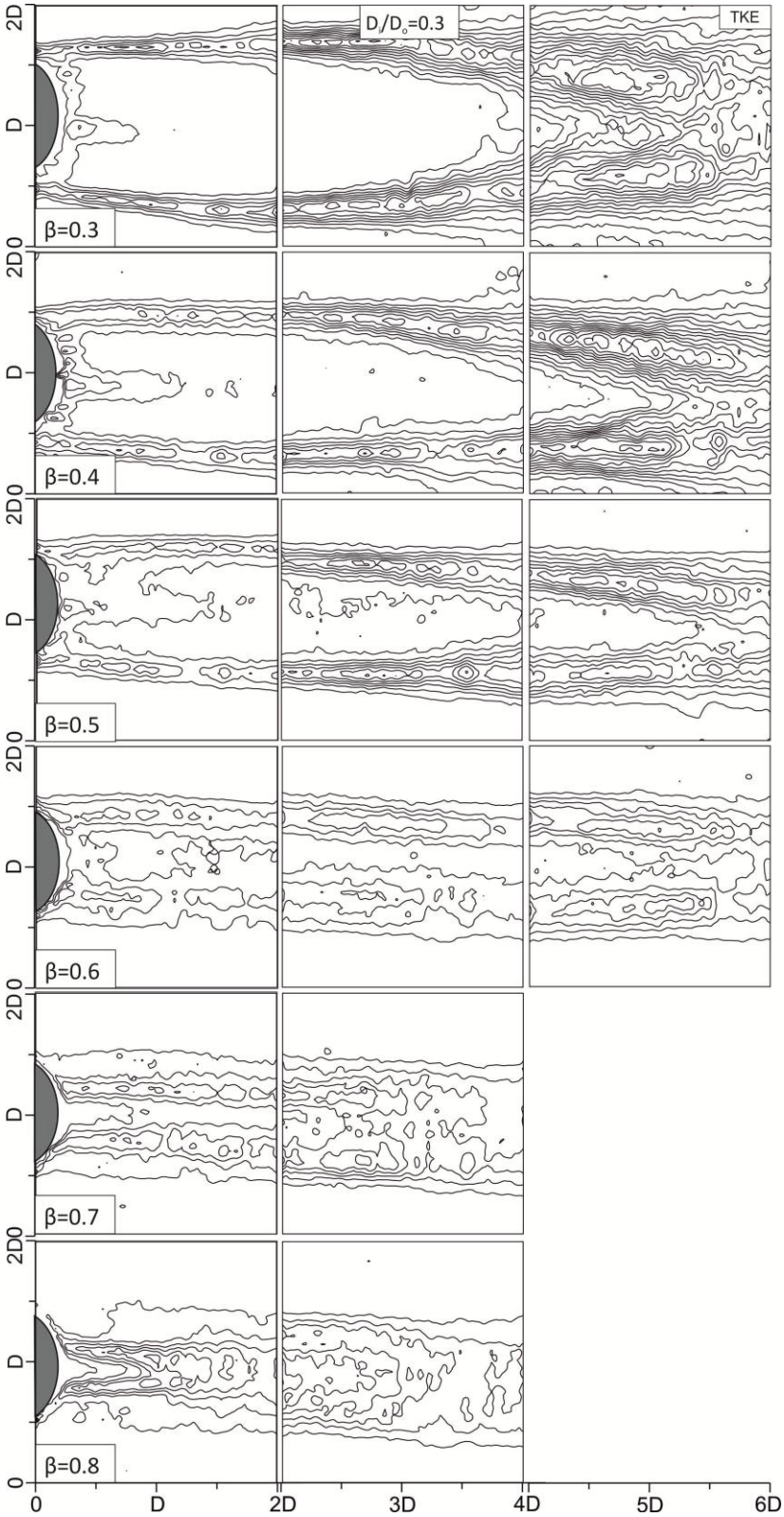


Figure 4.37. The TKE distribution downstream of the cylinder surrounded with arc ($\alpha=150^o$) for $D_i/D_o=0.3$ at different β cases

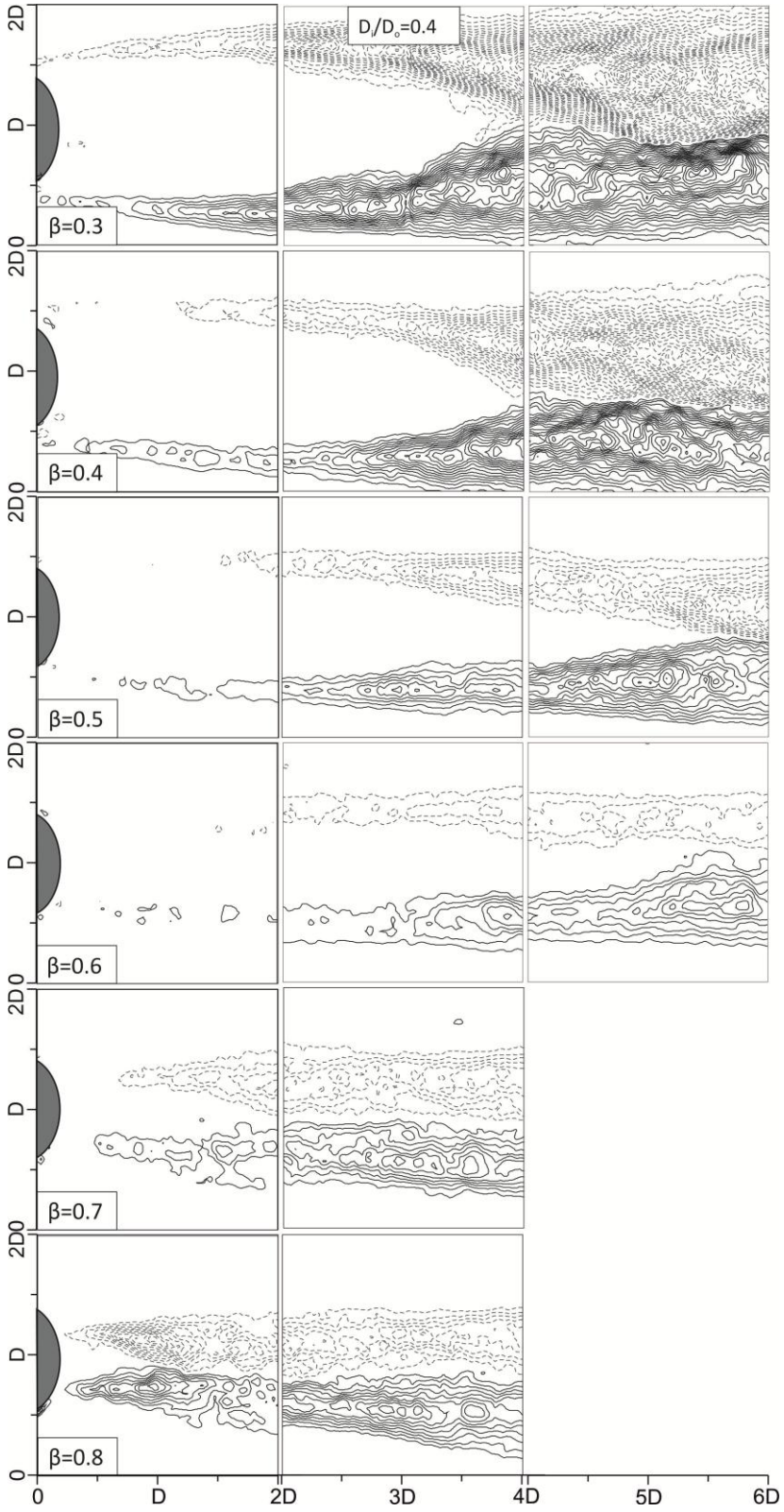


Figure 4.38. The Reynolds shear stress distribution downstream of the cylinder surrounded with arc ($\alpha=150^o$) for $D_i/D_o=0.4$ at different β cases

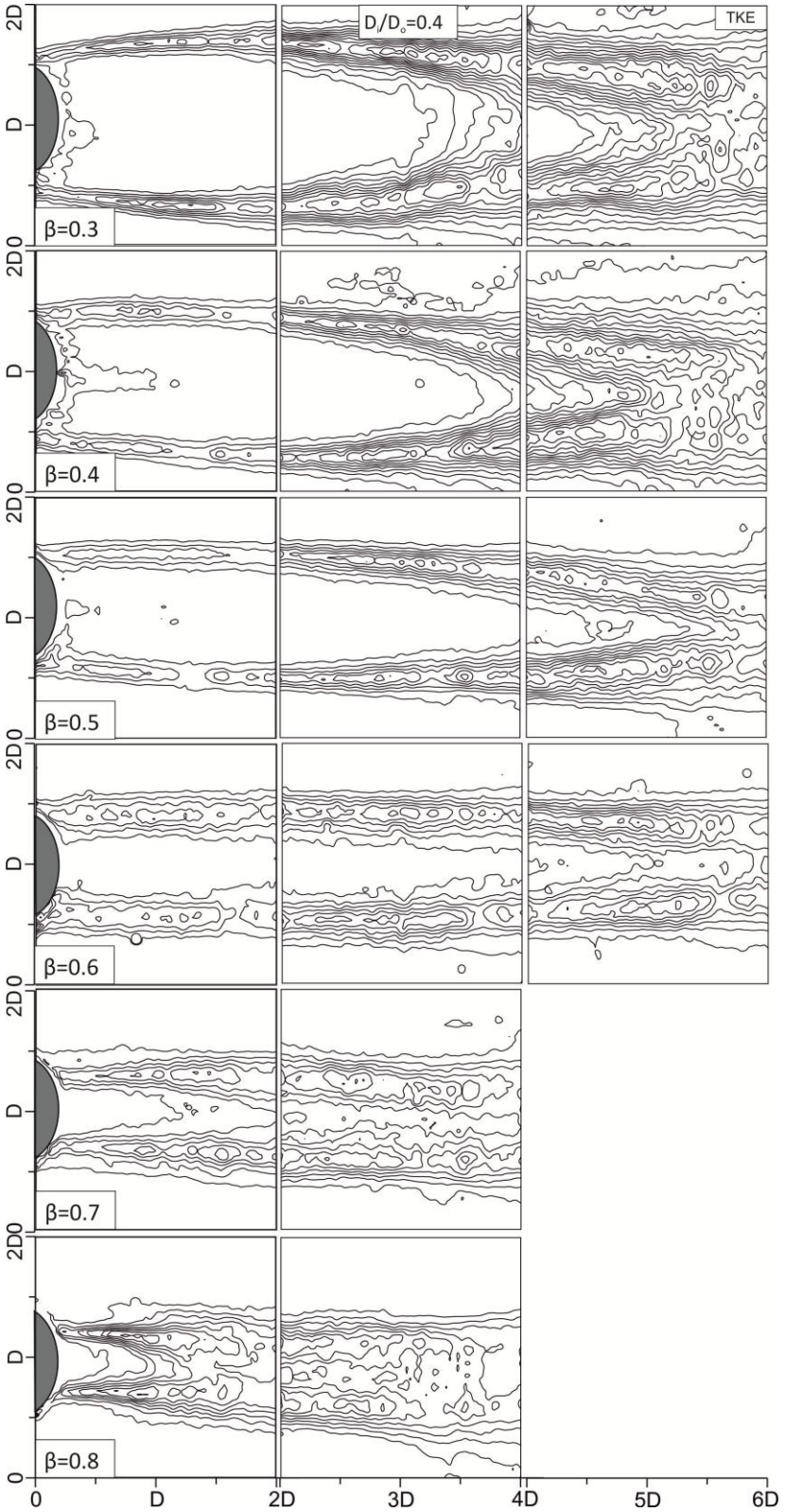


Figure 4.39. The TKE distribution downstream of the cylinder surrounded with arc ($\alpha=150^o$) for $D_i/D_o=0.4$ at different β cases

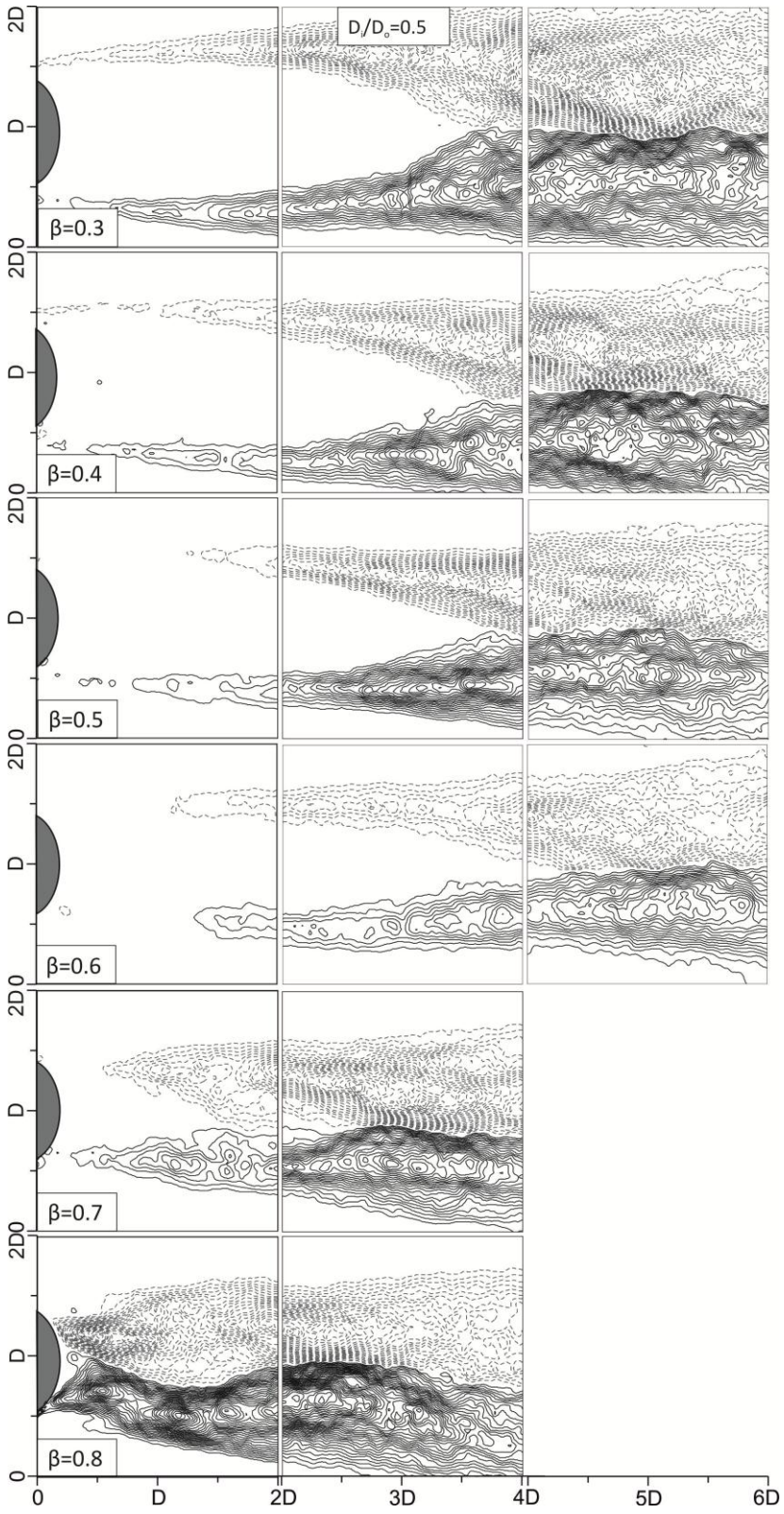


Figure 4.40. The Reynolds shear stress distribution downstream of the cylinder surrounded with arc ($\alpha=150^o$) for $D_i/D_o=0.5$ at different β cases

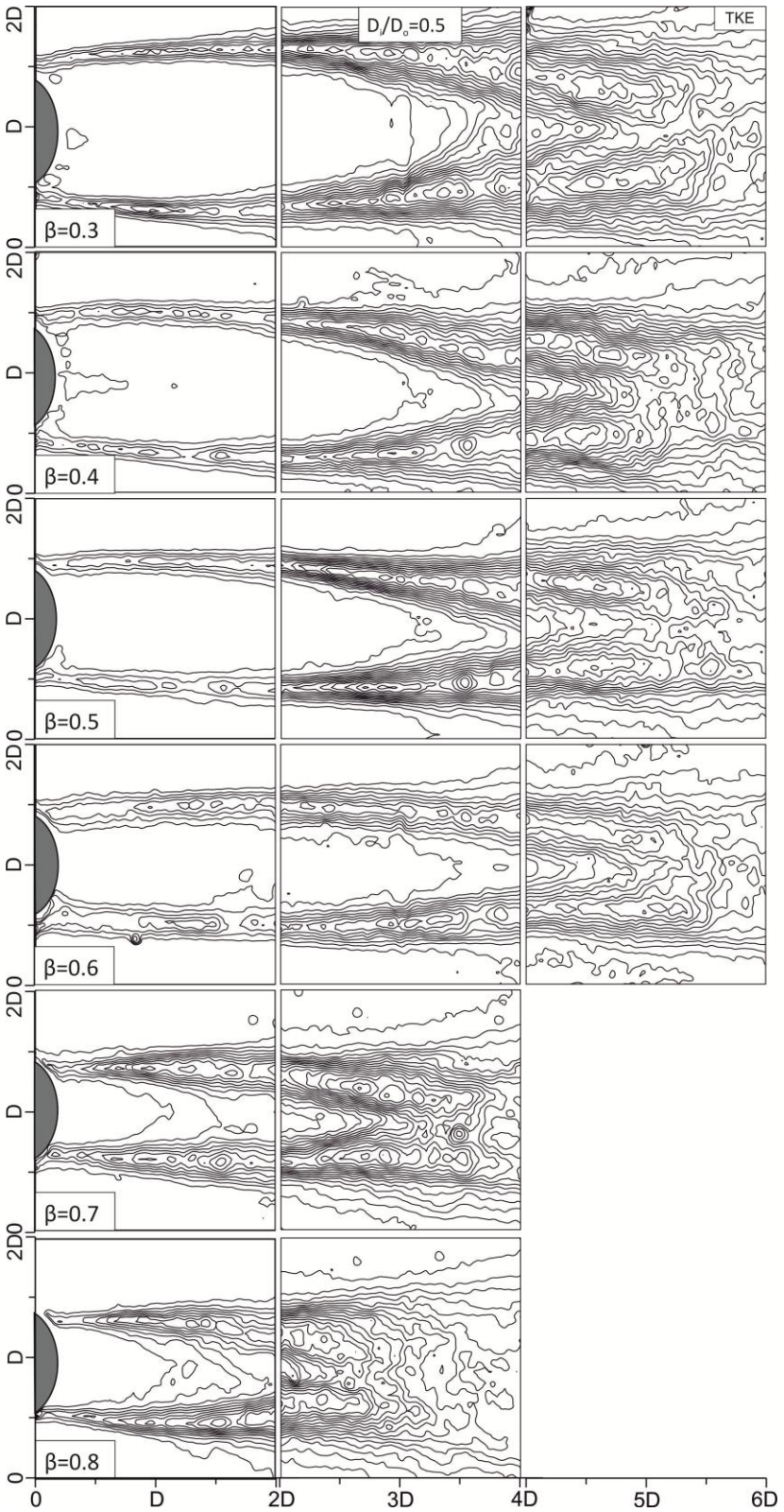


Figure 4.41. The TKE distribution downstream of the cylinder surrounded with arc ($\alpha=150^{o}$) for $D_i/D_o=0.5$ at different β cases

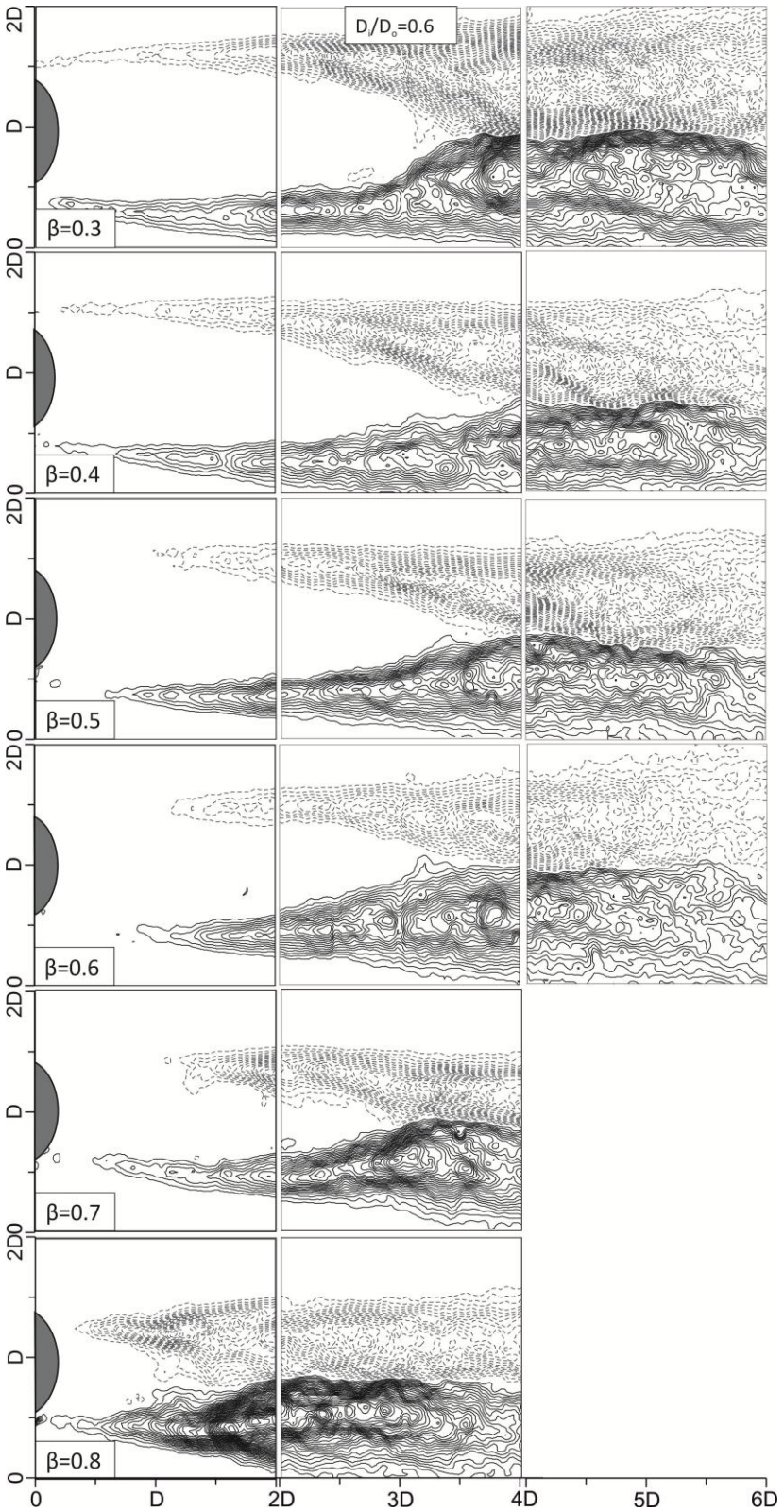


Figure 4.42. The Reynolds shear stress distribution downstream of the cylinder surrounded with arc ($\alpha=150^o$) for $D_i/D_o=0.6$ at different β cases

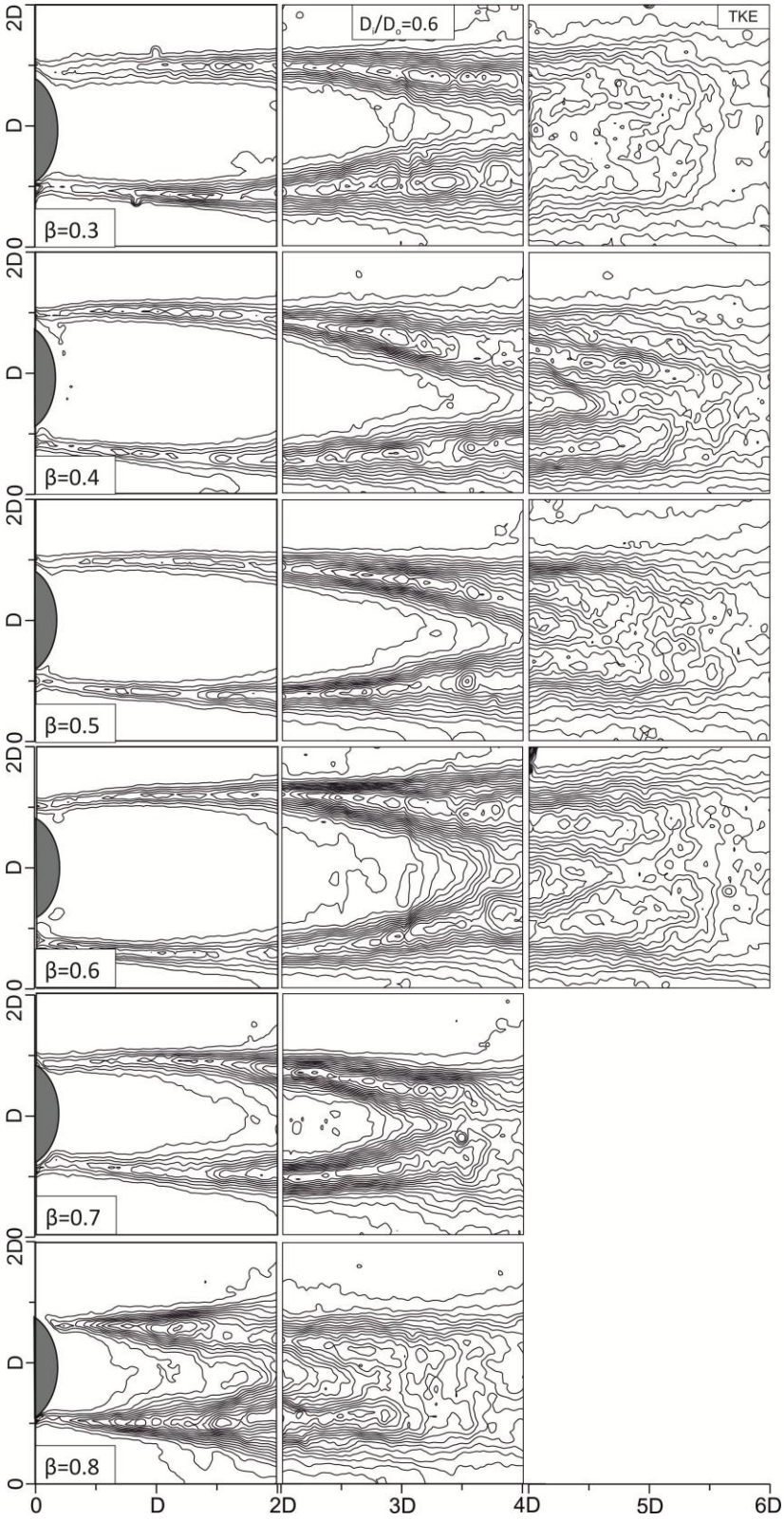


Figure 4.43. The TKE distribution downstream of the cylinder surrounded with arc (α=150^o) for D_i/D_o=0.6 at different β cases

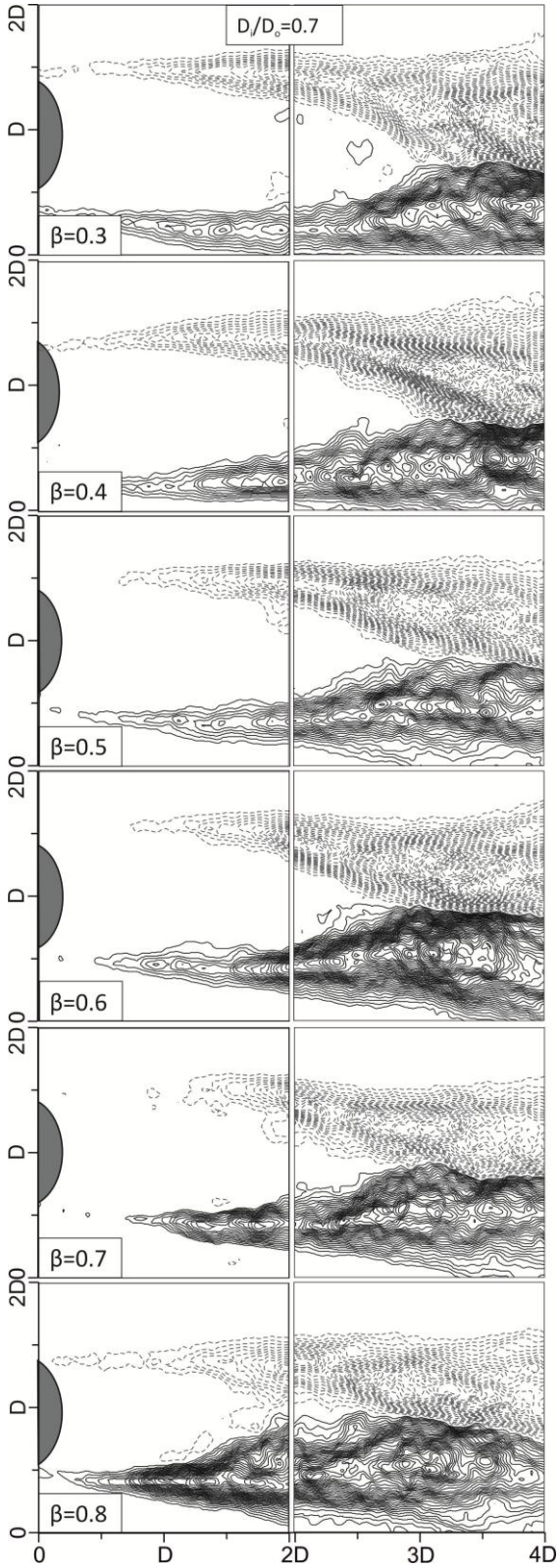


Figure 4.44. The Reymolds shear stress distribution downstream of the cylinder surrounded with arc ($\alpha=150^o$) for $D_i/D_o=0.7$ at different β cases

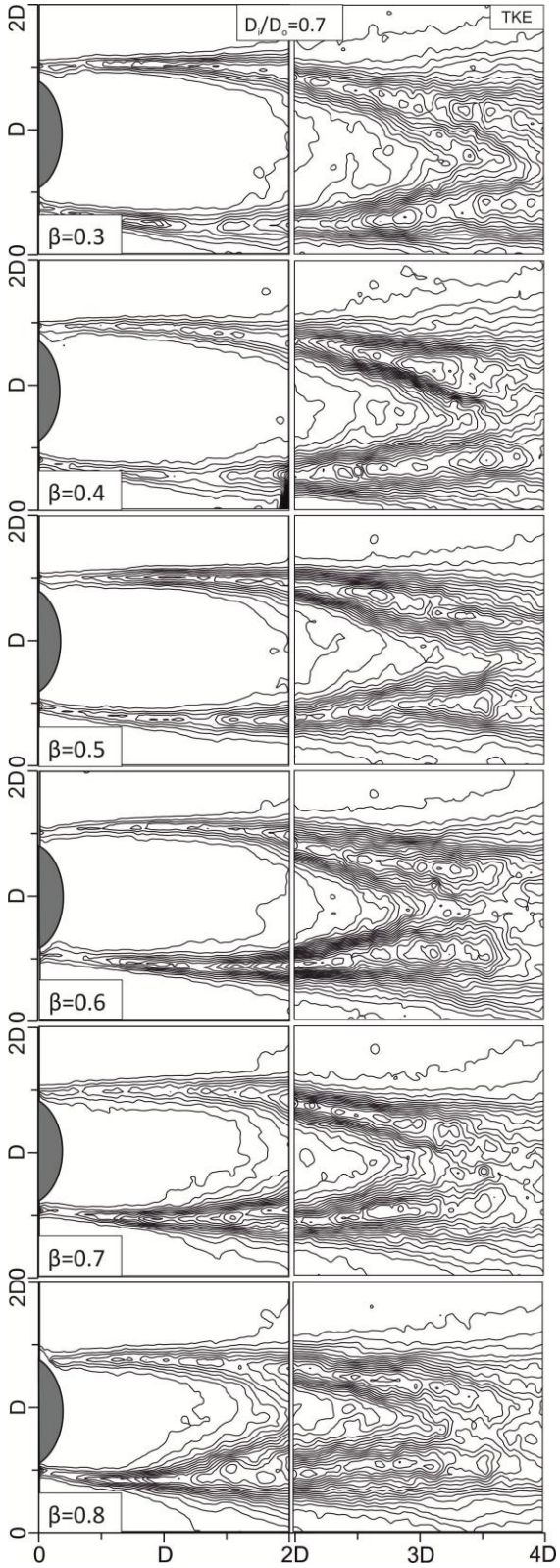


Figure 4.45. The TKE distribution downstream of the cylinder surrounded with arc ($\alpha=150^o$) for $D_i/D_o=0.7$ at different β cases

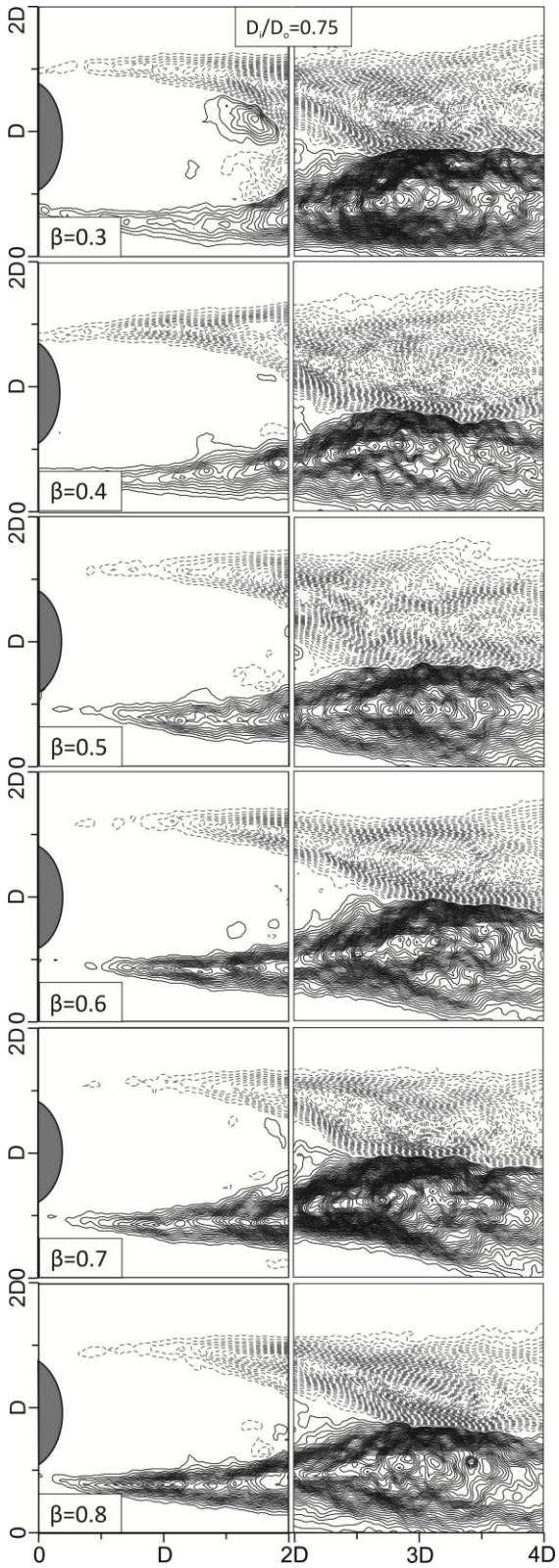


Figure 4.46. The Reynolds shear stress distribution downstream of the cylinder surrounded with arc ($\alpha=150^o$) for $D_i/D_o=0.75$ at different β cases

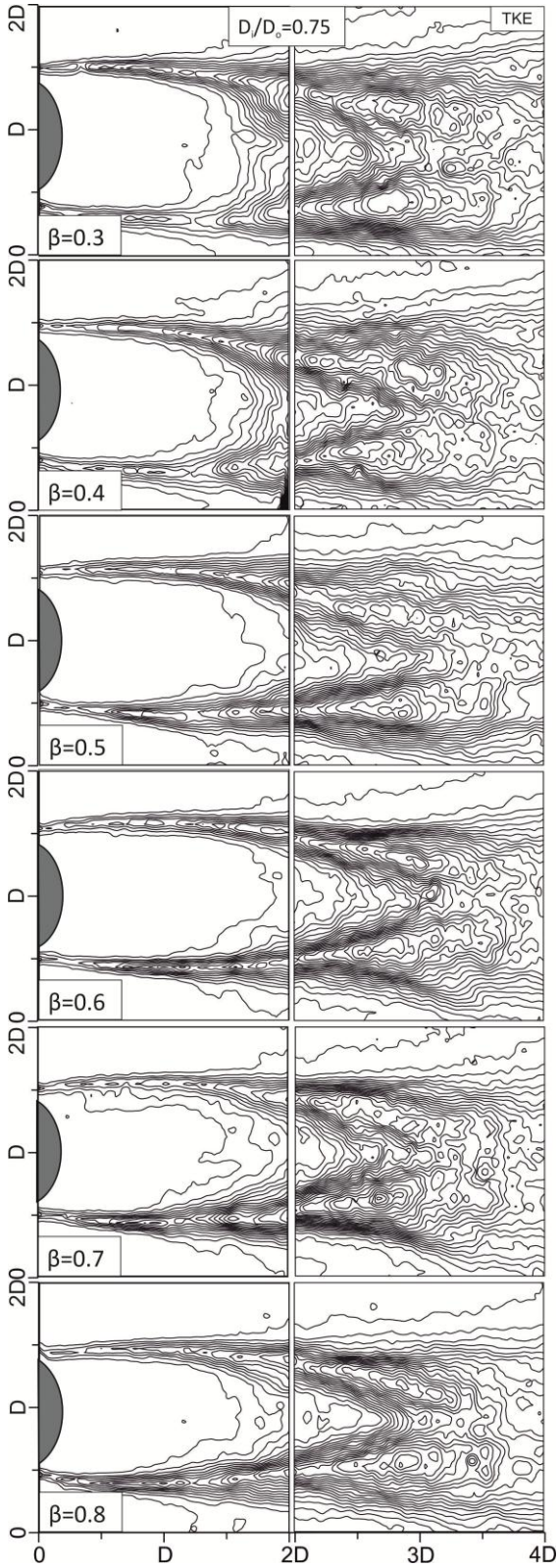


Figure 4.47. The TKE distribution downstream of the cylinder surrounded with arc (α=150^o) for D_i/D_o=0.75 at different β cases

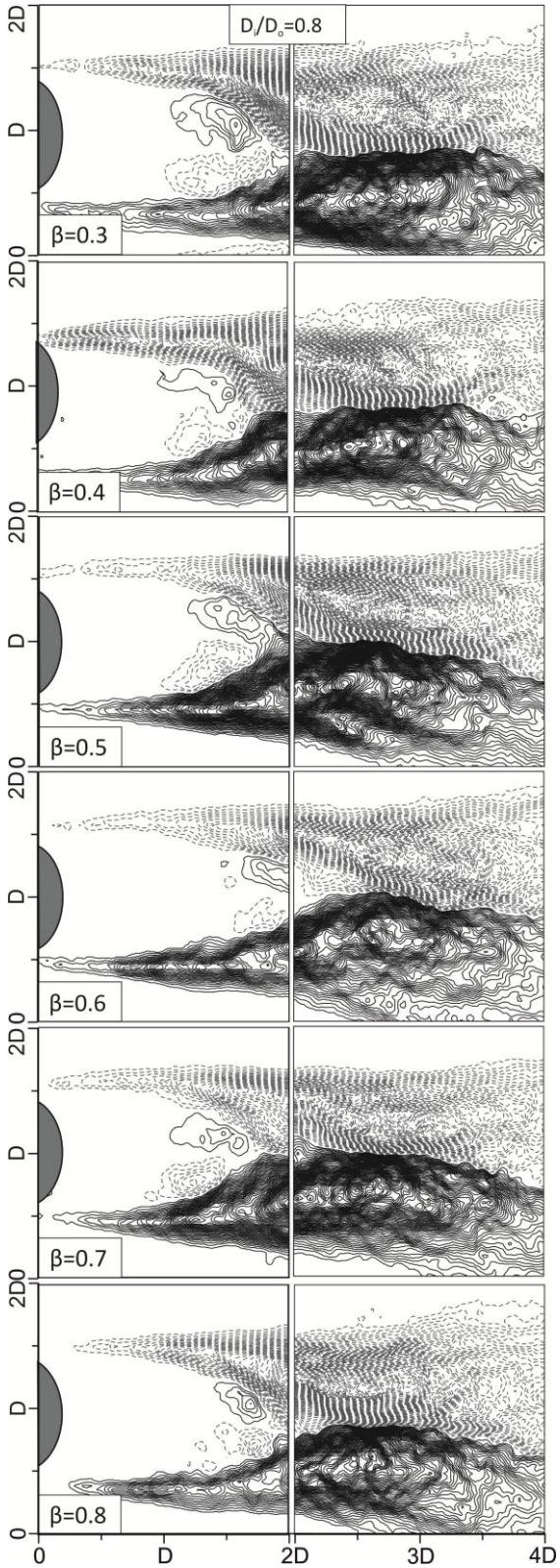


Figure 4.48. The Reynolds shear stress distribution downstream of the cylinder surrounded with arc ($\alpha=150^o$) for $D_i/D_o=0.8$ at different β cases

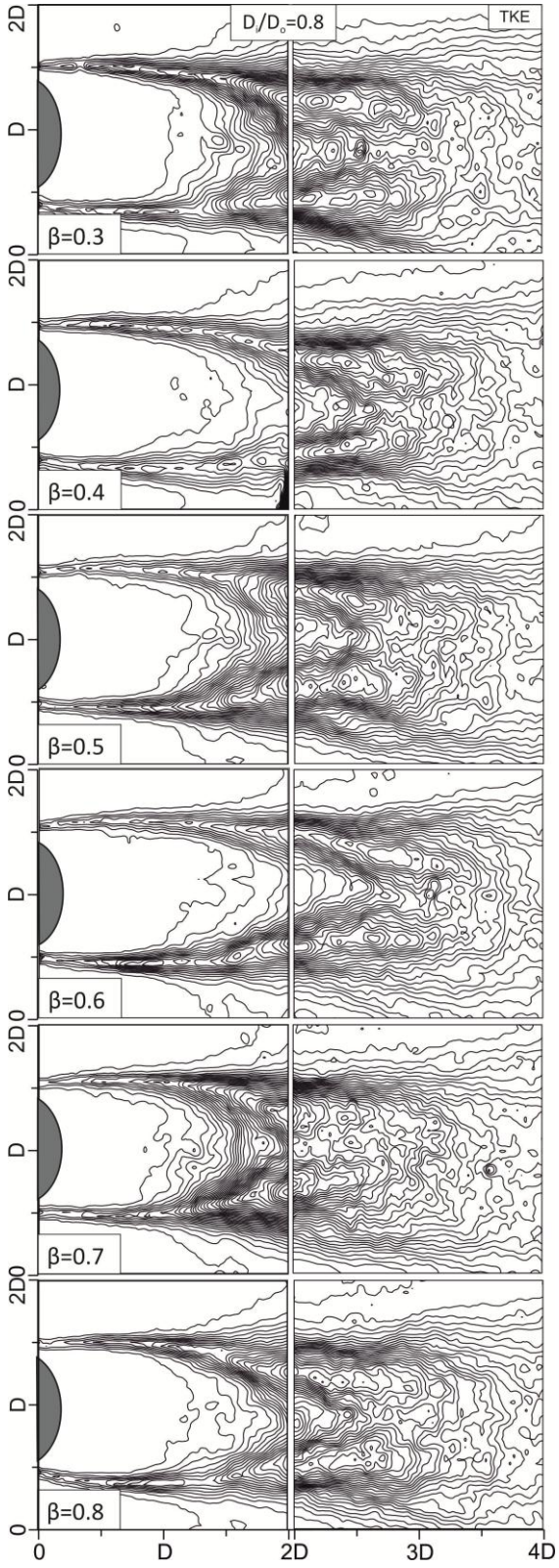


Figure 4.49. The TKE distribution downstream of the cylinder surrounded with arc ($\alpha=150^o$) for $D_i/D_o=0.8$ at different β cases

Figures 4.50 and 4.51 present the Reynolds shear stress and TKE contours obtained at $D_i/D_o=0.9$ for varying porosity. At this diameter ratio, outer cylinder completely loses its effect on the inner cylinder. It is observed that the arc angle of the outer cylinder is inadequate in surrounding the inner cylinder. So, turbulent flow structure is formed in the near wake of the cylinder couple.

In the case that the outer cylinder is an arc of 150^o, effects of varying porosity and diameter ratios on the peak magnitude of Reynolds shear stress and TKE are presented in Figure 4.52 by two dimensional graphics. Both graphs being consistent with each other, they show that at low diameter ratios such as $\beta=0.3$ and 0.4, increase the turbulence intensity. When compared with inner bare cylinder application, it is seen that higher diameter ratios are more effective.

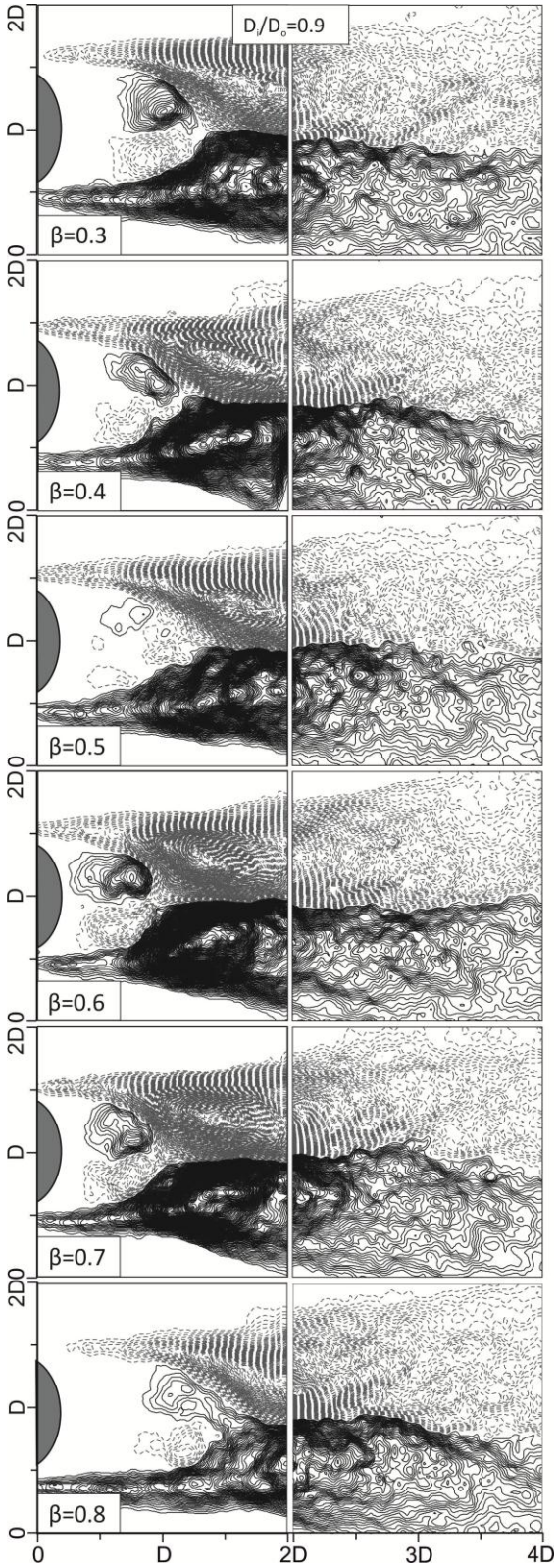


Figure 4.50. The Reynolds shear stress distribution downstream of the cylinder surrounded with arc ($\alpha=150^o$) for $D_i/D_o=0.9$ at different β cases

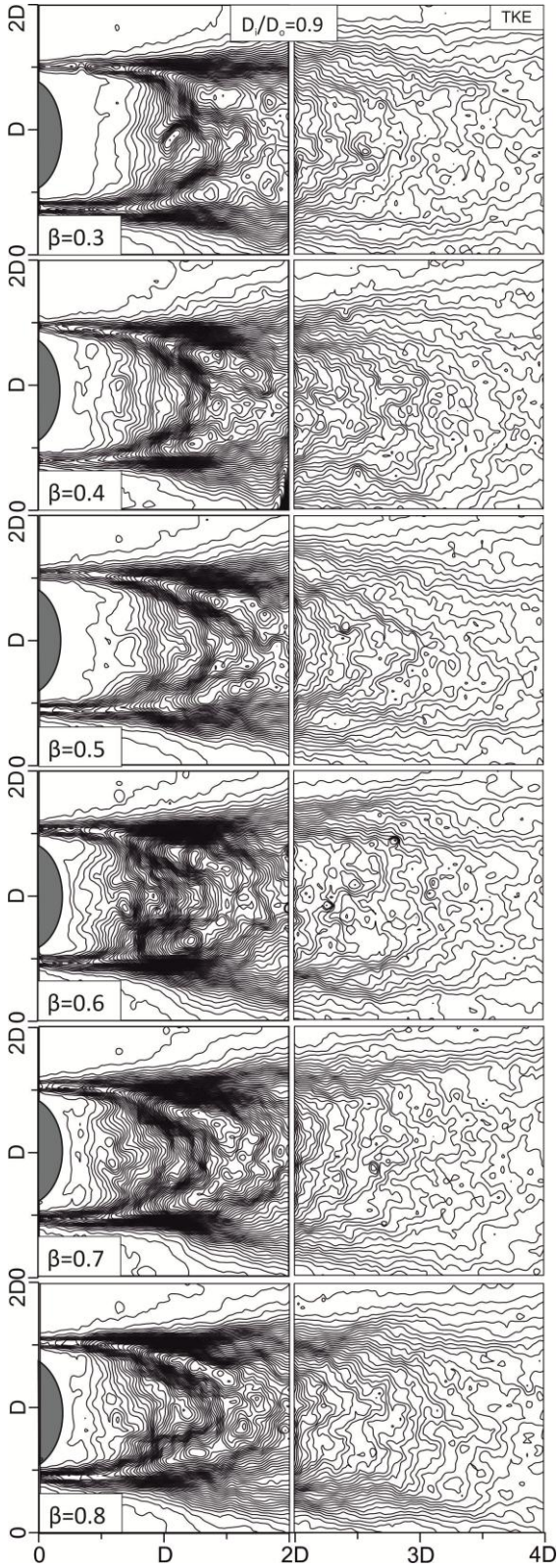


Figure 4.51. The TKE distribution downstream of the cylinder surrounded with arc ($\alpha=150^o$) for D_i/D_o=0.9 at different β cases

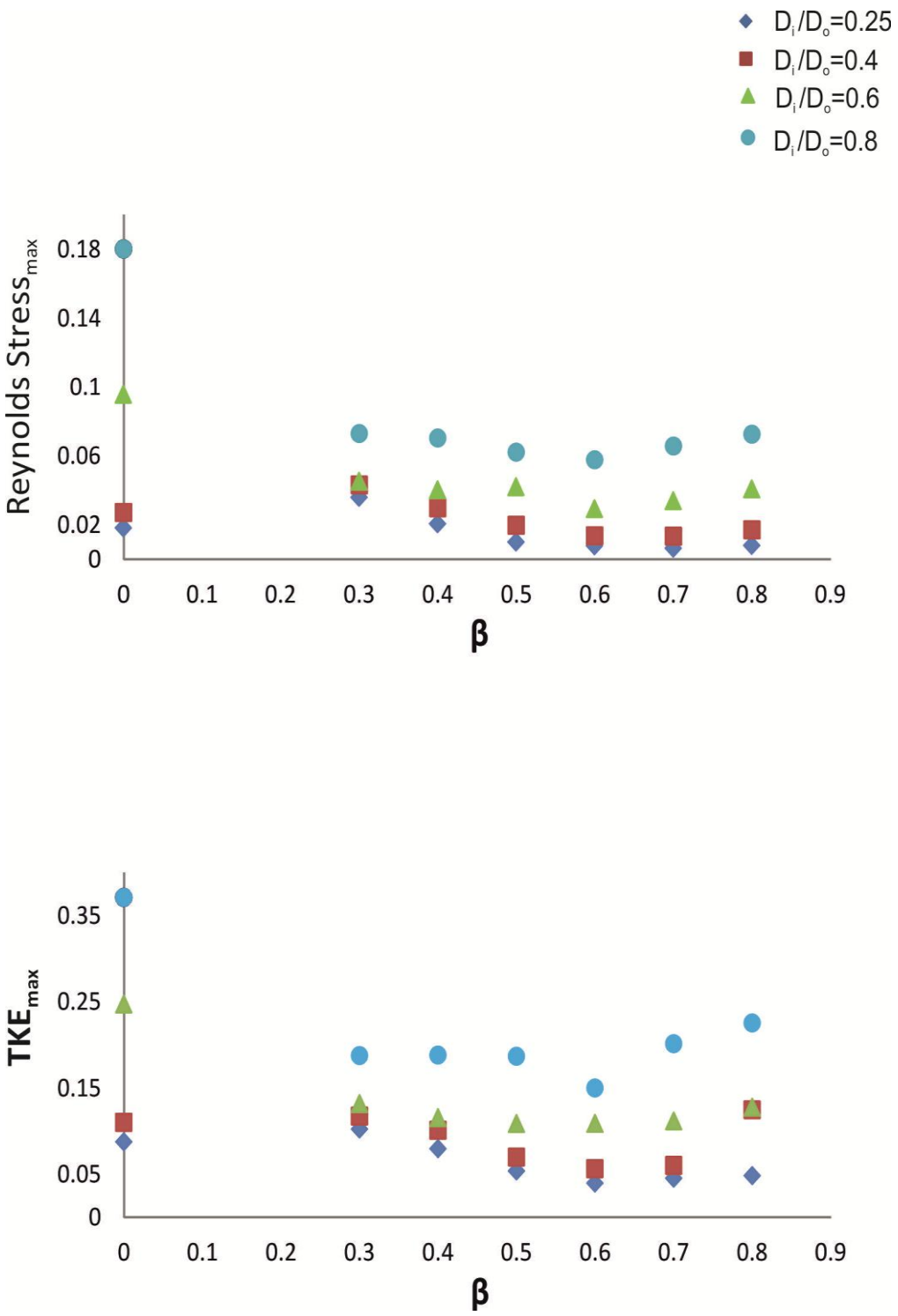


Figure 4.52. The variation of Reynolds $stress_{max}$ and TKE_{max} with β to demonstrate the effect of D_i/D_o for $\alpha=150^o$

The effects of 150^o outer cylinder on the time averaged vorticity in near wake region of the inner cylinder are shown from Figure 4.53 to Figure 4.60. While drawing time averaged vorticity contours minimum values and increments were taken the same as in the outer cylinder case. Figures 4.53, 4.54 and 4.55 present the effect of porosity on vorticity for the diameter ratios of D_i/D_o=0.25, 0.3 and 0.4, respectively. These exhibit similarities with the vorticity contours obtained from the case of $\alpha=180^o$ outer cylinder. However, for β=0.7 and 0.8 porosities the effect of the inner cylinder on flow structure increased further.

Figures 4.56 and 4.57 show the effect of porosity on vorticity structures respectively for D_i/D_o=0.5 and 0.6 diameter ratios. Comparing these diameter ratios with the half outer cylinder application ($\alpha=180^o$) shows that the magnitude in shear layers increased. The two separate vorticity couples (A and B) caused by the inner and outer cylinders at D_i/D_o=0.5 diameter ratio and β=0.7 and 0.8, are not formed in the case of $\alpha=150^o$. When compared with the bare cylinder shown in Figure 4.1, it is demonstrated that particularly porosities of β=0.5 and 0.6 are effective on the vortices to be moved downstream direction that occur in near wake region downstream of the cylinder.

Vorticity contours obtained for different porosities at D_i/D_o=0.7 and 0.75 diameter ratios are respectively shown in Figure 4.58 and Figure 4.59. Similar structures are formed in both diameter ratios and shear layers are shortened with respect to the previous diameter ratios and interact with each other in the second field of view. At D_i/D_o=0.7 diameter ratio and within the range of porosity $0.3\leq\beta\leq0.6$, the shear layers that elongate to the third field of view at $\alpha=180^o$ case to have effect in the second field of view for $\alpha=150^o$.

Figure 4.60-a show that at D_i/D_o=0.8 the outer cylinder constitute an effect on the flow structure yet the effect of porosity is completely got lost. In Figure 4.60-b, it is shown that at D_i/D_o=0.9, the inner cylinder is completely effective on the outer cylinder. The reason for this is the fact that sufficient fluid to cause jet flow does not enter through the holes on the outer cylinder due to decrease in the distance between the two cylinders and the inadequate surrounding of the inner cylinder by the outer cylinder with the increasing diameter ratio.

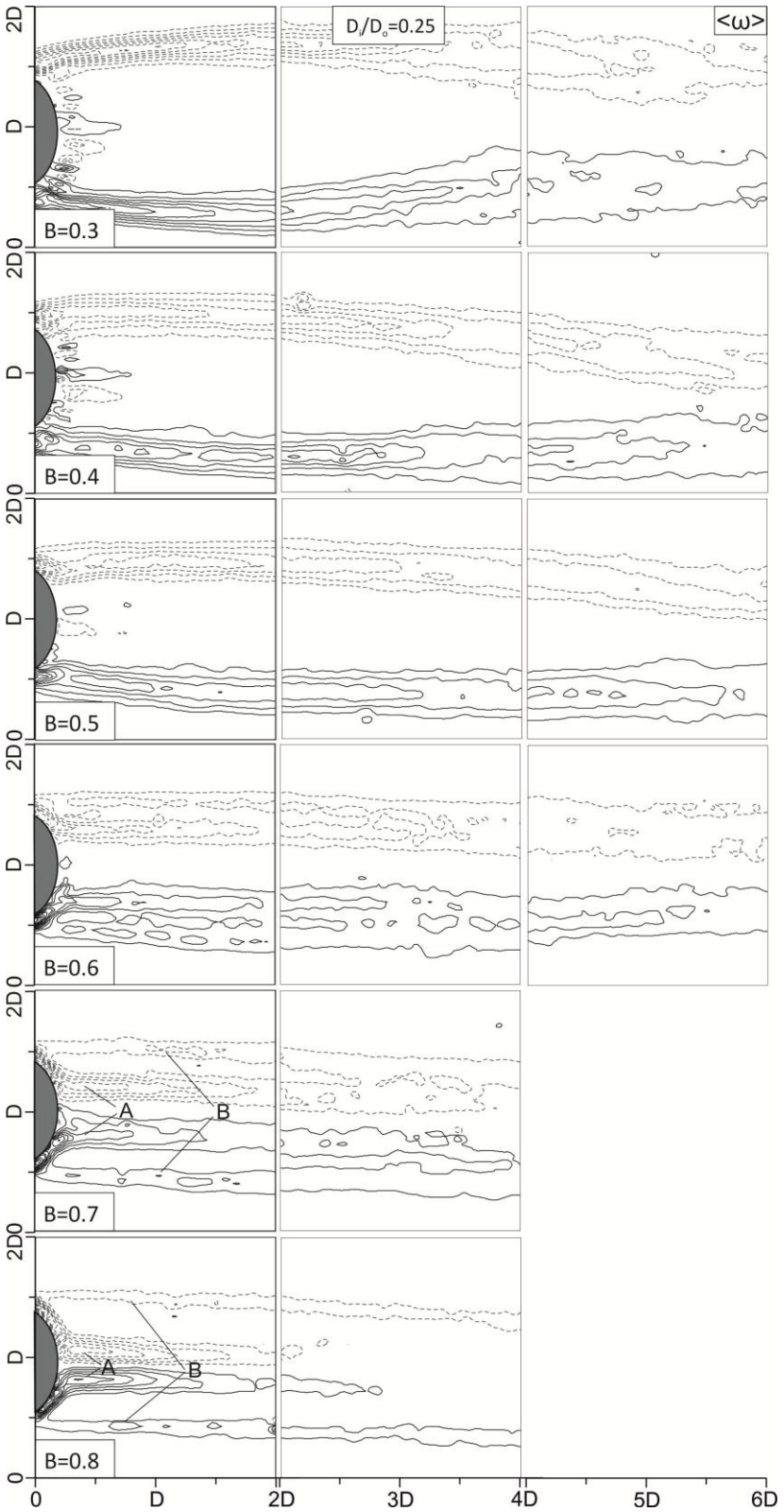


Figure 4.53. The vorticity distribution downstream of the cylinder surrounded with arc ($\alpha=150^o$) for $D_i/D_o=0.25$ at different β cases

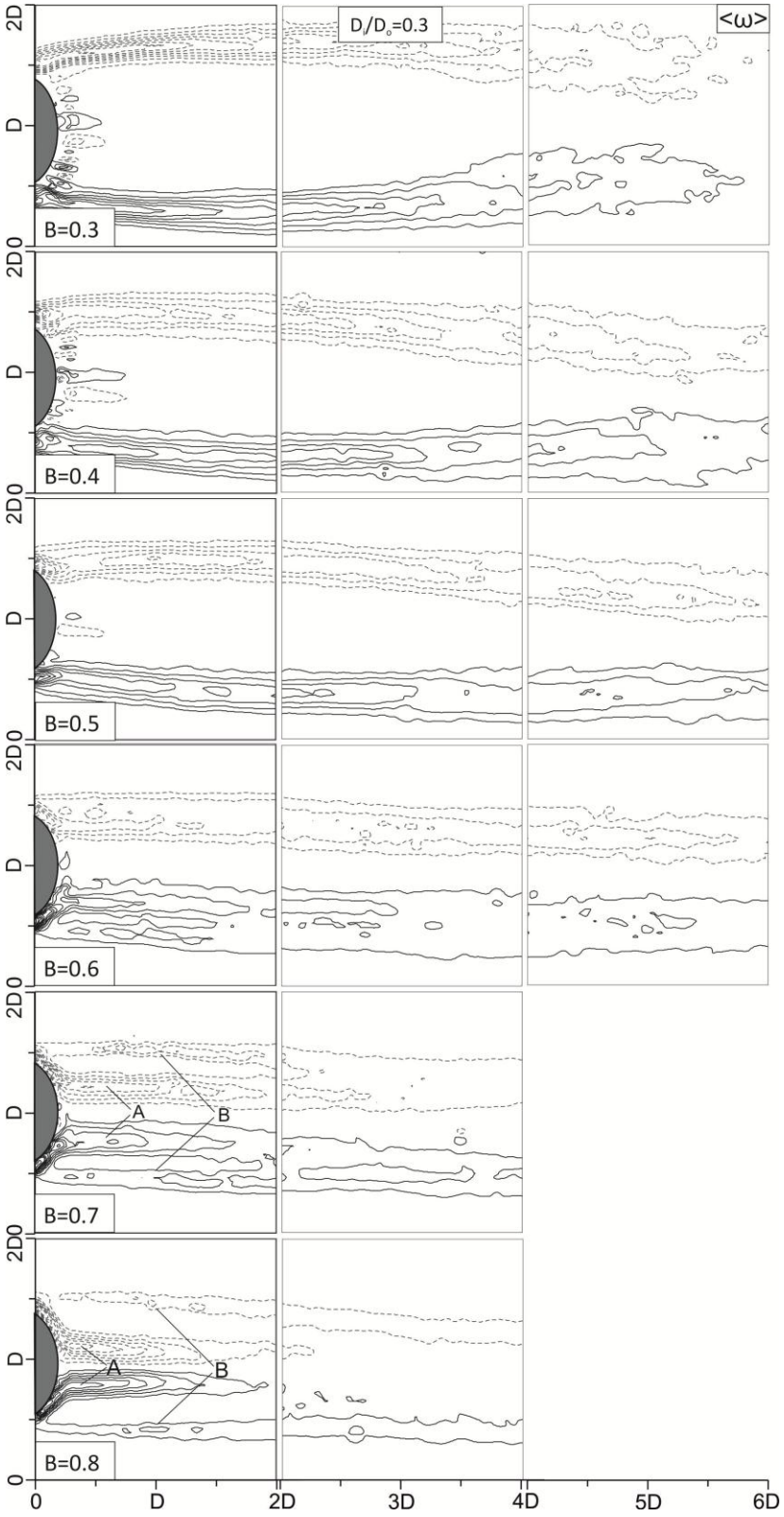


Figure 4.54. The vorticity distribution downstream of the cylinder surrounded with arc ($\alpha=150^o$) for $D_i/D_o=0.3$ at different β cases

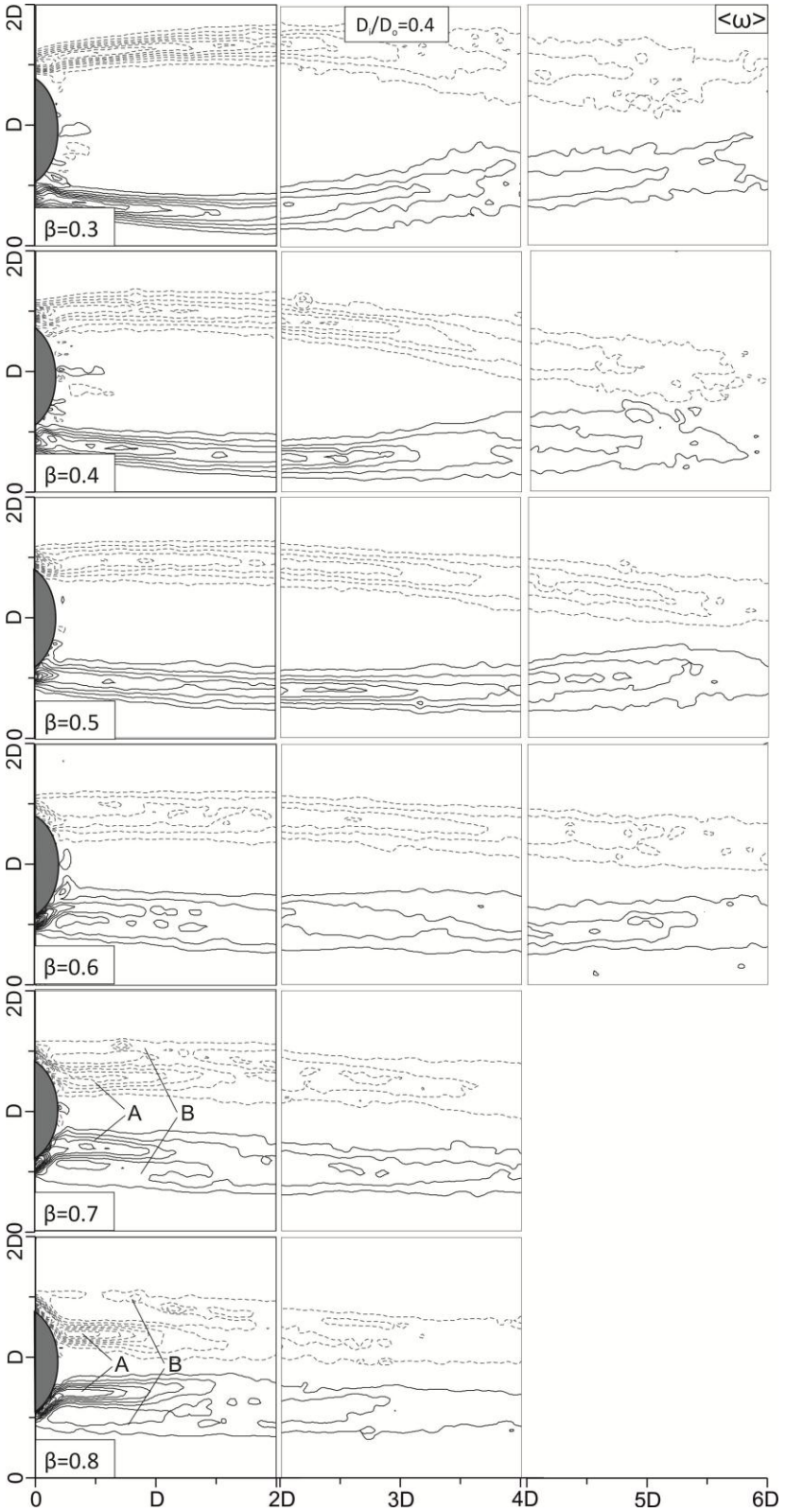


Figure 4.55. The vorticity distribution downstream of the cylinder surrounded with arc ($\alpha=150^o$) for $D_i/D_o=0.4$ at different β cases

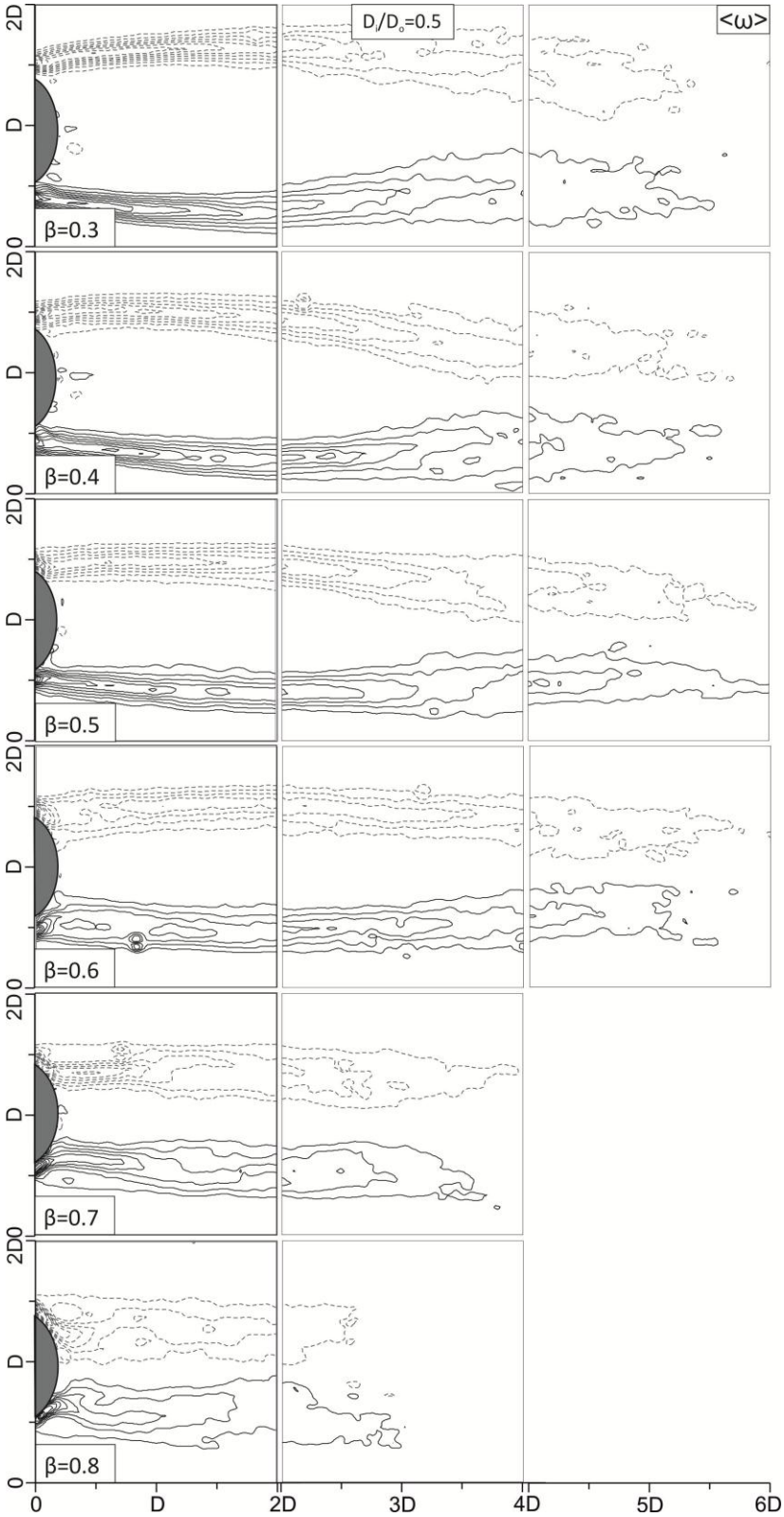


Figure 4.56. The vorticity distribution downstream of the cylinder surrounded with arc ($\alpha=150^o$) for $D_i/D_o=0.5$ at different β cases

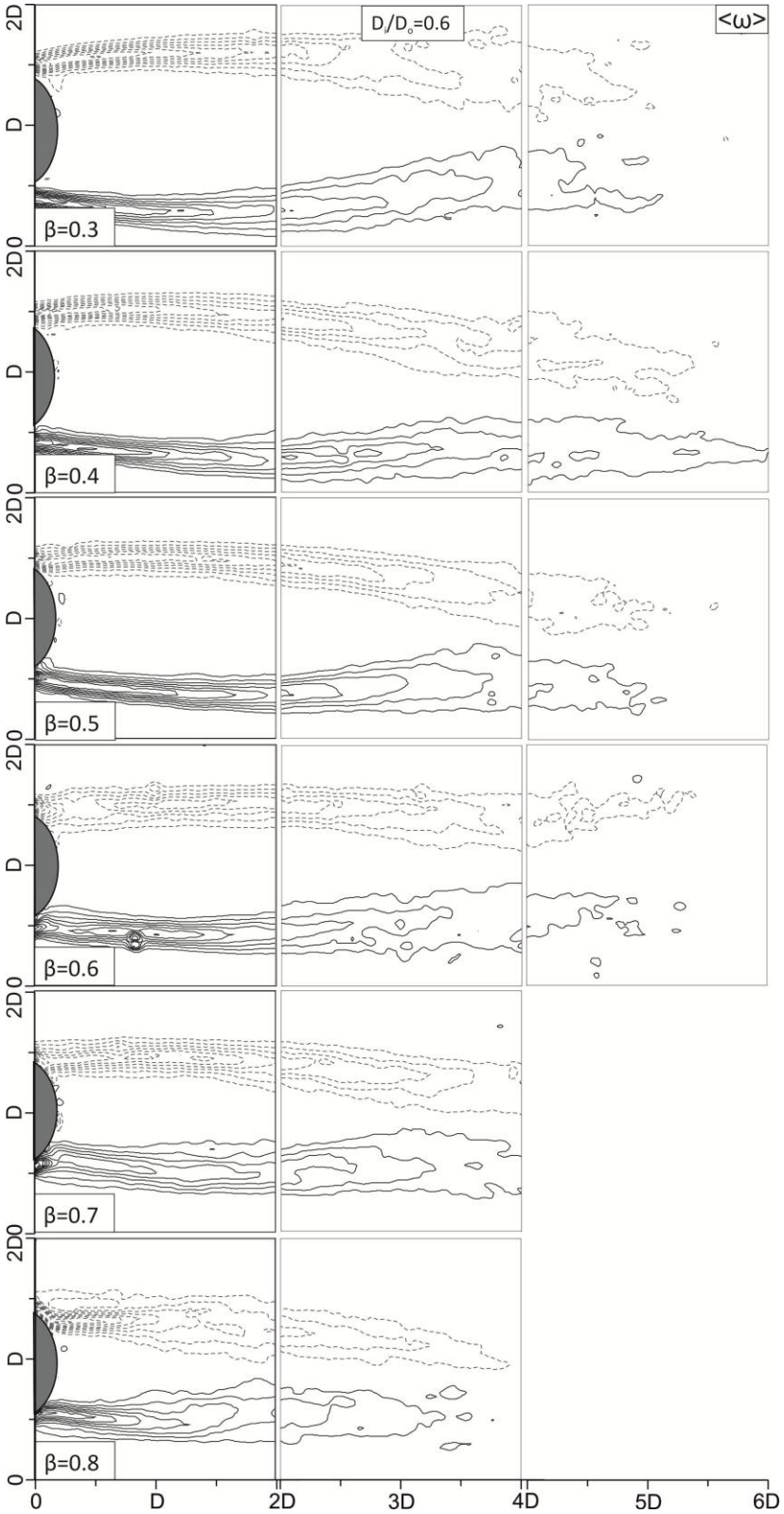


Figure 4.57. The vorticity distribution downstream of the cylinder surrounded with arc ($\alpha=150^o$) for $D_i/D_o=0.6$ at different β cases

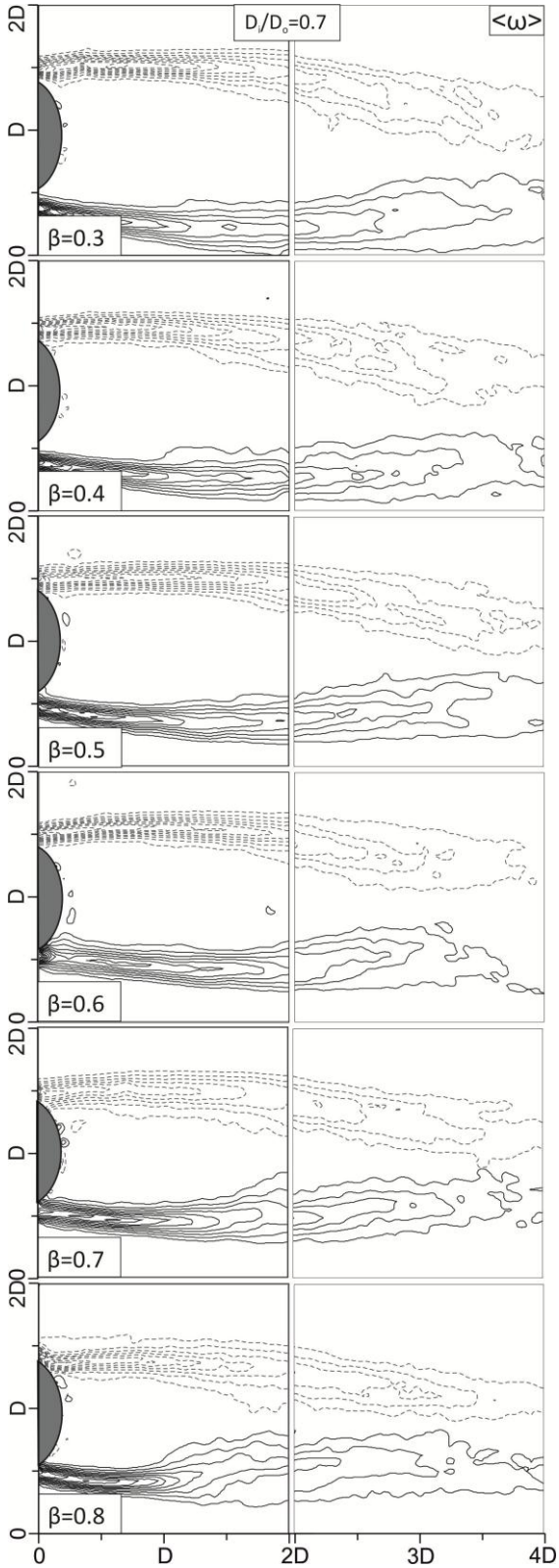


Figure 4.58. The vorticity distribution downstream of the cylinder surrounded with arc ($\alpha=150^o$) for $D_i/D_o=0.7$ at different β cases

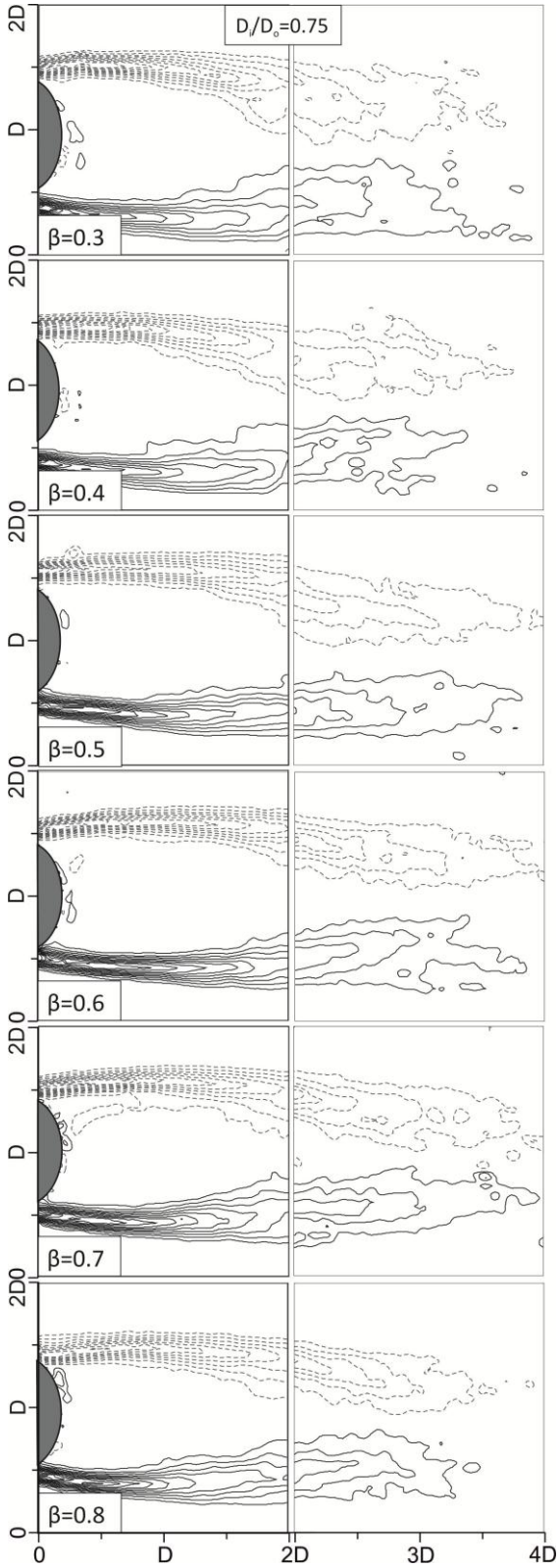


Figure 4.59. The vorticity distribution downstream of the cylinder surrounded with arc ($\alpha=150^o$) for $D_i/D_o=0.75$ at different β cases

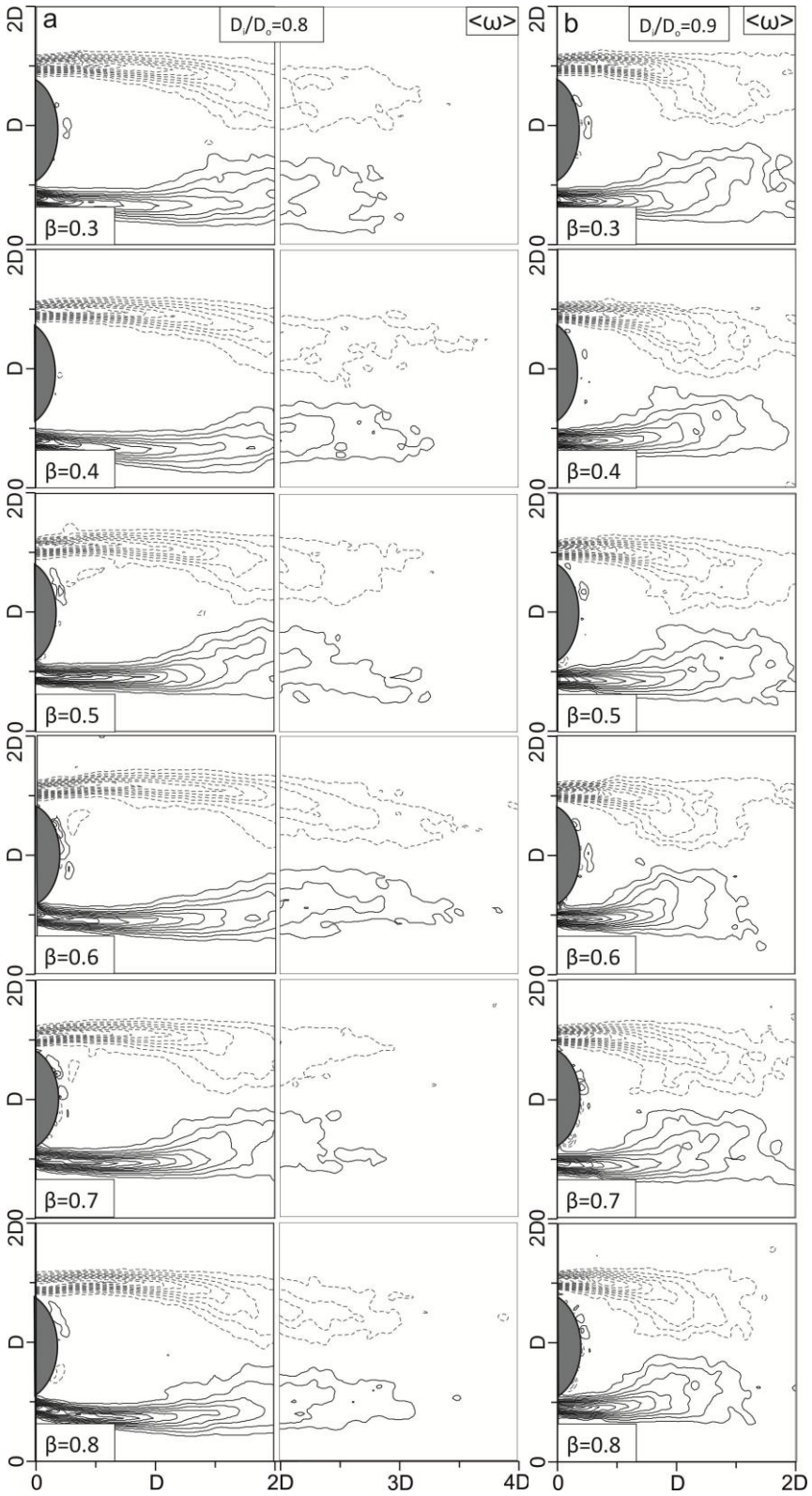


Figure 4.60. The vorticity distribution downstream of the cylinder surrounded with arc ($\alpha=150^o$) for D_i/D_o=0.8 (a), Di/D_o=0.9 (b) at different β cases

4.1.2.3. Angle of Arc α=120^o Application

Reynolds shear stress and TKE contours obtained from the case where the inner cylinder is surrounded by the 120^o outer cylinder are presented from Figure 4.62 to Figure 4.79. Figure 4.61 shows the Reynolds shear stress contours obtained from the case where only the outer cylinder was present. It is observed that low porosity causes higher turbulence in comparison with the previous outer cylinders.

The effects of porosity on Reynolds shear stress and TKE at D_i/D_o=0.25, 0.3 and 0.4 diameter ratios are presented in figures from 4.62 to 4.67. It is seen that the optimum porosity is β=0.6 at these diameter ratios. Turbulence caused by the outer cylinder at low porosities is higher than that caused by α=180^o and α=150^o outer cylinder. For instance, for D_i/D_o=0.3 and β=0.3 the peak magnitude of Reynolds shear stress and TKE were respectively obtained as 0.029 and 0.083 for α=180^o, 0.035 and 0.104 for α=150^o and 0.039 and 0.13 for α=120^o.

The effects of porosity on diameter ratios D_i/D_o=0.5, 0.6 and 0.7 are presented from Figure 4.68 to Figure 4.73. Since the points where the peak magnitude of Reynolds shear stress and TKE occurred in the near wake of the cylinder couple were obtained in the second field of view, experiments were not performed for these and other diameters for the third field of view. Comparison on these diameter ratios with the previous outer cylinder configurations shows that the peak magnitude of Reynolds shear stress and TKE increases. When compared with the bare inner cylinder application, it is demonstrated that the outer cylinder is effective. For instance, in the case where inner cylinder diameter was D_i=50 mm, the peak magnitude of Reynolds shear stress and TKE were obtained as 0.047 and 0.133. The results obtained for porosity β=0.6 and diameter ratio D_i/D_o=0.5 are 0.014 and 0.066 for α=180^o, 0.023 and 0.07 for α=150^o and finally 0.037 and 0.115 for α=120^o.

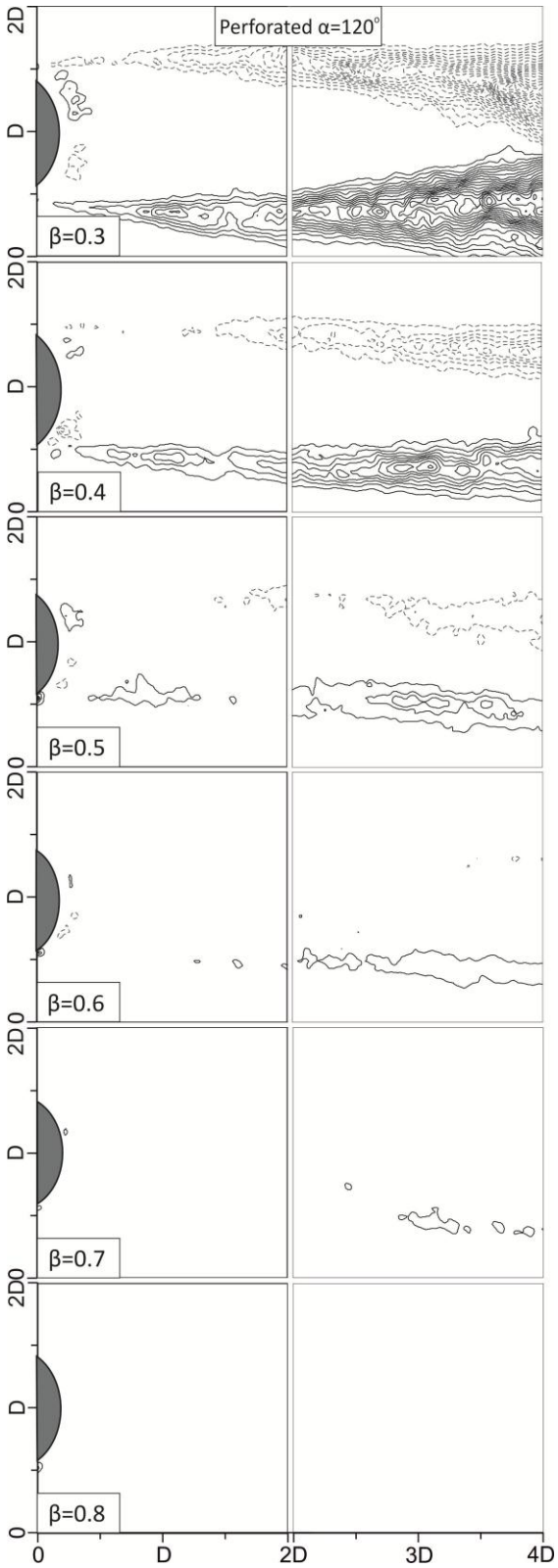


Figure 4.61. The Reynolds shear stress distribution downstream of arc ($\alpha=120^o$) for different β cases

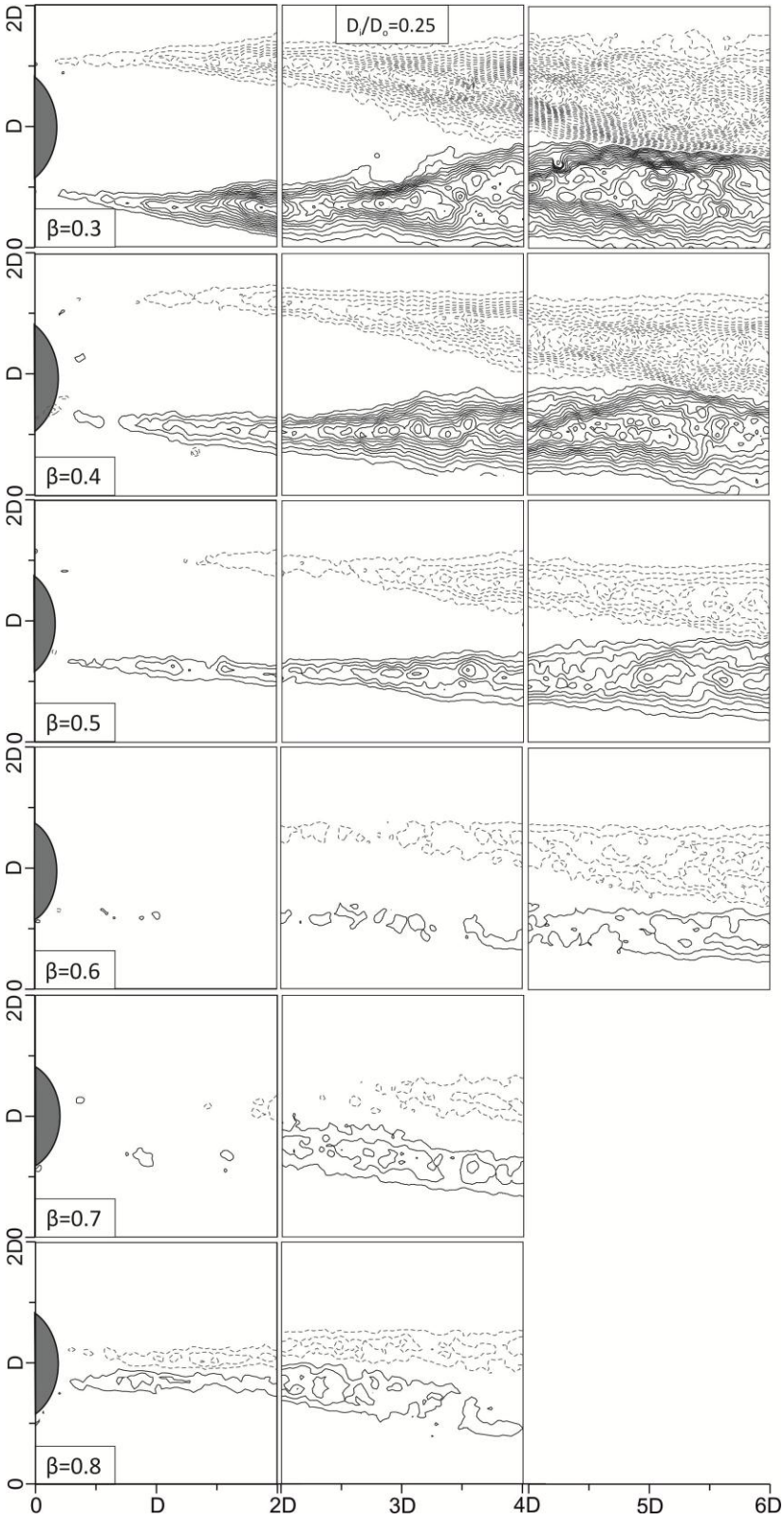


Figure 4.62. The Reynolds shear stress distribution downstream of the cylinder surrounded with arc (α=120^o) for D_i/D_o=0.25 at different β cases

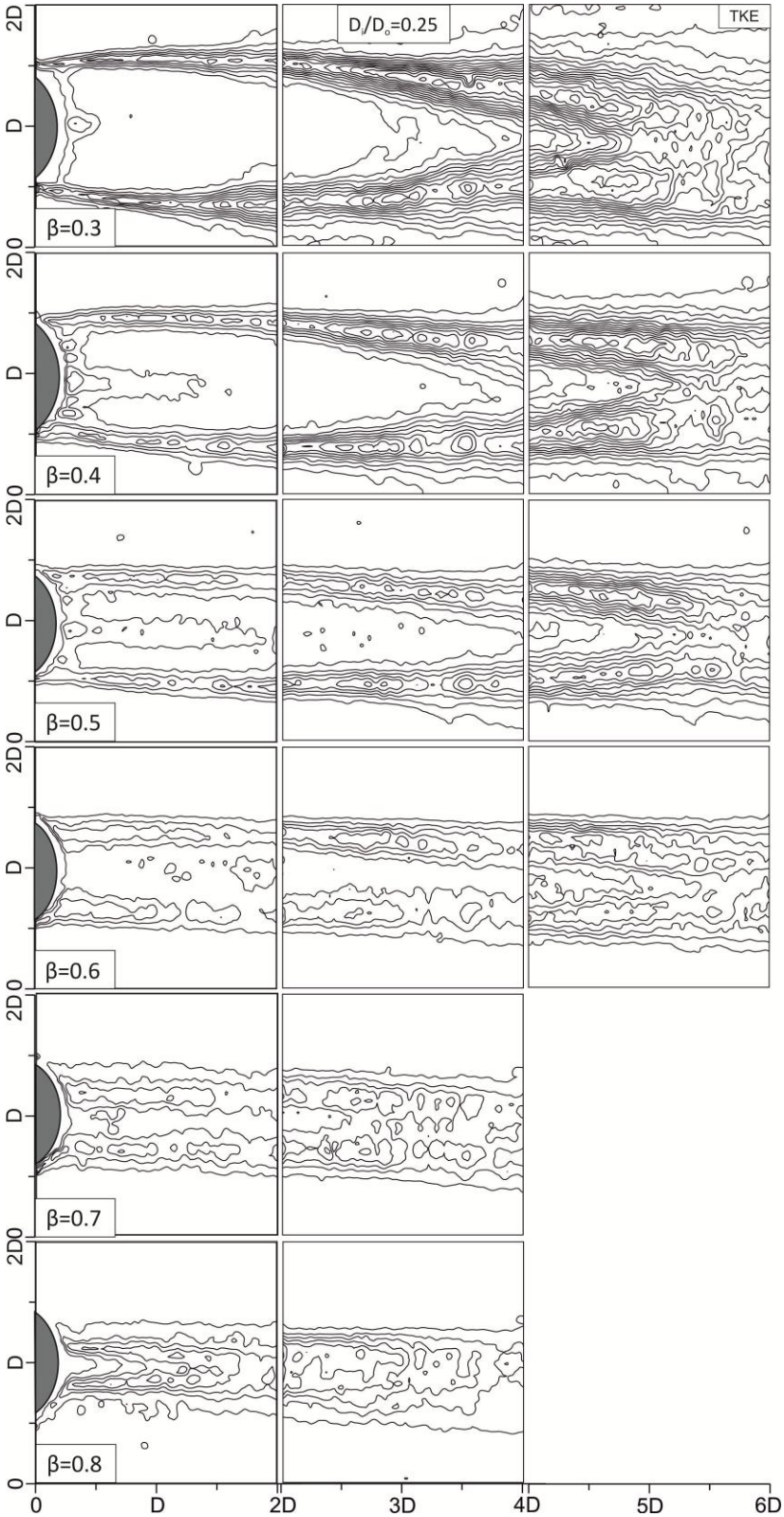


Figure 4.63. The TKE distribution downstream of the cylinder surrounded with arc ($\alpha=120^o$) for $D_i/D_o=0.25$ at different β cases

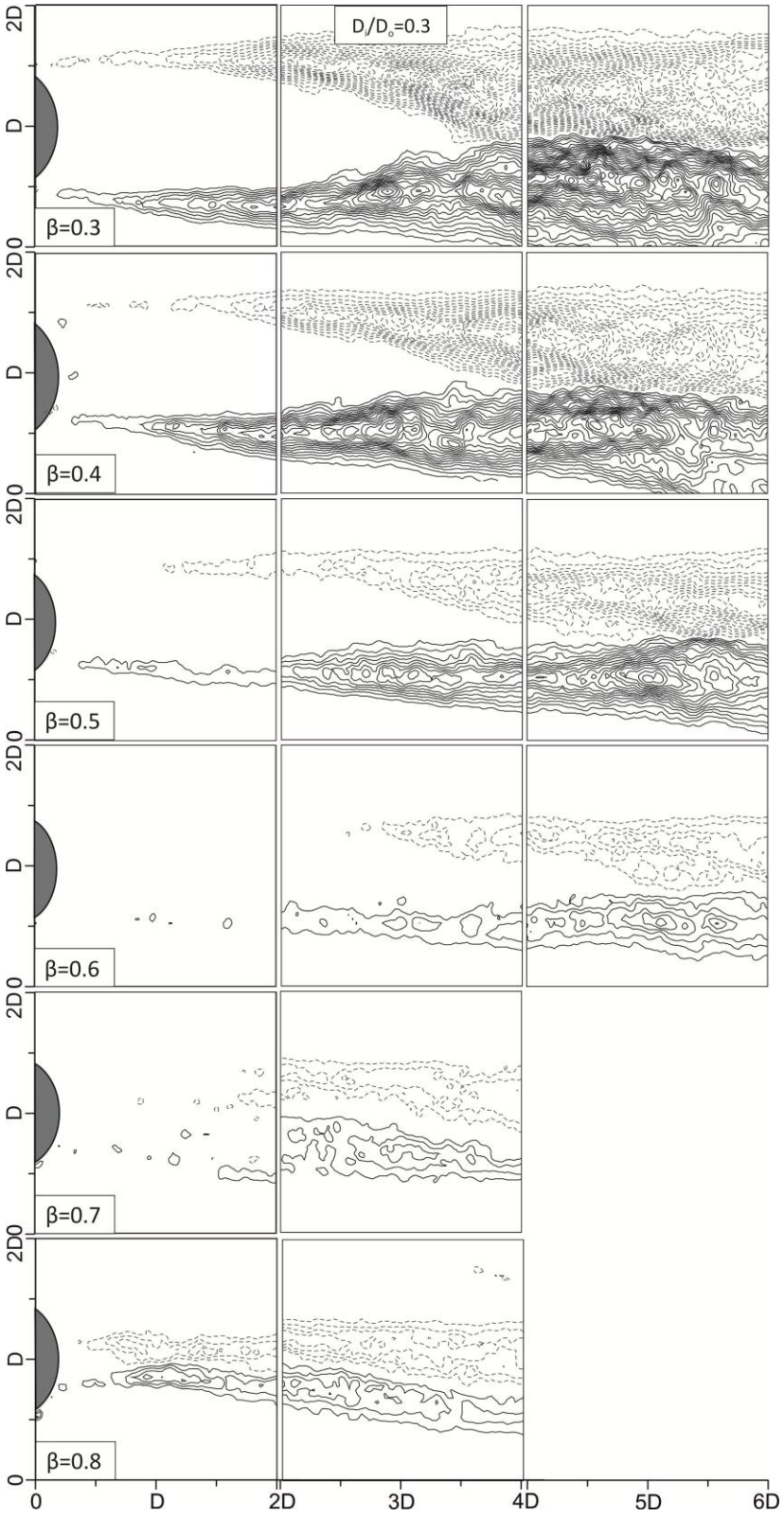


Figure 4.64. The Reynolds shear stress distribution downstream of the cylinder surrounded with arc ($\alpha=120^o$) for $D_i/D_o=0.3$ at different β cases

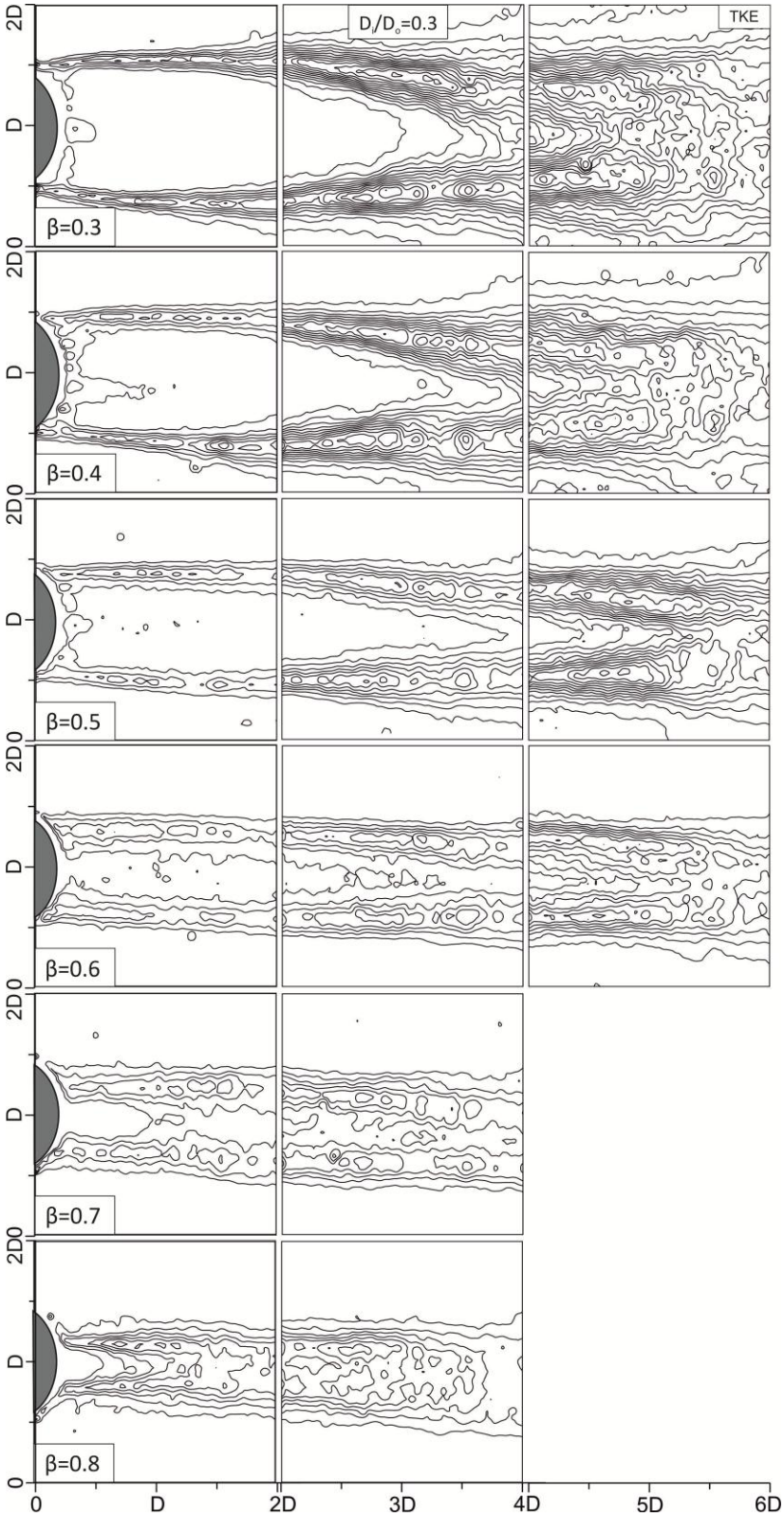


Figure 4.65. The TKE distribution downstream of the cylinder surrounded with arc (α=120^o) for D_i/D_o=0.3 at different β cases

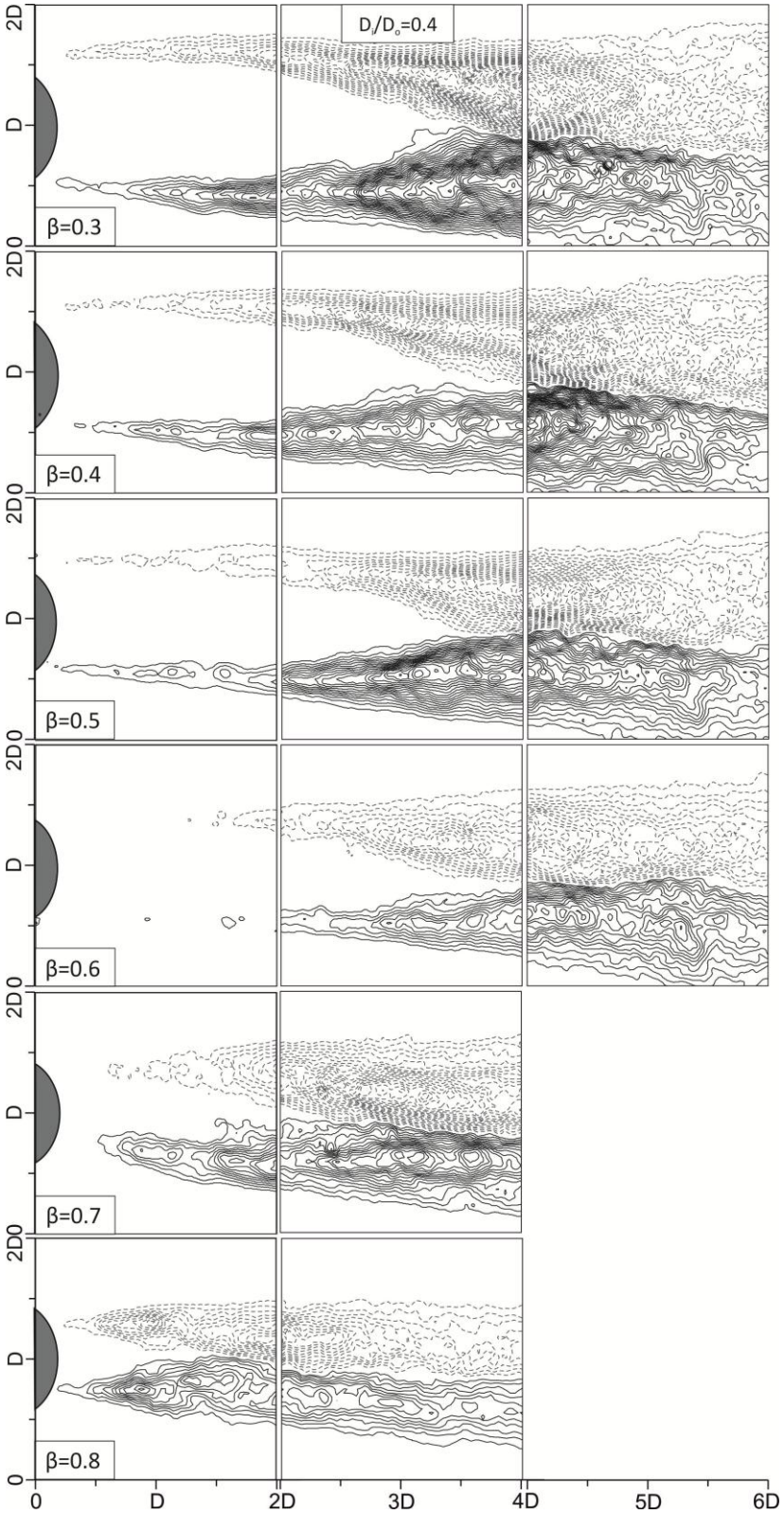


Figure 4.66. The Reynolds shear stress distribution downstream of the cylinder surrounded with arc ($\alpha=120^o$) for $D_i/D_o=0.4$ at different β cases

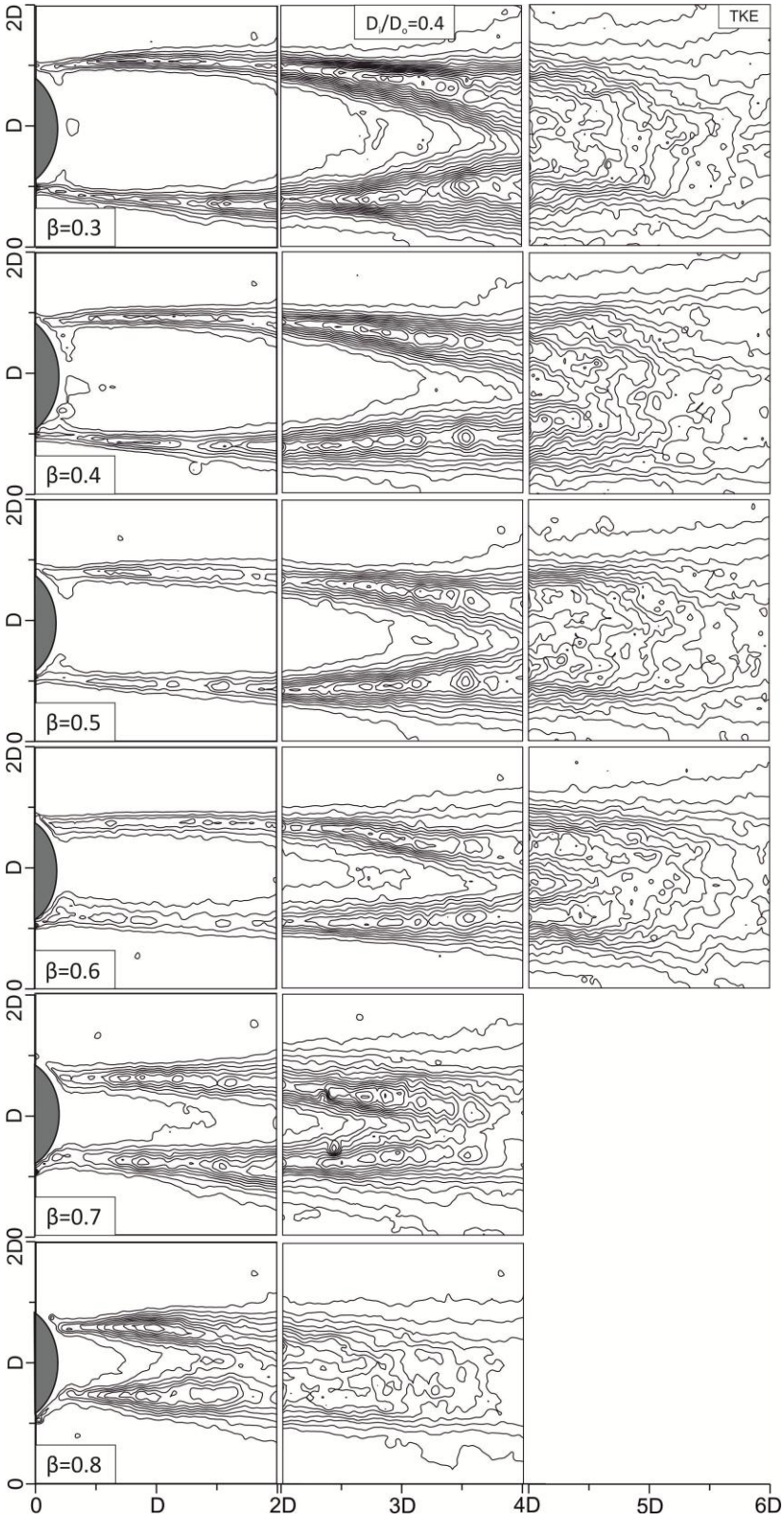


Figure 4.67. The TKE distribution downstream of the cylinder surrounded with arc ($\alpha=120^o$) for $D_i/D_o=0.4$ at different β cases

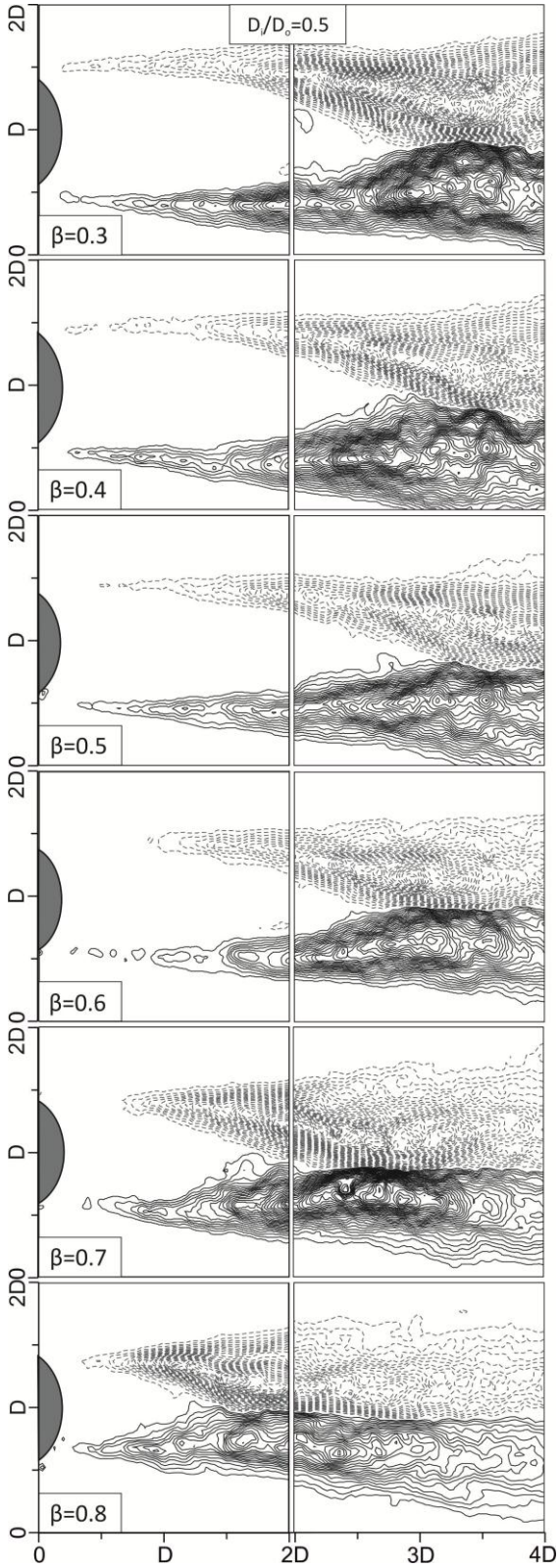


Figure 4.68. The Reynolds shear stress distribution downstream of the cylinder surrounded with arc ($\alpha=120^o$) for $D_i/D_o=0.5$ at different β cases

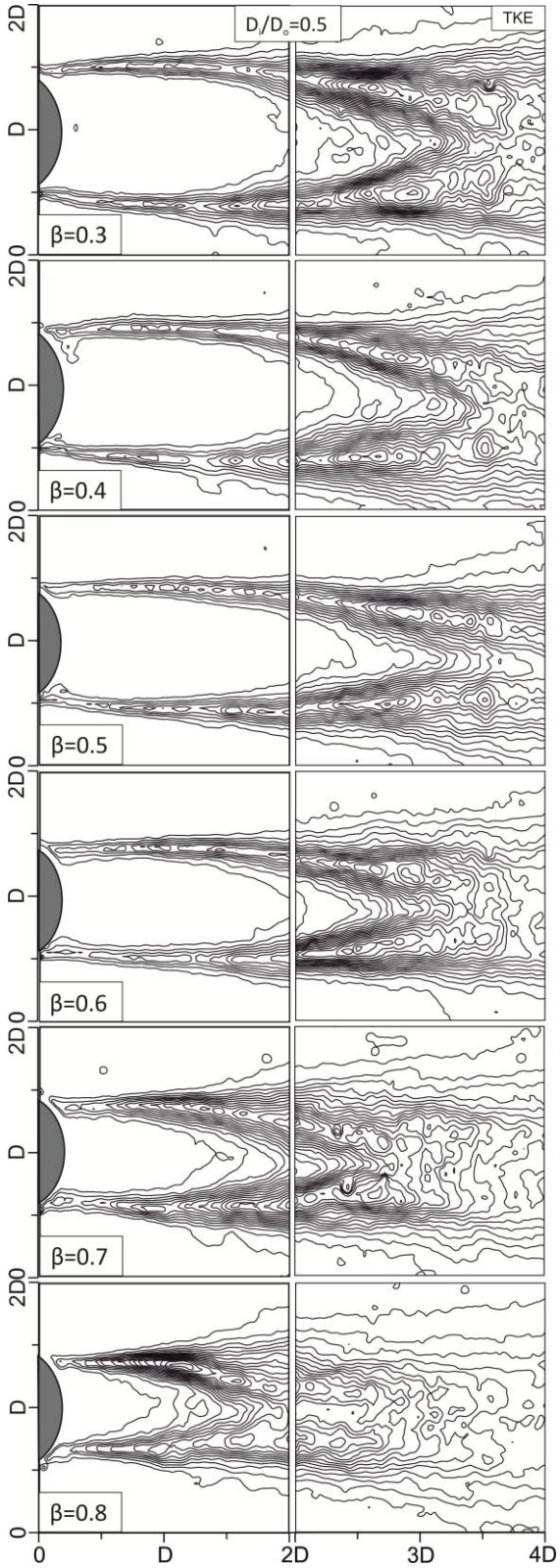


Figure 4.69. The TKE distribution downstream of the cylinder surrounded with arc ($\alpha=120^o$) for $D_i/D_o=0.5$ at different β cases

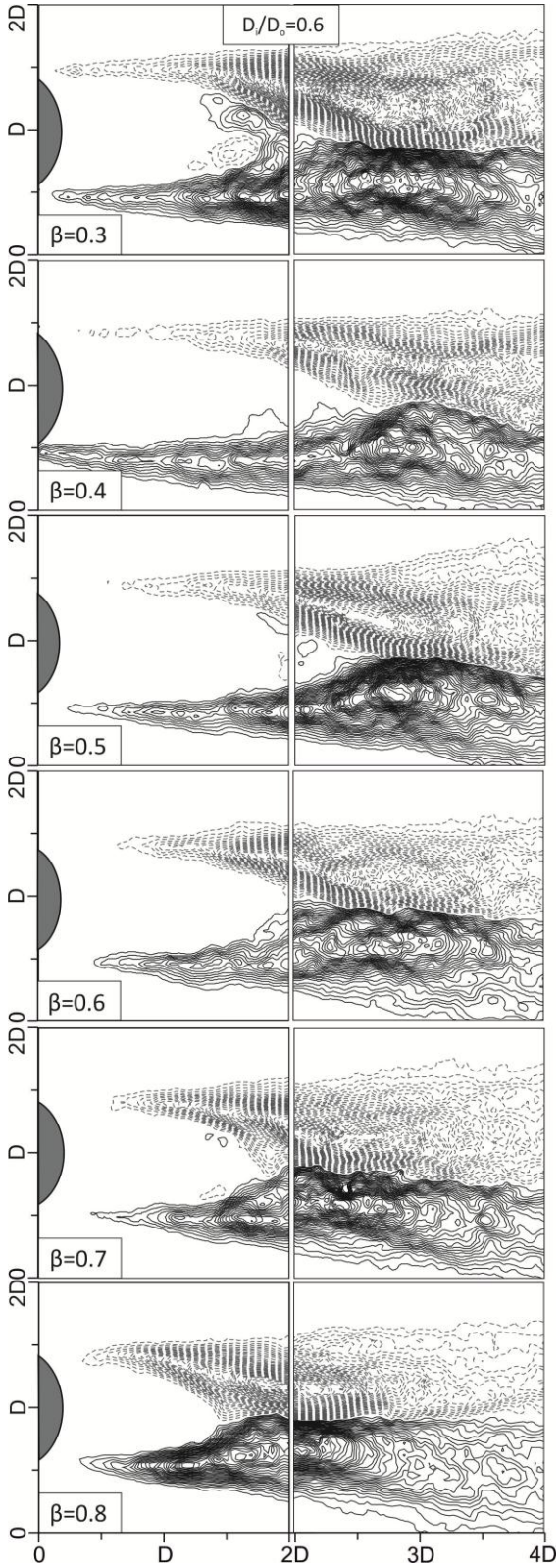


Figure 4.70. The Reynolds shear stress distribution downstream of the cylinder surrounded with arc ($\alpha=120^o$) for $D_i/D_o=0.6$ at different β cases

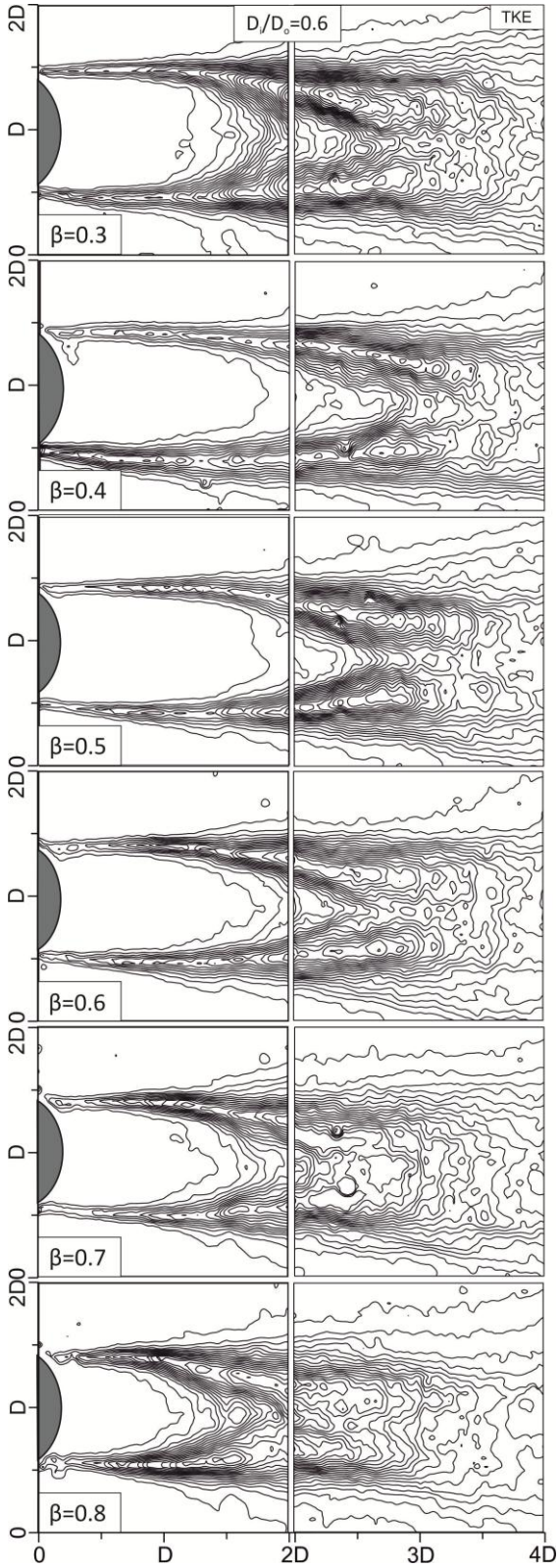


Figure 4.71. The TKE distribution downstream of the cylinder surrounded with arc ($\alpha=120^o$) for $D_i/D_o=0.6$ at different β cases

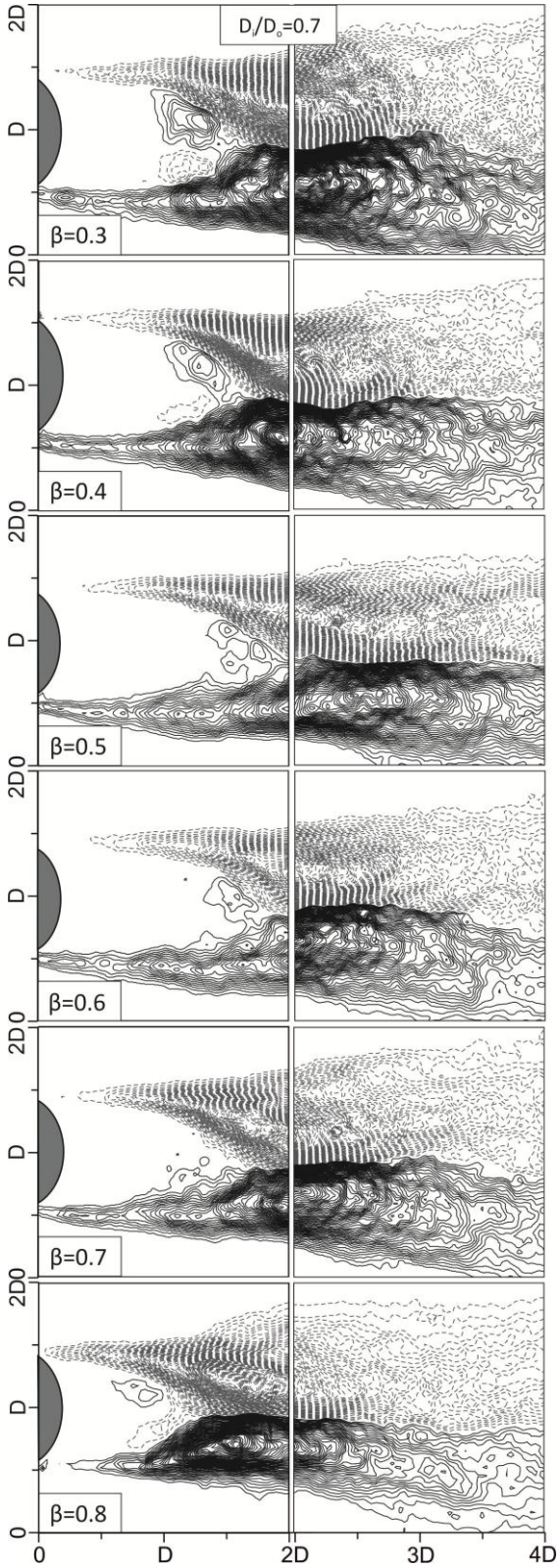


Figure 4.72. The Reynolds shear stress distribution downstream of the cylinder surrounded with arc ($\alpha=120^o$) for $D_i/D_o=0.7$ at different β cases

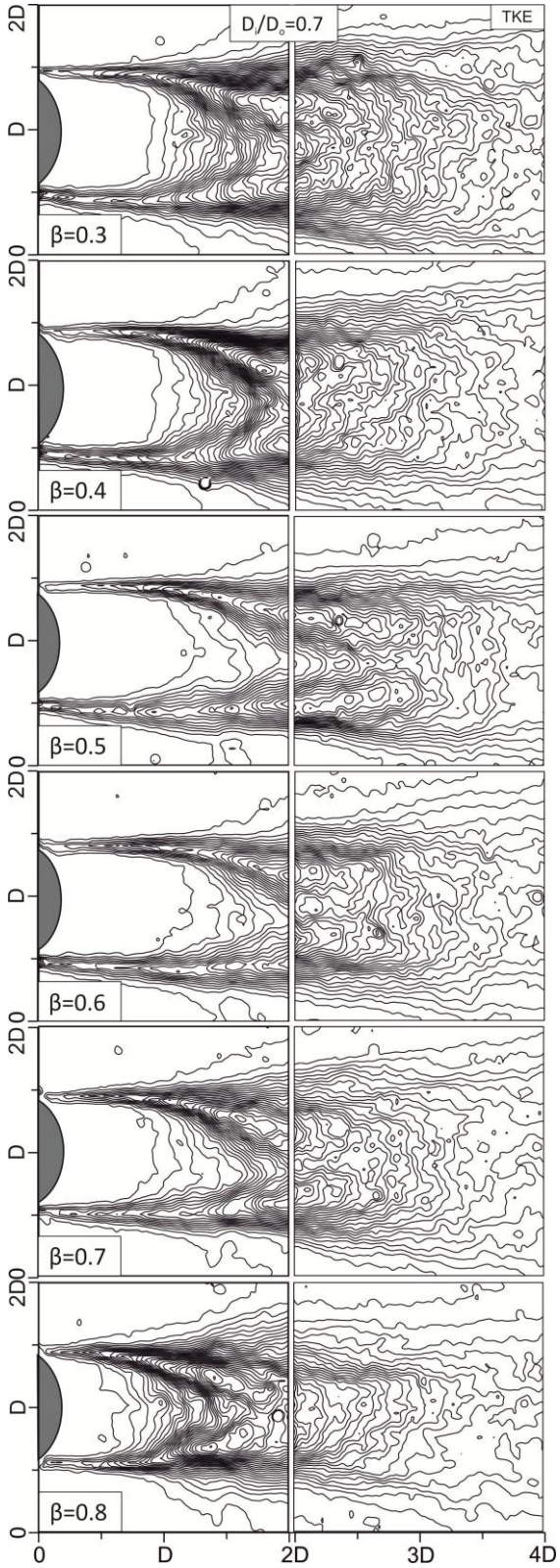


Figure 4.73. The TKE distribution downstream of the cylinder surrounded with arc ($\alpha=120^o$) for D_i/D_o=0.7 at different β cases

Figures from 4.74 to 4.79 present the Reynolds shear stress and TKE contours obtained for D_i/D_o=0.75, 0.8 and 0.9. At this diameter ratio, outer cylinder completely lost its effect on the inner cylinder. Flow characteristics at this diameter ratio exhibit similarity with the bare cylinder case shown in Figure 4.2. Due to the decrease in the distance between the two cylinders and the inadequacy of the outer cylinder in surrounding the inner cylinder, the cylinder couple started to act as a bare cylinder. As a result, it is concluded that these diameter ratios do not have any significant effect on the flow control.

The effects of varying diameter ratios on the peak magnitude of Reynolds shear stress and TKE for arc angle $\alpha=120^o$ outer cylinder are shown in the two dimensional graph presented in Figure 4.80. It can be seen from the figure that the larger diameter ratio increases Reynolds shear stress value and particularly at D_i/D_o=0.8, the values are approximately same with those of the bare cylinder case.

Time averaged vorticity contours obtained from all diameter ratios for outer cylinder $\alpha=120^o$ are presented from Figure 4.81 to 4.87. In order to well compare with the pervious outer cylinder arc angle, the minimum and increments were taken as the same in drawing the contours. It is understood that the diameter ratio is a significant parameter affecting the vortices in the near wake region. With the increasing diameter ratio, vorticity magnitude in the shear layers on each side of the cylinder also increases; shear layers shorten and get closer to each other on a point closer to the cylinder. Figure 4.87 shows in each column the respective vorticity contours obtained for D_i/D_o=0.75, 0.8 and 0.9. While with outer cylinder $\alpha=180^o$ arc angle the shear layers interact with each other in the second field of view, in the case of $\alpha=120^o$ outer cylinder arc angle they are observed to interact in the first field of view, as in the bare cylinder application, at D distance from the cylinder.

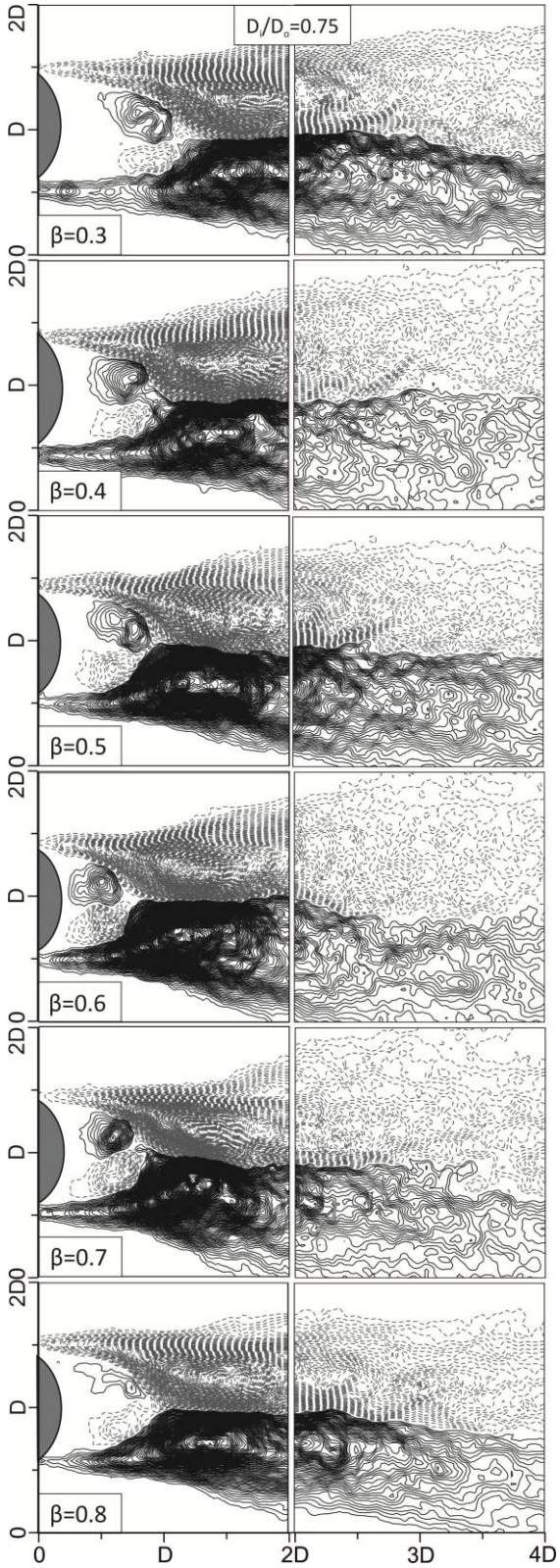


Figure 4.74. The Reynolds shear stress distribution downstream of the cylinder surrounded with arc ($\alpha=120^o$) for D_i/D_o=0.75 at different β cases

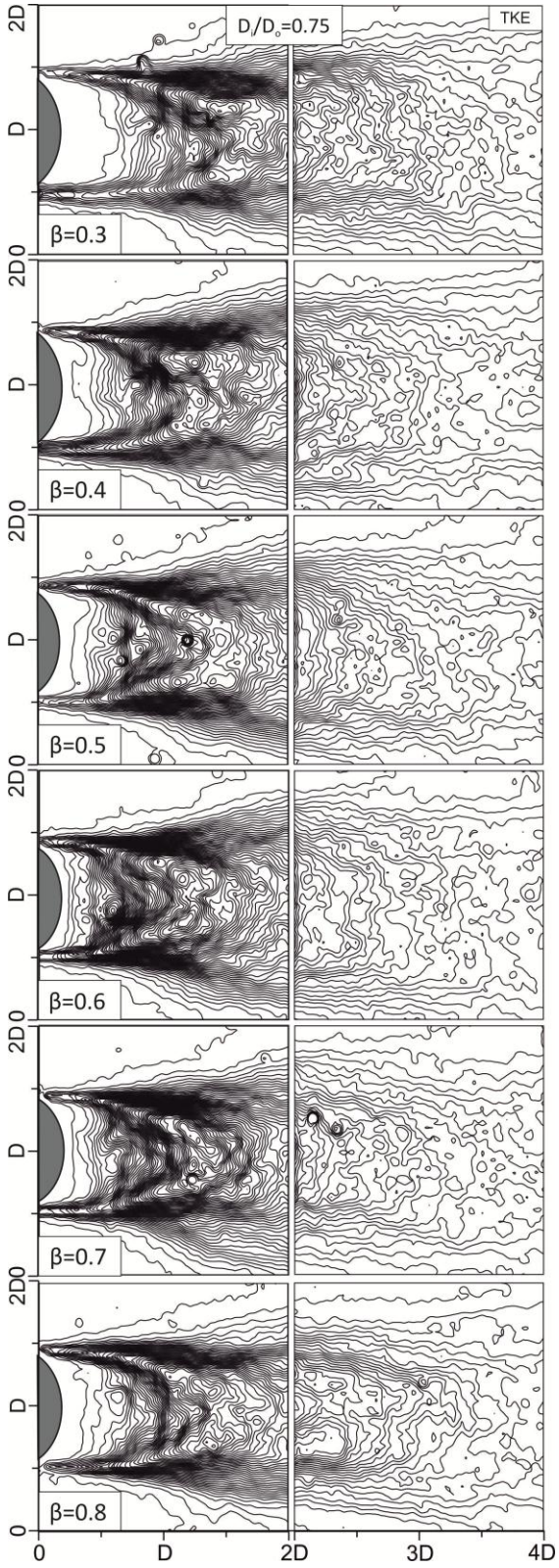


Figure 4.75. The TKE distribution downstream of the cylinder surrounded with arc ($\alpha=120^o$) for $D_i/D_o=0.75$ at different β cases

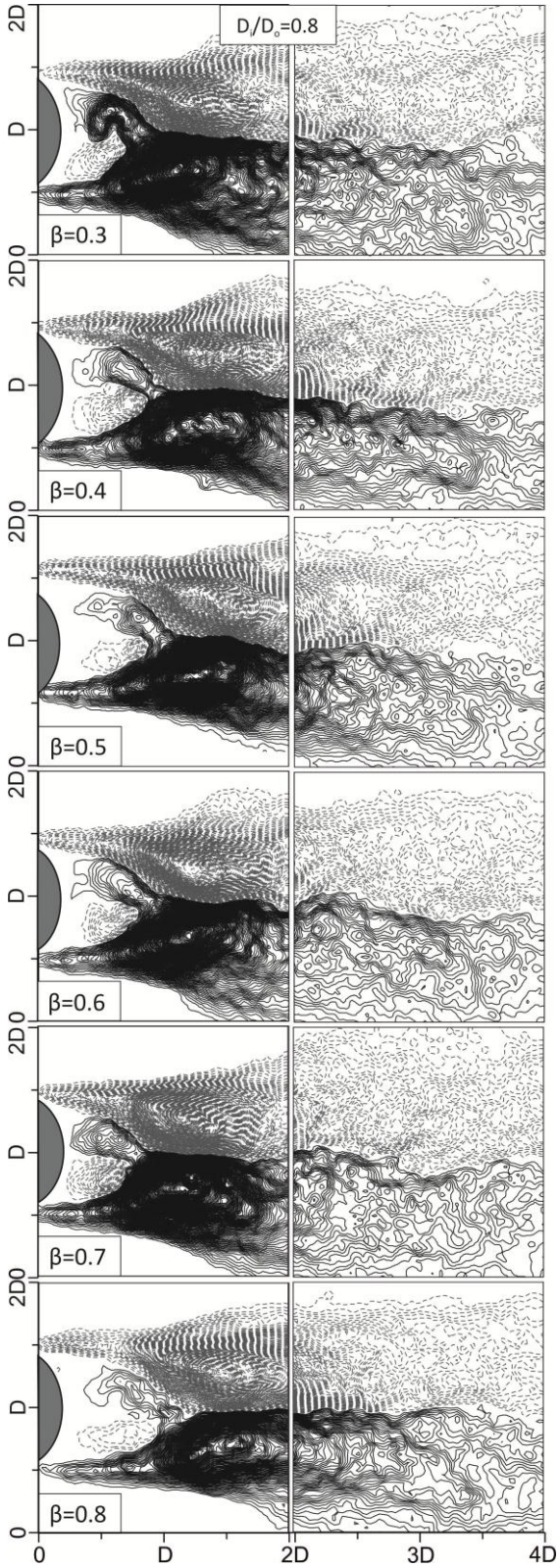


Figure 4.76. The Reynolds shear stress distribution downstream of the cylinder surrounded with arc ($\alpha=120^o$) for D_i/D_o=0.8 at different β cases

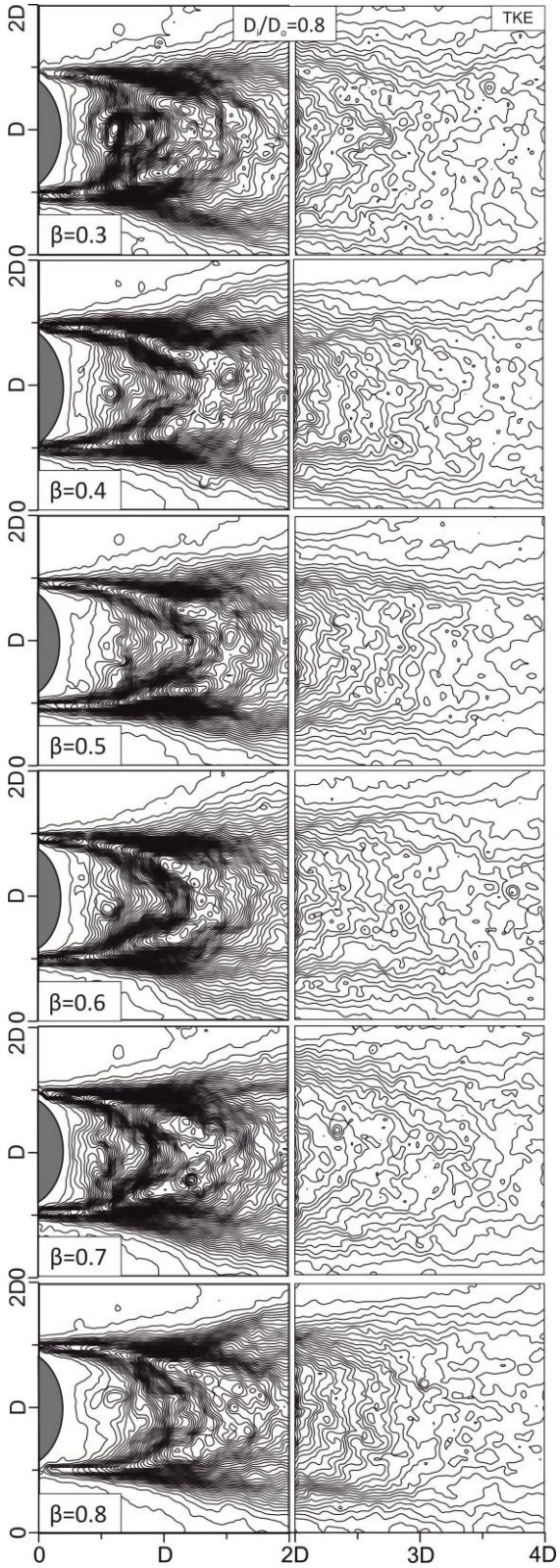


Figure 4.77. The TKE distribution downstream of the cylinder surrounded with arc ($\alpha=120^o$) for $D_i/D_o=0.8$ at different β cases

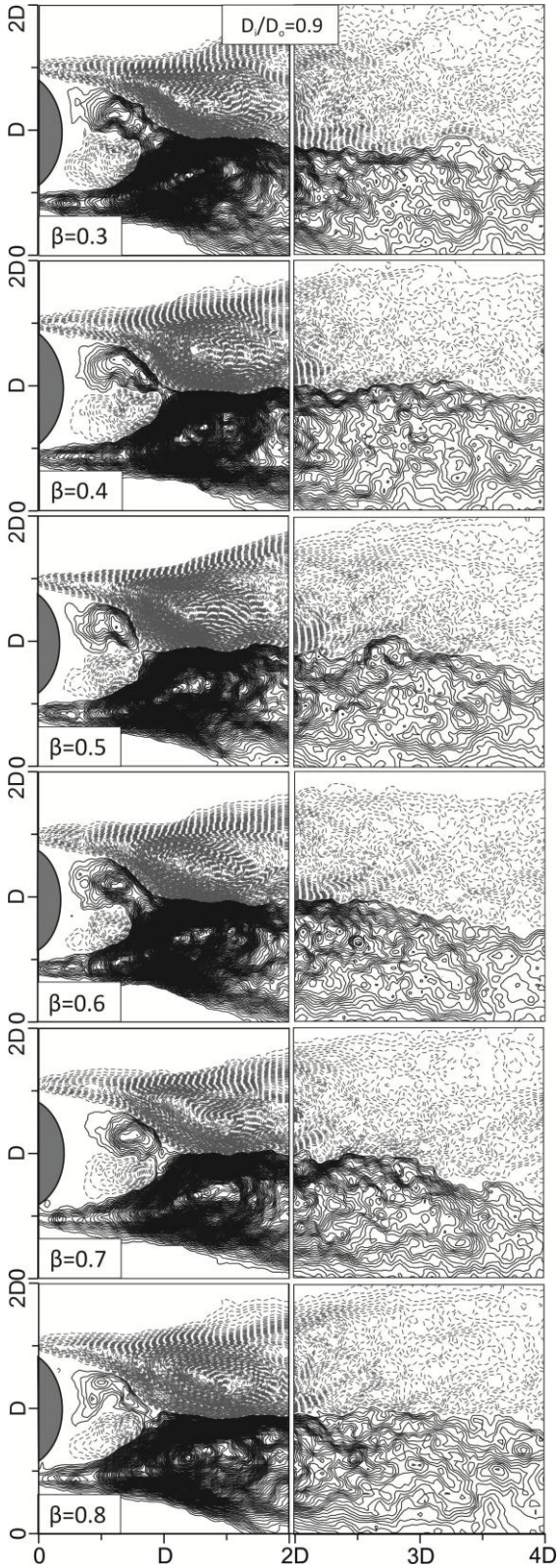


Figure 4.78. The Reynolds shear stress distribution downstream of the cylinder surrounded with arc ($\alpha=120^o$) for $D_i/D_o=0.9$ at different β cases

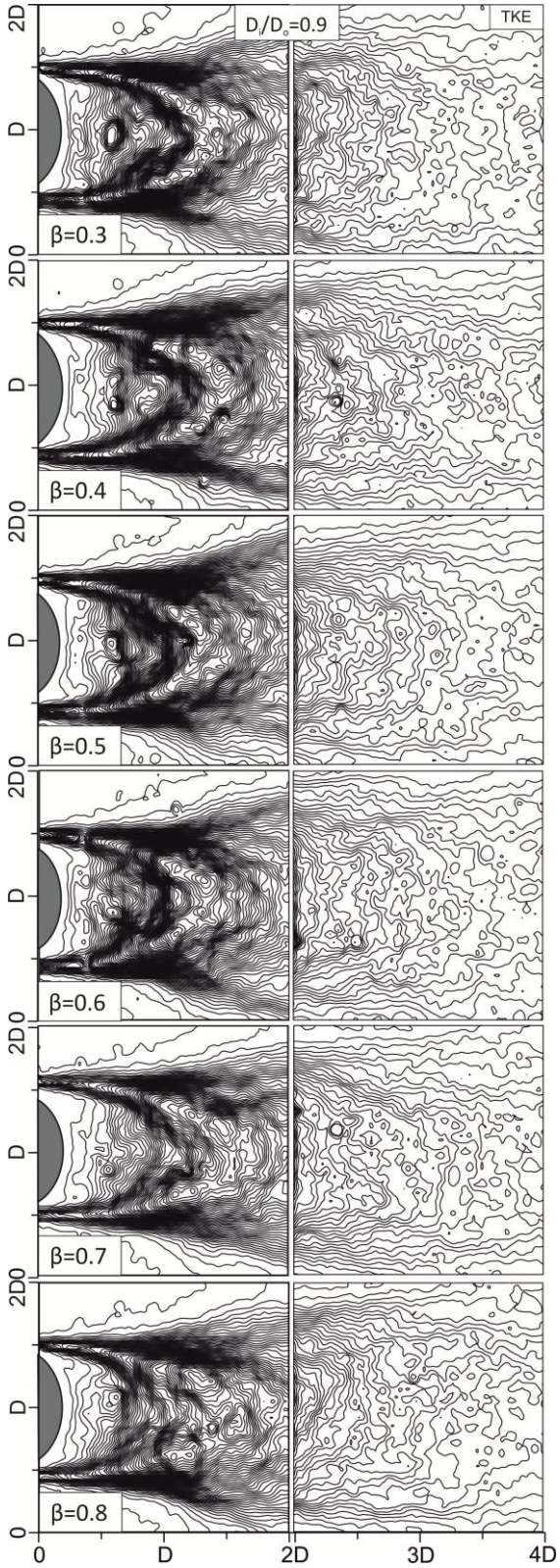


Figure 4.79. The TKE distribution downstream of the cylinder surrounded with arc ($\alpha=120^o$) for D_i/D_o=0.9 at different β cases

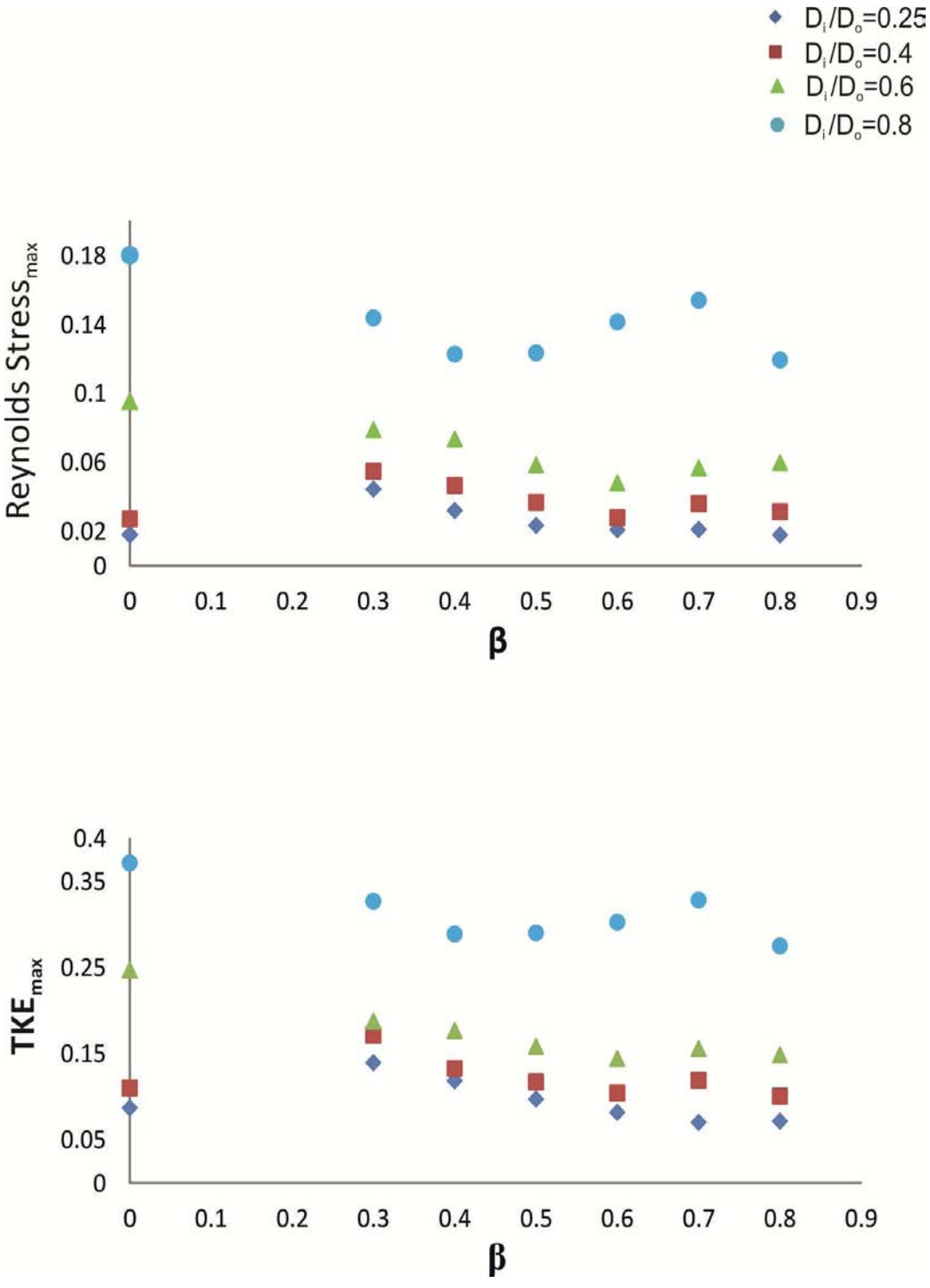


Figure 4.80. The variation of Reynolds stress$_{max}$ and TKE$_{max}$ with β to demonstrate the effect of D_i/D_o for $\alpha=120^o$

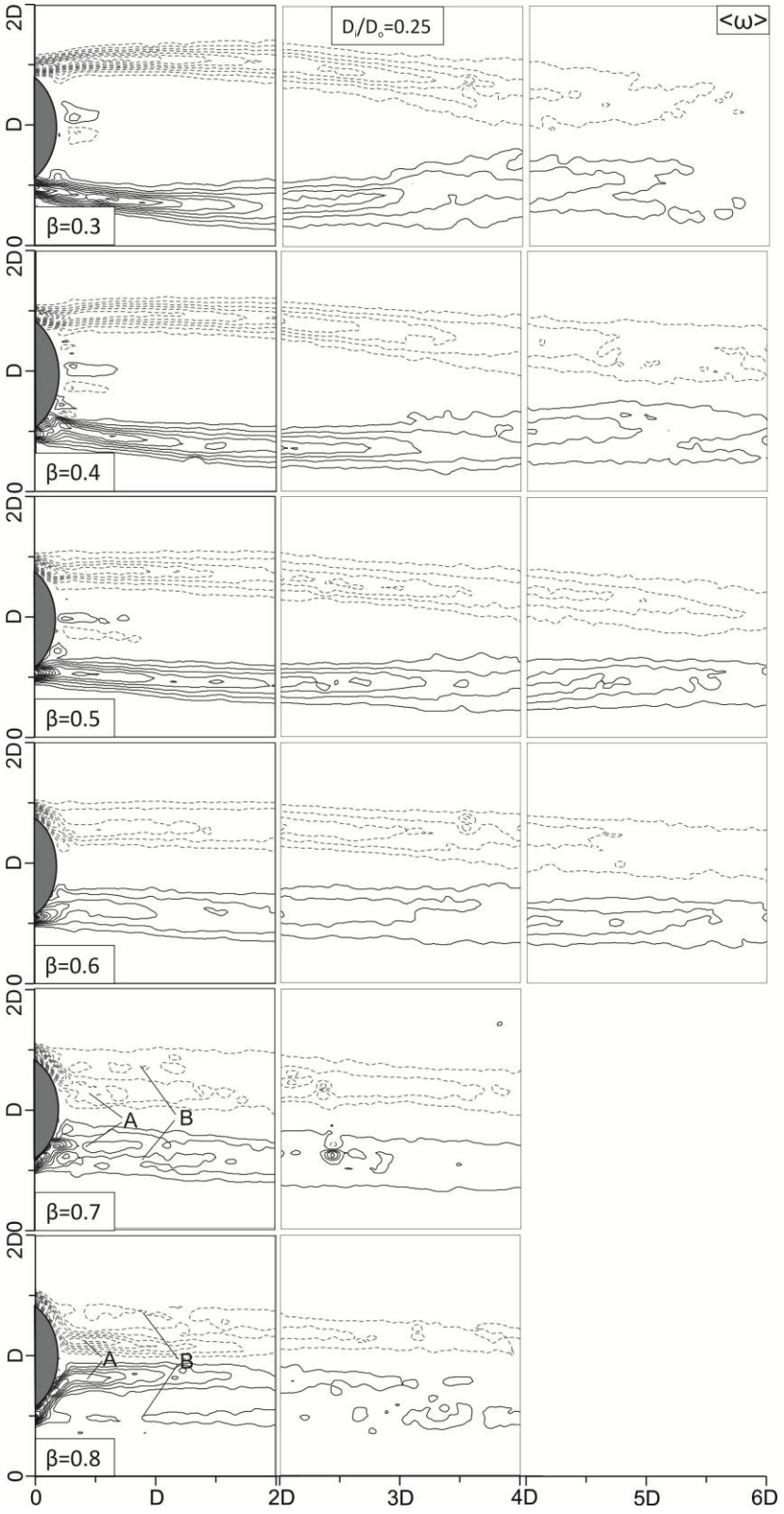


Figure 4.81. The vorticity distribution downstream of the cylinder surrounded with arc ($\alpha=120^o$) for $D_i/D_o=0.25$ at different β cases

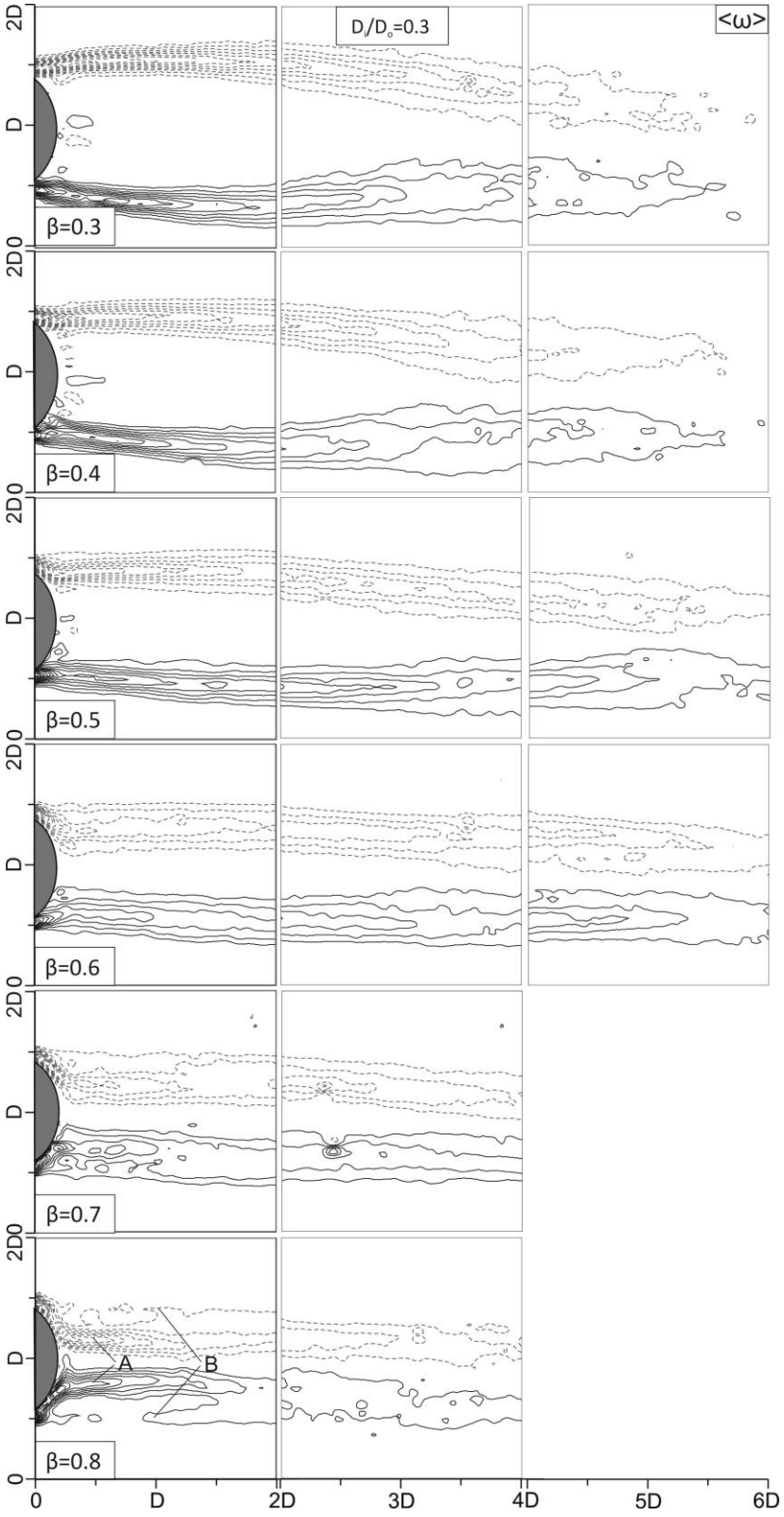


Figure 4.82. The vorticity distribution downstream of the cylinder surrounded with arc ($\alpha=120^o$) for $D_i/D_o=0.3$ at different β cases

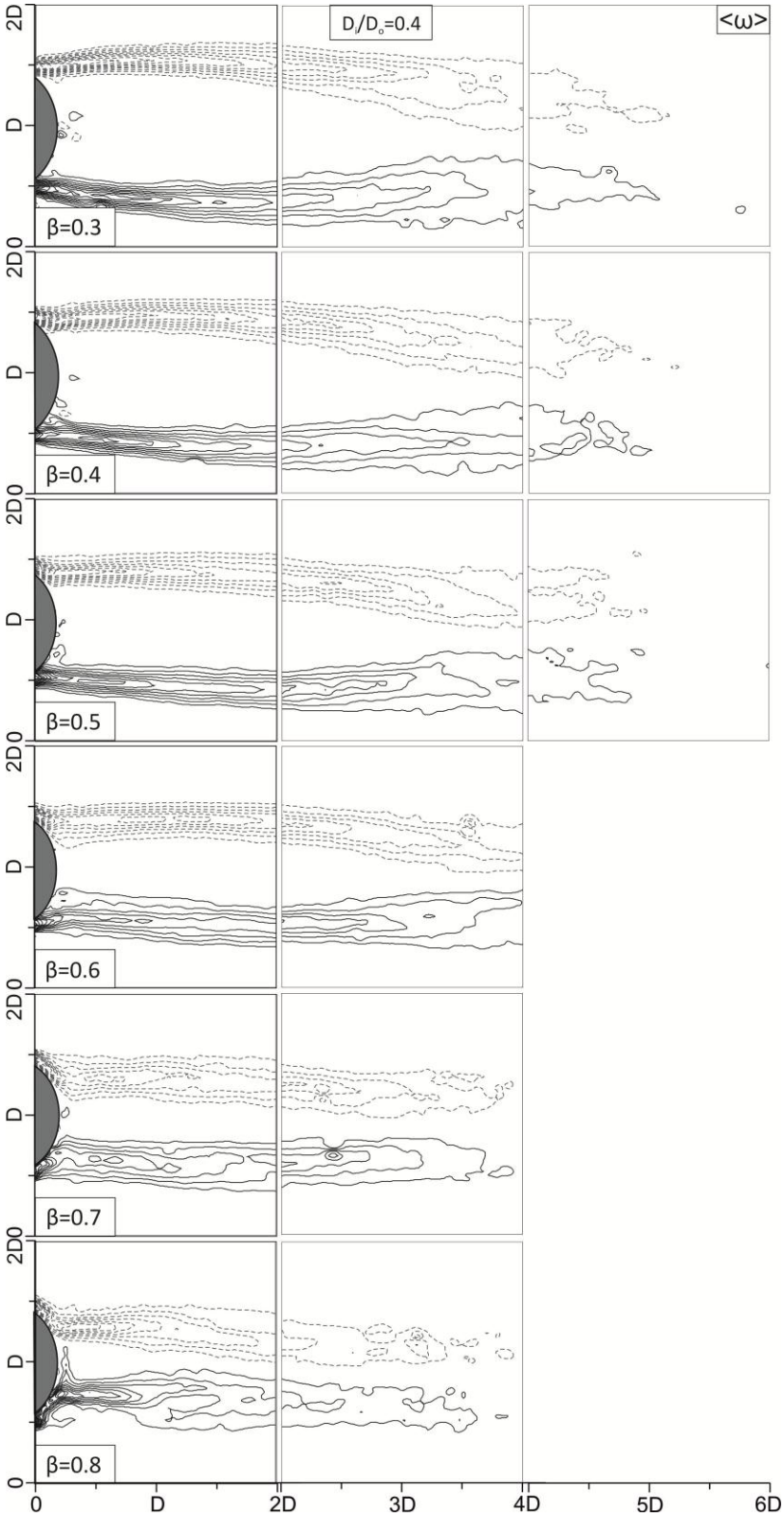


Figure 4.83. The vorticity distribution downstream of the cylinder surrounded with arc ($\alpha=120^o$) for $D_i/D_o=0.4$ at different β cases

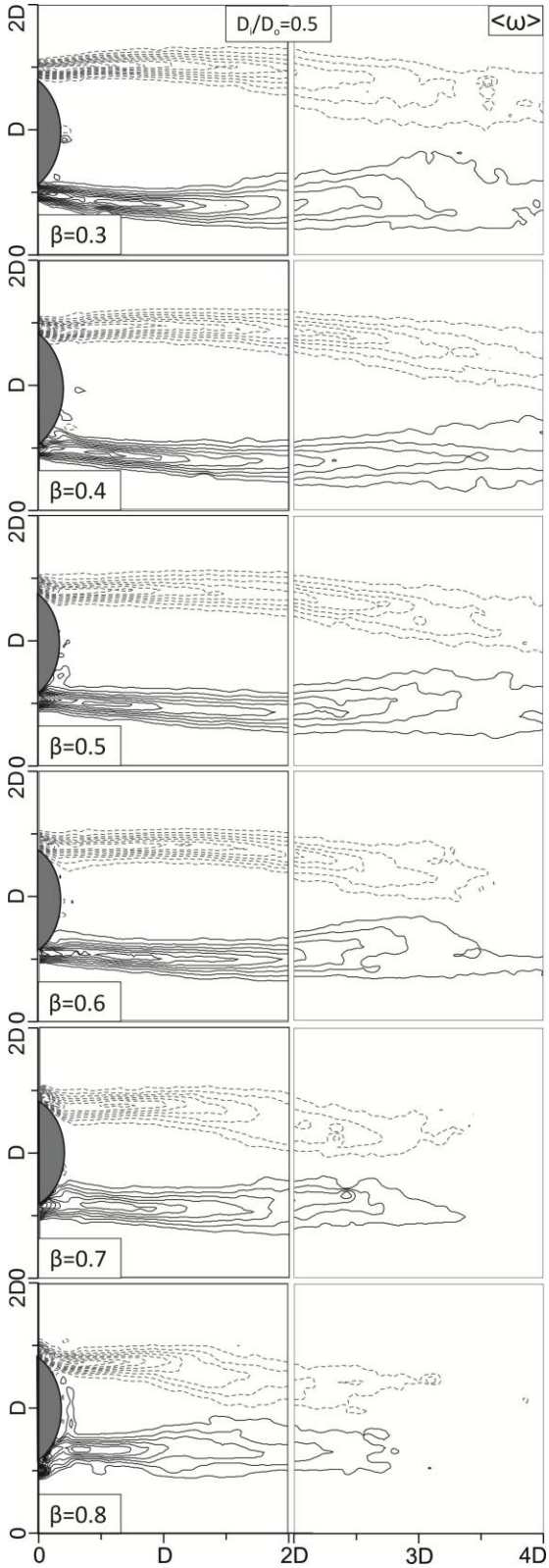


Figure 4.84. The vorticity distribution downstream of the cylinder surrounded with arc ($\alpha=120^o$) for $D_i/D_o=0.5$ at different β cases

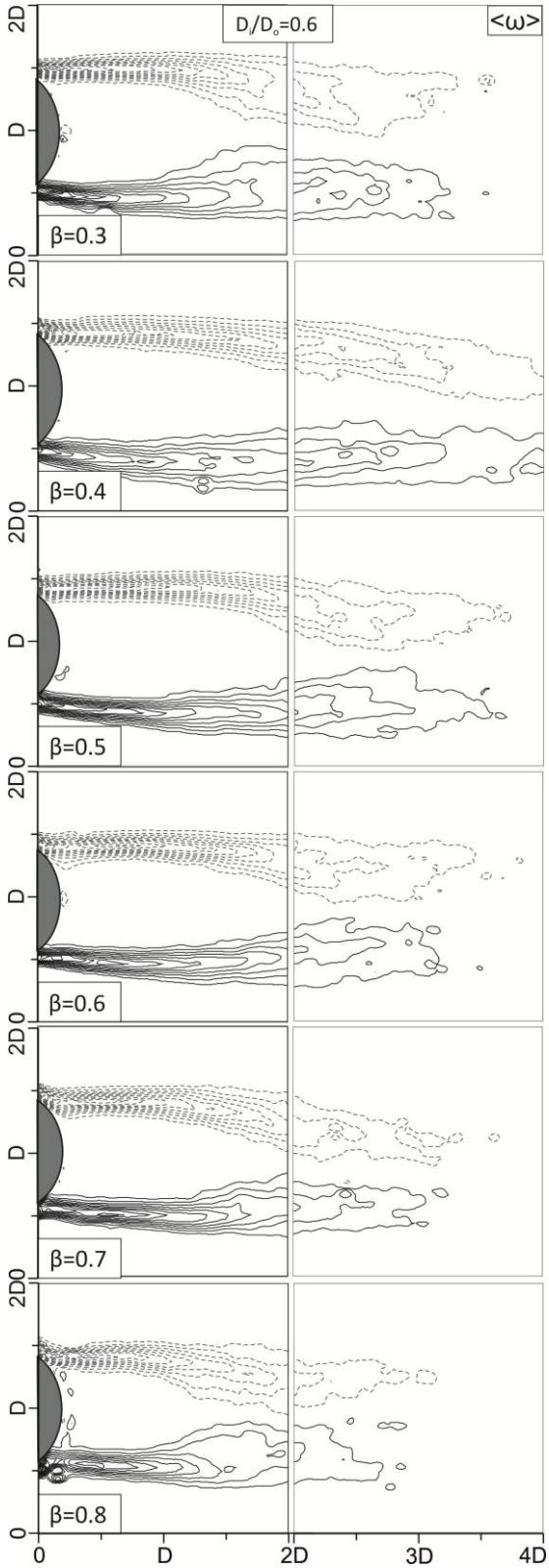


Figure 4.85. The vorticity distribution downstream of the cylinder surrounded with arc ($\alpha=120^o$) for $D_i/D_o=0.6$ at different β cases

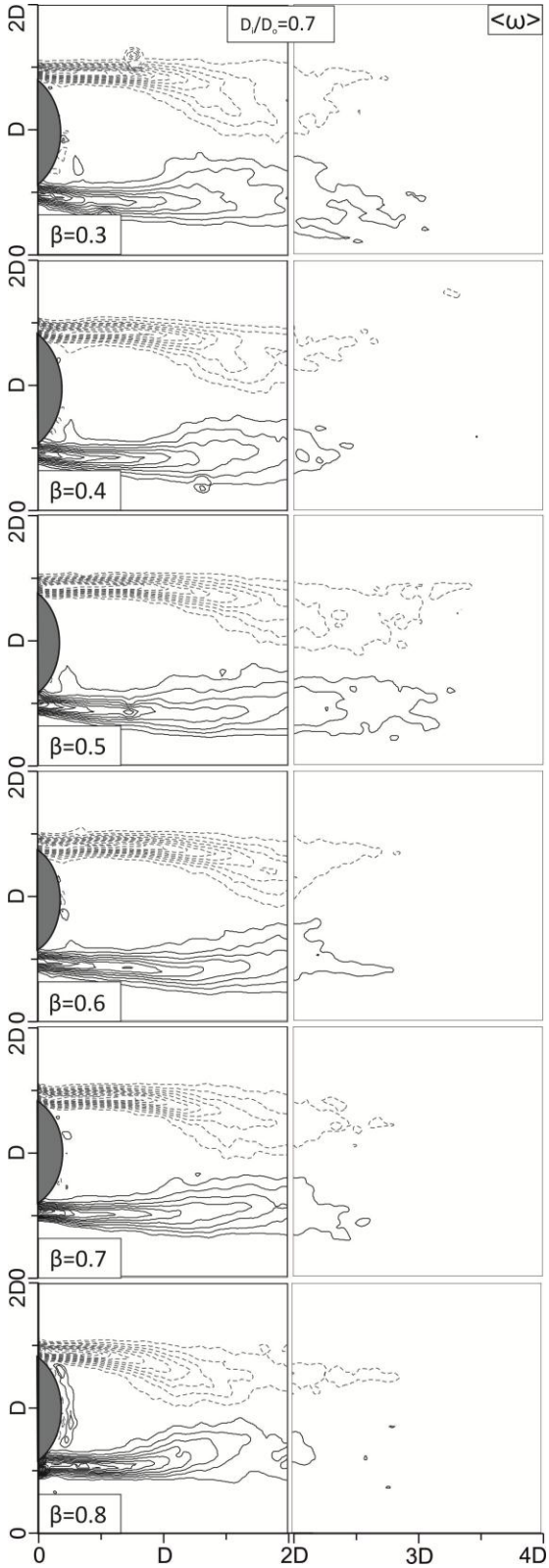


Figure 4.86. The vorticity distribution downstream of the cylinder surrounded with arc ($\alpha=120^o$) for D_i/D_o=0.7 at different β cases

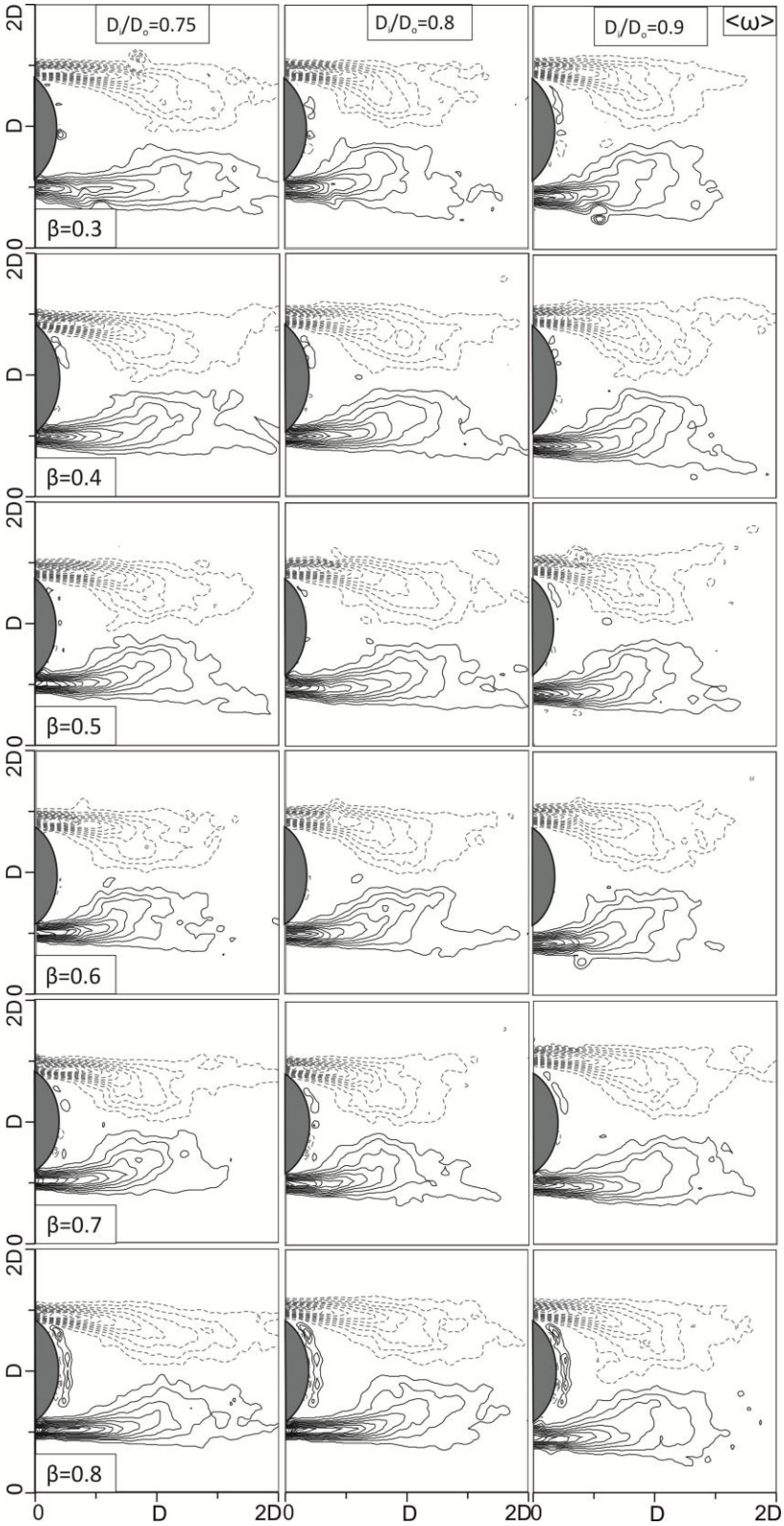


Figure 4.87. The vorticity distribution downstream of the cylinder surrounded with arc ($\alpha=120^o$) for $D_i/D_o=0.75$, $D_i/D_o=0.8$, $D_i/D_o=0.9$ at different β cases

4.1.2.4. Effect of Outer Geometries on Flow Structure

In Figure 4.88, variation of the peak magnitude of Reynolds shear stress obtained from angle of arc $\alpha=180^o$, 150^o and 120^o with the porosity are presented for different diameter ratios. When compared with the bare cylinder, at $D_i/D_o=0.25$ diameter ratio, low porosities (particularly $\beta=0.3$) further increase the Reynolds shear stress contours for $\alpha=150^o$ and $\alpha=120^o$. The results of higher porosities are close to each other for all arc angle. The reason of this is the fact that at high porosity number of the holes on the outer cylinder surface increases and loose its effect on the flow structure. The values obtained at $\beta=0.8$ are completely formed from the inner cylinder. The effect of arc angle becomes more obvious at higher diameter ratios. It is demonstrated that the optimum angle of arc is $\alpha=180^o$. Consequently, a decrease in Reynolds stress should be directly related to the drag force reduction of the circular cylinder as obtained by Fujisawa and Takeda (2003), Kim et al. (2006).

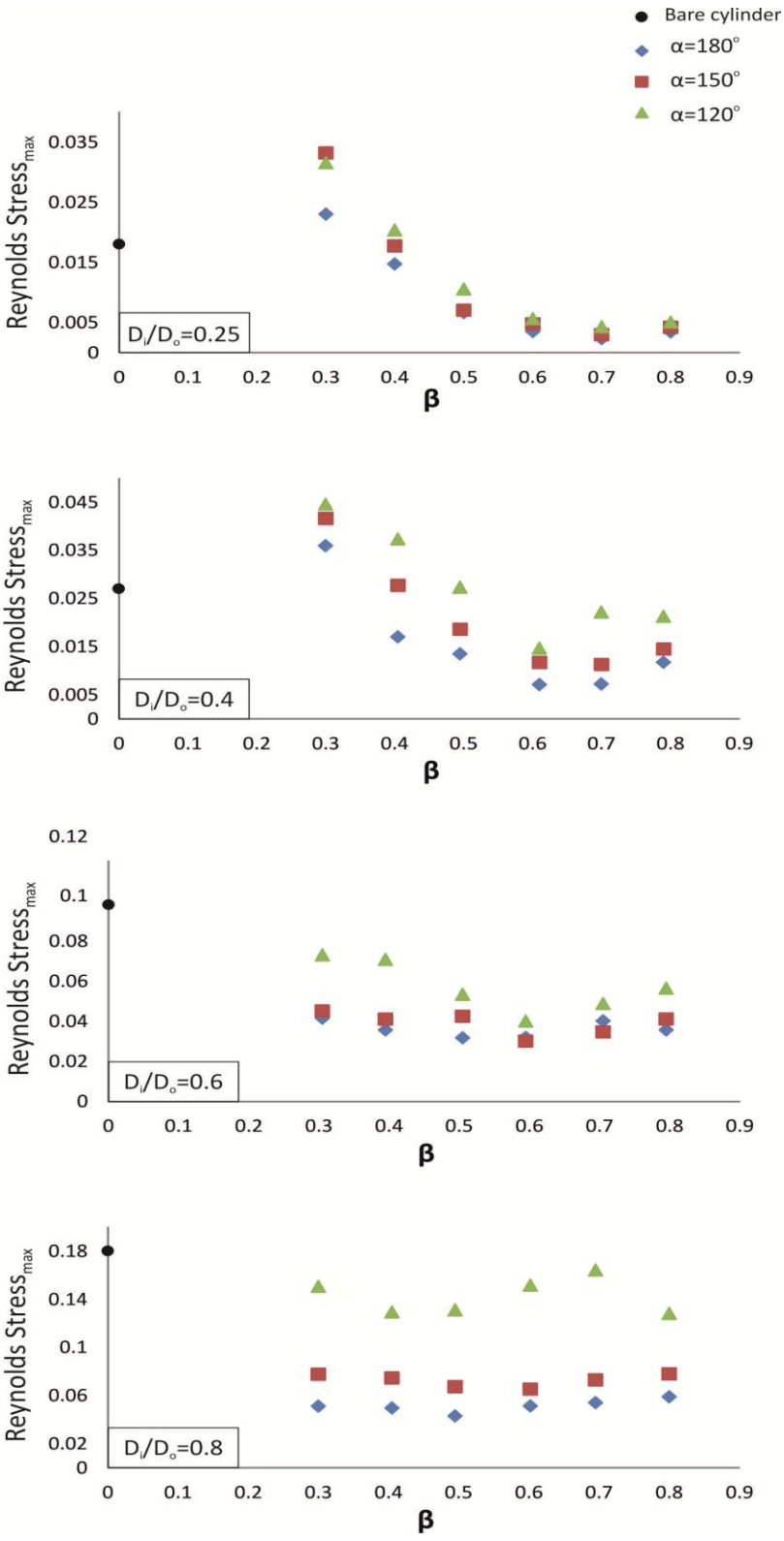


Figure 4.88. The variation of Reynolds stress$_{max}$ with β to demonstrate the effect of α for different D_i/D_o

5. CONCLUSIONS

In this study the effects of perforated semi cylinders (D_o) on the flow characteristics in the near wake of a circular cylinder (D_i) in shallow water were investigated quantitatively using Particle Image Velocimetry (PIV) techniques. Porosity of the outer cylinder (β), diameter ratio of the inner and outer cylinders (D_i/D_o) and the arc angle of the outer cylinder (α) were chosen as the parameters. In order to investigate the effect of porosity on the unsteady flow structure in the near wake region of the inner cylinder, half and quarter ($\alpha=180^0$, 150^0 and 120^0) outer cylinders of six different porosity (β=0.3, 0.4, 0.5, 0.6, 0.7 and 0.8) were used. The effect of diameter ratio (inner cylinder diameter / outer cylinder diameter) was also investigated by considering nine different diameter ratios as D_i/D_o=0.25, 0.3, 0.4, 0.5, 0.6, 0.7, 0.8 and 0.9.

Outer cylinder arc angle is an important parameter affecting the flow structure. The most effective control was obtained from the application with $\alpha=180^o$ spring length. Between the β=0.5-0.6 values of porosity, unsteady vortices formed in the near wake region of the inner cylinder are controlled for the most effective case. Although turbulence in the near wake increases at lower porosities, the values obtained at high diameter ratios are lower than the values obtained from the case of the bare cylinder. In comparison with the values obtained from the bare cylinder application, at D_i/D_o=0.75 diameter ratio and β=0.5 porosity, turbulence statistics are reduced by 80%. Also, the point, which the values of maximum turbulence statistics (Reynolds shear stress and Turbulence Kinetic Energy), shifts to a farther downstream compared to the case of outer cylinder. Particularly at D_i/D_o=0.5 diameter ratio, this point is shifted by 5D away from the cylinder. At porosity values larger than β=0.6, the effect of the outer cylinder on the inner cylinder decreases. Furthermore, an unsteady flow structure is formed in the near wake region of the outer cylinder.

REFERENCES

ABERGEL, F., TEMAM, R., 1990. On some control problems in fluid mechanics. Theoretical and Computational Problems in Fluid Dynamics, 1:303–325.

AKILLI, H., and ROCKWELL, D., 2002. Vortex formation from a cylinder in shallow water. Physics of Fluids, Turkey, 14 (9): 2957-2967.

AKILLI, H., AKAR, A., and KARAKUS, C., 2004. Flow Characteristics of Circular Cylinders Arranged Side-By-Side in Shallow Water. Flow Measurement and Instrumentation, Turkey, 15, 187–197.

AKILLI, H. , SAHIN, B. , TUMEN, N.F. , 2005. Suppression of vortex shedding of circular cylinder in shallow water by a splitter plate. Flow Measurement and Instrumentation, Turkey, 16:211–219.

AKILLI, H., KARAKUS, C. , AKAR, A. , SAHIN, B. , TUMEN, N.F. , 2008. Control of vortex shedding of circular cylinder in shallow water flow using an attached splitter plate. Journal of Fluids Engineering-T ASME, Turkey, 130:041401.

ALAM, M.M., MORIYA, M., TAKAI, K., SAKAMOTO, H., 2002. Suppression of fluid forces acting on two square prisms in tandem arrangement by passive control of flow, Journal of Fluids and Structures, 16 (8) 1073–1092.

ALAM, M.M., MORIYA, M., TAKAI, K., SAKAMOTO, H., 2003. Fluctuating fluid forces acting on two circular cylinders in tandem arrangement at a subcritical Reynolds number. Journal of Wind Engineering & Industrial Aerodynamics, 91, 139–154.

ALAM, M.M., SAKAMOTO, H., MORIYA, M., 2003. Reduction of fluid forces acting on a single circular cylinder and two circular cylinders by using tripping rods, Journal of Fluids and Structures, 18 (3–4) 347–366.

APELT, B., WEST, G.S., SZEWCZYK, A.A., 1973. The effects of wake splitter plates on the flow past a circular cylinder in the range $10^4 < Re < 10^5$, Journal of Fluid Mechanics, 61 (1) 187–198.

ASSI, G.R.S., BEARMAN, P.W., KITNEY, N., 2009. Low drag solutions for suppressing vortex-induced vibration of circular cylinders. Journal of Fluids and Structures, UK, 25 (2009) 666–675.

ASSI, G.R.S., BEARMAN, P.W., KITNEY, N., TOGNARELLI, M.A., 2010. Suppression of wake-induced vibration of tandem cylinders with free-to-rotate control plates. Journal of Fluids and Structures, Brazil, 26 (2010) 1045–1057.

BADR, H., COUTANCEAU, M., DENNIS, S., MENARD C., 1990. Unsteady flow past a rotating circular cylinder at Reynolds numbers 1000 and 10000. Journal of Fluid Mechanics, 220:459– 484.

BAEK, S.J., and SUNG, H.J., 1998. Numerical simulation of the flow behind a rotary oscillating circular cylinder. Physics of Fluids, 10, 869}876.

BAEK, H., KARNIAKIDIS, G.E., 2009. Suppressing vortex-induced vibrations via passive means. Journal of Fluids and Structures, USA, 25 (2009) 848–866.

BALACHANDAR, R., CHU, V.H., and ZHANG, J., 1997. Experimental study of turbulent concentration flow field in the wake of a bluff body. Journal of Fluid Engineering, 199: 263-270.

BALACHANDAR, R., CHU, V.H., and ZHANG, J., 1997. Properties of the mean wake recirculation region in two-dimensional bluff body wakes. Journal of Fluid Mechanics, 351, 167–199.

BALACHANDAR, R., TACHIE, T.M., and CHU, V.H., 1999. Concentration profiles in shallow turbulent wakes. Journal of Fluids Engineering, 121: 34-43.

BALACHANDAR, R., and RAMACHANDRAN, S., 1999. Turbulent boundary layers in low Reynolds number shallow open channel flows. Journal of Fluids Engineering, 121: 684-689.

BALACHANDAR, R., RAMACHANDRAN, S., and TACHIE, M.F., 2000. Characteristic of shallow turbulent near wakes at low Reynolds number. Journal of Fluid Engineering, 122: 302-308.

BALACHANDAR, R., and TACHIE, T.M., 2001. A study of boundary layer-wake interaction in shallow open channel flows experiments in Fluids, 30: 511-521.

BAZ, A. and RO, J. 1991 Active control of flow-induced vibrations of a flexible cylinder using direct velocity feedback. Journal of Sound and vibration, 146, 33-45.

BEARMAN, P.W., 1965. Investigation of flow behind a two-dimensional model with blunt trailing edge and fitted with splitter plates, Journal of Fluid Mechanics, 21, 241–255.

_____,1984. Vortex shedding from oscillating bluff bodies. Annual Review of Fluid Mechanics, 16, 195-222.

BEARMAN, P.W., OWEN, J.C., 1997. Reduction of bluff-body drag and suppression of vortex shedding by the introduction of wavy separation lines. Journal of Fluids and Structures, UK, 12, 123-130.

BEARMAN, P., BRANKOVIC, M., 2003. Experimental studies of passive control of vortex-induced vibration. European Journal of Mechanics B/Fluids, UK, 23: 9-15.

BISHOP, R. E. D. and HASSAN, A. Y., 1964. The lift and drag forces on a circular cylinder oscillating in a flowing fluid, Proc. R. Soc., London, Ser. A 277, 51.

BLACKBURN, H. M. and HENDERSON, R. D., 1999. A study of two-dimensional flow past an oscillating cylinder, Journal of Fluid Mechanics, 385, 255.

BLOOR, M.S., 1964. The transition to turbulence in the wake of a circular cylinder. Journal of Fluid Mechanics, 19: 290-304.

CHEN, D., and JIRKA, H., 1995. Experimental study of plane turbulent wakes in a shallow water layer. Fluid Dynamics Research, 16: 11-41.

CHEN, D., and JIRKA, H., 1997. Absolute and convective instabilities of plane turbulent wakes in a shallow water layer. Journal of Fluid Mechanics, 338: 157-172.

CHEN, Z., NADINE, A., 2003. Active control of cylinder wake. Communications in Nonlinear Science and Numerical Simulation, China, 10 (2005) 205–216.

CHU, H.V., WU, J.H., KHAYAT, R.E., 1991. Stability of transverse shear flows in shallow open channels. Journal of Hydraulic Engineering, 117(10): 1370-1388.

CIMBALA, J. N., NAGIB, H.M., and ROSHKO, A., 1988. Large structure in the far wakes of two-dimensional bluff bodies, J. Fluid Mech., 190, 265.

FENG, L.H., WANG, J.J., PAN, C., 2010. Effect of novel synthetic jet on wake vortex shedding modes of a circular cylinder. Journal of Fluids and Structures, China, 26 (2010) 900–917.

FFOWCS-WILLIAMS, J.E., and ZHAO, B.C., 1989. The active control of vortex shedding. Journal of Fluids and Structures, 3, 115-122.

FILLER, J.R., MARSTON, P.L. and MIH, W.C., 1991. Response of the shear layers separating from the circular cylinder to small amplitude rotational oscillations. Journal of Fluid Mechanics, 231, 481-499.

FUJISAWA, N., TAKEDA, G., IKE, N., 2003. Flow control around a circular cylinder by internal acoustic excitation. J Fluid Struct, 17:903–913.

FUJISAWA, N., TAKEDA, G., IKE, N., 2004. Phase-averaged characteristics of flow around circular cylinder under acoustic excitation control. Journal of Fluids and Structures, Japan, 19 (2004) 159–170.

GALVAO, R., LEE, E., FARRELL, D., HOVER, F., TRIANTAFYLLOU, M., KITNEY, N., BEYNET, P., 2008. Flow control in flow–structure interaction. Journal of Fluids and Structures, USA, 24: 1216-1226.

GERARD, J.H., 1964. The mechanics of the formation region of vortices behind bluff bodies. Journal of Fluid Mechanics, 25: 401-413.

_____, 1966. The mechanics of formation region of vortices behind bluff bodies, J. Fluid Mech. 25 401–413.

_____, 1966. The mechanics of formation region of vortices behind bluff bodies, J. Fluid Mech., 25 401–413.

_____, 1978. The wakes of cylindrical bluff bodies at low Reynolds number. Phil. Trnas. R. Soc. London A, 288: 351-382.

GIORIA, R.S., JABARDO, P.J.S., CARMO, B.S., MENEGHINI, J.R., 2009. Floquet stability analysis of the flow around an oscillating cylinder. Journal of Fluids and Structures, UK, 25 (2009) 676–686.

GRIFFIN, O. M. and VOTAW, C. W., 1972. The vortex street in the wake of a vibrating cylinder, Journal of Fluid Mechanics, 55, 31.

GRIFFIN, M.O., 1978. A universal Strouhal number for the 'locking-on' of vortex shedding to the vibration of bluff cylinders, J. Fluid Mech., 85 591–606.

GRIFFIN, M., and HALL, M.S., 1991. Vortex shedding lock-in and flow control in bluff body wakes. ASME Journal of Fluids Engineering, 113, 526-537.

GRUBISIC, V., SMITH, R. B. and SCHAR, C., 1995. The effect of bottom friction on shallow-flow past an isolated obstacle. J. Atmos. Sci. 48, 1985–2006.

HO, C.M., AND HUERRE, P., 1984. Perturbed free shear layers. Annual Review of Fluid Mechanics, 16: 365-424.

IGARASHI, T., 1978. Flow characteristics around a circular cylinder with a slit. Bull. Japan. Soc. Mech. Engrs, 21, 656–664.

INGRAM, G.R. and CHU, V.H., 1987. Flow around islands in Rupert bay: an investigation of the bottom friction effect. J. Geophys. Res., 92 (C13), 14521–14533.

INOUE, O., 1985. A new approach to flow problems past a porous plate. AIAA Journal, 23, 1916–1921.

KAHRAMAN, A., SAHIN, B., and ROCKWELL, D., 2002. Control of vortex formation a vertical cylinder in shallow water: Effect of localized roughness elements. Experiments in Fluids, 33: 54-65.

KIM, W., YOO, J.Y., SUNG, J., 2006. Dynamics of vortex lock-on in a perturbed cylinder wake. Phys Fluids, 18:074103.

KIM, S., ALAM, Md.M., SAKAMATO, H., ZHOU, Y., 2009. Flow-induced vibration of two circular cylinders in tandem arrangement. Part 2: Suppression of vibrations. Journal of Wind Engineering and Industrial Aerodynamics, Japan, 97: 312-319.

KNELL, B.J., 1969.The drag of a circular cylinder fitted with shrouds, Natl. Phys. Lab., UK, Aero. Rep. no. 1297.

KONSTANTINIDIS, E., BALABANI, S., 2007. Symmetric vortex shedding in the near wake of a circular cylinder due to streamwise perturbations. Journal of Fluids and Structures, Greece, 23 (2007) 1047–1063.

KUMAR, R.A., SOHN, C-H., and BANGALORE, H.L., 2008. Passive Control of Vortex-Induced Vibrations: An Overview. Recent Patents on Mechanical Engineering, Korea, 1, 1-11.

KUO, C.-H., CHIOU, L.-C., CHEN, C.-C., 2007. Wake flow pattern modified by small control cylinders at low Reynolds numer. Journal of Fluids and Structures, Taiwan, 23 (2007) 938–956.

KUO, C.-H., CHEN, C.-C., 2009. Passive control of wake flow by two small control cylinders at Reynolds number 80. Journal of Fluids and Structures, Taiwan, 25 (2009) 1021–1028. Journal of Fluids and Structures, Republic of Korea, 24 (2008) 2–17.

KWON K., CHOI, H., 1996, Control of laminar vortex shedding behind a circular cylinder using splitter plates. Physics of Fluids, 10:479– 485.

LEE, S.-J., LEE, J.-Y., 2008. PIV measurements of the wake behind a rotationally oscillating circular cylinder. Journal of Fluids and Structures, Republic of Korea, 24 (2008) 2–17.

LIM, H.-C., LEE, S.-J., 2004. Flow control of a circular cylinder with O-rings. Fluid Dynamics Research, South Korea, 35 (2004), 107-122.

LLOYD, P.M., and STANSBY, P.K., 1997. Shallow-water flow around model conical island of small side slope. I: Surface piercing. Journal of Hydraulic Engineering, 123: 1057-1067.

MUDDADA, S., PATNAIK, B.S.V., 2009. An active flow control strategy for the suppression of vortex structures behind a circular cylinder. Europian Journal of Mechanics B/Fluids, India, 29 (2010) 93–104.

NAKAMURA, H., IGARASHI, T., 2008. Omnidirectional reductions in drag and fluctuating forces for a circular cylinder by attaching rings. Journal of Wind Engineering, Japan, 96 (2008) 887–899.

OKAJIMA, A., TAKATA, H., and ASANUMA, T., 1975. Viscous flow around a rotationally oscillating circular cylinder. Reports of Institute of Space and Aeronautical Science, Tokyo, (532), 311-338.

ONGOREN, A., and ROCKWELL, D., 1988. Flow structure from an oscillating cylinder Part 1. Mechanisms of phase shift and recovery in the near wake. Journal of Fluid Mechanics, 191:197- 223

ONGOREN, A., and ROCKWELL, D., 1988. Flow structure from an oscillating cylinder Part 2. Model competition in the near wake. Journal of Fluid Mechanics, 191:225-245

OWEN, J.C., BEARMAN, P.W., and SZEWCZYK, A.A., 2001. Passive control of VIV with drag reduction. Journal of Fluids and Structures, UK, (2001) 15, 597-605.

OZONO, S., 1999. Flow control of vortex shedding by a short splitter plate asymmetrically arranged downstream of a cylinder. Physics of Fluids, 11, (10):2928 –2934.

RAY, P., CHRISTOFIDES, P.D., 2005. Control of flow over a cylinder using rotational oscillations. Computers&Chemical Engineering, USA, 29 (2005) 877–885.

ROSHKO, A., 1954.On the drag and shedding frequency of two-dimensional bluff bodies, NACA Tech. Note no.3169.

ROUSSOPOULOS, K., 1993. Feedback control of vortex shedding at low Reynolds numbers. Journal of Fluid Mechanics, 24, 267-296.

SAAD, M., LEE, L., LEE, T., 2007. Shear layers of a circular cylinder with rotary oscillation. Experiments in Fluids, 43:569–578.

SCHAR, C., and SMITH R.B., 1993. Shallow water flow past isolated topography. Part II: Transition to vortex shedding. Journal of the Atmospheric Sciences, 50: 1401-1412.

SHENG, J., MENG, H. , FOX, R.O. , 2000. A large eddy PIV method for turbulence dissipation rate estimation. Chemical Engineering Science, 55:4423–4434.

STRYKOWSKI, P.J. and SREENIVASAN, K.R. 1990 On the formation and suppression of vortex shedding at low-Reynolds-numbers. Journal of Fluid Mechanics 218, 71–107.

SHUKLA, S., GOVARDHAN R.N., ARAKERI J.H., 2009. Flow over a cylinder with a hinged-splitter plate. Journal of Fluids and Structures, India, 25: 713-720.

TACHIE, T.M., BALACHANDAR, R., 2001. Shallow wakes generated on smooth and rough surfaces. Experiments in Fluids, 30:467-474.

TANEDA, S., 1978. Visual observations of the flow past a circular cylinder performing a rotary oscillation. Journal of Physical Society of Japan, 45, 1038-1043.

TAO J.S., HUANG X.Y., CHAN, W.K., 1996. A flow visualization study of feedback control of vortex shedding from a circular cylinder. Journal of Fluids and Structures, 10:965 –970.

TEXIER, A., BUSTAMANTE, A.S.C., DAVID L., 2002. Contribution of a short separating plate on the control of the swirling process downstream a half-cylinder. Experimental Thermal and Fluid Science, France, 26: 565–572.

TOKUMARU, P.T., and DIMOTAKIS, P.E., 1991. Rotary oscillation control of a cylinder wake. Journal of Fluid Mechanics, 224, 77-90.

TURHAL, A.O., CUHADAROGLU, B., 2010. The effects of surface injection through a perforated square cylinder on some aerodynamic parameters. Experimental Thermal and Fluid Science, Turkey, 34 (2010) 725–735.

UNAL, M.F., and ROCKWELL, D., 1988. On vortex formation from a cylinder, Part 2: Control by Splitter-Plate Interference. Journal of Fluid Mechanics, 190: 513 529.

WANG, J., SHAN, R., ZHANG, C., FENG, L., 2010. Experimental investigation of a novel two-dimensional synthetic jet. European Journal of Mechanics B/Fluids, China, 29 (2010) 342_350.

WILLIAMSON, C.H.K. and ROSHKO, A., 1988. Vortex formation in the wake of an oscillating cylinder. Journal of Fluids and Structures, 2:355-381.

WOLANSKI, E., IMBERGER, J., and HERON, M.L., 1984. Island wakes in shallow coastal water. Journal of Geophysical Research, 89: 10553-10569.

WONG, H. Y., 1985. Wake stabilization by the action of base bleed. Trans. ASME: J. Fluids Engineering, 107, 378–384.

WOOD, C. J., 1964. The effect of base bleed on a periodic wake. J. R. Aero. Soc. 68, 477–482.

_____, 1967. Visualization of incompressible wake with base bleed, Journal of Fluid Mechanics, 29, (2) 259–272.

WU, W., YUAN, J., CHENG, L., 2007. Multi-high-frequency perturbation effects on flow-induced vibration control. Journal of Sound and Vibration, Hong Kong, 305, 226–242.

ZDRAVKOVICH, M. M. 1981 Review and classification of various aerodynamic and hydrodynamic means for suppressing vortex-shedding. J. Wind Engrs Indust. Aerodyn. 7, 145–189.

ZHANG, H., FAN, B.-C.., CHEN, Z.-H., 2009. Optimal control of cylinder wake flow by electro-magnetic force based on adjoint flow field. European Journal of Mechanics B/Fluids, China, 29, 53–60.

ZHANG, H., FAN, B.-C.., CHEN, Z.-H., 2010. Computations of optimal cylinder flow control in weakly conductive fluids. Computers&Fluids, China, 39 1261–1266.

ZHOU, L., CHENG, M.,HUNG, K.C., 2005. Suppression of fluid force on a square cylinder by flow control. Journal of Fluids and Structures, China, 21 151–167.

ZOU, L., LIN, Y., 2009. Force reduction of flow around a sinusoidal wavy cylinder. Journal of Hydrodynamics, China, 21(3):308-315.

CURRICULUM VITAE

Tahir DURHASAN was born in Adana in 1987. He finished Turgut Ozal High School in Adana and after the graduation he entered in Mechanical Enginnering Department of Ataturk University. He graduated as a Mechanical Engineer from the university in June 2009. He is working as a research assistant from August 2010.